In-situ Impedance Spectroscopy Studies of the Plasma Electrolytic Oxidation Coating Process

This dissertation submitted in partial fulfilment of the requirements for the degree of Doctor of Philosophy

by

Chen-Jui Liang

The University Of Sheffield.

Department of Materials Science and Engineering

June 2013

© 2013 C.J. Liang

ABSTRACT

Plasma electrolytic oxidation (PEO) is a relatively novel surface modification technique that provides excellent wear- and corrosion-resistant coatings on light-weight metals, in particular on aluminium. Formation of PEO coatings involves complex processes and mechanisms that are difficult to study. In this work, a new method of in-situ impedance spectroscopy is used to provide new insights into fundamental characteristics of PEO processes and coating formation mechanisms as well as to develop new means of process control.

This method is based on application of a variable frequency voltage perturbation signal to obtain impedance characteristics of the electrolyser during the PEO processing. The applied voltage signal and the current response are collected and post-processed to verify the system linearity, refine phase, reduce noise and spline the impedance spectra. The obtained spectra are then fitted with appropriate equivalent circuits to reveal mechanisms underlying the PEO process. Physical meaning of various circuit components is verified using specially designed experiments in which certain system characteristics are set up in such way to obtain controllable processing conditions, such as electric field distribution in the electrolyser, electrolyte resistance or coating thickness. The circuit analysis reveals specific RC and RL loops that can be related to individual processes associated with interfacial charge transfer and transport phenomena. Characteristic time constants corresponding to these processes are evaluated and their evolution with PEO treatment time is considered. Correlations of the process kinetics with phenomena observed during the PEO treatment of Al and coating growth characteristics are discussed.

Several experiments involving complimentary methods and devices are also designed and carried out to assist the main method in investigation of the PEO processes. COMSOL Multiphisics software package is used for modelling the distribution of electric field and electrolyte resistance in the electrolyser; ex-situ EIS analysis- for impedance spectra comparison with ISIS results; fractal analysis- for studying the effects of coating morphology on impedance spectra; specialized imaging multi-channel (SIM) framing camera- for real-time observation of discharge events; and FFT analysis of high-resolution current signals- for studying the information on individual discharge events. Based on these studies, the characteristics of PEO process are discussed from different aspects and these better understanding is eventually achieved.

ACKNOWLEDGMENTS

First and foremost, I would like to express my sincerest gratitude to my supervisors Dr. Aleksey Yerokhin and Prof. Allan Matthews for their invaluable guidance and suport throughout this work. Their foresight led me into this field and their assistance, and encouragement led me along the research on the characteristics of PEO process. I would also like to express my appreciation to Dr. Evgeny Parfenov for his knowledge and technical support with programs writing and problem solving of data acquisition.

My gratitude also goes to Dr. Adrian Leyland, Prof. Lyubov Snizhko and all the members of the Research Centre in Surface Engineering (especially Kostas Kanakis, Glenn Cassar, Nayef Alanazi, Po-Jen Chu, Omoniyi A Fasuba, Yong Hao Gao and Wing Kiu Yeung), who supported me throughout these years, past and present. Many thanks to all academic and technical staff at the Department of Materials Science and Engineering for their kind co-operation and help throughout my PhD studies. Specially thanks go Prof. Will Zimmerman and Dr. Jaime Lozano-Parada for the assistance with model design using COMSOL Multiphysics package. I also gratefully acknowledge the support of the UK EPSRC (Grant #EP/H051317/1) and the EPSRC equipment loan pool for provision of specialised ultra-high speed imaging multi-channel framing camera (SIM 16).

Finally, I would like to express my appreciation to my parents Jeng-Jong Liang and Wen-Yi Tiao, my brother Chen-Wei Liang and my girlfriend Ya-Fang Pang whose constant love, patience and encouragement I have relied on throughout my PhD study in Sheffield and to whom I dedicate this work.

Chen-Jui Liang
Sheffield
June 2013

TABLE OF CONTENTS

LIST OF FIGURES

LIST OF TABLES

Chapter 1

Introduction

In recent years, the application of metallic materials has shifted towards lightweight and functional metals, which have greater commercial value. For this reason, research and development on different kinds of functional materials based on lightweight metals becomes one of the key objectives in industry and academia.

Plasma Electrolytic Oxidation (PEO) is applied to many lightweight metals such as aluminum, magnesium, titanium, zirconium, to generate oxide ceramic coatings. The PEO process is prominent for its ability to obtain high quality coatings with excellent corrosion and wear resistance as well as good electrical, mechanical and thermophysical properties and good adhesion to the substrate. These coatings are of particular interest for key manufacturing sectors, including aerospace, biomedical, optoelectronic and energy devices and plant.

Compared to vacuum based plasma-assisted coating processes, the PEO process is preferred for its capability to provide non-line-of-sight treatment and an atmospheric pressure processing environment. However, PEO is a complex process which includes chemical, electrochemical, and plasma-chemical aspects that influence heat, mass and charge transfers. It is necessary to understand the characteristic associated phenomena and mechanisms of PEO coating formation well enough to attain adequate means of process control and improve coating quality.

1.1 PEO background and history

Plasma electrolytic oxidation is a process of plasma assisted electrochemical treatment of valve metals (Mg, Al, Ti, Zr, Nb, Hf, Ta, etc.) to obtain high quality (thick, hard and have good corrosion- and wear- resistance) oxide ceramic layers. It is a relatively new coating

technology [1,2], the development of which started less than 30 years ago. Within the PEO history, the phenomenon of a "spark discharge" had been first discovered by Sluginov [3], who looked into the behavior of metal electrodes in aqueous electrolytes under high voltages in the 1880s. Fifty years later, a more detailed research in this topic was carried on by Günterschultze and Betz [3]. The first application of the spark discharge for deposition was reported by McNiell and Nordbloom [4,5] in 1960s, who deposited cadmiun niobate on a cadmium electrode (anode) from the niobate electrolyte by using a spark discharge method. In the 1970s, Makov et al. used an arc discharge to deposit anodic oxide coatings on aluminum, and then improved the technique by increasing the voltage to achieve enough energy for producing plasma channels in the initial passive layer. He termed the spark discharge anodising as 'Micro-arc oxidation' [6]. From 1980s, more academics studied the PEO technique on various light metals in Russia and Germany [7,8]. In USA and China, researchers have also started to be involved in this subject around 1990s [9-12], However, after reviewing literature from Russia, Germany and USA, those developments seems to have been done independently without any knowedge exchange at that period.

In 1999, Yerokhin et al. presented a review of electrolytic plasma processing as an emerging surface engineering technology [1], including various plasma electrolytic deposition (PED) methods. Two types of PED process are now been studied: PES (Plasma electrolytic saturation), PEO (Plasma electrolytic oxidation).

In essence, the PES process utilizes a high voltage applied to the electrolytic cell to cause the metal surface to be saturated with ions, this technique is developed based on the mechanisms of heating in electrolytic plasmas, which results in activation of thermal diffusion. Depending on diffusing ions, PES can be categorised into PEC (Plasma electrolytic carburizing) [13], PEN (Plasma electrolytic nitriding) [14] and PEB (Plasma electrolytic boriding) [15], and their combinations.

PEO utilises a high potential difference between the anodic workpiece and an auxiliary/counter electrode in the electrolyte to grow surface oxide films. With voltage increasing, the current density rises causing such phenomena as rapid sparking and micro-arc discharging to appear at the surface of the metal workpiece, which affects the oxide film formation.

1.2 PEO treatment

PEO is a surface treatment technology developed based on the conventional anodising process and can be applied to several metals and alloys, including aluminium, titanium, magnesium, zirconium, and niobium. PEO is also known as Micro-arc Oxidation (MAO), Micro Plasma Oxidation (MPO), Anodic Spark Deposition (ASD), Spark Discharge Oxidation, Anodischen Oxidation under Funkenentladung (ANOF), and Spark Anodising. In contrast with conventional anodic oxide films, PEO coatings develop a two-layered morphology, with an amorphous outer layer with a coarse, porous morphology and an inner crystalline layer with numerous fine pores. The cavities are due to the generation of oxygen that may be associated with the crystallisation of amorphous component in the inner layer [16].

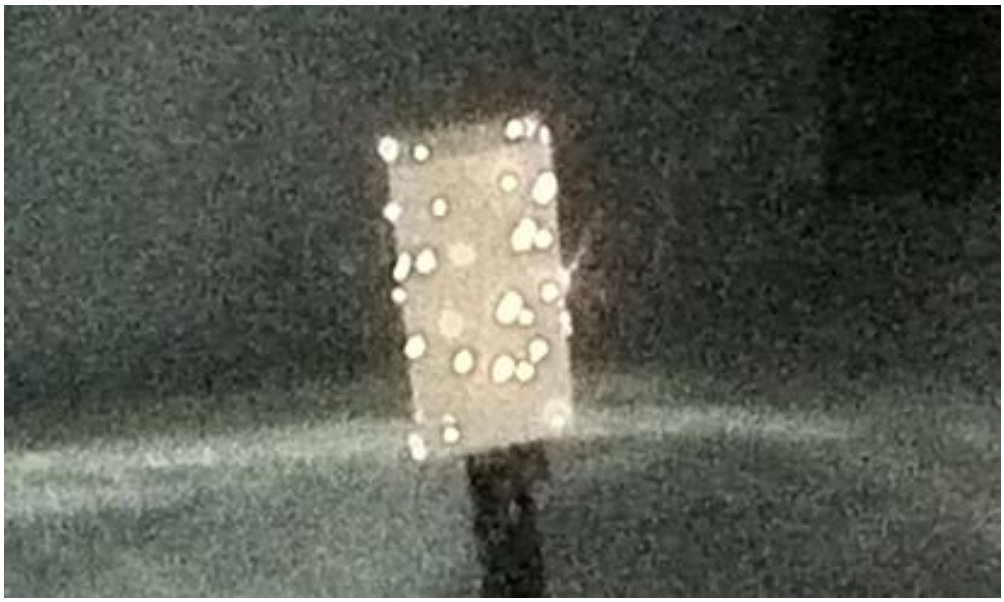

Fig. 1.1 Discharge phenomena during the PEO process (6×25×12 mm)

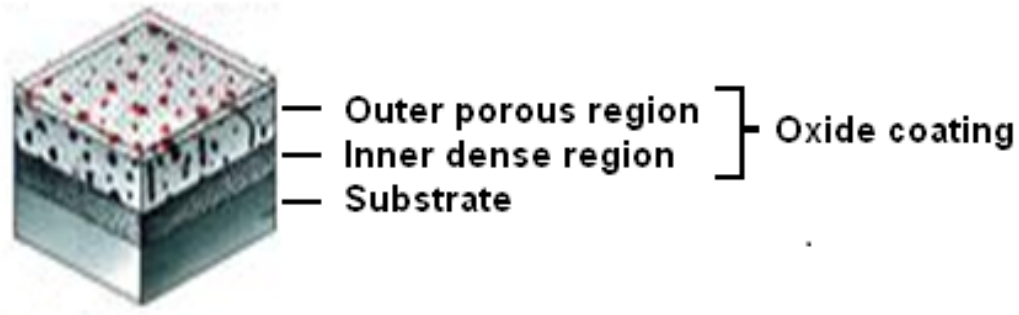

Fig. 1.2 Schematic of the PEO coating morphology

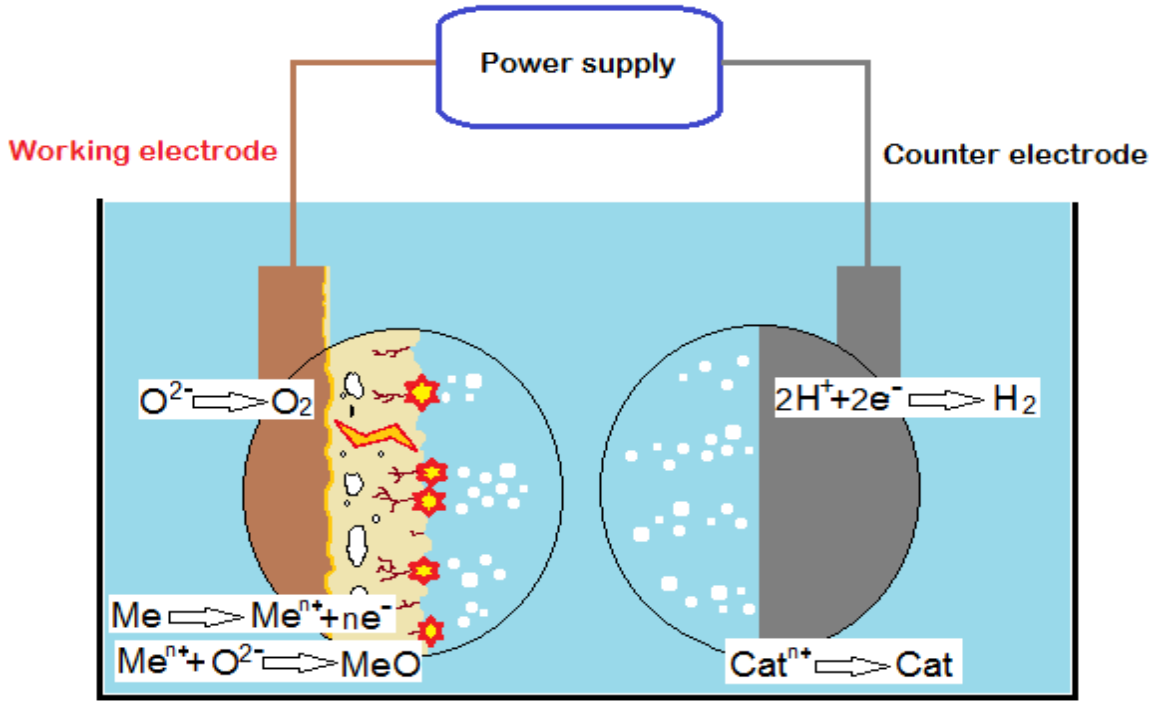

Fig. 1.3 Basic layout and electrode reactions for a typical electrolytic oxidation process

Four different stages of the PEO processes have been identified based on the phenomena occurring, characterised by various rates of the partial electrode processes. Overall current efficiency of the oxide film formation has been estimated to be in the range of 10 to 30% [17]. The overall rate of oxygen liberation at the anode exceeds the Faraday yield, which is probably due to the radiolytic effect of the plasma discharge (Fig. 1.4) on the adjacent electrolyte volume.

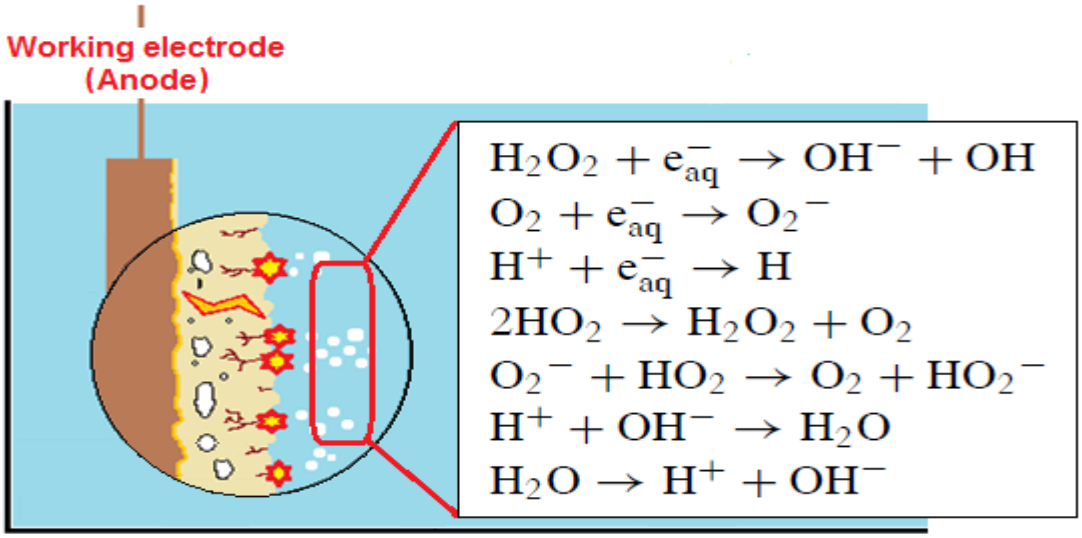

Fig. 1.4 Probable chemical reactions leading to oxygen liberation

Figure 1.5 shows a typical example of linear approximations of voltage transients in the four regions [1, 17], which can be characterised as follows. Region (I) exhibits the maximum voltage growth rate, corresponding to a conventional metal anodising process. In region (II), it slows down, indicating a decrease in the oxide film growth rate; oxygen bubbles first appear on the sample surface in this region. In region (III), the rate of voltage increase rises again; this usually corresponds to oxide recrystallisation and defect formation in the film structure. Region (IV) begins with intensive oxygen evolution, which creates suitable conditions for the onset of plasma microdischarge phenomena at the sample surface. The process becomes more steady-state, with the only changes observed in the discharge appearance which progresses gradually from a dense population of small and frequent microdischarges towards a smaller population of larger and longer-lived discharge events. The threshold voltage at which the plateau in region (IV) is entered decreases with increasing electrolyte concentration. In region (V), arc micro-discharges occurring throughout the film surface penetrate through to the substrate and transform into powerful arcs that may cause destructive effects such as thermal cracking of the film.

Comparing between conventional anodising and the PEO process [1], because of the participation of plasma phenomena, the principal physical-chemical process occurring in conventional electrolysis is much different from those in plasma electrolysis, which include heat treatment, melting, welding, soldering, etching, polishing, diffusion depletion and deposition at the electrode surface during PEO process.

Plasma chemical reactions, that usually occur around the area of gas accumulation on the surface of the oxide film, proceed in two steps as ionisation and condensation. In the ionisation step, thermal or impact ionisation occurs in the discharge region to dissociate molecules and produce free electrons. When plasma is formed across the discharge channel, high pressure and temperature are generated by electron avalanches in a very short period of time (less than 10^{-6} s). Under the high temperature, a portion of the metal matrix and alloying elements is melted out of the substrate, enters the discharge channel and gets oxidized. At the same time, the strong electric field in the discharge channel separates the negatively charged ions, then the positive ions that are released in to the electrolyte, whereas the negative ions join the interactions on the electrode surface. In the second step, condensation, the temperature drops sharply developing cooling rates as high as 10^{8}K/s. The compounds produced from the plasma are condensed forming high temperature phases, supersaturated solid solutions, nonequilibrium compounds [1], and the oxides such as TiO_2, MgO and Al_2O_3 are produced on the surface of the working electrode. These ceramic coatings provide different properties from the conventional anodising method, and will be discussed in the following sections.

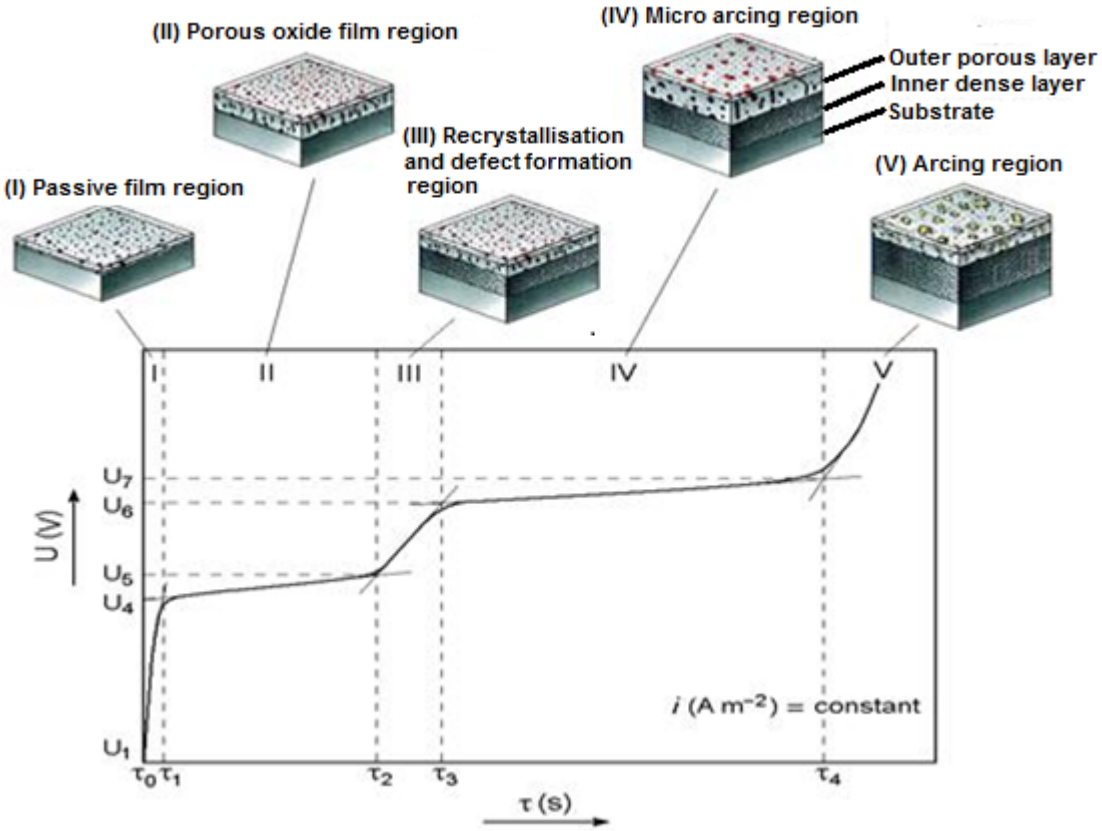

Fig. 1.5 Voltage-time diagram for the process of plasma electrolysis oxidation

1.3 PEO coating properties

Ceramic coatings produced by PEO treatment provide several benefits that are of particular interest for researchers and industry including [18]: (a) the PEO coatings are formed directly by oxidation of the metal and therefore are bound tightly with the substrate without any debonding; (b) PEO process is capable of non-line-of-sight treatment, which means one can form coatings on multiple sides of samples or even on substrates with complex geometry. (c) PEO treatment provides high coating growth rates and the typically treatment times are less than 60 minutes, to produce coating thicknesses of up to several hundreds of micrometers [19]; (d) PEO treatment provides excellent coating properties, including high surface hardness, corrosion and wear resistances, as well as dielectric strength.

Beside the aforementioned properties, PEO coatings are formed with pores, which size and population that are much higher than in PVD coatings. By selecting different treatment parameters, such as composition of electrolyte and treatment regime, the porosity and pores size can be controlled. This property can be desirable, e.g. in biomaterial applications of titanium and magnesium oxides. Last but not least, it is important that compared with other

surface treatment methods, the technological procedure of PEO treatment is much more simple as the process is carried out under atmospheric pressure. PEO treatments have less water consumption, emit less effluent and involve solutions which do not include the harmful substances, such as Pb, Hg, Cd, and Cr. Due to the above characteristics, the PEO treatment method is likely to be more widely applied.

1.4 PEO coating applications

Recently, PEO coated products have been applied in various industrial sectors, such as machine tools, aerospace, biomedical, optoelectronic, engineering equipment, and energy devices and plants. PEO coated products and related technologies are now developed in several companies and countries e.g. Keronite in UK, Tagnite and CeraFuse in USA, Machaon in Russia, and Maxgoxid-Coat in Germany. PEO treatments of aluminum, magnesium and titanium are increasingly used, as shown in the following.

PEO alumina is the common ceramic material and widely used in different areas, and is especially employed to withstand mechanical stress, corrosion, and high temperature. The Al ceramic coating made by PEO can be applied in different areas as in machine building, textile machine components, engine manufacturing, pumps, oil, gas and chemical plant. In automobile, it is applied for the cylinder blocks, piston and spark plug [20]. Recently, the PEO technique was used to treat the surfaces of mobile phone cases [21].

Magnesium provides good properties, such as low density, high specific strength, and electromagnetic shielding, and is applied in aerospace, communication and automotive industries. In the past decades, PEO treatment of magnesium has become popular in biomaterial applications as ligature wires, vessel anastomosis connectors, aneurysm treatment wires, artificial joints, etc.[22] because of good coating corrosion resistance and mechanical properties [23,24].

PEO treatment of titanium has similar applications as for aluminum and magnesium. Moreover, TiO_2 was found to possess excellent biocompatibility, and the porous morphology is beneficial for cell adhesion [25]. Recently, titania thin films have been demonstrated to have photocatalytic properties. In 1991, Gratzel et al. developed a new type of solar cell called the dye-sensitized TiO_2 solar cell [26], which used nano-scale TiO_2 powder to produce photoelectrode with high specific surface area. After dye-sensitized treatment, it can absorb light from visible part of the spectrum. TiO_2 coatings produced by the PEO technique were

recently studied to improve photovoltaic efficiency of the dye-sensitized components [27].

1.5 Research aims

In this study, new insights into coating formation mechanisms and methods of process control will be attained using in-situ impedance spectroscopy which is an emerging characterisation and diagnostic tool to study time-variable and non-linear processes, and is suitable to study the PEO process. To achieve the process control to improve coating quality, the following experiments were designed to investigate different characteristics.

First of all, it is noticed that strong electric fields have significant effects on characteristics of impedance spectra. To comprehend the effects of electric field distribution in the electrolyte, PEO processes were studied in equidistant and non-equidistant cell geometries.

Secondly, it is known that the electrolyte solution is one of the main factors influencing kinetics of the coating growth, its structure and properties. In-situ impedance spectroscopy was used to acquire fundamental characteristics of PEO processing of Al carried out in electrolytes with different conductivities and temperatures.

Thirdly, effects associated with non-uniform distribution of electric field and current density, variable coating thickness, topology or composition were modeled by constant phase elements (CPE). In this work, the effects of coating morphology on in-situ impedance spectra of the PEO process on Al were studied using a fractal approach. The fractal analysis is a useful method to investigate the properties of heterogeneous (e.g. rough, porous or multiphase) materials, which can provide a direct link to the CPE characteristics.

In the last part, the behavior of discharge events were investigated, which is a main effect on coating formation. Fast video imaging method was used to analyse the characteristics (intensity, size, duration and trajectory) of discharge events. A dual-channel digitalizer was used for the current transient study. The results of the study were assisted with in-situ impedance spectroscopy for better understanding of PEO process.

1.6 Thesis overview

Chapter 2 presents an overview of PEO processes and associated mechanisms, including the composition and morphology of PEO coatings, electrolyte composition, effects of power supply by using different current modes, plasma discharge phenomena, chemical reactions during the PEO process, and the dielectric breakdown phenomena.

Chapter 3 describes methodological approaches for PEO process modeling and deals with the experimental equipment and methods for studying coating methodologies, which leads to the introduction of the frequency response method, frequency sweep set-up for in-situ electrochemical impedance spectroscopy and the input power supply as well as providing an the introduction into the fundamentals and applications of electrochemical impedance spectroscopy. It also introduces the modeling software COMSOL-Mutiphysics package which was used to study the distribution of electric field and the new research method of in-situ impedance spectroscopy with corresponding data processing method, which is the main method for understanding of the PEO process. The last part of this chapter introduces the sample preparation and the SEM image analysis for coating morphology study.

Chapter 4 presents the results of experiments investigating electric field distribution effects on the PEO process. Three different shapes of working and counter electrode were chosen to present converging, parallel and diverging types of electric field. Equidistant and non-equidistant electrode arrangements were also studied for all types of electric field. COMSOL software was chosen to model the electric field distribution and measure the net resistance of the electrolyte. This chapter also discusses the impedance behavior of the PEO process revealed by in-situ electrochemical impedance spectroscopy. Both complex and Bode plots are studied in detail to understand the physical meaning of equivalent circuit elements and the chemical reactions during PEO process. The coating morphology both in the surface plane and on the cross-section are used to study the correlation between coating structure and the characteristics of the equivalent circuit.

Chapter 5 presents the results of the investigations on the effects of electrolyte characteristics on PEO of Al. Three main parameters were varied in this part of the study, namely temperature and conductivity of electrolyte as well as the different preformed coating thickness. Both in-situ and ex-situ electrochemical impedance spectroscopy are used here to reveal the plasma discharge effects.

Chapter 6 discusses the distribution behavior of electric field effects by using the CPE element from the fitting results of equivalent circuits of the PEO process and the data from the fractal analysis of coating morphology. On the other hand, the correlation between CPE elements/ fractal dimensions and coating morphology characteristics is also investigated.

Chapter 7 discusses the behavior of discharge events. In this work, a specialised image camera was used to observe the behavior the discharge events. The ultra-high speed images were analysed by specific discharge analysis program and 3D plots to investigate the characteristics of discharges such as duration, peak intensity, FWHM, trajectory, and the relative peak current density in the different conditions, such as applied voltage, varied exposure time, and at different time stages of PEO process. The results of the FWHM and trajectory of discharges from the above were correlation with the surface morphology.

Chapter 8 summarises the main conclusions derived based on results and discussion in this work, and provides the outlook for further researches.

Chapter 2

Overview of Plasma Electrolytic Oxidation Processes and Associated Mechanisms

In this chapter the processes taking place during the PEO treatment and underlying mechanisms undergo a detailed overview and categorisation as outlined in the following sections. Firstly, formation of composition and morphology in PEO coatings on different substrates is related to the coating properties. Secondly, electrolyte composition is discussed as one of the main parameters affecting the coating composition. A plasma discharge is the main phenomenon that differentiates the PEO treatment from conventional anodizing and also affects coating phase composition; so the behaviour and characteristics of discharge events is discussed next. Chemical reactions that occur during plasma electrolysis are significantly different from those taking place during conventional low-voltage electrolysis [1]. The breakdown phenomena play an important role in the coating formation, influencing its morphology and the plasma composition. These phenomena occur during PEO process, and the relevant information is finally overviewed. This analysis is essential for identifying the knowledge gaps in the current understanding of the PEO process and may be helpful in providing a better understanding of the mechanisms underlying the coating formation during PEO treatment.

2.1 Composition and morphology of PEO coatings

As follows from the previous chapter, the PEO technique is now receiving increasing attention as an important method of surface treatment because of superior coating properties. These properties are mainly influenced by the coating composition and morphology.

Therefore, these characteristics of PEO coatings are overviewed in this section.

This work is focused primarily on PEO treatments of Al because of it is one of the most widely used materials in both industry and consumer products. It is known as the second most abundant metallic element on the Earth. Aluminum is economical and widely used in machinery, transportation, packaging, construction, engineering equipment, especially for applications in energy devices and plants, because of light weight, manufacturability, high corrosion resistance, physical and mechanical properties [28]. From the environmental protection point of view, aluminum is 100% recyclable material, and to produce it from scrap requires 95% less energy compared to production of primary aluminium [29]. Only 26 kJ is required to melt 1 mol of metallic aluminum [30]. From European experience, the highest recycling rates of aluminum are about 42% in beverage cans, 85% in construction materials and 95% in transport vehicles [31].

Aluminum is a silvery white material with characteristics of lightweight, ductility, fatigue strength (aluminum alloys), heat tolerance and high thermal and electrical conductivity. It is also well known as a metal with ability to resist corrosion due to the passivation by the surface oxide layer (Al_2O_3). During recent decades, fabrication and application of aluminum oxide layers has been extensively studied.

Alumina is the main constituent of oxide coatings produced by the PEO treatment of aluminum substrates. It is a typical ceramic material, which was first applied as an insulator of spark plug in Germany 1931. Since then, alumina became one of the most significant materials and the most widely used oxide ceramic [32], because of the advantageous combination of high strength, hardness, heat tolerance, electrical insulation, corrosion and wear resistance. Alumina ceramics typically contain 85 to >99% Al_2O_3. There are several crystal types of aluminum oxide : α-, β-, γ-, θ-, δ-, and κ- Al_2O_3, of which α- and γ-Al_2O_3 are the main structural constituents of PEO coatings. Three most common types of alumina (α-, β-, γ- Al_2O_3) are introduced below.

Alpha alumina is a well known structural and engineering ceramic, wherein a high-purity α-Al_2O_3 is used as the raw material to produce artificial corundum, ruby and synthetic sapphire. Alpha alumina provides the highest stability and a dense structure due to the hexagonal close packed structure [33-35], in which Al^{3+} is distributed symmetrically around the octahedral interstices in the array of oxygen atoms (figure 2.1). Therefore α-Al_2O_3 has high lattice energy, melting and boiling points. Also, α-Al_2O_3 is not dissolved in water, alkaline or acidic solutions, which is beneficial for applications in refractory crucibles, tubes, firebricks, flame retardants and abrasives. Alpha alumina is the most stable phase with higher

critical free energy of nucleation $\triangle G_{\alpha}$, at which the metastable phases, e.g. γ-Al_2O_3 and θ-Al_2O_3 are transformed to α-Al_2O_3 when the temperature increases high enough (over 800℃)[36].

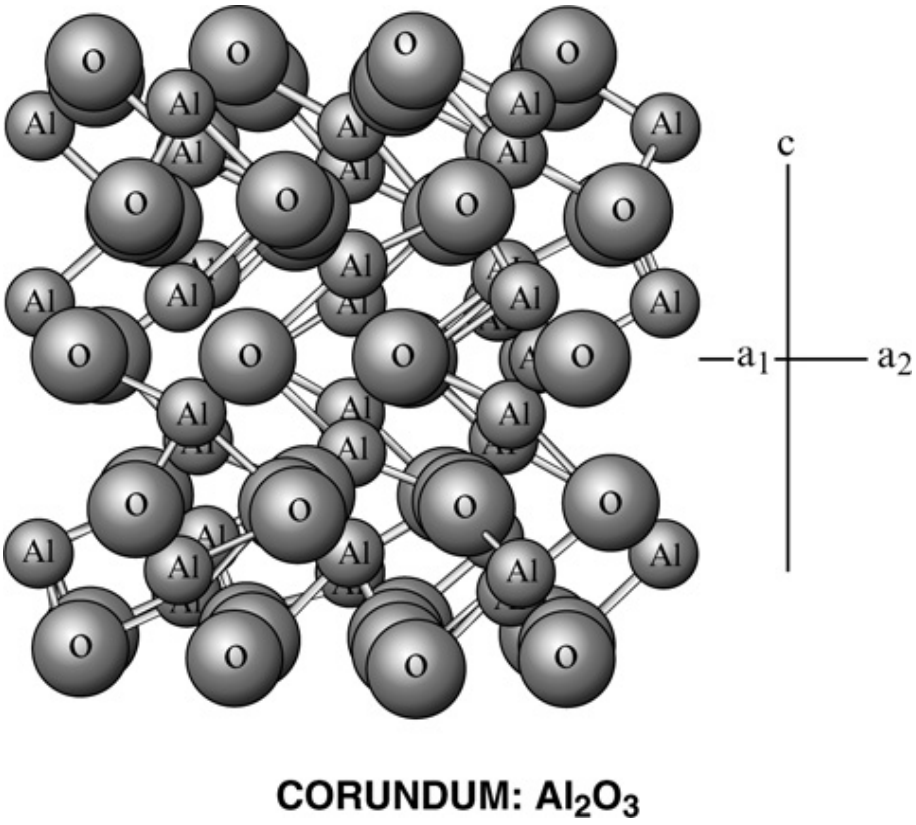

Fig. 2.1 Hexagonal close packed structure of α-Al_2O_3 (Corundum) [35]

Beta alumina [33] is not a pure alumina crystal, the chemical composition can be presented as $MeO{\bullet}6Al_2O_3$ (Me: Ca, Ba, Sr, etc.) or $Me_2O{\bullet}11Al_2O_3$ (Me_2: Na_2, K_2, Li_2, etc.), it is a kind of aluminate compound with high content of Al_2O_3. In the case of the β-Al_2O_3 structure and composition, it possesses significant ionic conductivity and relaxation polarization; hence it is not suitable for structural ceramic applications. However, β-Al_2O_3 can be transformed to α-Al_2O_3 by heating up over 1000 ℃.

Gamma alumina is one of the metastable oxide phases, and is the intermediate product of dehydration from aluminum hydroxide formed at relatively low temperatures e.g. 140~150℃. It has a face-centered cubic structure and Al^{3+} are irregularly distributed in the voids of octahedral and tetrahedral sites surrounded by oxygen atoms. It features relatively high lattice constant and low density; therefore it can be used as a sorbent with great activity, strong adsorption capacity and large surface area. Usually, γ-Al_2O_3 rather than α-Al_2O_3 is formed from liquid droplets at considerable overcooling by homogeneous nucleation during solidification, because of the lower critical free energy for nucleation and a higher cooling

rate promoting formation of solid oxide phases with closely packed rather than hexagonal structures [37,crys38]. When temperature reaches 1200℃, γ-Al_2O_3 can be fully transferred to α-Al_2O_3. Physical properties of α-Al_2O_3, and γ-Al_2O_3 are summarised in Table. 2.2.

Phase composition of PEO coatings is commonly identified by X-ray diffraction (XRD). Typical results of XRD analysis of PEO coatings with different thickness are shown in figure 2.2 [45]. It was found that α-Al_2O_3 formed larger crystals of the size in the range of 20 to 50 nm whereas 10-30 nm crystalline size was determined for γ-Al_2O_3. The properties of PEO coatings were related to the coating morphology, deposition and relative contents of α-Al_2O_3 and γ-Al_2O_3 phases (C_α and C_γ).

Table 2.1. Physical and mechanical properties of high-purity alumina ceramics [33,35]

Physical & Mechanical property	value	Physical & Mechanical property	value
Density [g•cm^{-3}] at 20℃	3.96	Mohs hardness at 20℃	9...14
Melting point [℃]	2050	Heat conductivity [W•m^{-1}•K^{-1}]	9.5
Elastic modulus [GPa] at 20℃	375	Flexural strength [>MPa] at 20℃	410
Tensile strength [MPa] at 20℃	220		

Table 2.2. Main crystallographic characteristics and physical properties of α-Al_2O_3, and γ-Al_2O_3 polymorphs [33]

	Crystal system	Lattice constant [nm]		Density [g•cm^{-3}]	Volume resistivity [ρ_v/Ω•m]	
		a	c		20 ℃	100℃
α-Al_2O_3	hexagonal	0.4741	1.296	3.95~4.1	10^{14}	-
γ-Al_2O_3	cubic	0.7895	-	3.42~3.62	-	75×10^{10}

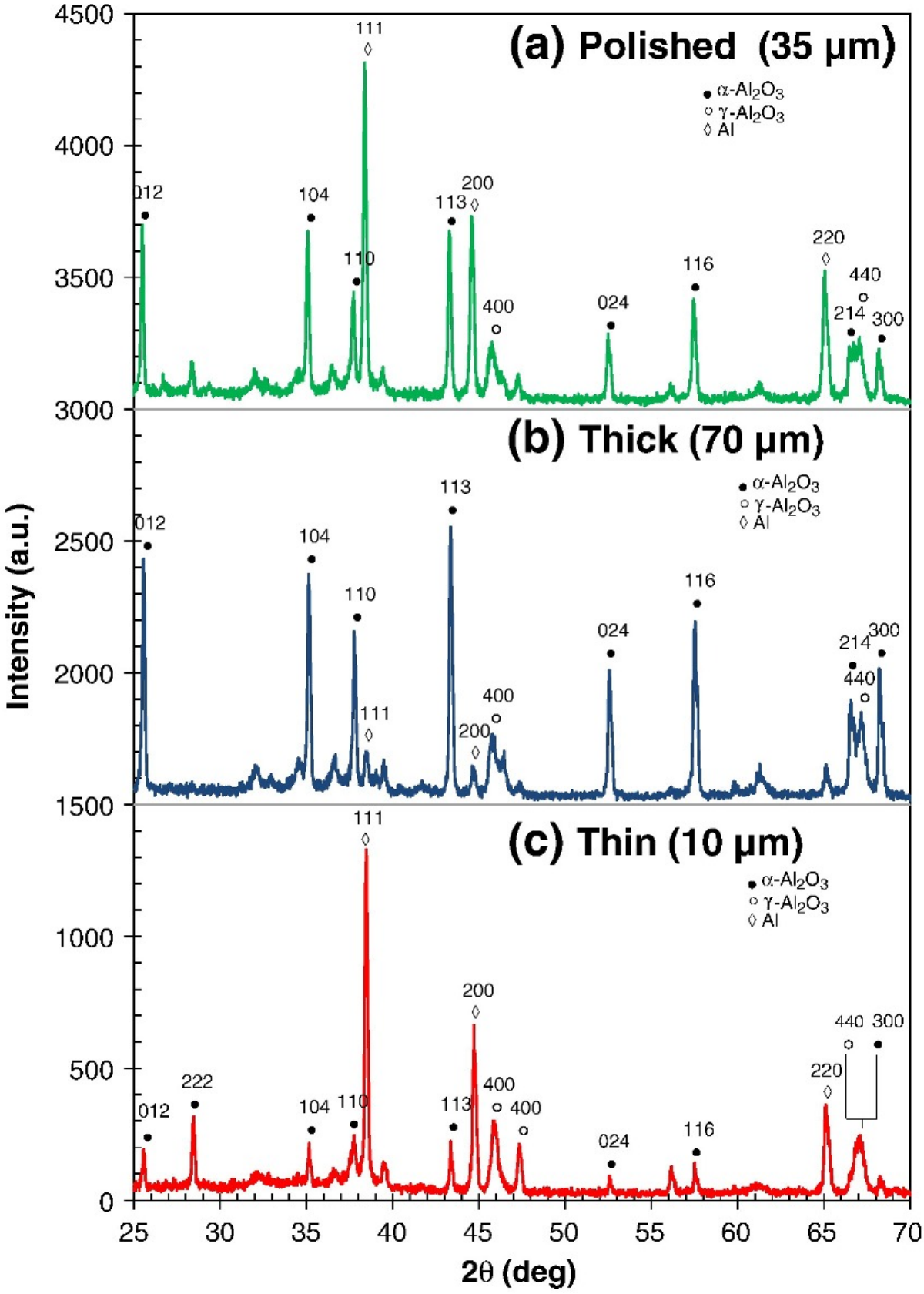

Fig. 2.2 XRD patterns (Cu radiation) presenting the phase composition of PEO coatings with different thickness formed on Al substrate [45].

Studies of the cross-sectional structure of PEO coatings formed on Al, typically show two distinct regions, i.e. an outer porous layer and an inner dense layer presented in figure 2.3. In some papers, these are termed as 'outer technological layer' and 'inner functional layer' [2] or 'loose layer' and 'compact layer' [39], respectively. The outer porous region consists mainly of lower temperature X-ray amorphous phase, and the inner dense one consists of higher temperature alumina modifications. It is because that a higher relative content of γ-Al_2O_3 phase is distributed in the outer porous layer and the high temperature α-Al_2O_3 phase is predominantly formed in the dense inner layer. The XRD spectra were used to show that near the coating surface, the ratio between gamma (C_γ) and alpha (C_α) phase component is around 11:3. The contents of both phases were around 50wt% in the inner layers [2,11,39]. W. Xue et al [39] reported the distribution of alpha phase along the depth of the PEO coating as shown in figure 2.4. It presents clearly the trend of C_α to increase when moving away from the surface. However, an interesting phenomenon appears in the region near to the coating/substrate interface, where C_α decreases again. In this adjacent to the interface region, complex phases were observed formed by the substrate alloying elements. The average hardness of the outer porous layer is around 14 GPa, which is lower than the dense layer (~18 GPa). Moreover, the hardness of each constituent has also been measured at 26, 17 and 7 GPa for α-Al_2O_3, γ-Al_2O_3 and amorphous alumina, respectively [39-43]. The average elastic modulus (measured by nanoindentation) also has higher values of 350-400 GPa in the inner dense layer, and around 250-350 GPa in the porous layer. The difference of H/E ratio between dense layer (0.048) and porous layer (0.047) is not significant.

The coating cross-section also reveals a morphology featuring roughness, microcracks and pores. High roughness is one of characteristic features of PEO coatings compared with PVD and CVD coatings. It has been reported that the surface roughness increases with increasing coating thickness [44]. Microcracks are the distinctive characteristics of the coatings affecting their properties, e.g. hardness, elastic modulus and corrosion resistance. From the SEM images, it can be observed that the microcraks are usually present around the pores. The formation of microcracks in PEO coatings is due to the intensive thermal stresses that are caused by high temperature gradients between hot molten parts of the coating and cold electrolytic solution [45]. However, the presence of microcrack networks helps reduce both the stiffness of PEO coatings and the misfit strain caused by temperature changes. It is also manifested that the stress relaxation is caused by microcracks formation process [40,46,47].

Porosity is another important characteristic of the coating morphology. It is believed that the pores arise from the oxygen evolution during the PEO process as shown in figure 2.5. [48,79]. Porosity and pore size can affect the coating properties, such as thermal and

corrosion resistance; it is also an important means to reduce high temperature and pressures during crystallisation of the coating material and the surface layer growth affected by oxygen dissolved in the molten oxide. Curran and Clyne also reported another probability to produce pore-like defects, due to the substrate dissolution [48]. Currently, the pores of PEO coatings are considered to have a useful function for application in biomaterials based on Ti and Mg alloy substrates, wherein porosity promotes cell adhesion to the surface. In another PEO application for dye-sensitized solar cells, high porosity and large pore size can also be a positive factor, as the formation of pores causes an increase in surface roughness and specific surface area that facilitate light absorption. From the SEM image (figure 2.3), it can be observed that the high coating porosity is achieved by superposition of different pore size around 10 μm and less than 3 μm. Similar to the work by Khan et al. [48], the large pores are distributed near the surface, whereas the small pores are located inside the large ones.

Surface morphology also bears some information indicative of the physical mechanisms operating during the coating formation. From figure 2.6, the volcano-like or so called "pancake" structures with craters located in the centre are dispersed over the surface. The physical mechanism responsible for the development of such a structure is conjectured to be the occurrence of discharge events, and the sink-holes (pipes) of craters are located at the relatively weak spots, where the discharges penetrates through the entire coating thickness. After the discharge is extinguished, the coating is reformed, with molten material solidified in the form of volcano-like eruption features. This produces craters with deep central shrinkage holes, while solidification of molten pools also forms brittle material on the periphery. This can also explain the formation of microcrack networks radially oriented around the craters [11,19,47,49]. Moreover, several structures of irregular shape can be observed near the volcano-like features that appear to have been formed when liquid globules had been ejected from the discharge channels.

The SEM image analysis of both surface and cross-section morphologies can help understanding the characteristics of PEO coatings. However, the coating morphology may be affected by several process parameters such as electrolyte composition, applied current mode and characteristics of discharge. The significance of these parameters has been noted and corresponding effects investigated thoroughly, with main results discussed in the following sections.

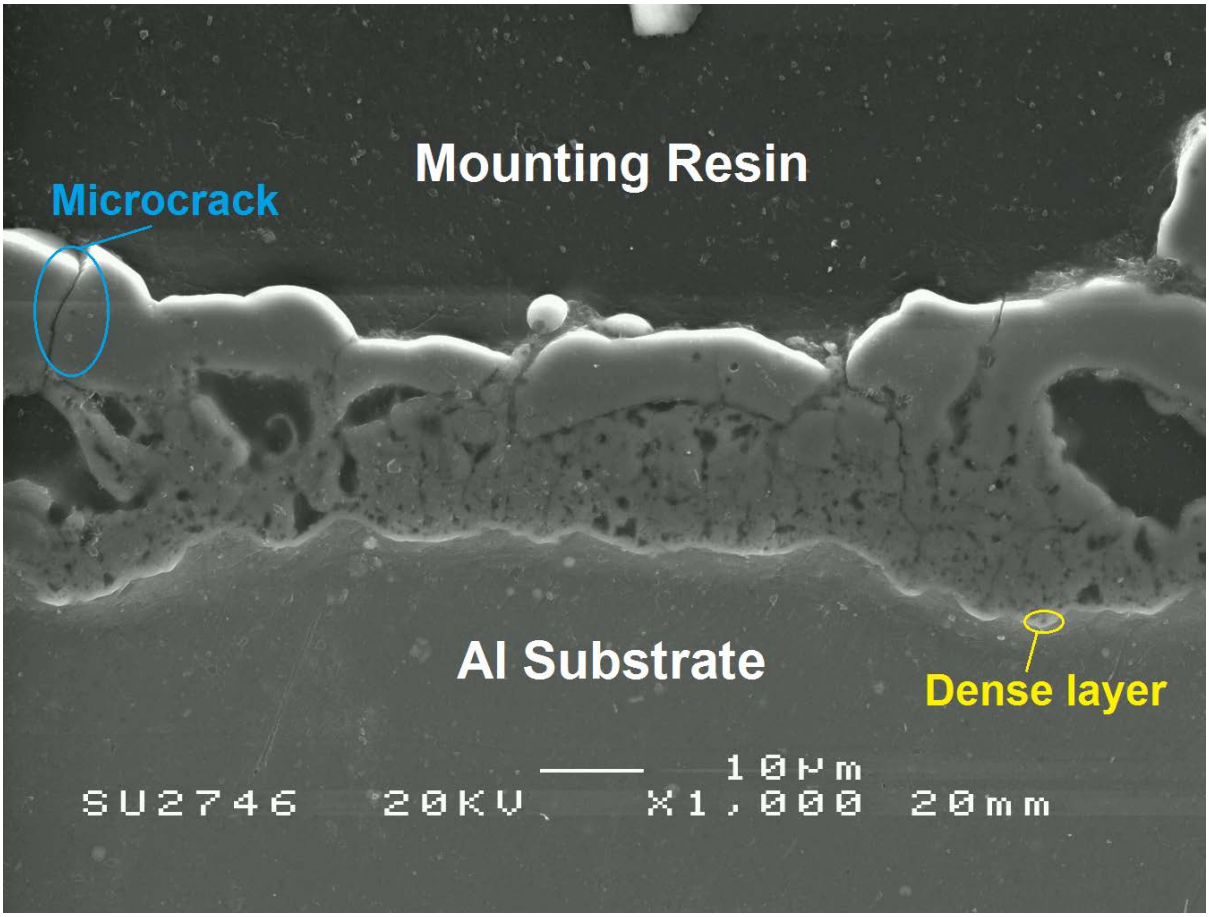

Fig. 2.3 SEM micrograph of cross-section morphology of a PEO coating on Al substrate.

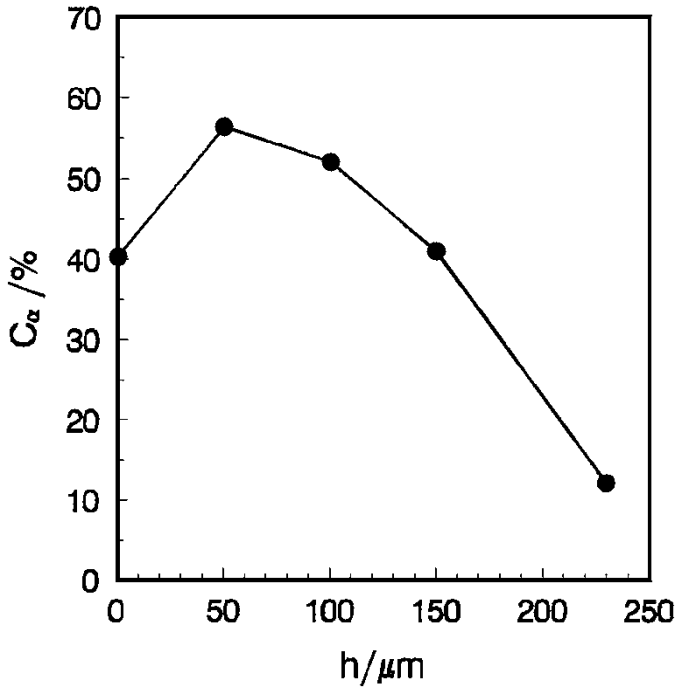

Fig. 2.4 Typical distribution of α-Al_2O_3 across the thickness of PEO coating [39].

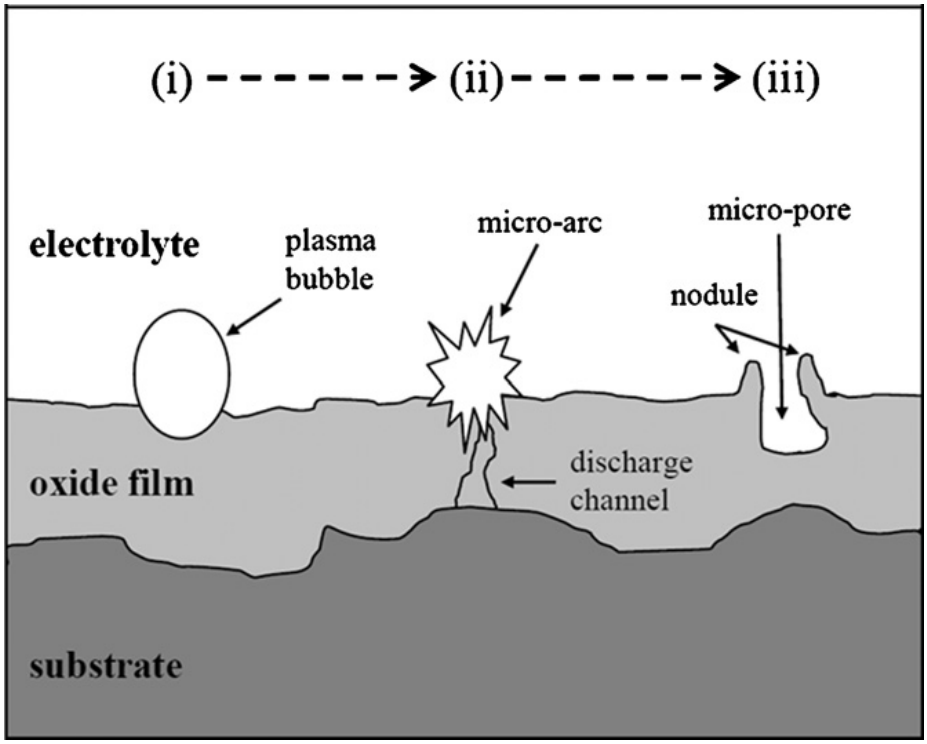

Fig. 2.5 Schematic diagram of pore formation in the PEO coating by bubble implosion [79].

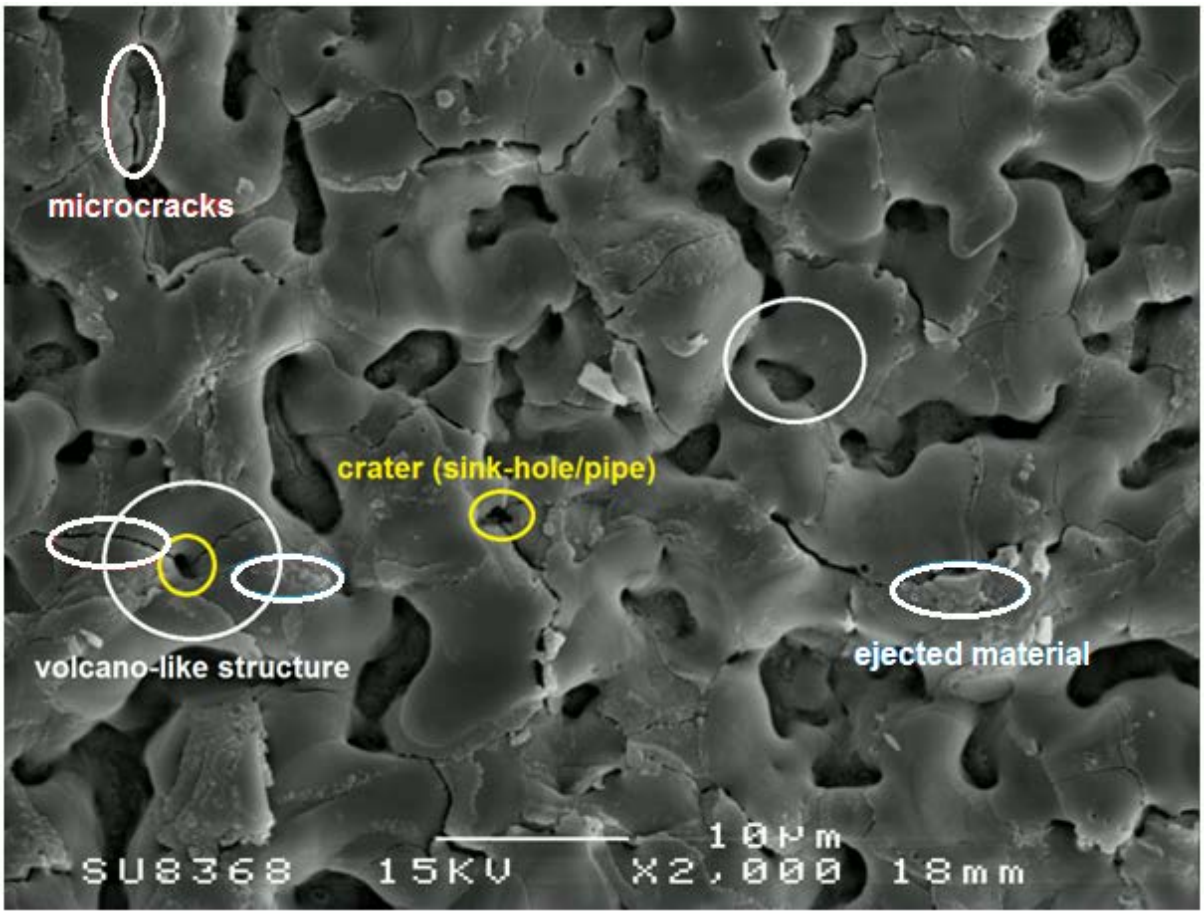

Fig. 2.6 SEM micrograph of PEO coating surface morphology on Al substrate.

2.2 Effects of electrolyte composition

The electrolyte is one of the main factors influencing the PEO process, coating formation and composition. As many authors noticed [1,50,51], the efficiency of the PEO process is affected by the electrolyte characteristics, such as concentration, pH, presence of activating anions and agitation conditions. It is believed that the main effect is on the efficiency of oxide formation due to the change of current density/impedance, sparking activity, chemical reaction rate, and thermodynamic equilibrium.

Two main types of constituents typically make up electrolytes for PEO of Al. Firstly, weak alkaline solutions are used to produce low conductivity electrolytes that could cause high ohmic drops, hence higher voltage can be easier to achieve for the required current density and discharge phenomena can easily commence. Secondly, different additives of passivating agents can be introduced depending on the coating formation/morphology required. The passivating agents are important ingredients influencing the coating morphology, composition and growth rate [1,52,53]. The common additives widely used in PEO process are silicates, phosphates, aluminates, etc. The choice of the electrolyte depends on required coating morphology and composition.

In the review of plasma electrolysis for surface engineering, Yerokhin et al. [1] reported that electrolyte selection for PEO requires careful matching of the metal-electrolyte combination. In particular for the PEO process, it is necessary to ensure the metal passivation which can be determined based on the polarisation test data. The following six groups of additives can be identified and their utility for the PEO process is discussed [1]:

1. Additives that provide fast dissolution of aluminium, e.g. NaCl, $NaClO_3$, NaOH, HCl, and $NaNO_3$.

2. Solution additives that provide slow metal dissolution, e.g. H_2SO_4, $(NH_4)_2S_2O_8$, Na_2SO_4.

3. Solution additives that provide metal passivation in a narrow range of voltage, e.g. CH_3COONa, or H_3PO_4.

4. Fluoride electrolytes, which are characterised by complex behaviour, e.g. KF, NaF.

5. Electrolytes promoting slight passivation of the metal.

6. Electrolytes promoting strong metal passivation, e.g. H_3BO_3, H_2CO_3, H_3PO_4, inorganic polymers, (e.g. SiO_4^{4-}, $Al_2O_4^{2-}$, WO_4^{2-}, MoO_4^{2-}) and phosphates of alkaline metals (which can form polymer anions).

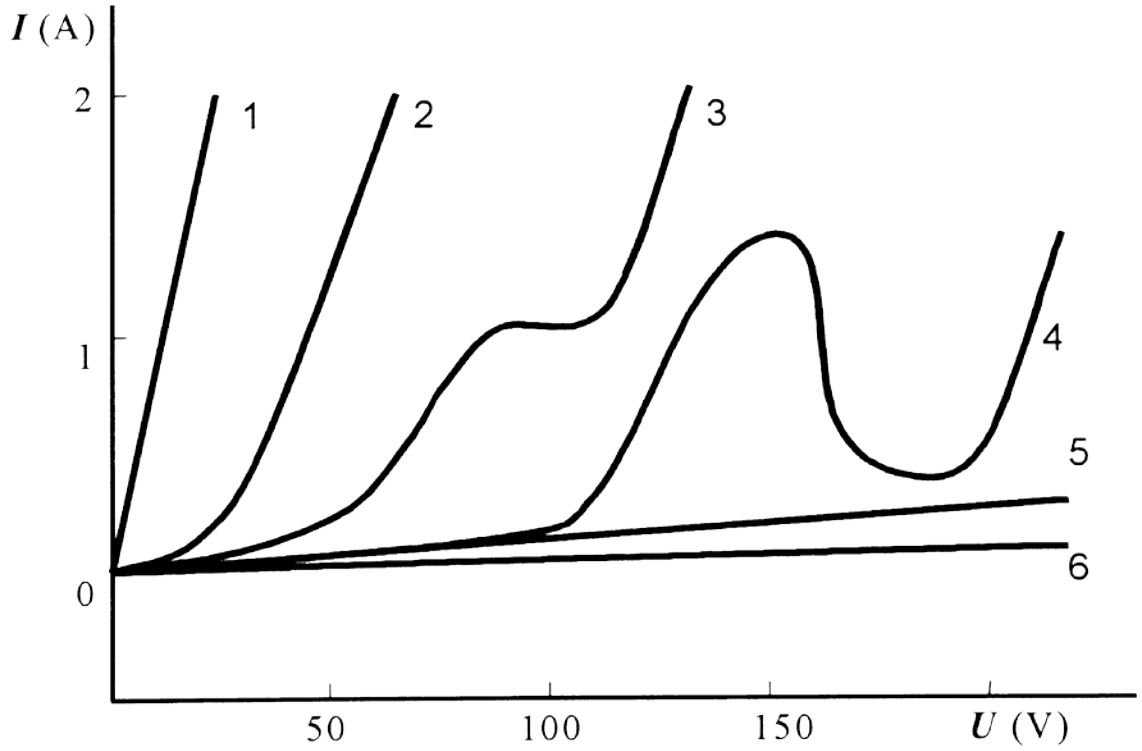

Fig. 2.7 Various electrolytes tested for PEO treatment on Al substrate [1].

Figure 2.7. shows typical polarisation curves of Al in the six groups of electrolytes considered for the PEO treatment. The electrolytes from groups 4~6 provide easily achievable breakdown voltage, which is highly beneficial for PEO coating production. These three groups of electrolytes were classified into four sub-groups in regard to their contribution to the coating composition, as follows [1]:

(a). Solutions that provide only oxygen into the coating;

(b). Electrolytes containing anionic components that incorporate other elements into the coating;

(c). Electrolytes containing cationic components that incorporate other elements into the coating;

(d). Suspensions that provides cataphoretic transport of macroparticles contributing to the coating composition.

The electrolytes of sub-groups (b) and (c) provide possibilities to modify the coating composition and properties, and enable coating formation by both deposition of electrolyte substances and substrate oxidation. These two types of electrolytes are considered as the most promising for PEO treatment in different applications.

From the aforesaid, the electrolytes can be chosen based on the ability to incorporate other elements into the coating from their cationic/anionic components. Substrate effects on the composition of PEO coatings formed in dilute silicate-alkaline electrolytes are discussed [1,2]. On Cu-containing Al alloys, the relative content of α-Al_2O_3 can reach up to 60%; γ-Al_2O_3 is the major phase in coatings formed on Mg-containing aluminium alloys and coatings based on mullite phase are formed on Si-containing substrate materials [1,2].

Different electrolyte characteristics have been investigated including concentration, pH and effects of different additives. For example, Ko et al. [54] studied the effects of electrolyte concentration on the PEO treatment of Mg with two KOH concentrations, 0.27M and 0.09M. It was reported that (a) the discharge phenomena occur at lower voltage; (b) the amount of MgO in the coating layer increases and (c) corrosion resistance increases with the increase in KOH concentration.

It is helpful to understand in more detail these effects on the formation and properties of PEO coatings. Sometimes, these studies are complimented with the studies of the effects of current density. Guangliang et al [55] reported the effects of current density on the phase composition and coating properties under the same electrolyte. The results presented the change of ratio (P) of α-Al_2O_3 to γ-Al_2O_3 in the range of current densities from 3 to 25 A/dm^2. The following three regions can be distinguished: In the first region with current density increasing from 3 to 10 A/dm^2, the P value keeps low, then it increases sharply in the range of 10~20 A/dm^2, and after that remains high in the third region of current density from 20 to 25 A/dm^2. From the analysis of SEM images, the morphology of coatings formed at low current densities is relatively coarse but featuring smaller pore size compared to those produced at higher current densities. Khan et al. [56] also studied the effects of current density and KOH concentration on the coatings formed by DC PEO treatment of Al. It was found that current density and electrolyte concentration strongly influence the coating structure; in particular the coating thickness and relative content of α-Al_2O_3 increase with increasing current density and decreasing electrolyte concentration; whereas residual stresses decrease with increasing current density.

Various additives to the electrolyte may also influence morphology and composition of PEO coatings. For example, (1) F^- ions can reduce the diameter of pores, surface roughness, and produce denser oxide coatings [57]; (2) addition of silicon in the electrolyte can increase the activity of discharge events and surface roughness [58]; (3) addition of Fe can modify the surface morphology of PEO coatings, increase hardness and reduce porosity [59]. Results of other investigations of the PEO process in different electrolytes are summarised in Table 2.3. These reveal effects of the electrolyte composition and pH together with other parameters, such as current density, voltage, and electrolyte temperature. However, it is difficult to discuss these characteristics individually. Effects of other parameters of the PEO process are discussed in the following sections.

This study is focused on understanding the effects of electric field distribution and the physical characteristics of electrolyte (temperature and conductivity) on the characteristics of the PEO process, which is seldom studied. It is generally believed that both the electric field distribution and electrolyte characteristics should influence the coating morphology however there is no clear understanding of the extend of such effects. Therefore, investigation of coating characteristics under different treatment parameters providing controllable variation of electric field distribution in the electrolyser and basic physical characteristics of electrolytic solutions is of great interest.

Table 2.3. Summary of studies addressing effects of electrolyte characteristics on PEO process and resulting coatings.

Substrate	Process parameters					Results		Ref.
	Applied current density	Applied voltage	Duration (min)	Temperature (K)	Electrolyte	Coating composition	Research aims/results of electrolytic characteristics effects	
Al	NA	200V AC (60Hz) with 260V DC	5 min	NA	0-8 g/L Na_2AlO_2 0-8 g/L Na_2SiO_3 0-0.5 g/L Na_2SiF_6 2 g/L NaOH	α-Al_2O_3, γ-Al_2O_3, mullite	(1) Na_2SiF_6 affects the surface roughness and decreases the size of discharge channels; (2) Silicate electrolytes provide thicker coatings; (3) Aluminate electrolytes provide denser coatings.	60
Al	15 mA/cm^2	NA	10-60 min	293±1	0.01M $Na_2WO_4.2H_2O$	α-Al_2O_3, γ-Al_2O_3, WO_3, W	(1) Coating morphology is strongly dependent on treatment time; (2) Content of Al and W is much higher at discharge channels; (3) Content of γ-Al_2O_3 increases with itime.	61
Al	46.7-140.7 mA/cm^2	NA	NA	288-310	0.5-2.0 g/L KOH	NA	(1) Lower electrolyte concentration facilitates achievement of a high voltage; (2) Higher current density provides achievement of high voltage; (3) Lower electrolyte concentration promotes oxide film formation and hinders Al dissolution.	17
Al	125 mA/cm^2	-160 to 600V	0.5-65 min	303	Na_2SiO_3	α-Al_2O_3, γ-Al_2O_3,	Discharge characteristic in PEO of Al, and evolution of phase composition are discussed.	62
Al	10-120 mA/cm^2	100-350 V	NA	323-333	0.3M $Na_2B_4O_7.10H_2O$	Al_2O_3, $Al_4B_2O_9$	Effects of electrolyte temperature and current density on coating morphology and composition are discussed.	63
Al	100 mA/cm^2	400-600V	90-150 min	343-353	2-10 g/L Na_2SiO_3	α-Al_2O_3,	(1) Inner layer contains a number of predominately	64

					1-2 g/L KOH	γ-Al_2O_3,	amorphous sublayers; (2) Intermediate layer has a nanoscale polycrystalline structure. (3) Porosity at nanoscale is observed in the inner and intermediate layers.	
Al	5 mA/cm^2	500V	30-60 min	303	0.025-0.05M NaOH, 0.033M Na_2SiO_3, 0.008M $Na_6P_6O_{18}$	α-Al_2O_3, γ-Al_2O_3, $AlPO_4$	(1) Study on the effects of electrolyte concentration and composition on coating morphology and Al-P-O/Al-Si-O phase distribution; (2) Correction between phase composition and coating thickness.	65
Al	100 mA/cm^2	NA	0-35 min	303	0.025 g/m^3 NaOH, 0.066 g/m^3 Na_2SiO_3, 0.008 g/m^3 $Na_6P_6O_{18}$	α-Al_2O_3, γ-Al_2O_3, θ-Al_2O_3		66
2024 Al	NA	300-520V	20-40 min	298-318	20 g/L NaH_2PO_4 15 g/L $C_6H_{15}NO_3$	NA	Elemental composition and concentration values of PEO coating in the region of accumulation of dispersed formations.	67
AM50 Mg	15 mA/cm^2	NA	30 min	283±2	10g/L Na_2SiO_3 1g/L KOH 10g/L Na_3PO_4	NA	Effects of Cl^- concentrations on electrochemical corrosion behaviour of Si-/P-PEO coating on Mg	68,71
AM50 Mg	0.3 mA/cm^2	Up to 1000V	5min	NA	Na_2SiO_3+KOH, Na_3PO_4+KOH, $NaAlO_2$+KOH	NA	Effects of SiO_3^{2-}, PO_4^{3-}, AlO_2^- anions on both surface and cross-sectional morphology, coating composition, and analysis by EIS.	69
AM50 Mg	NA	400V	10 min	318	3-10g/L K_2ZrF_6, 0-8g/L $NH_4H_2PO_4$, 0-3g/L KF, 0-5g/L $C_6H_5O_7Na_3$	NA	Effects of electrolyte composition on peak/final current density, coating morphology, elemental distribution and EIS analysis.	70

ACM522 Mg	30 mA/cm^2	NA	10 min	293	0.5 M $Na_3PO_4.12H_2O$	MgO, $Mg_3(PO_4)_2$	Effect of PO_4^{3-} anions on coating composition, surface and EIS analysis.	72
AZ31 Mg	NA	300V	30 min	294-298	4 g/L KOH, 20 g/L Na_2SiO_3, 10mL/L glycol, 0-8 g/L KF	MgO, MgC_2, MgF_2, Mg_2SiO_4, $MgSiO_3$	Effects of F^- concentration on coating composition, corrosion resistance, discharge characteristics and EIS analysis.	73
AZ31 Mg	0.5 mA/cm^2	NA	10 min	303	25g/L Na_3PO_4, 25g/L Sodium EDTA, 0-12g/L $Fe_2(SO_4)_3$	MgO, Fe_3O_4	Effects of Fe^{3+} concentration on coating composition, porosity of coating surface, and thermal/optical properties of PEO coating.	74
AM50 Mg	30 mA/cm^2	NA	15 min	275±2	$Ca(OH)_2$: Na_3PO_4 1(2g/L) : 2.5(5g/L), 1(2g/L) : 5(10g/L), 1(2g/L) : 7.5(15g/L)	MgO, $Mg_3(PO_4)_2$, $CaH(PO_4)$, CaO_2	Comparison of calcium concentration effects on voltage vs. time behaviour, both cross-section and surface morphology, chemical and phase composition and electrochemical corrosion behgaviour.	75
AZ31 Mg	60 mA/cm^2	Up to 650 V	10 min	NA	10 g/L $Na_2SiO_3.10H_2O$ +4 g/L KOH with 2g/L $NaAlO_2$/ $Na_2B_4O_7.10H_2O$/K_2TiF_6/ Na_3PO_4/CH_4N_2O	MgO, Mg_2SiO_4, $MgAl_2O_4$, MgF_2, $Mg_3(PO_4)_2$,	Effects of various additives on coating morphology, chemical reaction during PEO process, potentiodynamic study, and EIS study	76
Mg	200 mA/ cm^2	NA	10 min	283±3	Varying concentration of Na_2SiO_3, KOH and $NaAlO_2$	MgO, Mg_2SiO_4, Mg Al_2O_4	Effects of electrolyte concentration on surface morphology, pore volume, elemental and phase composition.	77
AM50 Mg	30 mA/cm^2	420 V	10 min	295±2	8g/L Na_3PO_4 + 18g/L	MgO,	Study of the coating phase composition, microstructure,	78,79

					NH_4OH 3g/L K_2ZrF_6 +1g/L NaH_2PO_2	MgF_2, t-ZrO_2, m-ZrO_2	corrosion resistance under different pH conditions and EIS by using two different electrolytes.	
AZ91D Mg	NA	350-400 V	60-120 min	NA	10-20g/L Na_2SiO_3, 3-8g/L KOH, 4-8g/L NaH_2PO_4, 5-10 g/L $Na_2B_4O_7$, 5-10 g/L KF	Mg_2SiO_4, MgO, α-Al_2O_3, Mg Al_2O_4	Effects of additives on surface roughness, surface and cross-section morphology, coating composition, potentiodynamic polarization and capacitance of PEO coatings.	80
AZ31 Mg	50 mA/cm^2	NA	10 min	288	10g/L Na_2SiO_3, 3g/L KF, 0-40 g/L CeO_2 particle	MgO, Mg_2SiO_4, CeO_2	Study of the effects of CeO_2 particle concentration on coating composition, voltage transients during PEO process, coating morphology and corrosion resistance.	81
Ti	200 mA/cm^2	NA	5 min	293	0.01M KOH, 0.02M K_3PO_4, 0.02M $K_4P_2O_7$	TiO_2 (anatase), TiO_2 (rutile), P_2O_5	Report on the effects of electrolyte on surface properties and coating morphology.	82
Ti	100 mA/cm^2	NA	10 min	313	0.066M Na_3PO_4, 0.034M $Na_2B_4O_7$, 0.006M Na_2WO_4, 0.1M $Ni(CH_3COO)_2$, 0.025M $(CH_3COO)_2$	TiO_2 (anatase), TiO_2 (rutile), NiO, CuO	Study on the thermal behaviour of Ni- and Cu-containing PEO coatings and the effects of coating composition and morphologies.	83
Ti	150 mA/cm^2	NA	30 min	294±1	0.001 M $H_4SiW_{12}O_{40}$, 0.001M $H_3PW_{12}O_{40}$	WO_3, Anatase, Ti	Study of PEO coatings formed using heteropolytungstate acids on coating composition, discharge events and coating morphology.	84

NA= not available.

2.3 Effects of current modes

PEO is a complex process including electrical, chemical, electrochemical, heat and mass transfer processes. The total oxide layer formation efficiency (required formation energy/overall consumed energy) is about 20~30% [85] caused by metal hydroxides and hydrogen peroxide formation, anodic gas evolution, solution heating and evaporation, etc. To estimate those side reactions both qualitatively and quantitatively and to achieve adequate process control, the effects of current modes of the power supply on the PEO process is worth considering.

The following four current modes can be used to produce PEO coatings: direct current (DC), alternating current (AC), pulse unipolar current (PUC), and pulse bipolar current (PBC) as shown in figure 2.8. In the early years, the PEO process was mainly implemented under DC mode. However, to achieve a better control over the PEO processes, AC and PBC modes are now being considered.

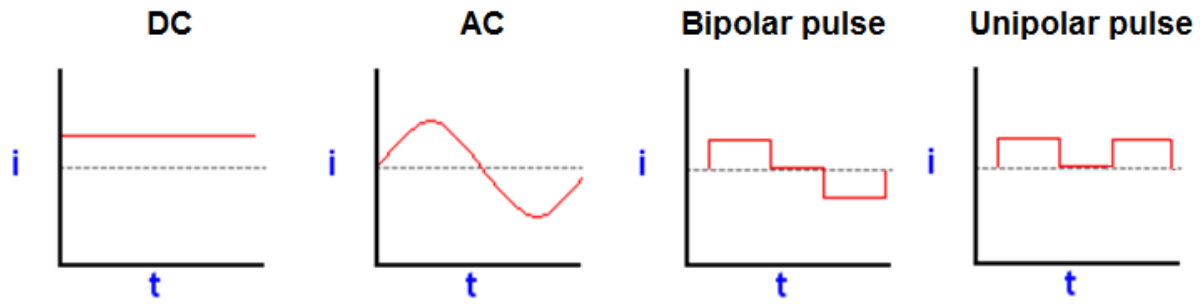

Fig. 2.8 Types of current modes (waveform) used in PEO research.

2.3.1 DC-PEO and PUC-PEO mode

DC-PEO mode utilises the simplest power supply to produce PEO coatings, it is only used for homogeneous alloy substrates and thin coatings since possibilities of controlling the process are limited [1]. The coating growth rate is usually around 1~2μm/min although the coating morphology is often coarse and porous. As regards to the properties of DC-PEO coating [86], on Mg substrate for example, the microhardness can be improved from ~HV75 for untreated Mg to HV150 for the PEO-coated one. In dry wear tests (against steel), DC-PEO coated samples provide only 1/3 of the friction coefficient of the untreated Mg

alloy, with the wear reduced also.

Yerokhin et al. [1] reported a pulsed unipolar mode (PUC), which allows to control the interruption of process and thus the discharge duration. Compared with the DC mode, the composition and structure of the coating produced is different. However, to reach the desired current density, a higher voltage (up to 1000V) may be needed, this might cause destructive effects, such as thermal cracking.

2.3.2 AC-PEO mode

Yerokhin et al. [87] reported that the AC-PEO mode provides more intensive and uniform sparking on the surface, with a possibility of partial reduction and dissolution of some oxide compounds during the negative half-cycles. This promoted formation on the surface of the rutile phase, lower oxides and intermetallics as well as hindered penetration of electrolyte anions in the film. Xin et al [88] noted that the PEO process under AC mode produced a smaller percentage of α-Al_2O_3 but better corrosion resistance of the coating than the DC mode, because less micro-cracks occurred. Specific characteristics of AC-PEO process include ability to form thick coating layers, obtain high hardness, large insulation resistance, and superior adhesion to the substrate [89]. Surface properties, such as abrasion, corrosion, and thermal shock resistance can also be improved [90, 91]. Yerokhin et al. [85] show the schematic diagram in figure 2.9 (a), which explains the current distribution during AC-PEO treatment of metals. The PEO mechanism under AC mode is illustrated schematically in Fig. 2.9 (b) [92].

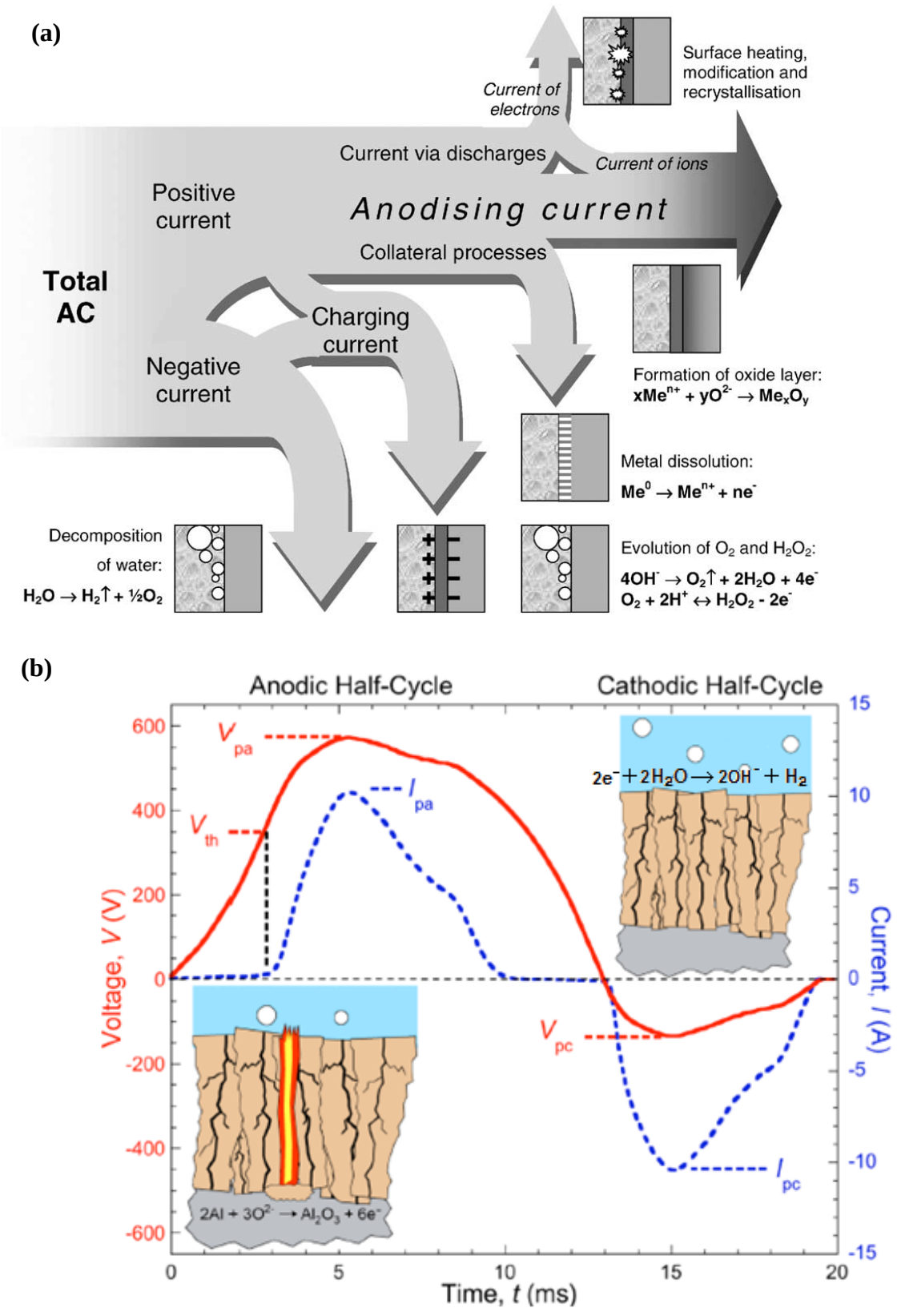

Fig. 2.9 Schematic diagram of (a) current distribution during the PEO treatment of metals in AC mode [85], (b) PEO process under AC mode with anodic and cathodic half-cycle.

2.3.3 PBC-PEO mode

To overcome the disadvantages of the AC-PEO process, such as low coating growth rate, the presence of a relatively thick porous outer layer (which must later be removed at the finishing stages of the manufacturing process) and low energy efficiency, Yerokhin et al. [53] suggested the PBP process. The coating growth rates provided by DC- and AC-PEO processes are only 1~2 μm min^{-1} [1] , however, utilizing a pulse bipolar current (PBC) PEO process allows coating growth rates to be increased up to 10 μm min^{-1} [93]. The enhancement effect of the PBC-PEO mode on coating properties and morphology is obvious, e.g. production of denser coating layers with higher micro-hardness and lower friction coefficient compared to the DC-PEO coatings. It is considered that the higher frequency PBC modes enable the generation of shorter yet more energetic microdischarge events [86]. It was found that the optimal combination of the coating growth rate and energy consumption can be achieved at a pulse frequency between 1 and 3 kHz. It has also been demonstrated that the new PBC-PEO process is capable of providing significant improvement in the coating morphology, when forming dense and uniform surface layers of 50 to 70 μm in thickness, in which the porous outer layer occupies only 10 to 15% of the thickness total.

The PBC mode requires an advanced power supply which allows independent control over the main pulse parameters, such as pulse duration, amplitude, duty cycle during both positive and negative biasing [53]. It is more suitable to achieve a better process control of the PEO treatment, however a large number experimental variables introduced makes it difficult to find optimum processing conditions using conventional methods of experimental design. It is noticed that the pulse frequency can affect the coating growth rate and specific energy consumption, indicating that there exist optimal frequency ranges for different types of substrate and electrolytes [86, 110, 111]. Despite these observations, the mechanisms underlying frequency effects on the PEO process and resulting coatings are still unclear, undermining the capabilities of conventional experimental approaches employed so far to study the PEO process. This outlines the need in development and exploration of new experimental techniques for investigation of the PBC PEO process. Within this context, the methods based on frequency response analysis of the studied system appear to be extremely promising. Of particular interest for the purposes of this study is the method of in-situ impedance spectroscopy, which has been recently developed [112] and adopted to the studies of the PEO process. The details of in-situ impedance spectroscopy technique and the setup of the PEO treatment system accommodated for this method are introduced in Chapter 3.

2.4 Chemical reactions during the PEO process

The PEO treatment is based on complex chemical, electrochemical and plasma-chemical processes that influence heat, mass and charge transfers at the metal-electrolyte interface. During the last decade, researchers have extensively discussed the main reactions both theoretically and experimentally. The following model of the plasma electrolytic oxidation provides basic understanding of the main electrochemical reactions taking place during the treatment [2,50]:

(1) Oxide formation due to the opposite migration of metal (Me) ionised at the metal–oxide interface and Oxygen adsorbed on the surface.

$$\mathrm{Me} \rightarrow \mathrm{Me}^{n+} + n\mathrm{e}^{-} \qquad (n = 2, 3, \text{or } 4) \qquad (2.1)$$

$$\mathrm{Me}^{2+} + \mathrm{O}^{2-} \rightarrow \mathrm{MeO} \qquad (2.2a)$$

$$2\mathrm{Me}^{3+} + 3\mathrm{O}^{2-} \rightarrow \mathrm{Me_2O_3} \qquad (2.2b)$$

$$\mathrm{Me}^{4+} + 2\mathrm{O}^{2-} \rightarrow \mathrm{MeO_2} \qquad (2.2c)$$

(2) Direct ejection of metal ($\mathrm{Me_{ej}}$) into the electrolyte, when electronic conductivity of the oxide film is developed around the breakdown voltage (usually > 400 V).

$$\mathrm{Me_{ej}} + n\mathrm{OH}^{-} \rightarrow \mathrm{Me(OH)}_n + n\mathrm{e}^{-} \qquad (n = 2, 3, \text{or } 4) \qquad (2.3)$$

(3) Under the same conditions, gaseous oxygen can also be liberated at the anode:

$$4\mathrm{OH}^{-} \rightarrow 2\mathrm{H_2O} + \mathrm{O_{2\,(g)}} + 4\mathrm{e}^{-} \qquad (2.4)$$

(4) At the oxide–electrolyte interface, outward moving metal cations react with OH^{-}.

$$\mathrm{Me}^{2+} + 3\mathrm{OH}^{-} \rightarrow \mathrm{Me(OH)}^{-}_{3} \qquad (2.5a)$$

$$\mathrm{Me}^{3+} + 4\mathrm{OH}^{-} \rightarrow \mathrm{Me(OH)}^{-}_{4} \qquad (2.5b)$$

$$Me^{4+} + 5OH^{-} \rightarrow Me(OH)^{-}_{5} \quad (2.5c)$$

(5) Chemical dissolution of metal oxides caused by instability of the protective oxide film.

$$MeO + 2OH^{-} \rightarrow MeO_2^{2-} + H_2O \quad (2.6a)$$

$$Me_2O_3 + 2OH^{-} \rightarrow 2MeO_2^{-} + H_2O \quad (2.6b)$$

(6) Precipitation of metal hydroxide driven by changes in pH near the film–electrolyte interface, this may result in sealing the pores in the oxide layer.

$$Me(OH)_{n\,(sol)} \leftrightarrow Me(OH)_{n\,(s)} \quad (2.7)$$

(7) In AC-PEO, the reaction of hydrogen gas evolution is also possible during the cathodic half-cycle.

$$2H_2O + 2e^{-} \rightarrow 2OH^{-} + H_{2\,(g)} \quad (2.8)$$

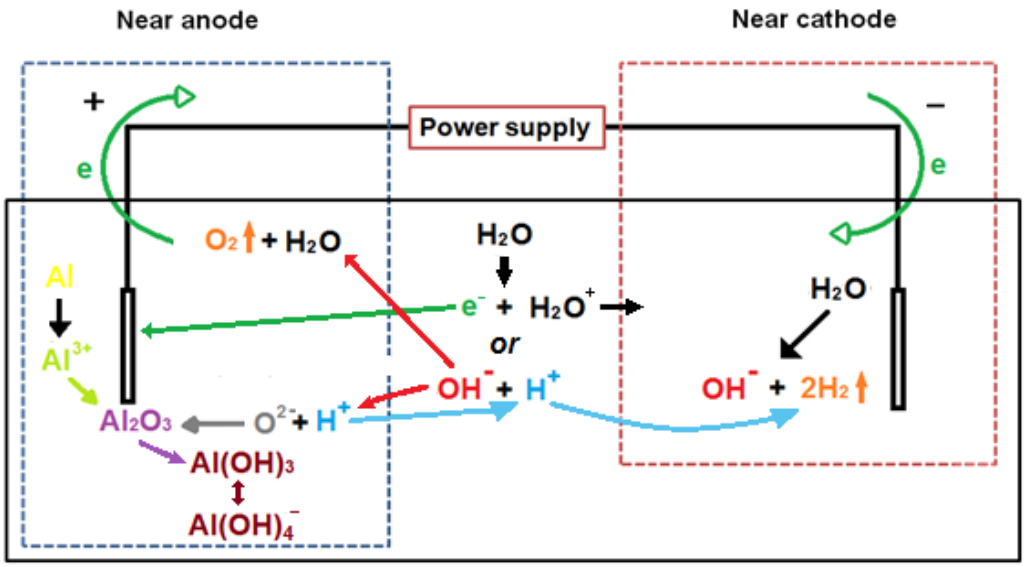

Fig. 2.10 Schematic of simplified chemical reactions during processing of Al in alkaline electrolytes.

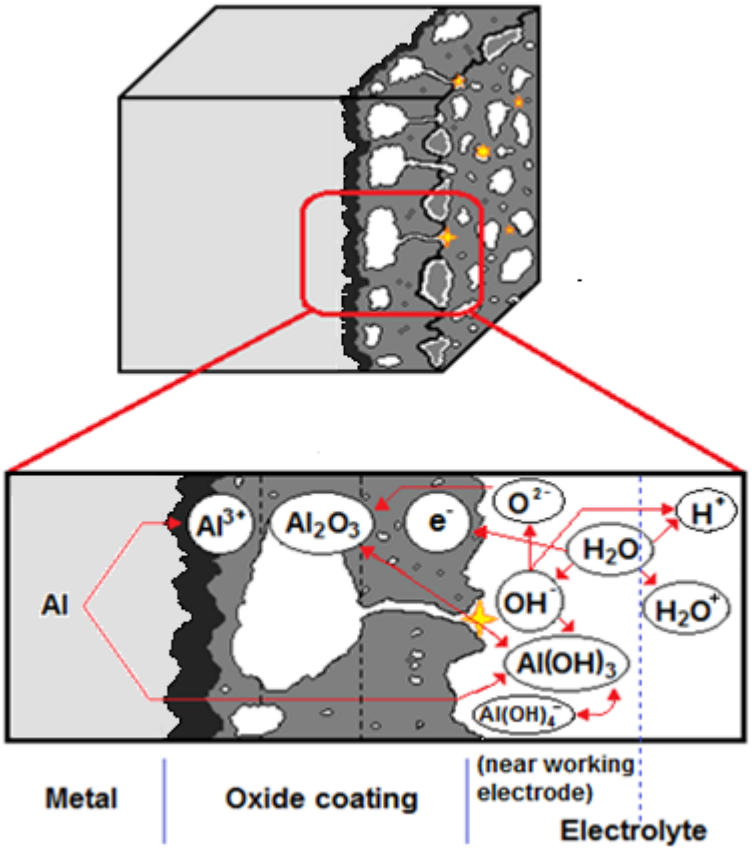

Fig. 2.11 Schematic of chemical reactions at the surface of alumina coating during the PEO process.

A simplified scheme of electrochemical process taking place during the PEO treatment of Al in an alkaline electrolyte in the regions of (1) anode; (2) cathode, and (3) in the bulk of the electrolyte is shown in figure 2.10. It is assumed that during the PEO process, the chemical reactions are varied and become more complex due to the involvement of different electrolyte additives or alloying elements of the substrate. Moreover, during the PEO process a variety of complimentary plasma thermochemical reactions occur [1], that result in specific surface structures formed by metastable high temperature phases, amorphous and complex compounds. The discharge plays an important role in triggering the primarily compound dissociation, and causes the components of plasma to form products condensed within the discharge channel. Therefore, when the cooling rate reaches 10^8K/s, unique high temperature phases, supersaturated solid solutions and nonequilibrium compounds can be formed on the surface. This underlines the importance of plasma discharge phenomena for the entire PEO process and makes the understanding of discharge nature and underlying mechanisms crucial for the progress of PEO technology.

2.5 Discharge phenomena

Understanding discharge behaviour is crucial for characterisation of the PEO process; it influences growth mechanism, composition, morphology and properties of the coatings formed. The growth of the oxide film is based on the breakdown occurring at weak (often thinner) sites of the coating. Size and spatial density of discharge channels are the two observable characteristics of the breakdown. Therefore, investigations of size and population density of discharge channels formed during the PEO process are relatively abundant. Matsuzawa et al. [94] found that the surface of the oxide film formed under intense luminescence is remarkably rugged, while that with weak luminescence is entirely uniform. Sundararajan and Krishna [19] investigated number and size of the pores produced by discharge events; and Yerokhin et al. [95] reported the results of microdischarge spatial density, fraction of the sample surface area being instantaneously covered by active discharge sites and mean average current density in a single microdischarge. The characteristics of discharge events studied by researchers can be categorised as follows:

2.5.1 Duration of discharge events

The duration of discharge events has been investigated in several papers. However the results reported in the literature are scattered. Arrabal, et al [99] studied the discharge duration using fast video imaging (5400 to 20000 frames per second) during PEO processing of Mg. In his study, the shortest duration of discharge was in the range $\leq$ 0.05 - 0.185ms; the longest living discharges lasted from $\leq$ 1 to $\leq$ 4ms; and the average lifetime was in the range of 0.5 - 1.1ms. In the work by Dunleavy, et al [97], discharge lifetime during the PEO process on Al was estimated in the range of 10-100μs. Three methods were applied in that study, optical emission spectra, correlation with imaging and monitoring of electrical characteristics in the DC mode. A similar duration range (10-100μs) was reported by Long, et al [109] based on electrical measurements.

Yerokhin, et al [62] applied imaging methods to observe the discharge events during AC PEO process on Al. The individual discharge duration were $\leq$ 7.5ms. He also indicated that the lifetime of discharge could be at least two orders of magnitude larger than the expected duration of conventional electron avalanche events [62]. Matykina, et al [96] studied the discharge duration using a high-speed imaging with 10ms exposure time and 40ms interframe

time during the PEO process on Ti at different applied voltages. Discharge durations were ~35-100ms, ~35-260ms and ~100-800ms at 300V, 370V and 430V, respectively. From the literature review, the discharge durations are ranging from about 10 to 10^3μs.

From the above discussion, it follows that the observed duration of the discharge, varies in which it is often limited by the resolution of the experimental equipment employed for the study. Events from each studies are different with a wide range from 10^{-5} to 10^{-1}s. Therefore, discharge events require careful investigation at a higher temporal resolution. To study the discharge lifetime during the PEO process of Al in this work, an ultra-high speed imaging system is used. Compared with the imaging systems used previously, the ultra-high speed imaging system with multi-channel framing camera can provide 12bit digital images, and also a wider control over the exposure and interframe times that can be varied in the range from 1ns to 10ms. This creates an opportunity for more detailed investigations of the characteristics of discharge events such as the intensity, FWHM and displacement trajectory at different time scales. Further discussion of the ultra-high speed imaging system and the corresponding devices is carried out in section 3.6.

2.5.2 Size and spatial density of discharge events

The size of an individual discharge event is one of the main physical characteristics that can be measured based on optical imaging. Both size and density of discharge events are changed in different stages of the PEO process.

Yerokhin, et al [62,100] reported the mean diameter of the light spot to be around 160μm, which were most common discharge events during the whole PEO process. The lightest discharge density was about 6×10^7 $m^{-2}s^{-1}$ around 10 min from the beginning of the process, and then decreased to about 2.6×10^7 $m^{-2}s^{-1}$ after 60min. This work was carried out on Al substrates, using a frame rate of 24Hz. Matykina, et al [96] studied the discharge size and density studied during DC PEO process on Ti with the frame rate and exposure time of 24Hz and 10ms, respectively. The discharge density was about 5×10^6 $m^{-2}s^{-1}$ at about 160s from the beginning of the process. It increased to around 2×10^7 $m^{-2}s^{-1}$ after 900s and reached the maximum of 3×10^7 $m^{-2}s^{-1}$ after 760s. The discharge diameter was in the range from ~80 to over 370μm. Arrabal, et al [99] applied fast video imaging at 5400 frames per second with the exposure time of 185μs to the PEO process on Mg substrate. The discharge density was reported in the range from 10^8 to 10^9 $m^{-2}s^{-1}$.

However, in these studies the effects of exposure time on the apparent characteristics of discharge events such as size, optical intensity, and location was often ignored. Due to the fact that these discharge characteristics are strongly influenced by exposure time in the optical imaging system, the associated effects require careful attention. Therefore, an ultra-high speed imaging system and corresponding devices are also used in this work to study the size evolution of individual discharge events during its lifetime.

2.5.3 Current characteristics of discharge events

Fluctuations or pulses observed in the electrical response signal of the PEO process provide another manifestation of discharge events. Kasalica et al [101] presented the discharge event by plots of current and voltage variation during the discharge lifetime as shown in figure 2.12. In his work, the peak current of discharge event was around 1mA, while the average energy was 0.2μJ. The discharge current density was also estimated to be around 10^9 Am^{-2}. Yerokhin et al reported that the current density of discharge events during the PEO process changed with the duration of the process [95], to be around 5×10^4 Am^{-2} during the first minute, and then dropping to around 2×10^4 Am^{-2} after 80 minutes of the treatment. The surface area covered by the discharge was evaluated by studying the total area fraction apparently undergoing discharge at any given time during the treatment. These results were calculated from the analysis of stills video images taken at 24 Hz frame rate with unspecified exposure time. Further values of current density of discharge events reported by Dunleavy, et al [97,98], where the peak current of individual events spanned the range from ~8 to ~40mA (figure 2.13). The data of the above reports indicate the discharge currents are in the order from 1 to 10^2mA and the current density is in the range of 10^4 to 10^8Am^{-2} in a customised small area system. The differences provided by these studies are obvious, leaving major uncertainties regarding the actual range of discharge current densities.

From the above work, the evaluations of the size of discharge events are affected by the setup of the imaging system, especially by the exposure time. In this work, the characteristics of discharge events are therefore investigated not only by ultra-fast video imaging at different exposure times, but are also in association with high-resolution current signals obtained using a 16 Bit dual-channel digitalizer.

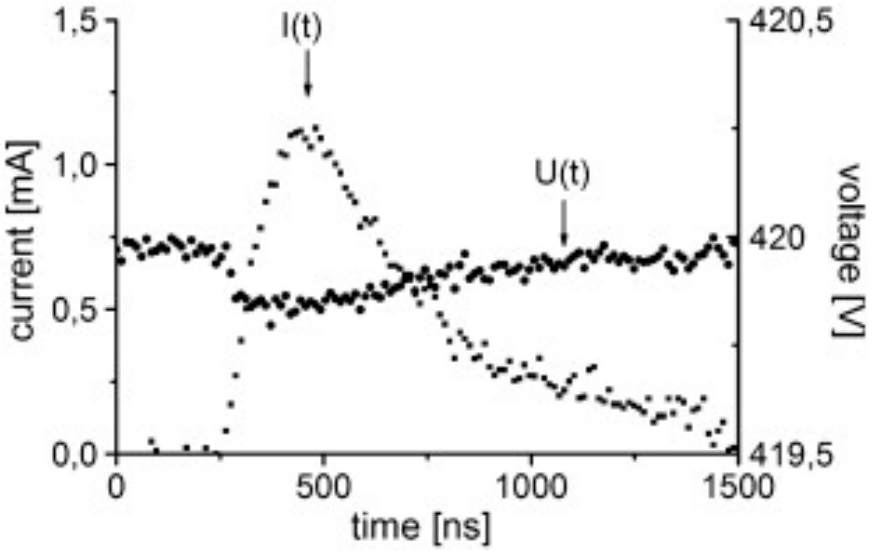

Fig. 2.12 Current and voltage variation during one breakdown event [101].

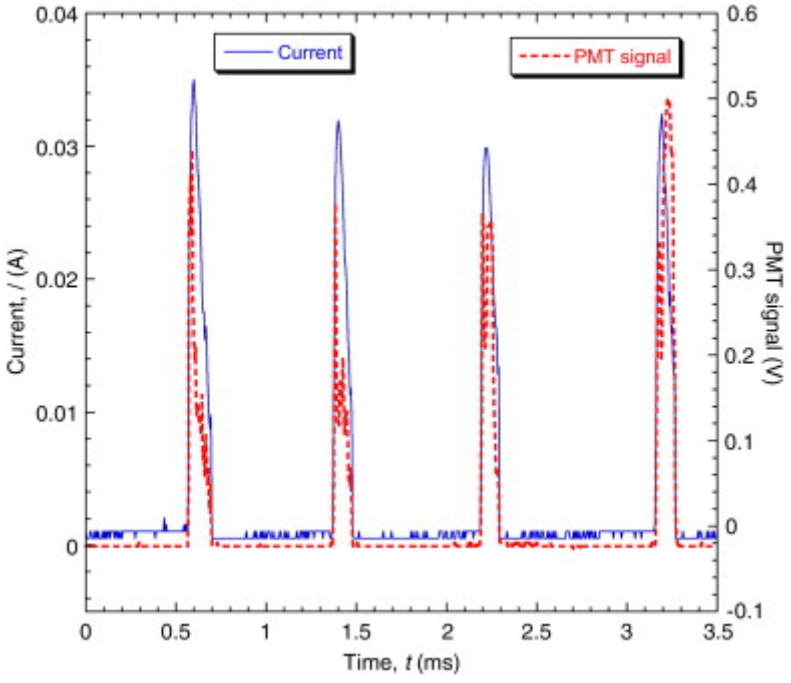

Fig. 2.13 Typical sequence of current pulses corresponding to individual discharge events, and associated light emission, obtained using a photomultiplier tube [97].

2.5.4 Diagnostics of the optical emission of discharge

Research focused on investigation of discharge events has increased significantly during the last several years. Optical emission spectroscopy (OES) is the most frequently used method to identify and observe the temporal evolution of spectral lines attributed to the discharge in the visible and near UV region. Jovovic et al. [102] carried out a spectroscopic study of PEO processes on Mg and Al. Three estimations of plasma electron density N_e were performed using H_β line. The analysis of the Balmer lines (H_α and H_β) indicated that two processes occurred in the plasma during the micro-discharge event. Two lower N_e values (~$1.2 \times 10^{15}/cm^3$ and ~$2.3 \times 10^{16}/cm^3$) were derived from the H_β line shape, while the two larger N_e of 1.6×10^{17} cm^{-3} and 1.2×10^{17} cm^{-3} were related to magnesium and aluminum species, respectively. Incorporation of metal species into plasma is believed to take place during the PEO of Mg and Al because of low melting temperatures (T_M) of these elements, 650℃ and 660℃, respectively. Titanium and tantalum have much higher melting points of 1668℃ and 3017℃, therefore, the metal lines were not detected in OES during corresponding PEO processes. Jovovic, et al., [103] have also performed spectroscopic characterization PEO of Al in acid and alkaline electrolytes. Hussein et al. [104] reported the spectroscopic study of plasma discharge during PEO process with different current densities at various time stages from 0 to 60 min. Wang et al, [105] studied the effects of various electrolyte composition on characteristics of optical emission spectra of plasmas during the PEO processing of Mg. However, attempts to correlate optical emission to the electrical response of the PEO system appear to have so far failed in providing any valuable insights. The main reason here seems lying in the fact that optical emission may be caused by electron transition within the species and not necessarily be associated with generation or transfer of charge in the system.

Other investigation methods such as ultra high-speed imaging and spectral analysis of current signal, have progressed steadily and these are utilised in this work to study the characteristics of discharge events including lifetime, size, spatial density and current transient at the sub-microsecond time scale.

Since the mechanism of discharge depends on the type of breakdown, the study of the breakdown phenomena occurring during the PEO process is required. Of particular interest is initiation of discharge, however, it is extremely challenging task for the in-situ methods. Several models of this phenomenon are reported, as discussed in the next section.

2.5.5 Generation of discharge

Oxide breakdown is the process of discharge initiation, leading to formation of discharge channels that perforate the coating during the PEO process [108]. As microscopic characterisation confirms, a passive oxide film is formed on the metal surface as soon as anodic polarisation is applied, then the passive film may begin to dissolve. It can be noted that the formation of the passive oxide film conforms to Faraday's law and the dissolution may correspond to the pitting potential of the coating material. In region II of figure 1.5 in section 1.2, a porous oxide film rapidly grows due to the anodising under galvanostatic conditions; the voltage rises slowly, and the maximum value of it is typically limited by the range of 150–250 V. In region III (figure 1.5), the electric field strength in the oxide film reaches a critical value beyond which recrystallisation occurs and defects are formed in the porous oxide film due to a small sparking, in which a barrier oxide film starts, formed near the metal substrate. The barrier oxide film acts as a passive electrical component, i.e. capacitor with high capacitance. When the electric field strength in the barrier oxide film causes the voltage to reach the breakdown value, the discharge events start occurring.

The oxide breakdown event is catastrophic and irreversible. Figure 2.15 illustrates the development of the breakdown in the barrier oxide film. The breakdown is believed to be caused by microscopic defects under high electric field conditions [108]. Defects within the oxide are usually called traps, where the degraded oxide can trap charges. When more traps are created in the oxide film, promoting an accumulation and overlap of the trap defects eventually forming a conductive path (soft breakdown) through the oxide [108]. Once there is a conduction path, new traps are created by thermal damage, which in turn allows for increased conduction. The cycling of conduction leading to increased heat and further increased conduction leading to thermal runaway finally results in lateral propagation of the breakdown spot. The oxide film within the breakdown spot starts to melt, and a conductive filament is formed in the breakdown hole. This type of breakdown is called hard breakdown [108]. The critical potential for the barrier oxide film breakdown appears less anodic (more negative) than the general transpassivation potential. The breakdown hole is highly penetrably and provides a localized leakage path for electrons and ions. However, due to the small size of the hole, the new barrier oxide forms rapidly in it. Due to high breakdown voltage (generally higher than 300 V) and local current density, a very high temperature is developed in the conductive filament. If the energy released is greater than the formation heat of the barrier oxide, it leads to structural changes from porous to barrier oxide at the interface.

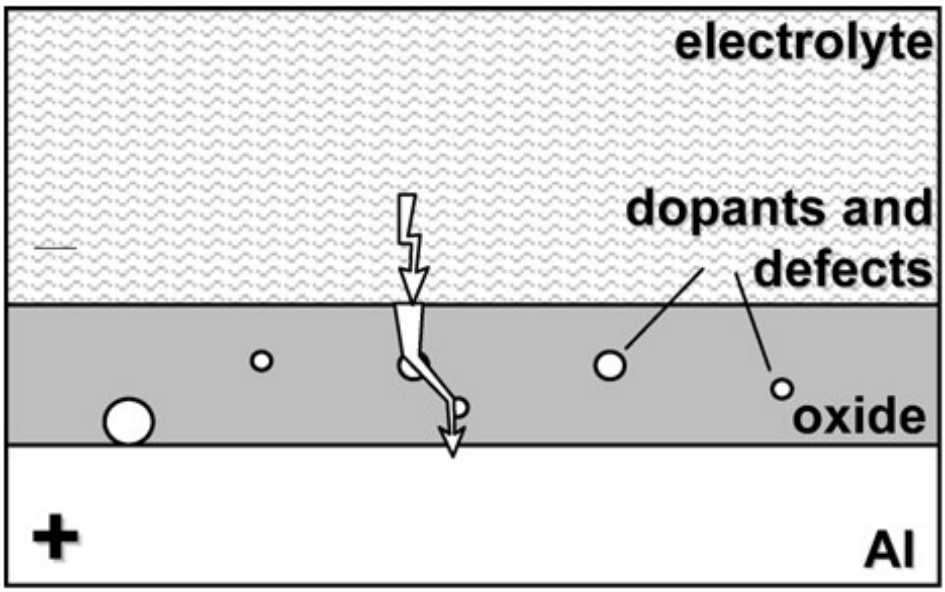

Fig. 2.14 Assumed model of the oxide film dielectric breakdown

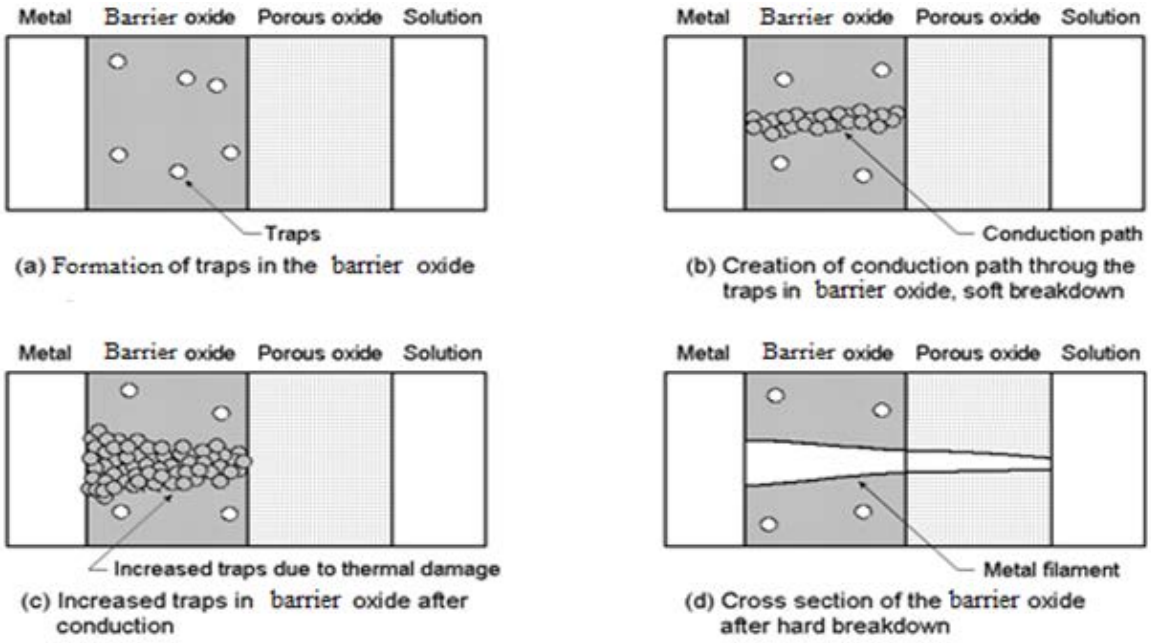

Fig. 2.15 Schematic of the barrier oxide breakdown

2.6 Breakdown of oxide films

Whilst the previous sections have discussed the role and characteristics of discharge events occurring during the PEO process, here the emphasis is given to the breakdown phenomena that initiate the discharge event. Dielectric breakdown is considered to be a common mechanism for the breakdown of the growing oxide film during the PEO process, The dielectric breakdown is often affected by the high electric field. In this case it is developed due to the loss of electrical insulating capacity of the dielectric materials. Dielectric breakdown takes place when the external electric field increases to a limit when all dipoles in the medium break and free charges develop causing the material to behave like conductor. Here, the maximum electric field up to which the dielectric can exist is called a dielectric strength of the medium.

Beside the effects of electric field, there are three other conditions that can lead to the dielectric breakdown: (a) Thermal breakdown, which is often observed for non-ideal dielectrics that may permit some leakage current. The electrical energy loss has to be dissipated as heat. If the heat dissipated is less than the heat generated, the temperature of the dielectric materials increases progressively, eventually resulting in local melting, and then high current through the dielectric material can develop; (b) Electro chemical breakdown - due to the external effects, such as electric field and temperature etc., a chemical change may occurs in the dielectric, which would result in deterioration of the electric insulation performance; (c) Defect breakdown - when there are defects, pores or cracks, in the medium, its dielectric strength is decreased and the material can be ionised easily to becomes conductive.

More specifically to the anodic oxide films on valve metals, it is suggested that a so-called 'electric breakdown' can trigger the discharge events, following the electron avalanche mechanism. This term introduced by Wood, et al [106] in 1967 indicates that when electrons are transferred from the electrolyte to the oxide film, they are accelerated by the electric field and then impact on atoms to hit out more electrons. A large number of electrons must be generated to achieve the electric avalanche breakdown, according to this mechanism.

During 1973-1977, Ikonopisov has brought forth a phenomenological model [107] to point out that during the oxidation process the ionic current causes a increase in oxide film thickness and does not directly affect the electric breakdown. On the contrary, the electronic current which exists as a leakage current has low correlation with the film growth, but the

electric breakdown mechanism is triggered. The leakage current may be instigated by a hair crack in the barrier oxide layer, electrolyte ion penetration, or trace alloy elements intrinsic in the substrate. The main phenomenological equations governing this process are as follows:

$$U_B = \frac{\varepsilon_m}{r_e} \ln j_B - \ln J_e(0) \tag{2.9}$$

$$U_B = A_B - B_B E^{1/2} \tag{2.10}$$

$$U_B = \alpha_B + \frac{\beta_B}{T} \tag{2.11}$$

$$U_B = a_B + b_B \log \rho \tag{2.12}$$

where ε_m is the energy of the electron being accelerated; J_e (0) is the electron avalanche current density at the interface between the thin oxide film and solution; U_B is the breakdown voltage; J_B is the critical electronic current density when electric breakdown occurs; r_e is a coefficient; E is electric field; T is temperature; ρ is resistivity. A_B, B_B, α_B, β_B, a_B, b_B are constants. The mechanism of the electric avalanche can cause both types of high electric field and thermal breakdown in the materials. Once the electric avalanche occurs, it can trigger the dielectric breakdown; the electrons that trigger this process in the PEO coating are mainly generated by the polarisation of H_2O as shown in figure 2.10.

According to Yerokhin et al [62], the formation of microdischarge during the PEO process can be conjectured in several models. One model assumes that microdischarges appear as a result of oxide film dielectric breakdown in a strong electric field (Fig. 2.12). This breakdown phenomenon is caused by the electron avalanches induced by film dopants and structure defects. However, it appears that this model does not fit the spatial, temporal and electrical characteristics of microdischarge phenomena.

The above breakdown phenomena are believed to underpin the plasma microdischarge events occurring during the PEO process. However, there is no direct evidence to prove that these phenomena actually take place, because it is difficult to resolve the within the discharge lifetime because of the limitations of existing methods of process characteristation. Therefore, new in-situ study methods are required to clarify the phenomenology and the corresponding mechanisms of the PEO process.

2.7 Aim and objectives

Based on the above analysis, the overall aim and specific objectives of this research have been defined as follows:

Aim: To achieve better understanding of the plasma electrolytic oxidation process of Al based on application of new in-situ research tools.

Objectives:

1) Identify, develop and adopt new research methods capable of providing novel information crucial for understanding of the mechanisms underlying the PEO process.
2) Investigate effects of electric field distribution in electrolyser on characteristics of the PEO process and coating growth behaviour on Al.
3) Study effects of electrolyte temperature and conductivity on the characteristics of PEO process on Al.
4) Compare characteristics of the oxide-electrolyte interface under conditions of free corrosion and at the potentials of dielectric breakdown for PEO coatings on Al with different thicknesses.
5) Investigate the temporal and spactial evolution of individual discharge events and correlate with electrical characteristics of the PEO process on Al.

Chapter 3

Methodological Approaches to the Modelling of PEO Processes

Complex phenomena driven by various mechanisms discussed in the introduction to the PEO treatment in the previous chapter are difficult to study using conventional techniques. Therefore, several new methods are employed in this work to provide a detailed understanding of the PEO process. These include in-situ impedance spectroscopy, an approach to modelling based on electrochemical impedance spectroscopy; the COMSOL-Multiphysics modelling of electric field distribution; fractal analysis and ultra-high speed imaging of discharge events. In this chapter, these main research methods are introduced and discussed and their use during the PEO process study is outlined.

3.1 Electrochemical impedance spectroscopy (EIS)

Electrochemical impedance spectroscopy (EIS) is an important technique in applied electrochemistry and materials science, which has been known for more than a century. It is a powerful method to investigate the mechanisms of electrochemical reactions by analysing a current response to the small AC perturbation of potential with variable frequency. The result is presented in plots of two impedance loci in the complex plane and typically plots of frequency-dependent impedance magnitude and phase angle. An equivalent circuit is used to model EIS results using classical electrical components (resistors, capacitors, inductors) and specialized electrochemical elements (e.g. Warbug diffusion element or Constant Phase Element (CPE)). Each element in the model has a known impedance behaviour. The information from EIS results can then be studied. The EIS techniques becoming increasingly

popular in different research fields.

3.1.1 Background of EIS

The development of EIS can be traced back to Oliver Heaviside's work in 1872, investigating of transient response of electrical circuits with applications of Laplace transforms. At that time, the concepts of inductance, capacitance and impedance of electrical circuits was introduced. [113,114]. Later, in 1894, Nernst applied the Wheatstone electrical bridge to measure the dielectrical constants from aqueous electrolytes and different organic fluids [114]. In 1899, Warburg developed expressions for diffusion behaviour derived from the impedance function [113,114].

In the early 20th century, Finkelstein applied the impedance technique to analyse the dielectric response of an oxide film[114]. Impedance spectroscopy was next used to measure the capacitance of mercury electrodes and to develop models for the study of the electrified interface [113]. The mercury electrodes were chosen because they provide a uniform and easily refreshable interface which is polarizable over a wide range of potentials [114]. In the 1920s, this technique was applied to biological systems such as vegetable cells, suspensions of blood, muscle fibers, skin tissues and membranes [114]. A few years later, K.S. Cole found that the capacitance was a function of frequency from the analysis of cell membranes [114]. Fricke reported the relationship between frequency exponent of impedance and also observed the constant phase angle in 1932 [114]. In 1941, K. S. Cole and R. H. Cole presented the frequency-dependent dielectric constant in a complex plot (imaginary part and real part of dielectric constant as y and x axis, respectively), which is so called 'Cole-Cole plot'. They also suggest the use of a constant-phase element (CPE). In the next decade, Frumkin and Grahame explored the double-layer structure, and provided a fundamental understanding of it using EIS technique [114].

Impedance spectroscopy began to be applied in more complicated systems around the 1950s. In 1960, I. Epelboin and G. Loric reported that the low-frequency inductive loop can present the behaviour of an intermediate reaction [114]. De Levie developed the theory of porous and rough electrodes with impedance response by transmission line models [113,114]. Around 1970, frequency response analysers were developed. Furthermore, J.R. Macdonald et al developed the nonlinear complex regression techniques [113,114]. These techniques led to the EIS applications on corrosion mechanisms and electrodeposition in the 1980s. In the late 1980s, the application of Kramers-Kronig transforms (KKT) in EIS for treating optical data is

worth mentioning. KKTs provide an independent method to check the validity of the impedance data which is in compliance with linear systems theory [113,114].

EIS is currently becoming an important technique and is used in different application fields, such as characterization of materials, solid state devices, corrosion of materials, and electrochemical power sources. Before employing the EIS technique in these application, it is necessary to understand the theory and analysis methods.

3.1.2 Fundamental theory of EIS

An unknown internal structure of a physical system can be considered as a black box. The internal structure of the black box cannot be observed and measured directly. However, there is still an input and output with the black box. When given a perturbation signal from the input terminal, there will be a signal which can be received at the output terminal, and this is called 'response' signal [115]. If the internal structure of the black box is a linear stable structure, then the output signal is a linear function of the input perturbation signal. Therefore, this output signal is a linear response of the input perturbation signal. By applying the above principle, the unknown internal structure can now be studied by the perturbation and response signal. The relational function between the perturbation signal and response signal is called the 'transfer function' [114-116]. Laplace transfer is used to present the relation between the functions of perturbation and response signal as shown below:

$$R = H(s) \cdot D \tag{3.1}$$

where the *R* and *D* present the functions of response and perturbation, respectively. *H(s)* is the transfer function with Laplace frequency *s*. In this equation, the types of perturbation signal and waveform can be different [115].

The EIS technique is based on the above principle, which uses a ratio between potential and current as the transfer function with a sine wave as the perturbation waveform. In here, the transfer function is called an immittance. By using a sine wave as the perturbation waveform, the transfer function is becoming a frequency-response function. Therefore, when the internal system is linear and steady, the angular frequency ω of the response sine wave signal should be the same as the input sine wave signal. In the above system, the variation of frequency f and ω relating to the transfer function can present information on the internal system. To make certain of the accuracy of the transfer function, it is necessary to consider

the three requirements in this technique as: (1) causality, (2) linearity, and (3) stability [115]. Causality is the requirement to make sure the output signal only responds from the input perturbation signal. In other words, it should avoid the interference of the noise. If the system follows the requirement of causality but not linearity, harmonics at non-excited frequencies may appear which will disturb the response signal. Stability is the requirement to avoid the changing of internal structure caused by the input perturbation signal.

In the EIS technique, the transfer function can be presented as the following equation:

$$Y = G(\omega) \cdot X \tag{3.2}$$

in the equation, *G* is the a frequency function with an angular frequency ω. *Y* and *X* are the input and output signal, respectively. When the sine wave voltage and current are set as the input and the output signals, respectively, the formal quantity obtained by dividing the output by the input provides admittance. If we exchange the sine wave current and voltage to input and the output signals, respectively, the result will present impedance [115].

From the equation 3.2, *G(ω)* is a frequency-dependent vector, which can be presented as the complex function of angular frequency ω as:

$$G(\omega) = G'(\omega) + jG''(\omega) \tag{3.3}$$

where $j = (-1)^{1/2}$, *G'(ω)* and *G''(ω)* are the real and imaginary parts, respectively. In the study of impedance *Z*, equation 3.3 can be transformed as follow:

$$Z = Z' + jZ'' \tag{3.4}$$

where Z' and Z'' present the real and imaginary parts of impedance, respectively. The frequency-dependent response values of Z' and -Z'' can be presented as a complex plot (figure 3.1a), in which -Z'' is used as the ordinate axis and Z' is set-up as the abscissa axis. In the complex plot, impedance can be represented as a vector of length |Z|, whereas $|Z|^2 = Z'^2 + Z''^2$. The correlation between |Z| and frequency are presented as one of the Bode plots as shown in figure 3.1b. The other Bode plot is presented as the correlation between the phase angle and frequency (figure 3.1c), in which the phase angle is the angle between vector |Z| and Z' axis. Therefore, the value of phase angle can also be calculated as tan θ = -Z''/Z.' The Bode plots can assist the complex plot to understand the behaviour in relation with different frequencies, which is difficult to observe directly from the complex plot.

The physical meaning of the system internal structure can now be studied using complex and Bode plots. To understand the behaviour of electrochemical systems in detail, equivalent circuit analysis is used to fit the plots in both complex and Bode planes. Equivalent circuits are used to setup a model with elements that can present (or approach) the same locus in both Complex and Bode plots, and then the elements are used to help explain the physical meaning of the processes taking place in the electrochemical system. Elements in the equivalent circuits include conservative electrical components such as resistors, capacitors, and inductors. These elements in the equivalent circuit exhibit known impedance behaviour during the EIS modelling. Moreover, to reflect a more complex behaviour of the electrochemical system, specialized electrochemical elements such as Warbug diffusion element and Constant Phase Element (CPE) are developed. The physical meaning of the elements in the equivalent circuits is discussed in the following section.

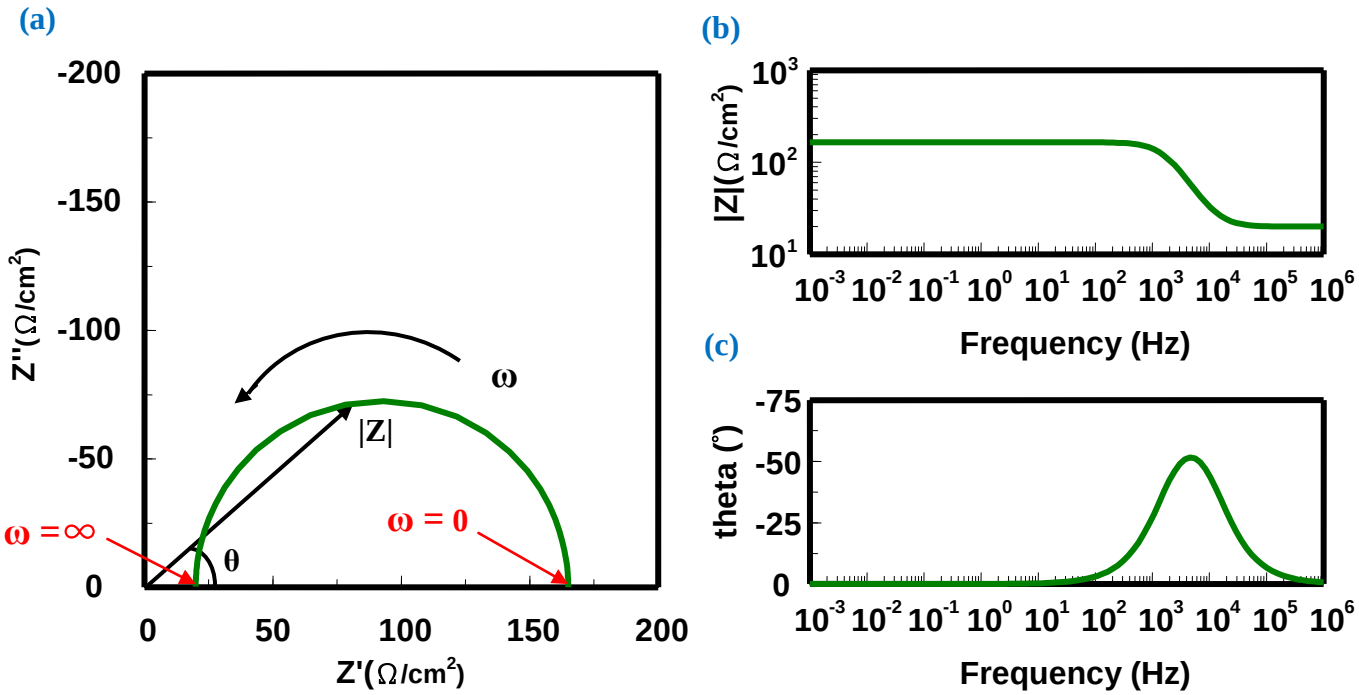

Fig. 3.1 Common presentation of EIS data as (a) Complex plot, (b) Bode plot (impedance versus frequency) and (c) Bode plot (phase angle versus frequency)

3.1.3 Physical meaning of equivalent circuit elements

Equivalent circuit analysis is a useful method that helps in understanding the electrochemical system. In the equivalent circuit, each element presents an impedance behaviour. In this section, the common elements and their impedance behaviour is introduced.

Resistance R is an element that only presents the real part of the impedance. From the definition, resistance is frequency independent (R = E/I = Z (Impedance). In the electrochemical system, R is used to describe several phenomena: (1) electrolyte resistance, (2) polarisation resistance, (3) charge transfer resistance [114,115,117]. The electrolyte resistance is dependent on the current terminal area and the characteristics of the solution, such as the type of ions, ionic concentration and temperature. It can be presented as the equation:

$$R = \frac{l}{K \cdot A} \tag{3.5}$$

where K is the conductivity of solution, A and l are the bounded area and length of the uniform distribution path of carried current. Normally, the current distribution in the electrolytic cell is not uniform, therefore it is difficult to calculate the resistance of the electrolyte using just the above equation. Fortunately, in the impedance spectra, the resistance of the electrolyte can be observed at the highest frequency data point ($\omega \rightarrow \infty$) in the complex plot. The polarisation resistance R_p is used to present the resistance to the current flow when the electrode is polarized. In this case, the current value can be related by the reaction kinetics and diffusion behaviour both toward and away from the electrode [116]. The charge transfer resistance R_{ct} can be observed for a simple electrochemical reaction running with kinetic control. When R_{ct} is known, the exchange current density of reactions can be calculated under certain conditions [115].

Capacitance is an element that provides the imaginary part of the impedance and is a function of frequency as presented in equation 3.6. From the equation, impedance of capacitance is inversely proportional to the frequency.

$$Z = \frac{1}{j\omega C} \tag{3.6}$$

In electrochemical systems, there are two situations where the impedance can show capacitive behaviour. Firstly, at the electrode-electrolyte interface the charge redistribution takes place forming a double layer. The positive ions in the electrolyte are absorbed onto the electrode, with an excessive concentration of electrons formed in the electrode surface. Therefore, a so-called diffuse mobile layer is formed with negative ions are attracted towards the electrode (figure 3.2) [114,118]. The 'Double layer' is composed of inner absorbed fixed layer and outer diffuse mobile layer. Therefore, under AC conditions, the double layer in the rising and falling polatisation half-cycle charges and discharges, respectively. The magnitude of the double layer capacitance C_{dl} is affected by the type of ions, ion concentration, roughness of the electrode surface and the temperature of electrolyte.

The second situation is associated with the coating capacitance C_c, in which the coating layer behaves as a capacitor. The value of C_c can be calculated using the following equation:

$$C_c = \frac{\varepsilon\varepsilon_0 A}{d} \tag{3.7}$$

where ε is the permittivity of the coating material, ε_0 is the permittivity of vacuum, A and d are the coating area and thickness, respectively.

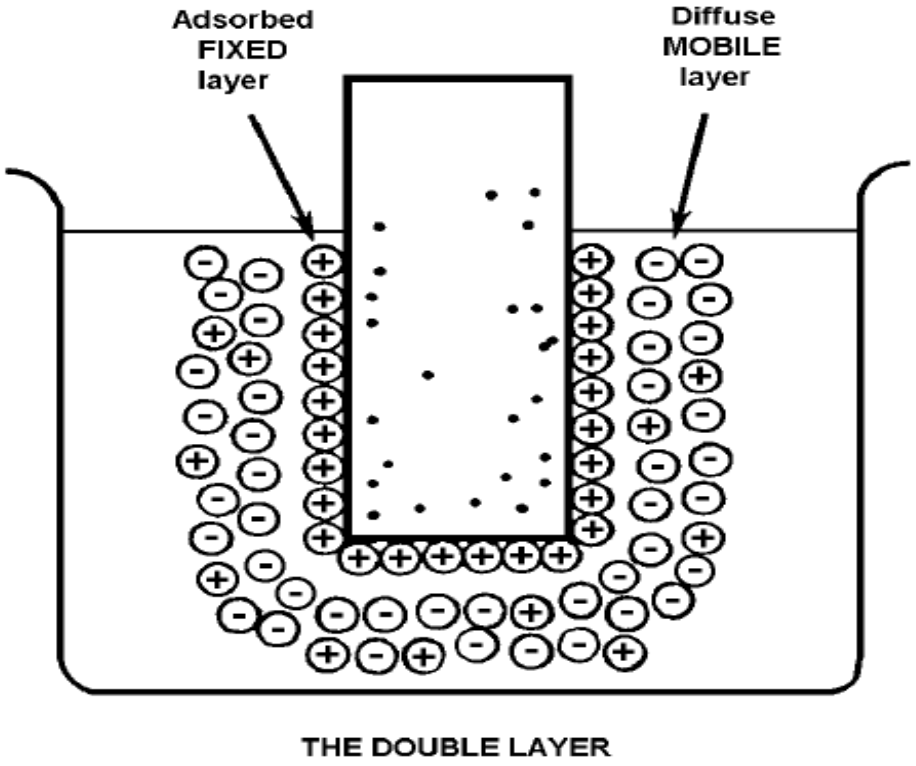

Fig. 3.2. Schematic diagram of the double layer [118]

Additional elements were developed and applied to describe complex electrochemical phenomena, such as constant-phase element (CPE) and Warburg diffusion element [114]. CPE is an element used to represent a frequency independent distribution. The definition of CPE is shown as follows:

$$Z(\omega) = \frac{1}{\mathrm{Q}(\mathrm{j}\omega)^{\alpha}} \tag{3.8}$$

where Q is a numerical value, which depends on the empirical constant α. When α = 1, Z(ω) describes the impedance of capacitance, and Q is an ideal capacitance (C); when α = 0, Z(ω) describes a resistor; and when α = -1, Z(ω) describes the impedance of inductance, and Q presents an inductance (L). In the common corrosion study, CPE is used in the equivalent circuit analysis in several situations, to describe (1) using a rough, fractal electrode [119], (2) a non-uniform double layer region [118], (3) inhomogeneous reaction rates on the surface [120], (4) a varying thickness or composition of a coating [121] and (5) non-uniform current distribution [122].

The Warburg element is used to model diffusion. Two different Warburg elements W_O and W_S were developed to describe unlimited (infinite) and constrained (finite) conditions of diffusion, respectively. Under the infinite diffusion layer, the definition of Warburg impedance is:

$$Z = \frac{\mathrm{R_d}}{\sqrt{(\mathrm{j}\omega)}} \tag{3.9}$$

where R_d is the diffusion resistance. Under the assumption of a finite diffusion, the impedance produced by the diffusion of species in the electrolyte follows the equation below:

$$Z = \mathrm{R_d}\frac{\tanh\sqrt{(\mathrm{j}\omega)\tau}}{\sqrt{\tau}} \tag{3.10}$$

where $\tau = \delta^2/D$ is the diffusion time constant. δ is diffusion layer thickness and D is the diffusion coefficient.

Inductance (L) is an element which is attributed to the relaxation reactions or adsorption processes to produce intermediate reaction products [69,116]. The impedance of inductance

is

$$Z = \mathrm{j}\omega L \tag{3.11}$$

From the above equation, inductance is dependent upon frequency. Similar to capacitance, inductance provides only imaginary impedance. Inductance is usually used to describe adsorption processes [114]. A metal (M) dissolves through an adsorbed intermediate (I_{ads}) following the equation 3.12, which reacts in a second electrochemical step (equation 3.13) to form the final product P [114]:

$$M \rightarrow I_{ads} + e^- \tag{3.12}$$

$$I_{ads} \rightarrow P + e^- \tag{3.13}$$

The above section described the elements commonly used to design an equivalent circuit and simulate an electrochemical system. Unobserved electrochemical mechanisms occurring during the process can be easily revealed and studied by the EIS method. Based on the powerful and versatile EIS technique, Parfenov and Yerokhin have developed an in-situ impedance spectroscopy (ISIS) technique which can be used to investigate the mechanisms of the phenomena occurring during the PEO process. This can facilitate process control in PEO treatment.

3.2 In-situ impedance spectroscopy technique

Parfenov et al. [123] developed and applied the frequency response method to study the PEO process. It can be used for both process control and diagnostics. Two signal modes were employed, such as the small and the large signal mode. The small signal mode is a common linearization of the system under a DC polarisation system which is analogous to the EIS method; the large signal mode is used for the system identification under AC and pulse current regime. In their next paper [112], a new method of in-situ impedance spectroscopy (ISIS) is developed and proven to be useful to investigate the micro-discharge mechanism during the PEO process. By using the ISIS method, specific phenomena and mechanisms of PEO can be investigated in more detail.

3.2.1 PEO processing setup for ISIS studies

The fundamental theory underpinning the ISIS method is basically the same as for the traditional EIS technique but the method is applied in-situ during the PEO process, using a

frequency sweep of bipolar voltage pulses from 20 Hz to 20 kHz. The PEO equipment setup for application of the ISIS method is shown in figure 3.3 [125].

The power supply is important because the characteristics of the PEO process are dependent upon the characteristics of the power supply [123]. The following three types of power supplies can be used [125]: (1) A linear power supply circuit, which requires having an output power transistor operating in a linear mode and controlled from a sine wave generator; (2) an electric machine converter, for which the power supply should have a motor and an AC generator on one shaft rotating at a controlled frequency; (3) a switching power supply, which can provide a high efficiency of power conversion with pulsed output voltages smoothed by a low pass filter.

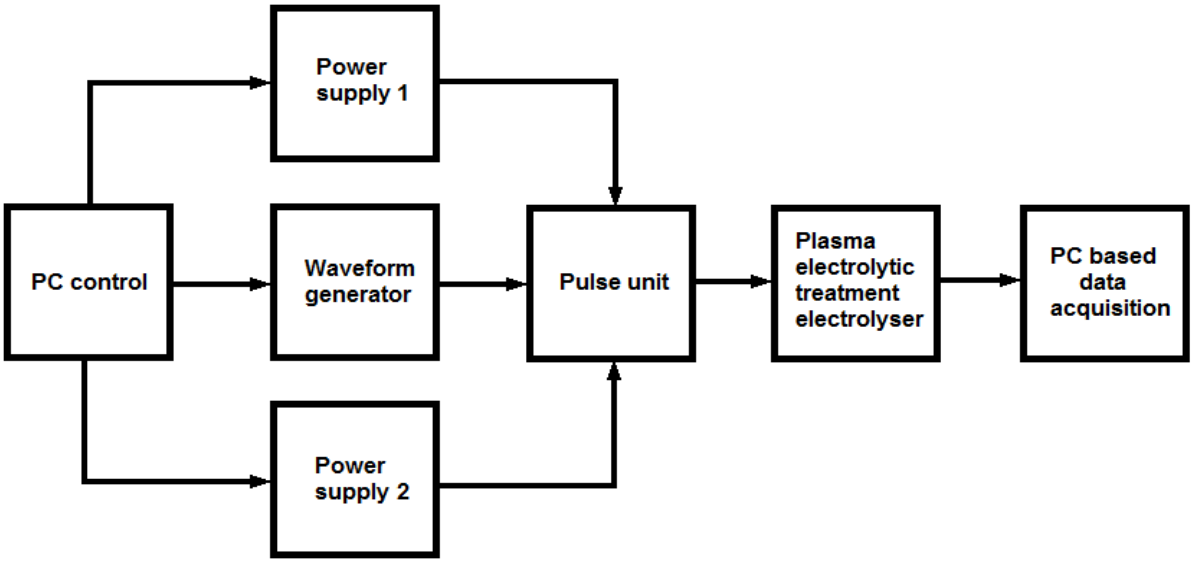

Fig. 3.3 Configuration of power supply, PEO treatment equipment electrolyser and data acquisition system

The modern switching power supply equipment was suggested for the PEO treatment, because the treatment could be more effective in pulsed modes and would provide better surface properties than the linear one [53]. In this work, the power supply consists of two DC units with 10 and 20kW spectrum which are controlled via a pulsing unit with specially developed software. The switching features of the power supply are used to produce a bipolar pulse squared waveform which is similar to that of a sine wave. Another advantage is that the auxiliary port is included to introduce control pulses from an external pulse generator, which means the frequency swept signal can be produced from the external source [125]. The development of appropriate waveforms for the frequency response studies is addressed in the next section of this chapter.

The signal with the appropriate waveform is chosen as the input source; in turn, the response output signal is then received by a PC based data acquisition system. The collected data then undergoes a post-treatment and is transformed to a required form for presentation.

3.2.2 Frequency response method

In the frequency response (FR) technique, two modes are used for direct identification, i.e. the small and the large signal mode, as shown in figure 3.4 [123]. The large mode provides AC magnitude which is comparable with the DC one. This current mode enables identification of PEO systems that work in AC, pulse or pulse reversed regimes, providing conditions of dynamic breakdown. The small signal mode employs AC perturbation for which the magnitude is significantly less than the DC one. This approach is similar to the conventional EIS technique employed to a biased system in a linear region of the current voltage diagram.

Ideally in the ISIS method, a sine wave of AC current mode should be chosen. However this is technically difficult to achieve using the equipment suitable for PEO processing. With the pulsed power supply; the voltage waveform can be setup to provide a close approximation of the implied sine wave, by adjusting the durations and magnitudes of the voltage pulses and durations of the pauses between them. The complex function to investigate the impedance of the PEO process can be expressed as follows [123]:

$$\dot{Z}(\mathrm{j}\omega) = \mathrm{Z}(\omega)e^{j\varphi(\omega)} \tag{3.14}$$

where ω is the radian frequency, Z(ω) and φ(ω) are the impedance magnitude and the phase angle as functions of frequency; $\mathrm{j} = \sqrt{-1}$. The value of Z is defined as the absolute value of the frequency-dependent impedance (at the frequency of interest ω) and can be calculated by the value of voltage U(ω) divided by current I(ω):

$$\mathrm{Z}(\omega) = \frac{U(\omega)}{I(\omega)} \tag{3.15}$$

The definition of phase angle φ is the frequency-dependent phase shift (at the frequency of interest ω) between the voltage u(ωt) and current i(ωt) sine waves, which can be expressed as follows [123]:

$$u(\omega t) = \mathrm{U_A}\sin(\omega t + \psi_U) \tag{3.16a}$$

$$i(\omega t) = \mathrm{I_A}\sin(\omega t + \psi_I) \tag{3.16b}$$

$$\varphi = \psi_U - \psi_I \tag{3.16c}$$

The ISIS method can be applied to investigate the PEO process using this frequency response approach. Early application of the ISIS method and the comparison with the low voltage EIS technique have been presented by Parfenov and Yerokhin [112]. In their conclusions: (1) the results from ISIS are similar to those obtained by EIS for both thin and thick coatings; (2) a similarity between ISIS and EIS is found at the high frequency range (5 kHz~20 kHz); (3) the main difference is in the lower frequency region (1 Hz ~5 kHz), which is believed to be associated with the influence from PEO process itself. Therefore, the feasibility of ISIS method has been proven. Further accuracy verification of the developed method along with linearity evaluation of the processes studied will be discussed in the following sections.

In this work, PEO treatments were carried out in a bipolar pulse current mode with frequency logarithmically swept from 20 Hz to 20 kHz every 0.48 s. The selected frequency range is due to the limitation of the data acquisition card and the minimum duration (5μs) of the step of the plus waveform. As shown in figure 3.5, a DC superimposed AC waveform was chosen, with square pulses controlled by an external waveform generator to investigate the effects of electric field, electrolyte characteristics and coating morphologies during the PEO process. At the initial stage, under all conditions, the voltage increased to reach the pre-set value (547 V) in the ramp time of 15sec.

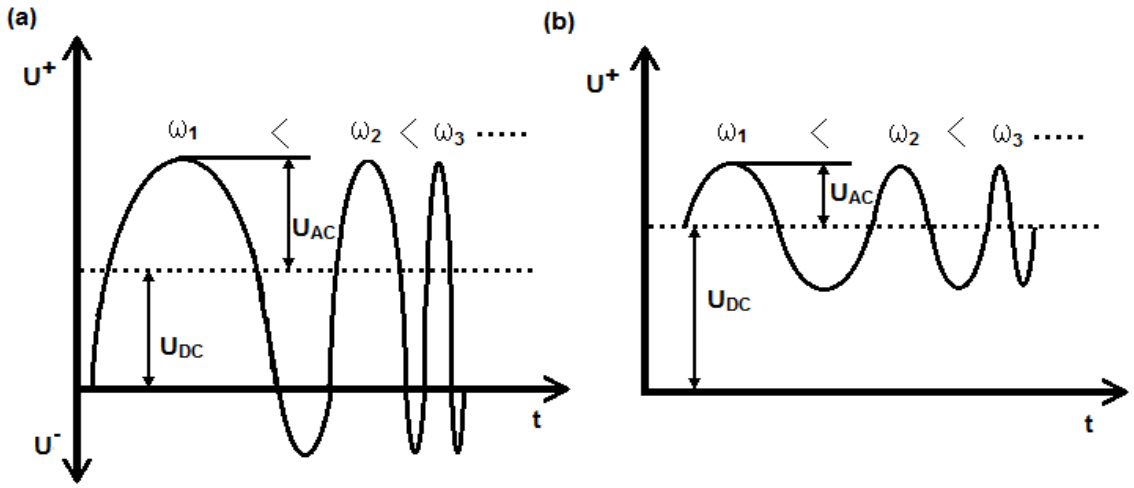

Fig. 3.4 Two modes of frequency swept voltage waveform for frequency response studies of the PEO process (a) large signal and (b) small signal.

(a)

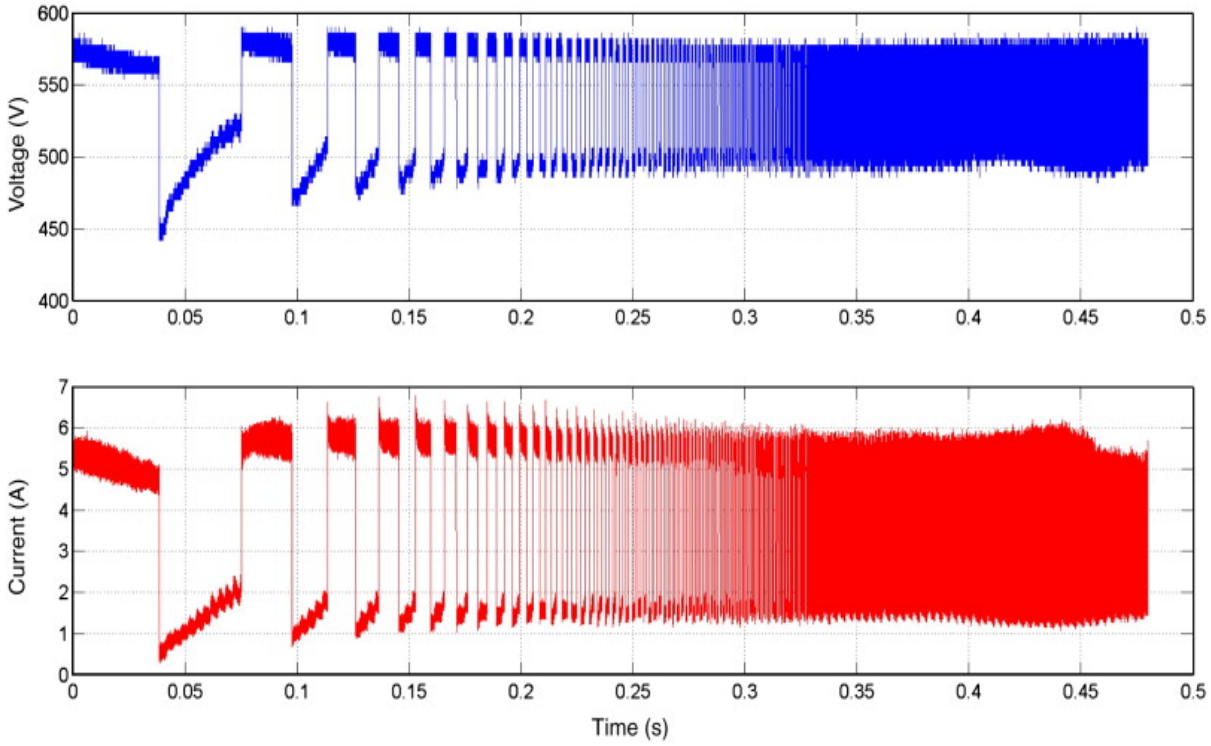

(b)

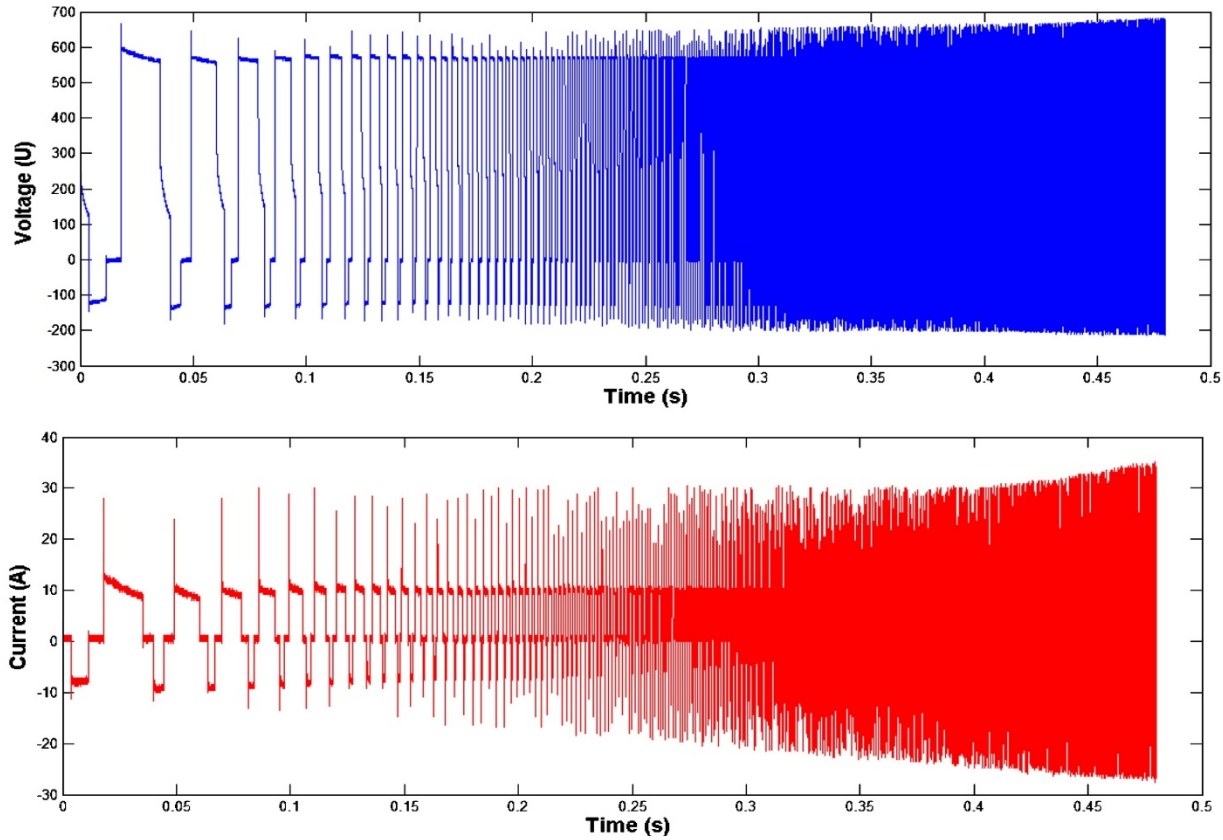

Fig. 3.5 Characteristic voltage and current waveforms during the PEO treatment of Al (a) small signal (V_{dc} = 316.5 V and V_{ac} = 230.5 V) [124], (b) large signal (U_{av} = 265 V and U_m = 385 V) [112].

3.2.3 Evaluation of PEO system linearity and noise

Similar to the EIS technique, the system studied by the ISIS method should satisfy the requirement of linearity. ISIS is based on the frequency response method in which the studied object is treated as a linear time-variant system with slowly evolving parameters, which can be considered time invariant within a very short period of time (typically several seconds). Yerokhin and Parfenov tested and verified the linearity of the PEO system to justify the application of ISIS method for modelling of the PEO process [125]. From their research, it follows that the system non-linearity may affect the impedance spectra especially in the lower frequency region. This can also be contributed to by the noise in the system, which would further affect whole the impedance spectra.

In the linear systems theory, if the internal structure of the system which is treated as a black box are linear and stable, then the output is a linear function of the input perturbation signal. Therefore, the output must contain the same harmonic content as the input. From the previous sections, the voltage waveform provides a close approximation of the implied sine wave. The harmonic parameters such as magnitudes of AC and DC input signal components were used instead of explicit pulse parameters as frequency, positive and negative voltage pulse magnitudes and duty cycles [123]. The appropriate pulse waveform can be developed, with given parameters of AC and DC components. The implied sine wave is described as:

$$\mathrm{U(t)} = \mathrm{U_0} + \mathrm{U_1}\sin(\omega t) \tag{3.17}$$

where U_0 and U_1 are the components of DC and AC, respectively. The phase angle of the AC components is zero. The pulse approximation can be described by Fourier series as [123]:

$$\widehat{\mathrm{U}}(\mathrm{t}) = \mathrm{U_0} + \sum_{\mathrm{n}=1}^{\mathrm{n}} \mathrm{U_n} \sin(n\omega t + \psi_n) \tag{3.18}$$

where U_n and ψ_n are the magnitude and the phase angle of the nth harmonic. The phase angle of the first harmonic is zero [123]. If the system under the impedance test is linear, then the output I(t) of the system operator $G\{\cdot\}$ must process the same harmonic. which is:

$$\begin{aligned}\mathrm{I(t)} = \mathrm{G\{U_0\}} + \mathrm{G\{U_1\}}\sin(\omega t + \psi_1) + \mathrm{G\{U_2\}}\sin(2\omega t + \psi_2) + \\ \cdots \mathrm{G\{U_n\}}\sin(n\omega t + \psi_n)\end{aligned} \tag{3.19}$$

From the definition of the linear system, the harmonic sine functions are the

eigenfunctions of the Fourier transform, and they appear outside of the system operator in (3.19). Therefore, the system linearity can be estimated in the frequency domain following the linearity property of the Fourier transform.

This linearity check was applied in the ISIS method when investigating the PEO process. More details of the experimental procedure and the results of linearity testing for the studied PEO process are discussed in section 3.2.5.

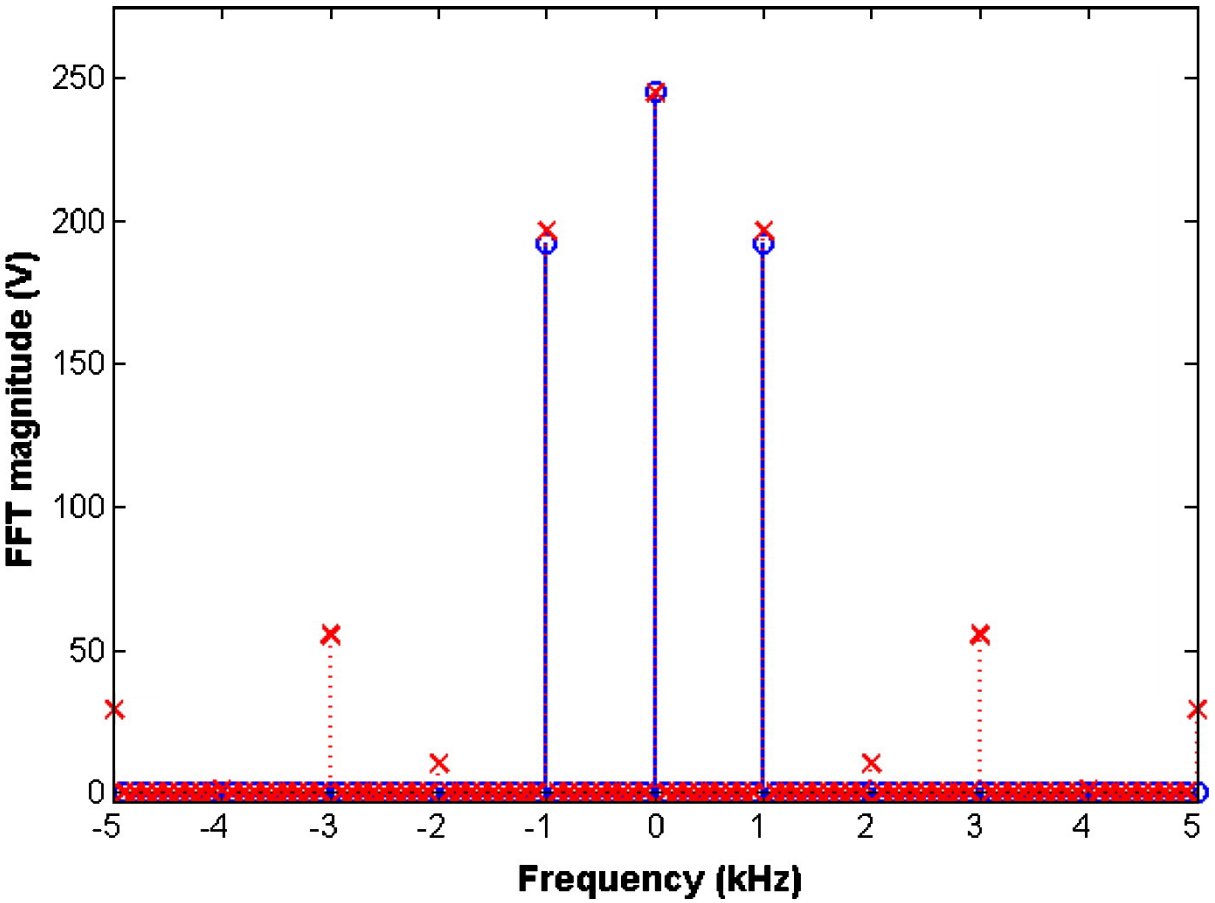

Fig. 3.6 An example of a Fast Fourier Transform spectrum for implied sine wave (circles) and its pulse approximation (crosses) [123].

3.2.4 Accuracy verification of the ISIS method

In the previous section, the linearity verification of the ISIS data has been discussed. For the accuracy verification, simple experiments were carried out using linear circuits composed of resistors and capacitors as shown in figure 3.7(a). These tests were designed with a simple circuit (figure 3.7(b)), for which several resistors were connected in series to achieve the net resistance at R1= 22Ω and R2= 143Ω, and several capacitors were connected in parallel to achieve an RC loop with total capacitance of 0.67, 1 and 2μF. The characteristics of the power supply and the current mode in these experiment were exactly the same as the PEO treatment, except for the test duration which was 5 minutes, to ensure statistical significance of the data recorded.

(a)

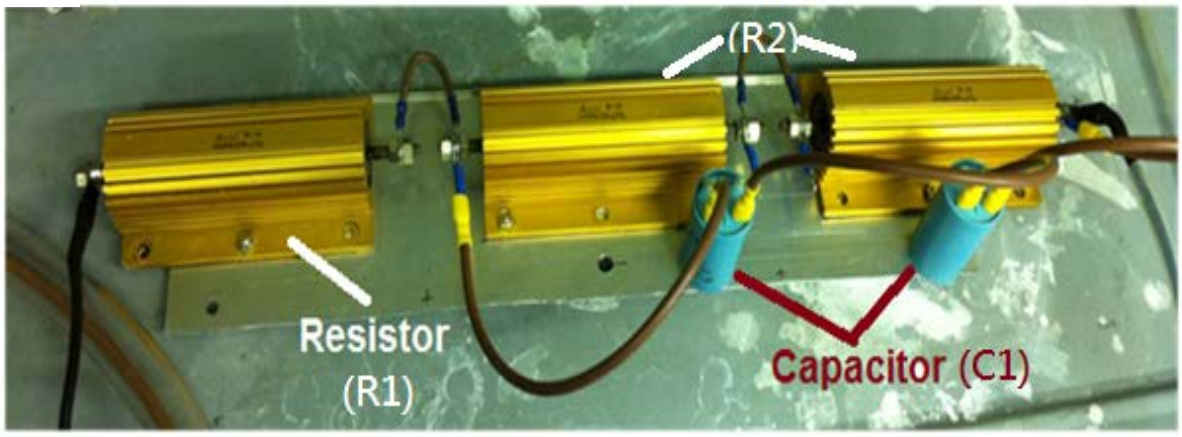

(b)

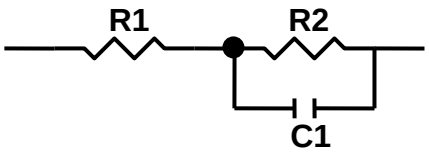

Fig 3.7. The experimental device with resistors and capacitors for in-situ IS program testing.

To confirm that the test results are accurate, the fitting results in both the complex and Bode plots and the error analysis were performed using Zview software. Figure 3.8(a) represents the results of ISIS tests of the linear circuit with R1 = 22Ω, R2 =143Ω and C1=

0.67μF. The five curves present the impedance data recorded every minute during the test. The three dimensional Bode plots on the left illustrate how the impedance spectrum changes with time, indicating a very stable behaviour of the linear system under the test. The fitting results and the errors are shown in figure 3.8 (b) and (d). Comparison of the impedance spectra obtained by the ISIS method with the fitting result, shows that the fitting spectra match well with the experimental data points, but slightly deviate from the splined data in both the complex and Bode plots. This deviation is however negligible, because of the fitting errors are all lower than 1% .

Figure 3.9 and 3.10 show the results of ISIS tests and the fitting using a Zview software of the linear circuits with two different net capacitances of 1 and 2μF, respectively. Comparing the data for all capacitances, the impedance spectra in the complex plot are similar. However in the Bode plots, the inflection points of impedance modulus and corresponding phase angle peaks are moved towards lower frequency region with the increase in capacitance. The comparison between the results of ISIS tests and the fitting results for the circuits with 1 and 2μF capacitance is similar to that with 0.67μF, yielding 0.5 ~ 1% error.

To discuss the discrepancy between the results from the ISIS method and the fitting result, the following points should be made. First of all, R1 from the fitting value ($R1_{fit}$) is slightly higher than the nominal value ($R1_n$) under all capacitance conditions. Secondly, the value of $R2_{fit}$ is around 3~4Ω lower than $R2_n$. Thirdly, $C1_{fit}$ is about 20% bigger than $C1_n$ under all capacitance conditions. However, the C_n has its own 10% standard deviation mentioned on the capacitors. A possible reason for the discrepancy is a gradual temperature increase due to the Ohmic heating during the testing. The initial temperature of the circuit is around 25℃, but it reached around 110℃ by the end. The values of resistances and capacitances changed with the temperature. Usually, the capacitances increase and resistances decrease with increasing temperature. During the PEO treatment, the temperature effects can be avoided by controlling the electrolyte temperature using a cooling system. The noise of the system can be the other cause of the discrepancy. The noise is an inevitable phenomenon in the method used and will be evaluated and discussed in the following section.

From the accuracy verification, the accuracy of the ISIS method has been evaluated to be 99%. The error can be reduced by controlling the electrolyte temperature during the PEO process.

(a)

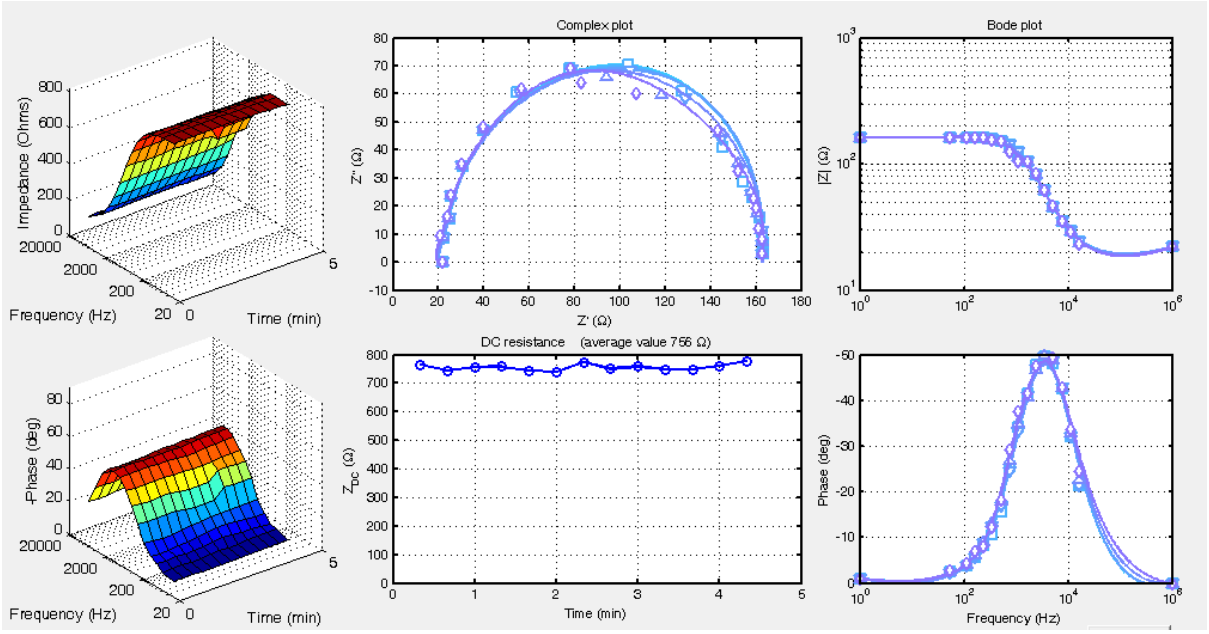

(b)

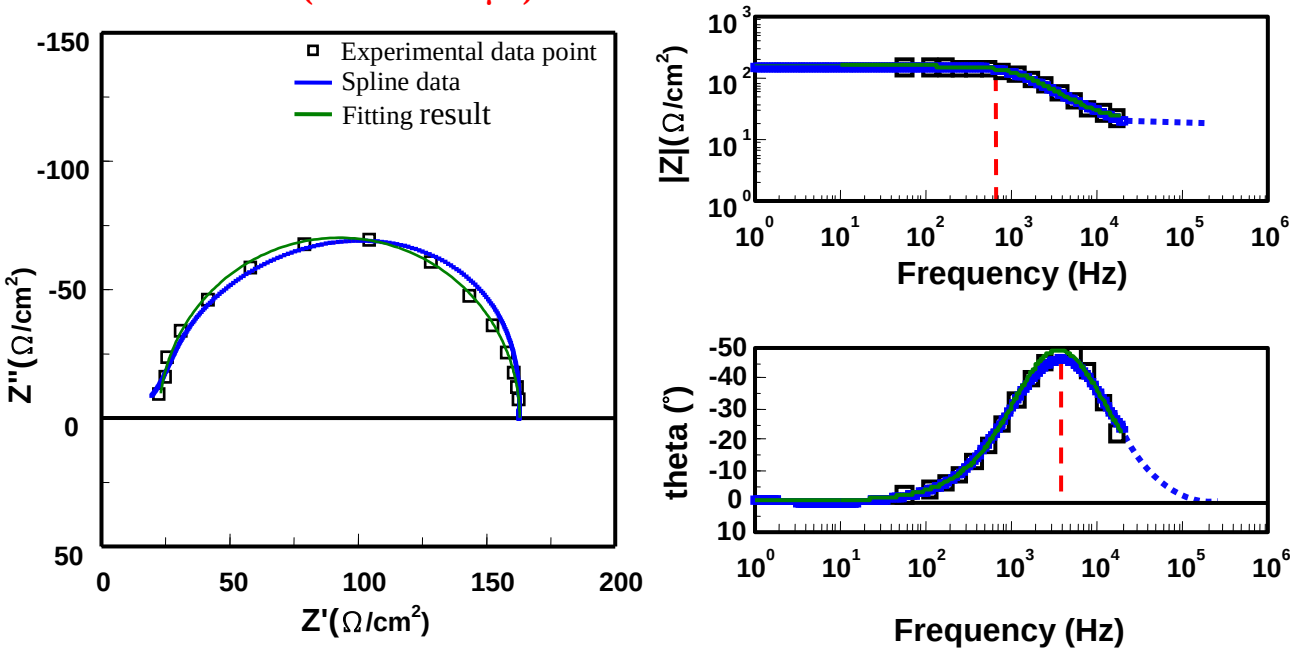

(c)

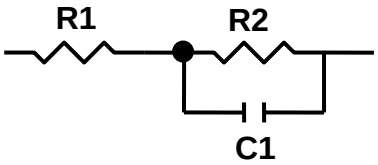

Element	Freedom	Value	Error	Error %
R1	Free(+)	22.5	0.079813	0.35472
R2	Free(+)	140.4	0.19428	0.13838
C1	Free(+)	8.4541E-7	2.369E-9	0.28022

Fig. 3.8. Accuracy verification of ISIS method using a linear circuit with the net resistance and capacitance of 165(Ω·cm^2) and 0.67(μF/cm^2), respectively: (a) results from ISIS method, (b) fitting by Zview software, and (c) fitting value and errors.

(a)

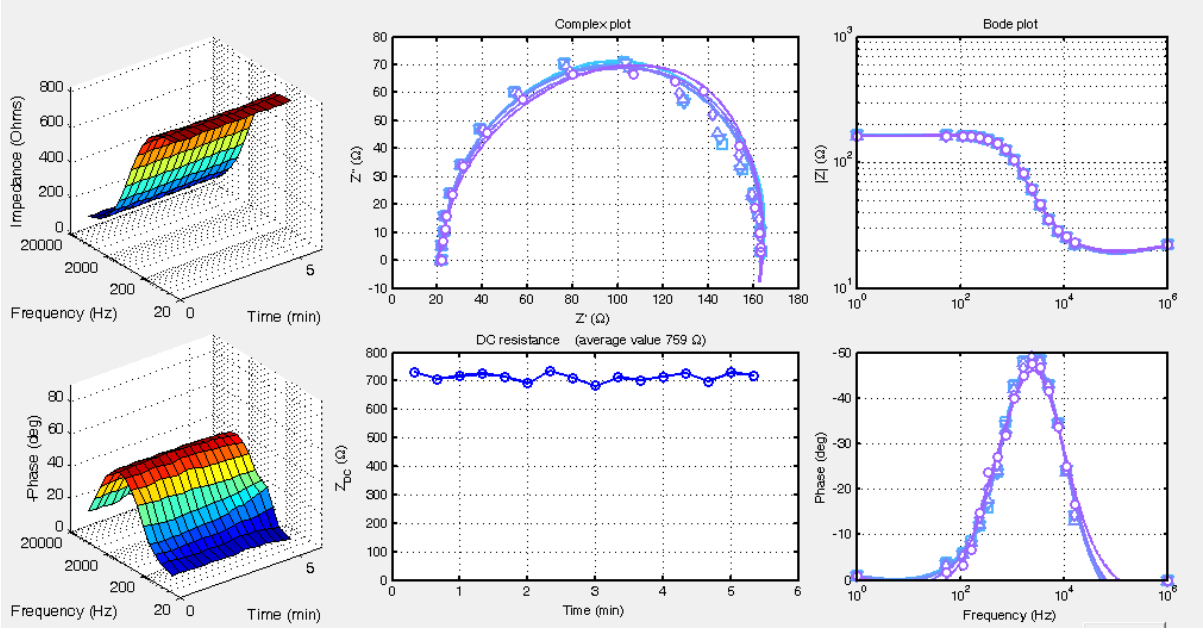

(b)

In-situ IS test (165Ω & 1μF)

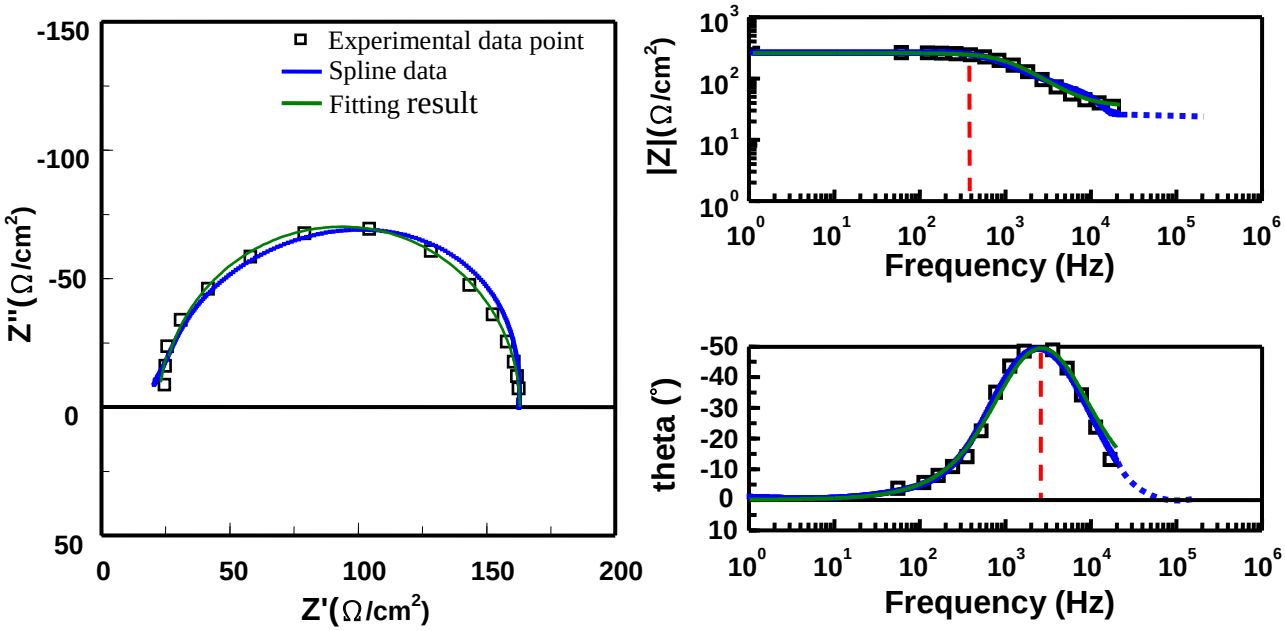

(c)

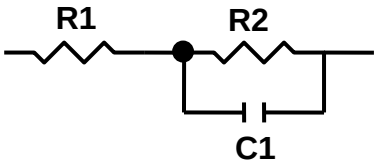

Element	Freedom	Value	Error	Error %
R1	Free(+)	22.22	0.23365	1.0515
R2	Free(+)	140.6	0.65373	0.46496
C1	Free(+)	1.1592E-6	1.0508E-8	0.90649

Fig. 3.9. Accuracy verification of ISIS method using a linear circuit with the net resistance and capacitance of 165(Ω·cm^2) and 1(μF/cm^2), respectively: (a) results from ISIS method, (b) fitting by Zview software, and (c) fitting value and errors.

(a)

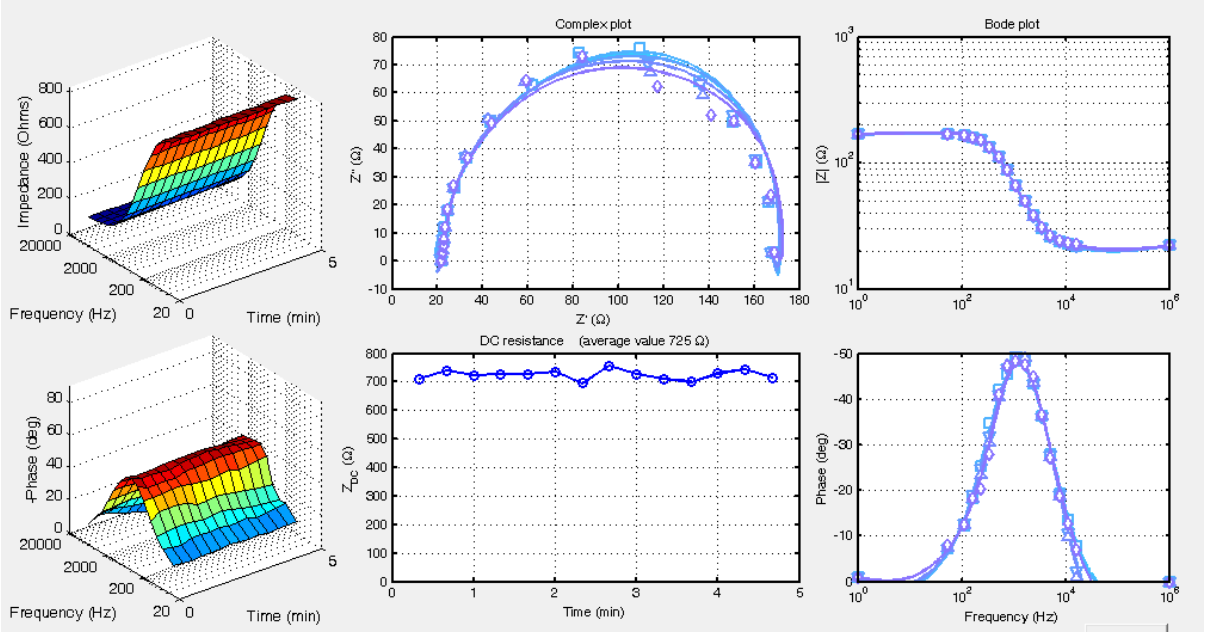

(b)

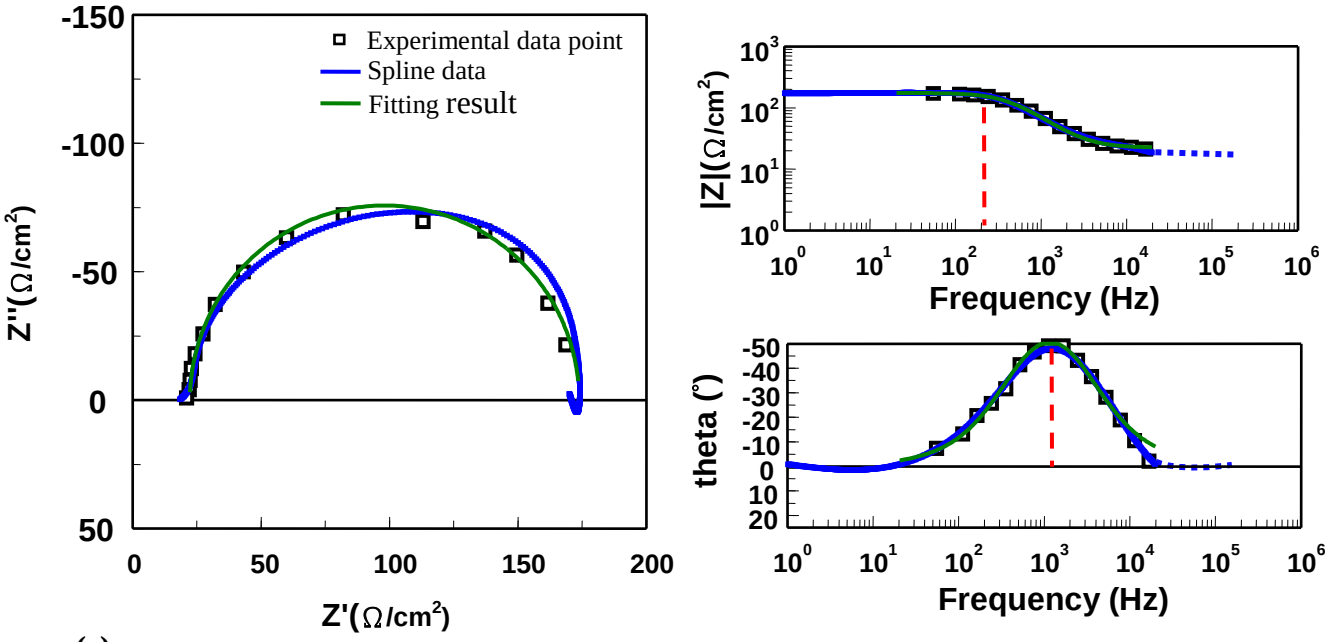

(c)

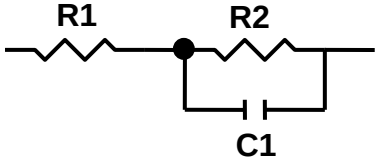

Element	Freedom	Value	Error	Error %
R1	Free(+)	22.34	0.097931	0.43837
R2	Free(+)	141.5	0.5739	0.37881
C1	Free(+)	2.5188E-6	1.202E-8	0.47709

Fig. 3.10 Accuracy verification of ISIS method using a linear circuit with the net resistance and capacitance of 165($\Omega \cdot cm^2$) and 2($\mu F/cm^2$), respectively: (a) results from ISIS method, (b) fitting by Zview software, and (c) fitting value and errors.

3.2.5 Data validation for impedance modelling of PEO process

In this section, evaluation of the system linearity and impedance estimation in the frequency domain are discussed. This justifies the application of the ISIS method to the PEO process as a properly linearized object. Two experiments were set up for testing the linearity of ISIS data, such as (1) the linear RC system discussed in the previous section, and (2) the PEO process of Al operated under intensive sparking mode at U_{DC} = 265 V and U_{AC} = 385 V.

Figure 3.11 represents the testing results. In the linear RC system, the average noise and nonlinearity are about 3 and 11%, respectively. The maximum of noise and nonlinearity are observed at the maximum value of phase angle and the highest slope of the impedance modulus curve as shown in figure 3.11(a) and (b). The noise is relatively higher in the PEO system (5.6%) but still under 10% for this complex environment. The maximum of noise and nonlinearity were varied between 5 and 15%, and also observed at the same location in the linear RC system as shown in figure 3.11(c) and (d).

The FR linearity program, the purpose of which is data validation for subsequent modelling, was developed and added in the package which enables implementation of the ISIS method, which the linearity property of the system. Figure 3.12 shows the results of the system linearity evaluation for the PEO process operated under a parallel-equidistant electric field. From the figure, it is clearly seen that the maximum error of impedance modulus at about 10% is observed below 200 Hz. The spectrum-average estimate of the system linearity is 95%, and relatively higher nonlinearities are observed at high and low frequency ends at the spectrum. This allows the PEO process to be treated as properly linearised object.

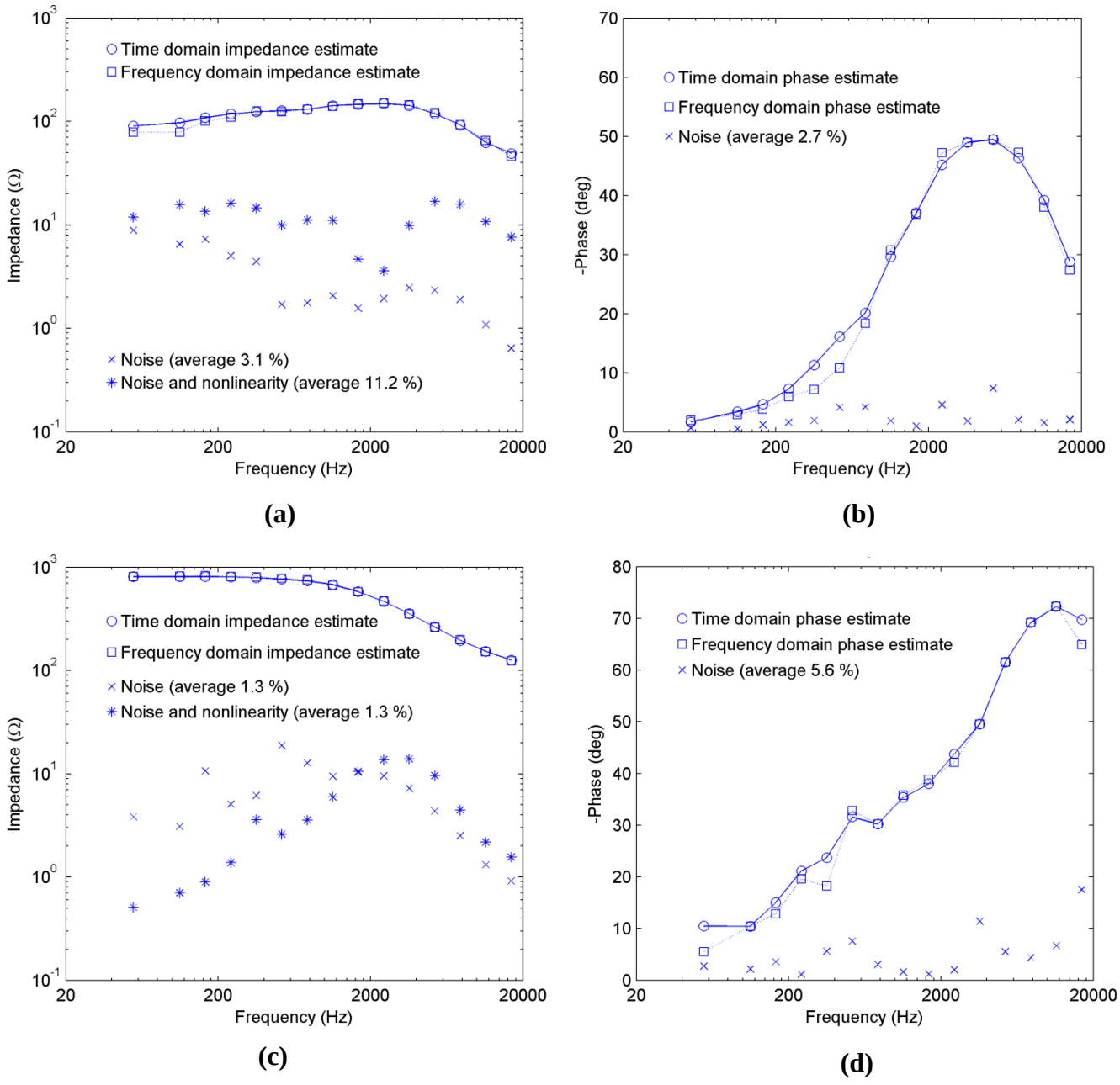

Fig. 3.11. Impedance modulus and phase angle spectrum estimates from time domain (○) an frequency domain (□) approaches applied to the frequency swept signals with U_{DC}=265 V and U_{AC}=385 V for parallel RC circuit (a), (b) and for PEO process (c), (d) at t=20 min. Noise (×), noise and nonlinearity (∗) estimates are also shown.

(a)

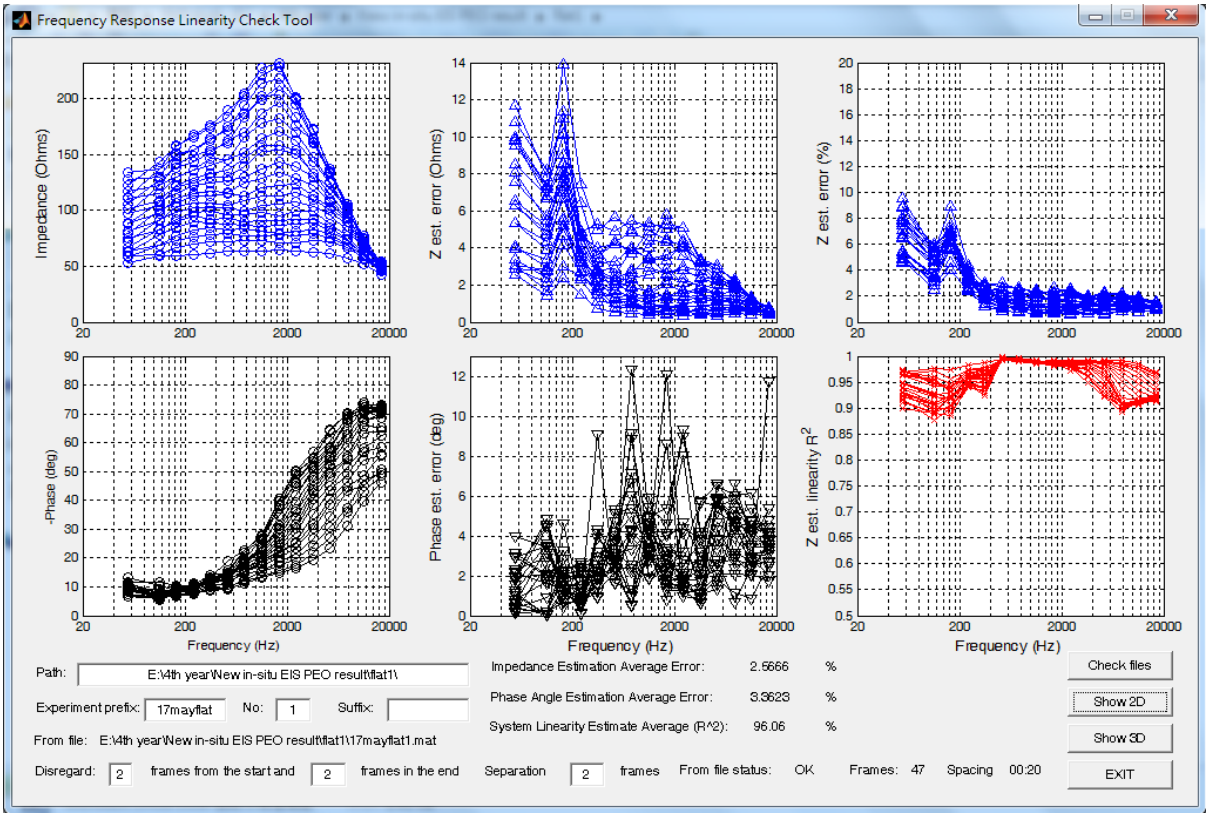

(b)

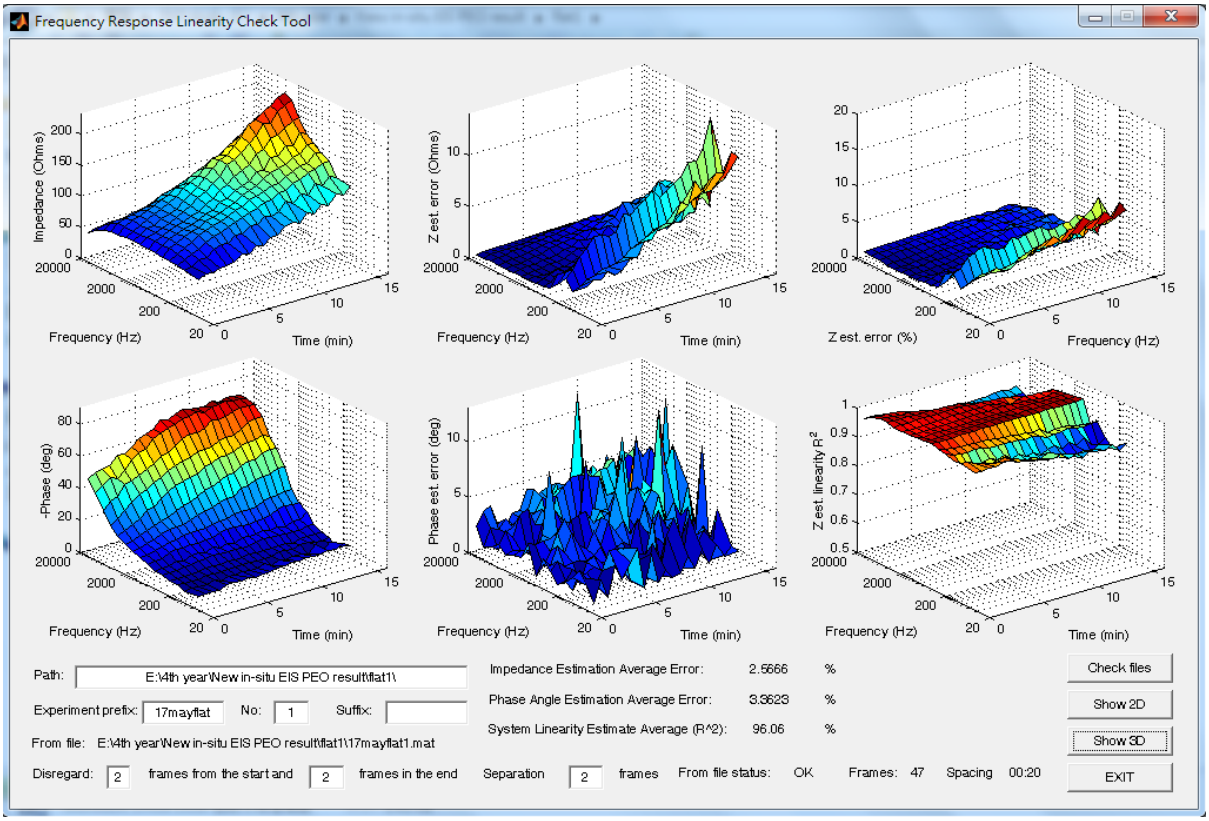

Fig. 3.12. The screenshot of 'Frequency Response Linearity Check Tool' interface, showing results of impedance data evaluation for the parallel-equidistant conditions of the PEO process, (a) 2D, and (b) 3D presentation.

3.2.6 Data processing with post-treatment

Initial analysis of the original files containing as recorded current and voltage signals is performed using a dedicated program (FR analysis) which operates in a Matlab environment. FR analysis also presents the received data in the form of Bode plots for quick viewing. Then the linearity check tool is used to validate the impedance data for subsequent modelling. The data are then processed by a "FR smooth program" to refine the phase, reduce noise and smooth data. In the last step, the FR spline program is used to transfer the data in the form suitable for modelling. In here, the first two steps belong to the data processing and the others relate to the post-treatment. As a result of the step by step processing, the data can be subjected to conventional EIS analysis.

3.3 COMSOL-Mutiphysics modelling

To understand the current distribution in the electrolyser during the PEO process, a COMSOL modelling software package was used. It also helps to understand the distributions of electric field and current density during the PEO process. COMSOL was also used to model the net resistance of the electrode for one of the boundary conditions of impedance spectra (R_∞) under different PEO treatment conditions such as different electric field distributions and the electrolyte characteristics in this work.

3.3.1 Introduction of COMSOL

COMSOL – Multiphysics Model package is a high performance finite element analysis software, which can be easily setup to solve several simple physical models both individual and jointly including chemical and plasma processes. COMSOL has now been widely applied in many fields of electrical and chemical engineering, heat transfer, earth science, MEMS, and a structural mechanics. It also provides a specific web-based database, containing examples, problem solutions, knowledgebases, technique support, and even publications search, which is beneficial for scholarly communication.

3.3.2 Finite element method

The finite element method (FEM) is a numerical solution method based on breaking down a complicated object (strong form) into smaller parts (weak form) which are easy to control, [126,127]. The complicated object can be divided into triangles, tetrahedrons, and hexahedra, that create a mesh. Therefore, the complicated object is now reformulated with meshes. In the new formation, the partial differential equation is called a finite element. The strong form has to be divided because the field variables are required to be continuous and have continuous partial derivates up through the order of the equation. The weak forms have the same but relatively weaker constraint conditions, which are discontinuities and integrable. This is also the requirement in mathematics [126]. Figure 3.13 shows an example of the finite element mesh for circle.

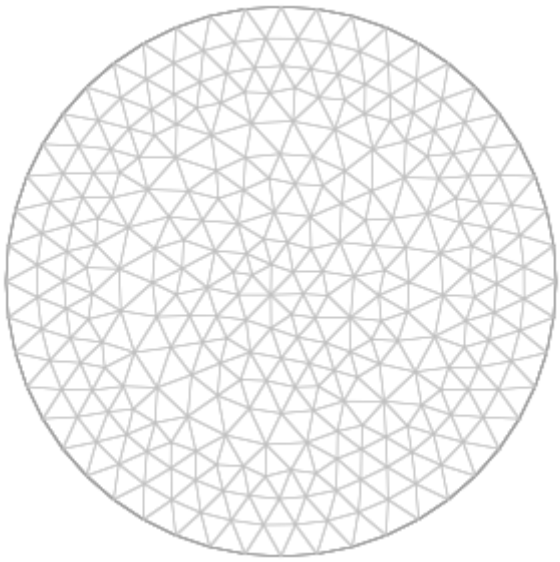

Fig. 3.13 Finite element mesh for circle object (subdivided into 548 triangles).

To compare the finite element method with the well-known finite difference method (FDM), the FEM discretises the solution by expanding the solution with a piecewise polynomial function, whereas the FDM discretises the equation by replacing the differential operators with finite difference. In object analysis, the FDM is much easier to apply and calculate, but it is relative complex and setup software/programs are required for the FDM

method. The major advantage of the FEM is that the finite element mesh can easily treat complex geometries, which may lead to problems in the case of FDM.

COMSOL is a modelling software that can solve multi-physics problems, which makes it an appropriate method to model complicated mechanisms underlying the PEO process. In this study, COMSOL was used to model the resistance of the electrolyte and the distribution of electric field and current density under different geometric conditions.

3.3.2 Model setup in COMSOL

In this study, a relatively simple COMSOL model was considered to assist observation of the electrolyte resistance, as well as distributions of electric field and current density under different types of electric field determined by different cell geometries.

Here, the parallel type of electric field condition with equidistant electrode layout was selected as the sample for presenting the model geometric setup (fig. 3.14). For modelling the electrolyte resistance and the distribution of electric field and current density, a real size model geometry was setup. The physical model was setup in *Conductive Media DC module* with built-in equation for the sub-domains:

$$-\nabla \cdot d(\sigma \nabla V - J^e) = d \cdot Q_j \tag{3.21}$$

where d is the thickness of electrolyte, σ is electric conductivity of electrolyte, V is voltage, J^e is external current density, and Q_j is current source. In this work, the value of σ was setup as 0.606 S/m; V was setup in boundary domain; J^e and Q_j were assumed 0 (no external current density and current source) and d was keep as 1. In the boundary domain, the electrolyser was setup as an electric insulator; counter electrodes were setup as V=0; and the working electrode was set as V=500V to simulate a 500V voltage drop between the electrodes. In the point domain, to avoid the point discharge phenomena, all the points were set as 0V. Finally, the overall electrode area was set as a constant $0.01327 m^2$. All parameters were setup with the same values in all conditions of electric field and cell geometrics besides the shape of the electrodes. The results of modelling and the discussion are presented in Chapter 4, which deals with the investigation of effects of electric field on impedance characteristics of the PEO process.

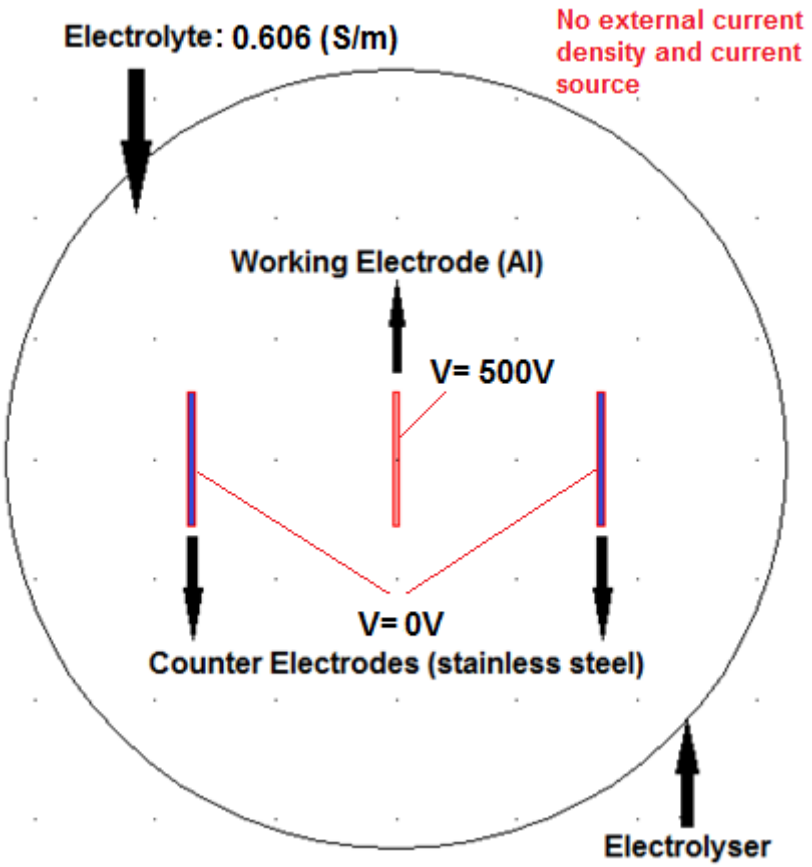

Fig. 3.14 The overhead view of the electrolyser in the model domain with boundaries corresponding to the working electrode, counter electrode, electrolyte, and electrolyser walls.

3.4 Coating characteristics and morphology study

Scanning Electron Microscopy (SEM) is an indispensable method for characterisation of produced coatings. A JEOL-6400 is used to observe the coating morphology after the PEO treatment. From SEM images, the structure of PEO coating is studied to understand the effects of different treatment parameters when investigating the PEO process with the ISIS technique, a cross-section image of the coating is required to assist development of the equivalent circuit, and justify the meaning of circuit elements. For the electric field distribution study, both surface and cross-section images are needed to provide statistical characteristics of the coating layers, such as thickness, roughness, porosity, etc.

EDS is used to analyse the coating composition and sometimes to identify the unknown particles. EDS mapping is employed to investigate the distribution of passivating agents across the coating thickness.

3.4.1 Thickness measurements

The Elcometer 355 modular thickness gauge system equipped with standard No. 4 Anodisers probe provide a non-destructive method for coating thickness measurement in this work. The accuracy of the measurement is about ±1 μm. The is based on generation of a small electromagnetic field in the probe. When the probe is pressed on a dielectric coating surface, it induces an eddy current in the conductive substrate, which results in a field that can be measured by the probe. Based on the intensity of the signal, the range of the measured thickness varies from 1 to 1000 μm. Before using this equipment, determination at the baseline (a zero point) of the instrument with a standard reference substrate and calibration with standard films of known thickness are necessary. Usually, ten to twenty measurement are taken in random location to evaluate the average coating thickness with a standard deviation (±0.1 μm). It should be noted that the porosity in the conductive substrate can cause a significant error, but it is not a common case. Some shapes of the sample are not suitable for this equipment because of insufficient surface area for the probe. To confirm that the thickness measurements are accurate, cross sectional SEM images of the coated samples are used.

3.4.2 Coating morphology study

SEM is of a specimen common method to observe the topography, chemical composition, and microstructure, which utilised a focused beam of high-energy electrons to generate a signal at the surface of a solid object [128,129]. Among the limitations of SEM, the magnification range is usually between 20X to 30000X, which means the size of sample is limited 10 to 5×10^{-6}mm [128,129]. Samples must be stable under the vacuum environment to about 10^{-5}~10^{-6}torr, which means that the types of sample are usually limited to a dry solid without gas evaporation. In the preparation, all samples were addressed with several steps, such as sectioning, cold mounting, and polishing. Samples were also sputter-coated with carbon to avoid surface charging, because of the low conductivity of the PEO coatings.

In this work, A JEOL JSM 6400 SEM was used for electron microscopy. This was operated at 15 to 20 kV and with the samples positioned at a working distance of 15 mm. Secondary electrons and backscattered electrons are used to study the sample morphology and topography in both surface plane and cross-section, and for illustrating contrasts in

composition in multiphase samples [129]. An energy dispersive X-ray spectroscopy (EDS) detector attached to the SEM instrument is used to determine and quantify the coating composition. The function of EDS mapping is used to study the distribution of elements on both surface and cross-sectional images.

3.4.3 Investigation of coating characteristics

Both surface and cross-section SEM images are analysed using ImageJ and ZEISS-KsRun software to determine the coating characteristics. ImageJ is a Java-based image processing program which is in the public domain from National Institute of Health and was created by Rasband [130]. By using these softwares, the coating characteristics, such as coating thickness, pore size, porosity, surface roughness, interface roughness and true area of the coating surface can be measured. These characteristics are used in the study to provide a better understanding of impedance behaviour in ISIS experiments and compare results obtained under various experimental conditions.

3.5 Fractal analysis method

While SEM and morphology processing programs are used to analyse the characteristics of coating morphology, fractal analysis is another method employed to evaluate the fractal dimensions of the coating morphology.

Fractals are defined as rough or fragmented shapes of geometric parts, which can be subdivided as several pieces and each of them is a reduced copy of the original one [131]. Fractals are usually used in the investigation of natural landscapes in geology and complex geometries in mathematic. Due to the crinkly and uncommon shape of the fractals, it is difficult to make measurement by conventional methods. Therefore, fractals are often characterised by their fractal dimension. Fractal dimension is very often a non-integer number with the range of 1~3 to describe the fractals, which measures and determines the (1) irregularity, (2) boundary fragmentation degree and (3) differs from Euclidean objects (point, line, plane, etc.) of each fractal [131].

Fractal analysis is a method to evaluate fractal behaviour and fractal dimension from images, that is, complex graphics or multi phase images can be transformed to a simple value (fractal dimension) for investigation and comparison. In 1984, Mandelbrot et al. [132] showed that the fractal study is applicable to studies of materials surfaces in scale of

micrometer, and the method called "Slit island analysis" has been developed. After that, fractal dimensions of surfaces have been widely studied in fractography [132-133]. A box method is another technique to establish the fractal dimension, from black and white images [131,134,135]. This method uses squares (boxes) to cover all fractals in the images, then the box size distribution is divided. Therefore, the slope of the distribution line is referred to as the box dimension [131], which is used as an appropriate of fractal dimension. Currently, the box method of determining the fractal dimension is very common in several fractal analysis software. Here, Fractal3e analysis software [136] is the fractal analysis program chosen in this work.

When applying the EIS method to the investigation of coatings, in most cases, the distributed properties are modeled by constant phase elements (CPE) that can be associated with different factors, including variable coating thickness, morphology and composition. The method of fractal analysis can also be used to investigate the coating properties, such as porosity, pore size and even roughness [138,139]. In 1985, Nyikos and Pajkossy published a paper [137] about relation of the fractal dimension to the CPE-P value in equivalent circuits used to simulate EIS data. Risovic et al. [134, 140, 141] compared fractal dimensions of microstructure from SEM images with the study of roughness and porous surface by using electrochemical impedance spectroscopy. It was found that the fractional dimensions derived from gray-scale image analysis are only slightly higher than the CPE-P values obtained by equivalent circuit fitting of the EIS data. This study demonstrated that the correlation between the CPE-P value and fractal dimension of the object is possible to trace, although with a limited degree of accuracy. In principle, this approach can also be applied to the ISIS experiments to separate the effects of coating morphology and electric field distribution in the impedance spectra.

3.6 Ultra High-Speed Imaging (UHSI)

During the PEO process, individual discharge events evolve in a very short time frame (around 10^{-4}~10^{-5} s). Therefore, a specialised ultra-high speed imaging multi-channel (SIM) framing camera (fig. 3.15) is used to take images of discharge events at a rate of up to 10^{-9}s (fig. 3.16). Up to 16 separate channels were used to take the images at once, with delay time between the channels and exposure time for each channel. The images from SIM already include the information of coordinates and an arbitrary value of relative intensity in a *.TIF file. By using this instrument, the behaviour of discharge events can be investigated in detail for different time scales.

A special image analysis program was developed to investigate characteristics and behaviour of individual discharge events. Several functions are incorporated in the program analyse the image downloaded in the *.TIF file, including zoom in/out, Gauss fitting with R^2 and transfer from pixel to μm. Discharge characteristics included intensity, peak shape determined by Gauss fitting, discharge location, location of maximum intensity, and full width at half maximum (FWHM). The program interface is shown in figure 3.17. This program facilitates investigation of the behaviour of the discharge.

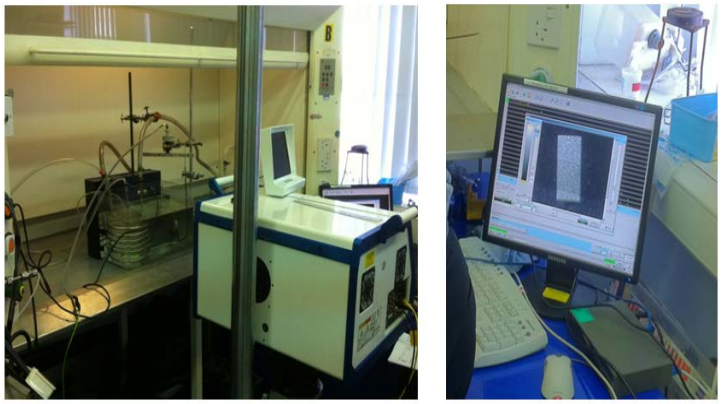

Fig. 3.15 A Specialised Ultra-High Speed Imaging Multi-Channel SIM-16 Camera.

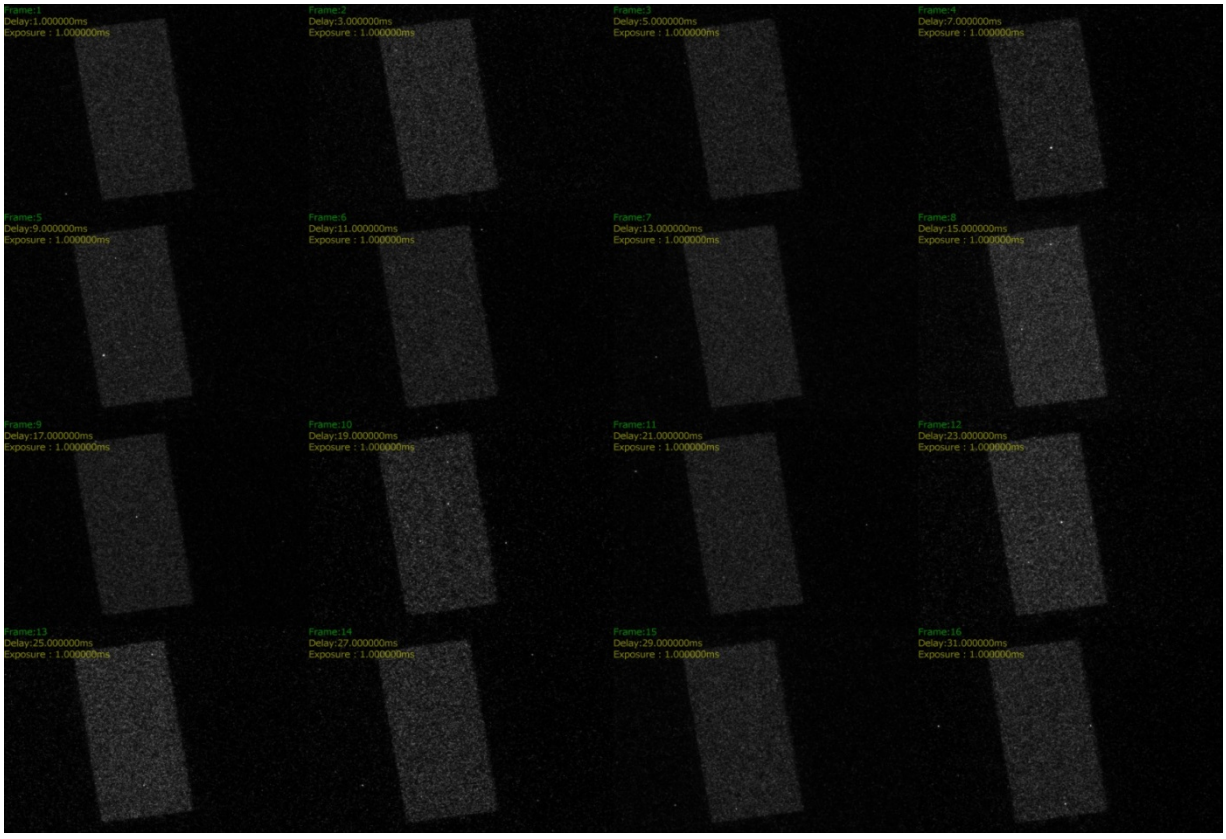

Fig. 3.16 An example of images of discharge events occurred on Al from muiti-channel framing camera.

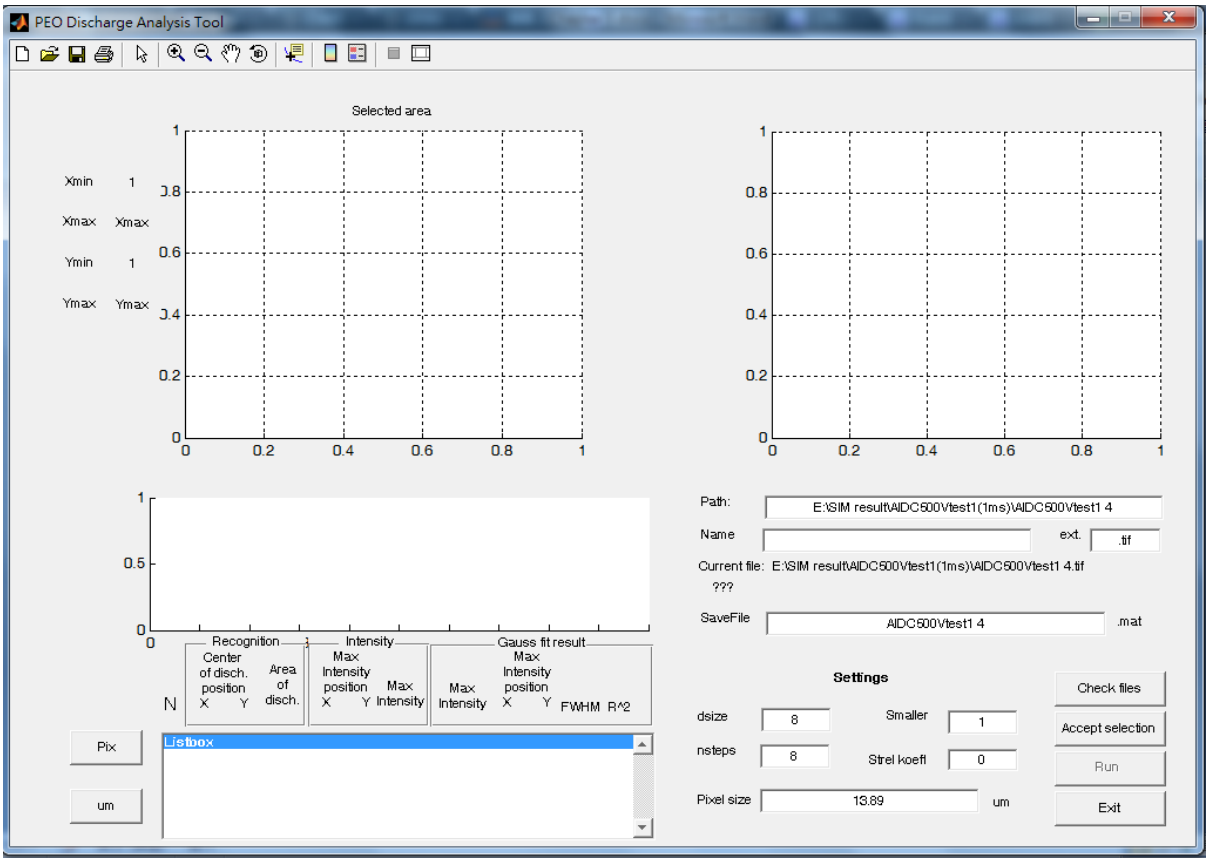

Fig. 3.17 The PEO discharge analysis program interface.

By applying the above methods and devices, the aim and objectives of this work can be pursued. The effects of electric field distribution in electrolyser and the effects of electrolyte temperature and conductivity on characteristics of PEO process will be investigated using the ISIS method together with COMSOL Multiphisics software package. Ex-situ EIS analysis will be used to compare impedance spectra with ISIS results. Fractal analysis will assist in the study of the effects of coating morphology on impedance spectra and the specialized imaging multi-channel (SIM) framing camera - for real-time observation of discharge events. Finally, the FFT analysis of high-resolution current signals will be applied to study the information on individual discharge events. Based on these studies, in depth investigation of the characteristics of PEO process can be carried out.

Chapter 4

Effects of Electric Field Distribution on the Process of PEO of Al

Electric field distribution in the electrolyser is one of the main factors affecting the PEO treatment, but has been seldom discussed. From electrochemical standpoint, it influences the current density distribution and therefore electrochemical reaction rates at the electrode surfaces. This could lead to differential coating growth rates in different locations on the sample surface, affecting local thickness, morphology and ultimately, the performance of PEO coatings. Observation of the evidence of such behaviour in situ, during the PEO processing, is therefore of great scientific and practical importance. In this study, various electrode configurations are employed to provide cells with different equidistant and non-equidistant geometries, and characteristics of frequency response from such cells are studied using the ISIS method.

4.1 Introduction

As discussed in section 3.2, in-situ impedance spectroscopy is a new method to acquire fundamental characteristics of plasma electrolytic oxidation (PEO) processes. In this technique, a variable frequency voltage waveform is used as a perturbation signal to obtain impedance characteristics of the electrolyser during the PEO processing. Yerokhin and Parfenov et al. have demonstrated feasibilities of this technique when operating in both the large and the small signal PEO modes [123,124]. It was however noticed that electric field distribution in the electrolyser may have significant effects on characteristics of the impedance spectra. To comprehend these effects, PEO processes are studied here in different cell geometries.

During the experiments, the voltage and current waveforms were acquired and processed using specially developed software to derive characteristics of impedance, magnitude, and phase angle. To assist data analysis, the characteristics were refined to eliminate process-inherent wild points and noise, as well as to smooth and convolute data. The detail of data processing and post-treatment is in section 3.2.4. The COMSOL software package was used to model and represent the distribution of electric field in the cells; these distributions were then correlated with immittance in the PEO electrolyser obtained by impedance spectroscopy. The fundamentals of COMSOL modeling and the detail of model design are provided in section 3.3. The modeling results in the form of the net electrolyte resistance are then compared between the cells with (1) uniform, converging and diverging electric fields; (2) non-equidistant and equidistant electrode layouts. Effects of different electric field conditions on the characteristics of coating morphology, such as thickness and porosity are discussed.

4.2 Experimental set-up and investigate methods

To investigate the effects of electric field distribution on the PEO process, the experiments were designed to provide distinct electric field distribution. In-situ impedance spectroscopy [112] was chosen as the main research method. Several complimentary methods were also selected: (1) COMSOL modeling - to evaluate the net electrolyte resistance as the boundary condition of impedance spectra for different inter-electrode layouts, and to observe the distribution of electric field and current density in the electrolyters; (2) Electron microscope analysis - to study the characteristics of coating morphology affected by various electric field conditions.

4.2.1 Sample preparation and the set-up of the electrode layout

To provide different types of electric field distribution, 6082 aluminum alloy (0.6% Mg; 0.7% Mn; 1% Si; and Al balance) samples of three different shapes with the same surface area (~1000 mm^2) as wire, rectangles and disks were selected. These three shapes were chosen to provide converging, parallel and diverging electric fields in the electrolyser, respectively.

Rectangular samples 22mm × 22mm × 1mm in size had both main surfaces preliminary

polished up to Ra ~ 0.1µm. Two stainless steel plates of the same surface area were chosen as counter electrodes and located on each side of the samples. The inter electrode distance set up for equidistant and non-equidistant systems is shown in Figure 4.1b. Wire samples with length 133mm × diameter 3.3mm were used as supplied with Ra ~ 1µm. A stainless steel cylinder with same length was located around the wire samples to provide converging electric field. In the equidistant condition, the wire sample was located in the middle of the cylinder, and displaced towards one side, for non- equidistant condition, as shown in Figure 4.1a. Disk samples with diameter 35.2mm × thickness 2.5 mm were preliminary polished to achieve Ra ~ 0.1µm. The threaded stainless steel wire was used as a counter electrode on the middle and at the edge of Al disks to provide equidistant and non-equidistant conditions, respectively (Figure 4.1c). The surface area of the counter electrodes was chosen twice or more the surface area of Al samples. Details of the electrode layout in all electric field conditions are presented in Table 4.1.

The electrolyte was composed of 1 g/l KOH, 2 g/l $Na_4P_2O_7 \cdot 10H_2O$, 2 g/l Na_2SiO_3. The PEO treatments were carried out in a 2-litre glass beaker equipped with cooling and agitation systems. During the treatment, the electrolyte temperature was maintained at ambient conditions.

Table 4.1. Experimental design of the electrode layout for different electric field conditions

Electric field type	Electrode layout	
	Equidistant (mm)	Non-Equidistant (mm) Short / long
Converging	~35	17.5 / 50.5
Parallel	34	25 / 43
Diverging	16	7 / 25

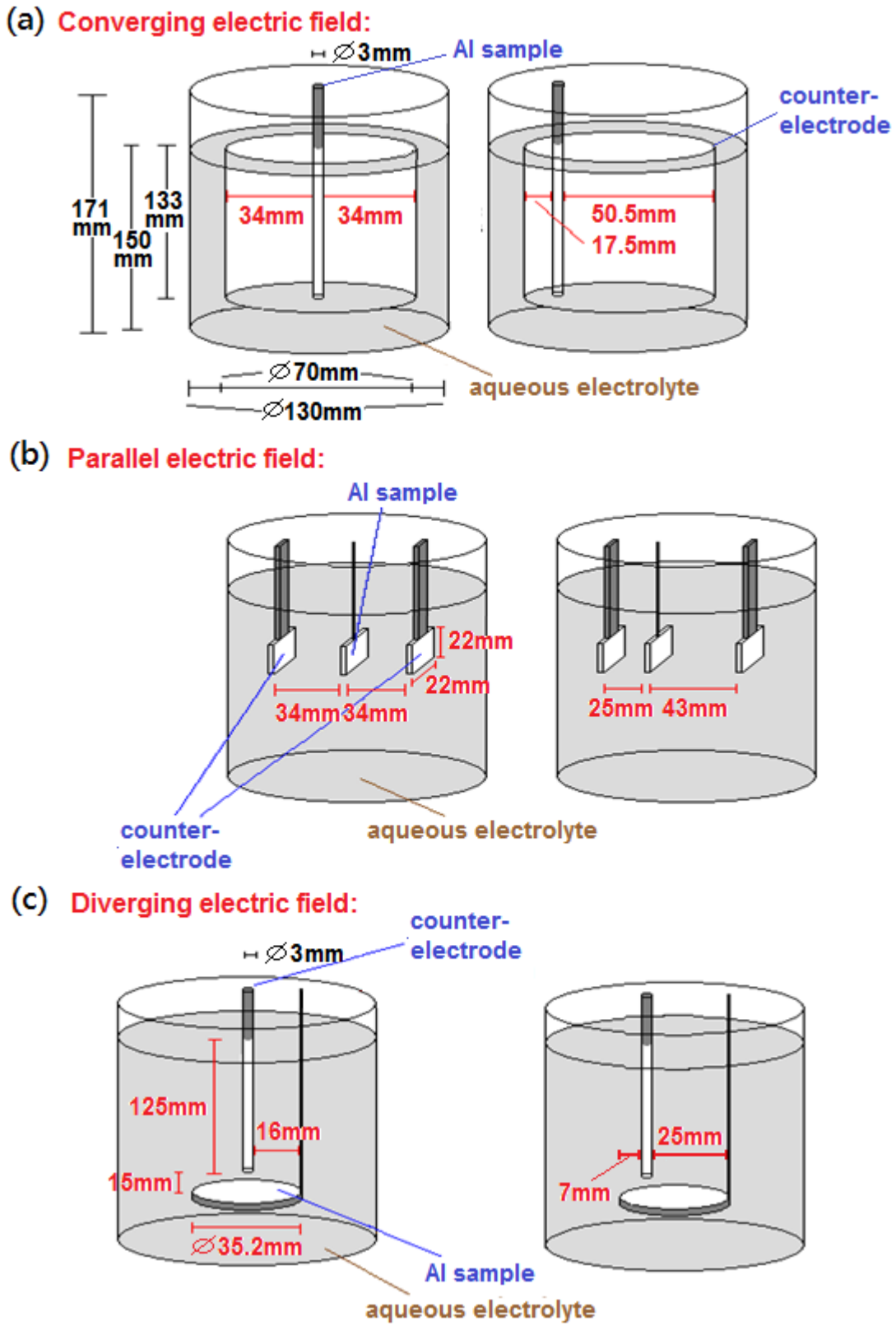

Fig. 4.1. Equidistant (left) and non-equidistant (right) cell geometries accepted in the experiments to provide different types of electric field (a) converging – wire samples, (b) parallel – rectangular samples, (c) diverging – disk samples.

4.2.2 In-situ impedance spectroscopy

In this study, In-situ impedance spectroscopy is chosen as the main method to investigate the effects of electric field distribution on the process of PEO. The experimental equipment system follows the previous work [123]. The PEO treatments were carried out in a bipolar pulse current mode with frequency logarithmically swept from 20 Hz to 20 kHz every 0.48 s. Specially designed rectangular pulses simulating a DC superposed AC waveform (presented in section 3.2.2 and figure 3.5) were chosen and controlled by an external waveform generator.

The frequency response data were acquired throughout the treatment, for which the duration τ was fixed at 15 min. After the PEO treatments, the acquired voltage and current waveforms were processed using a specially developed refining software to eliminate process-inherent wild points and noise, as well as to smooth and convolute data. This also allows to provide boundary condition and resistance of the electrolyte as well as normalise the data over the sample surface area to eventually derive characteristics of impedance, admittance, and phase angle. Obtained in such way, impedance spectra were supplied for further analysis and simulation using equivalent circuit method (Zview software) in order to visualise and analyse the effects of electric field distribution on the impedance spectra of the PEO process, during PEO treatment.

4.2.3 Distribution of electric field in the electrolyte

For the three different types of electric field considered to investigate the effects of electric field on the PEO process. A COMSOL – Multiphysics Model package [126] was used to model the distribution of electric field, current density and resistance in the electrolyte. The results of modeling can assist in observation of the distribution of the above characteristics influenced by different electric field conditions and electrode layouts.

4.2.4 Net electrolyte resistance evaluation

For in–situ impedance spectroscopy investigations, the net electrolyte resistance is an essential input parameter, which is difficult to evaluate in the case if the whole cell is employed, containing electrolytes with relatively high resistance.

A simplified 2D DC configuration was considered. The detail of the model design and parameter setup are discussed in section 3.3.2. In the modeling, the electric potential and total current densities were evaluated and then used to calculate the electrolyte resistance by Ohm's law (R= U/I). The electrolyte resistances at the surface of the Al electrode were evaluated and averaged for all electric field conditions.

4.2.5 Coating evaluation

To study the characteristics of PEO coatings formed in all conditions of electrode layouts, few instruments and methods were chosen. The coating thickness was measured non-destructively using an Elcometer 355 modular thickness gauge system equipped with an accuracy of about ±1μm (section 3.4.1). Fifteen measurements were taken from coating surface during each thickness test to get average thickness. Rectangular type samples were measured on both main surfaces to obtain the average thickness in the equidistant condition. On the other hand, two sides of rectangular surface were measured separately in the non-equidistant condition. Disk samples were measured in the centre and edge region in the equidistant condition. Three different locations were measured, such as the region near the counter electrode, in the centre, and the region far away from the counter electrode. Because of the shape of the wire samples, the coating thickness could not be measured by this instrument. In this case, SEM analysis was performed to study the coating thickness.

A Jeol JSM 6400 scanning electron microscope was used to study coating morphology and microstructure. When employ the SEM, 10 images were taken at ×1000 magnification on each sample for statistical study. A ZEISS-KsRun software was used to evaluate the PEO coating thickness distribution in the SEM images. Twenty measurements were taken at each SEM imagines. The probability density of coating thickness and pore size were obtained to quantify morphology characteristics of PEO coatings produced under different electric field effect conditions. Surface and interface roughness were also measured on the two randomly selected SEM images per sample using the ZEISS-KsRun software.

4.3 Modeling of Electric field distribution in the electrolyte

To investigate the effects of electric field on the process of PEO coating formation, COMSOL has been chosen to model the distribution of electric field, resistance of electrolyte and total current density in the electrolyte under different types of electric field and electrode

layout. From the 2D modeling results, the background color in figures 4.2 ~ 4.4 represents the distribution of electrolyte resistance, which shows a clear change with location between the electrodes. The magnitude of the resistance of electrolyte under the converging electric field conditions is around 10 times smaller than under the conditions of parallel and diverging electric field. The difference between parallel and diverging conditions is negligible.

The contour line represent the distribution of electric potential. The difference of the distribution of electric potential between equidistant and non-equidistant layout in all electric field conditions can be visualised from the modeling results. This is a complimentary method to evaluate the distribution of coating thickness.

The arrows and streamlines represent the direction of the total current density. Under the non-equidistant layouts, the current density between working electrode and the near counter electrode is significantly higher. In figure 4.3, the direction of current goes toward both side of two counter electrodes. The current density is lower between the working electrode and the far side of the counter electrodes. In the figure 4.4, the underside of working electrode was designated as " insulation region", hence, no current occurs around that region. In the experiment, the underside of the disk samples was covered by insulated rubber tape.

From the COMSOL modeling it follows that, the effect of different types of electric field distribution is significant. Therefore, the obvious differences of coating morphology, current evolution and impedance spectra under different electric field conditions can be expected especially between converging electric field and the other two conditions.

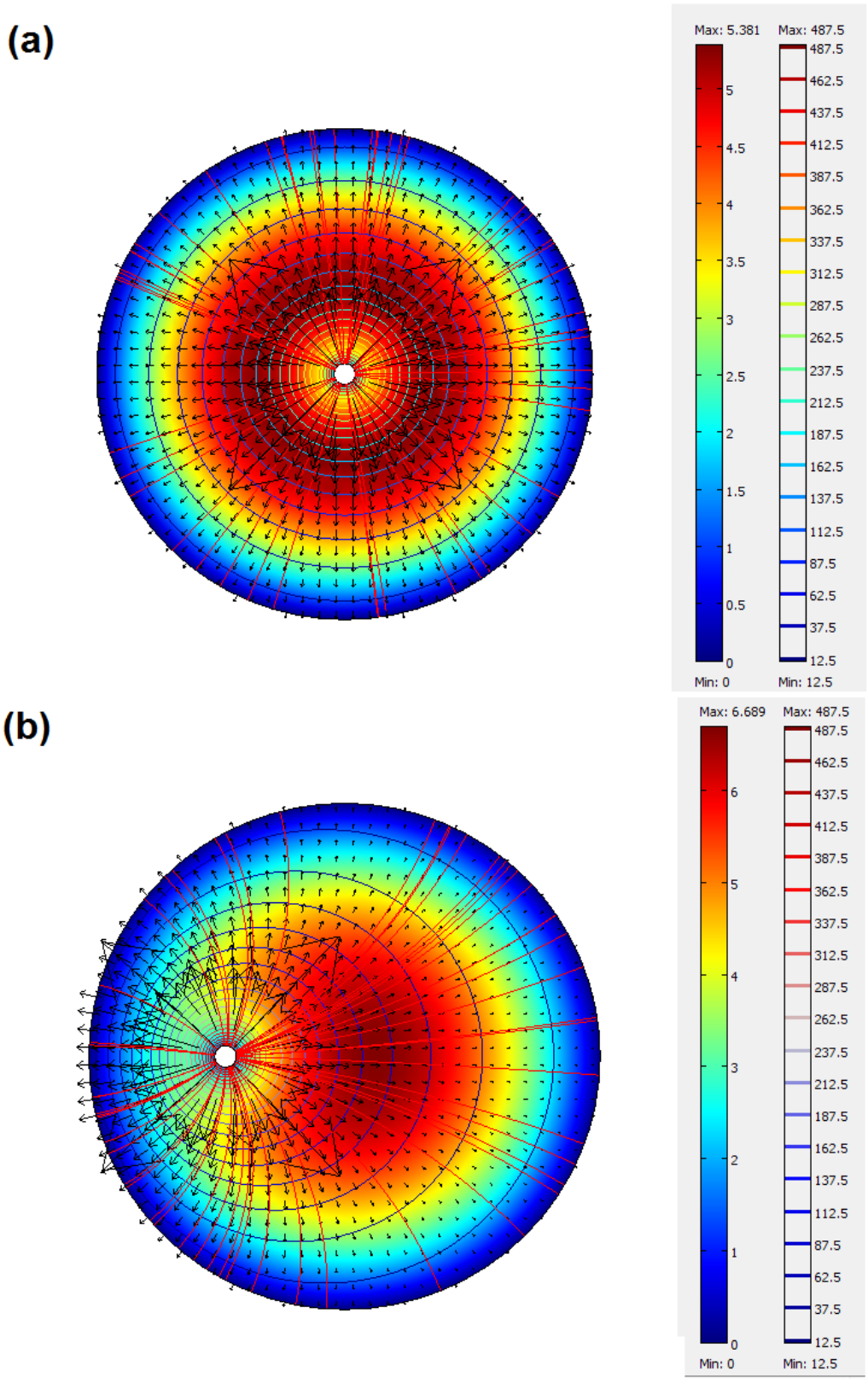

Fig. 4.2. The COMSOL modeling results of 2D distributions of surface: electrolyte resistance [Ω-m^2]; contour line: electric potential [V]; arrow and streamline: total current density, in the electrolyte under (a) Converging - equidistant, (b) Converging - non-equidistant, layouts.

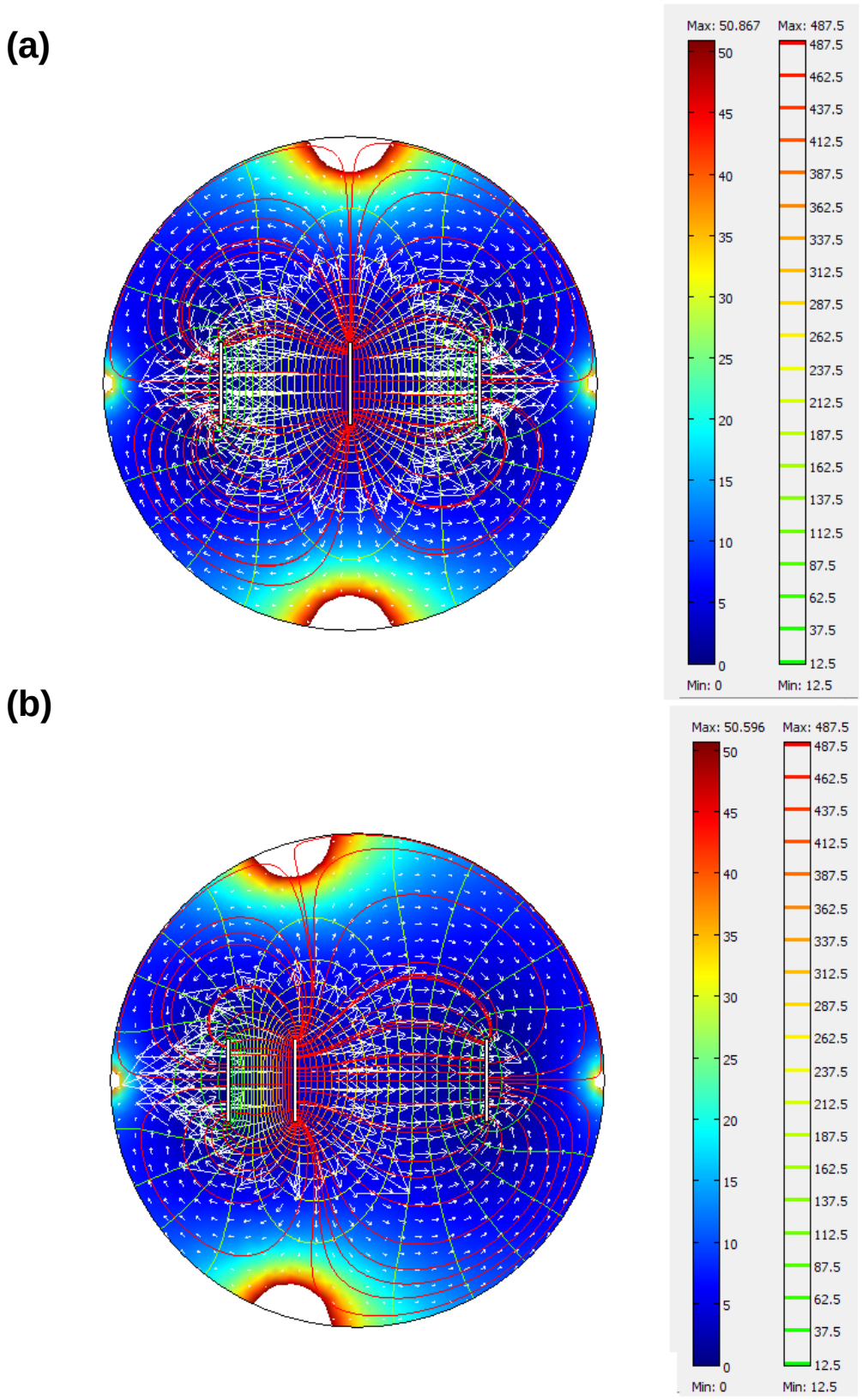

Fig. 4.3. The COMSOL modeling results of 2D distributions of surface: electrolyte resistance [Ω-m^2]; contour line: electric potential [V]; arrow and streamline: total current density, in the electrolyte under (a) Parallel - equidistant, (b) Parallel – non-equidistant, layouts.

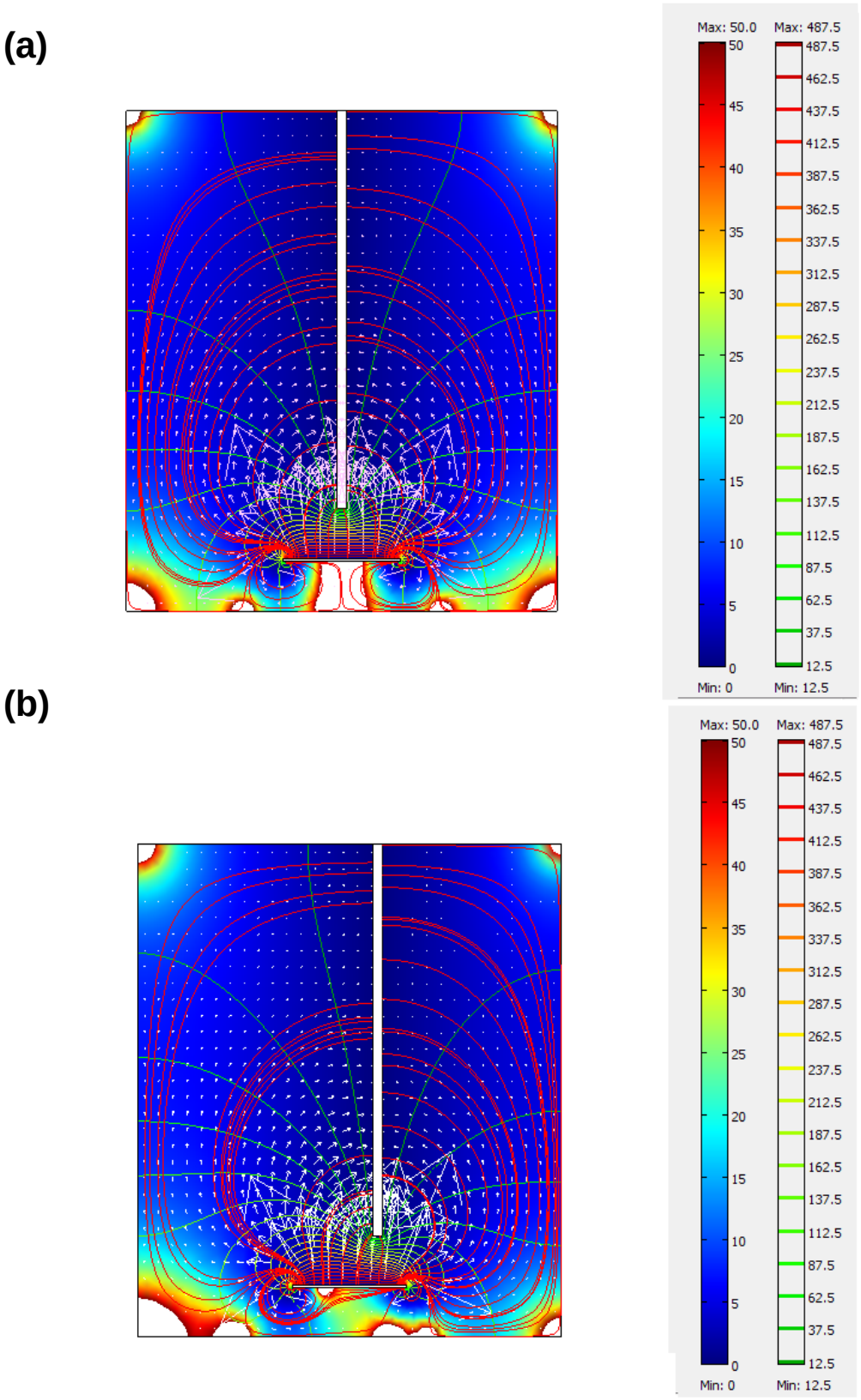

Fig. 4.4. The COMSOL modeling results of 2D distributions of surface: electrolyte resistance [Ω-m^2]; contour line: electric potential [V]; arrow and streamline: total current density, in the electrolyte under (a) Diverging–equidistant, (b) Diverging–non-equidistant, layouts.

4.4 Current density evolution

Since the experiments were carried out under the voltage control mode, the response of current was recorded using a data acquisition device with sampling rate of 0.5Hz. Figure 4.5 shows current density evolution during PEO treatments under the conditions designed to reproduce all studied electric field types and cell geometries. At the initial stage, under all conditions, the current density increases according to the ramp time set up for the voltage increase to the pre-set values, which are 547 V and -86 V in this study. After the required voltage is reached, the current density is gradually reduced with the time of PEO treatment. In the results, the converging electric field provides higher current densities than other conditions, especially when the voltage reaches the required value, an evident current peak is present. Therefore, the duration of transition to the steady-state under the converging electric field conditions is longer. In all cases, non-equidistant geometry provides higher current densities than the equidistant one. At the final stage of the treatment, the value of current density is about 0.5 A/cm^2 in the converging electric field, whereas it is about 0.1 A/cm^2 and 0.15 A/cm^2 higher than parallel and diverging electric field, respectively. In the case of diverging electric field, it can be noticed that the discharge commences at the edge of the sample. The edge effects were observed in both parallel and diverging geometries, which affecting the current evolution.

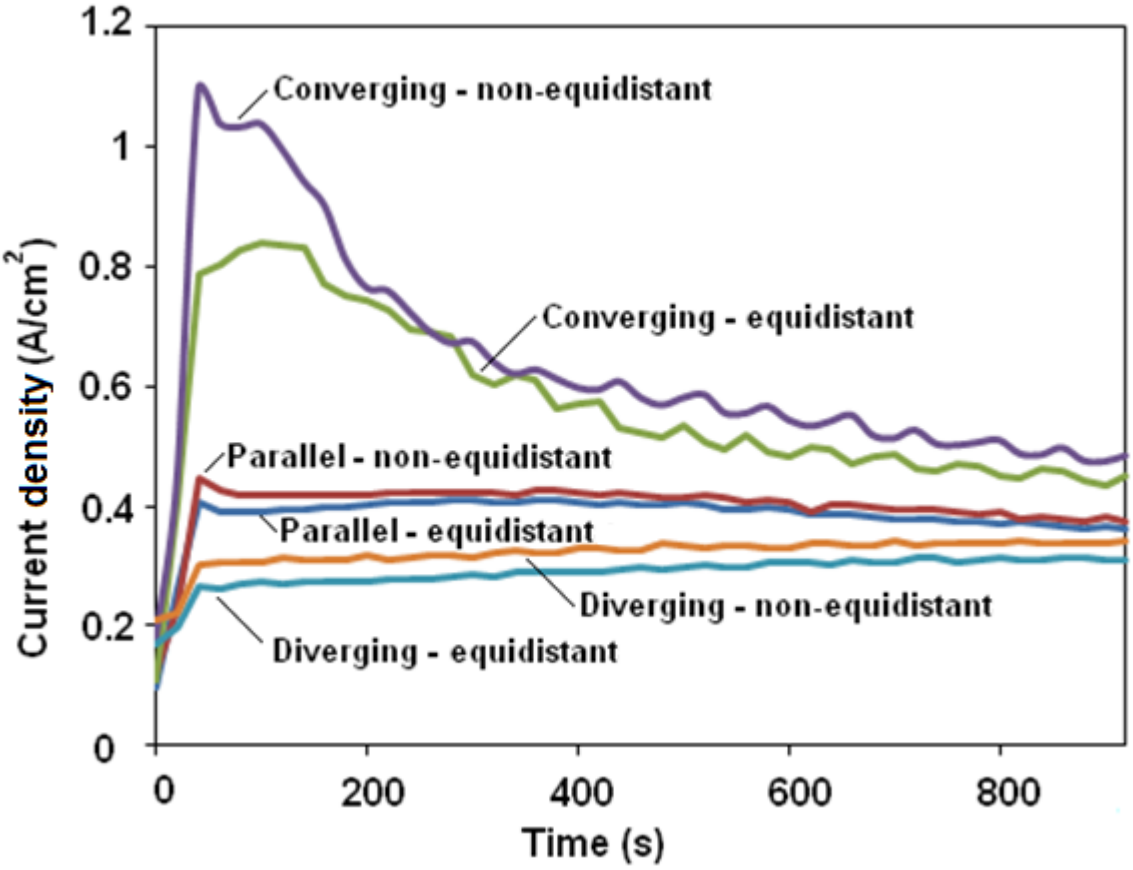

Fig. 4.5. Evolution of current density with time in experiments with different electric field types and inter electrode layout

4.5 Characteristics of coating morphology

4.5.1 Thickness measurements

The PEO coating thickness is shown in Table 4.2. Coating thickness difference between both sides of surface in parallel equidistant type is approximately 0.5μm, and the difference between short and long distance in the non-equidistant geometry is around 0.6μm. The difference is very small and hard to make a description of the electrode layout effect under parallel electric field conditions on the PEO coating thickness.

From thickness measurement on the coatings produced under diverging electric field conditions, the coating at the edge is about 0.7μm thicker than in the central area in equidistant layout. For the non-equidistant layout, near to the counter-electrode parts of the coating is 0.7μm thicker than that in the central region and the region far away from the

counter-electrode. However, the thickness difference is as small as its deviation, which makes the effect of electric field effect distribution under this condition statistically negligible.

To compare the coating thickness between parallel and diverging electric field conditions, the thicker coatings were produced under the parallel electric field in both electrode layouts. The difference in coating thickness between parallel and diverging conditions is relatively obvious under equidistant layout. In both the parallel and diverging electric field conditions, the difference of coating thickness between the near counter-electrode region and the region far away from counter-electrode were similar (~0.6μm).

Table 4.2. Coating thickness under different electric field conditions and electrode layouts

Layout / Electric field	Equidistant (μm)	Non-Equidistant (μm) Short / long
Parallel	**15.1 ± 1.1**	**14.0 ± 1.1 / 13.4 ± 1.5**
Diverging	**Centre: 10.2 ± 0.4 Edge: 10.9 ± 0.7**	**Centre: 11.5 ± 0.4 Edge: 12.2 ± 0.7 / 11.6 ± 0.7**

4.5.2 SEM morphologies

The SEM images (Figure 4.6) show the cross-sections of PEO coatings produced under different electric field conditions and electrode layout. For the same duration (15 min), the treatments performed under the converging type of electric field produced 2 times thicker oxide layers than others, but the difference in thickness under equidistant and non-equidistant layout appears to be negligible in all electric field types (Figure 4.6).

From the cross-sectional images, it can be seen that there are two layers in the coatings, even though the thickness of the inner layer is much less than that of the outer part. The difference in porosity of the coatings produced under the converging and other electric field

types is obvious. It can be seen that the coatings produced under the converging electric field condition have substantial amount of tiny pores with diameter ranging from 1 to 3μm though the outer coating region (figs. 4.6(a)-(b)), is obviously different from other samples. A small number of large pores (diameter < 15μm) is obvious in the coating produced under the converging electric field condition.

Coating thickness and porosity distributions are shown in figure 4.7 and 4.8, respectively. These data indicate that the morphology of PEO coatings produced in cells with different geometries is significantly different. From the probability density of thickness, it can be seen that the thicker coatings produced under converging electric field, especially in non-equidistant electrode layout. On the other hand, the difference in the thickness of PEO coatings produced under converging electric field conditions with equidistant and non-equidistant is significant. The highest probability density of coating thickness distributed at the range of 25~30μm and 15~20μm in the non-equidistant and the equidistant electrode layouts, respectively. This difference is negligible for both the parallel and diverging conditions. This conjectures that the inter electrode distance effect on electric field during PEO treatment is significant only for converging conditions.

In contrast with impedance plots (figure4.9 (h)), PEO coatings thickness have an inverse relationship with the magnitude of impedance spectra. The difference in impedance spectra under equidistant and non-equidistant electrode layouts is more significant.

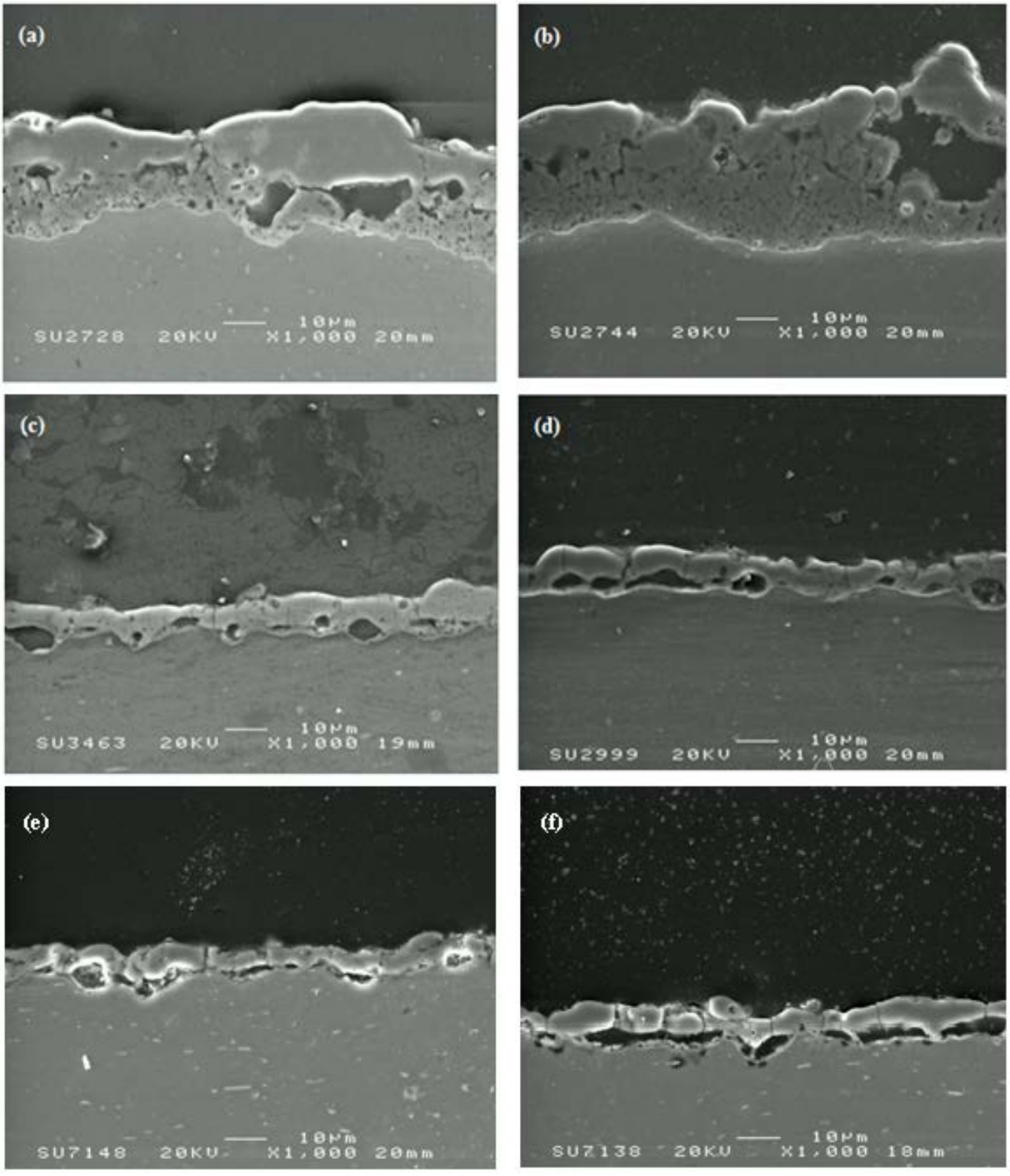

Fig. 4.6. SEM morphology of PEO coating on the samples treated under different electric field conditions and electrode layouts: (a) converging equidistant (b) converging non-equidistant, (c) parallel equidistant, (d) parallel non-equidistant, (e) diverging equidistant, (f) diverging non- equidistant

Probability density distribution of the coating porosity shows two interesting effects. Firstly, substantial amounts of extreme pore sizes (0~3μm and >15μm) are present in the coatings produced under the converging electric field condition. Secondly, coating formed in the non-equidistant electrode layout has slightly more pores in the range from 3~6μm to 9~12μm.

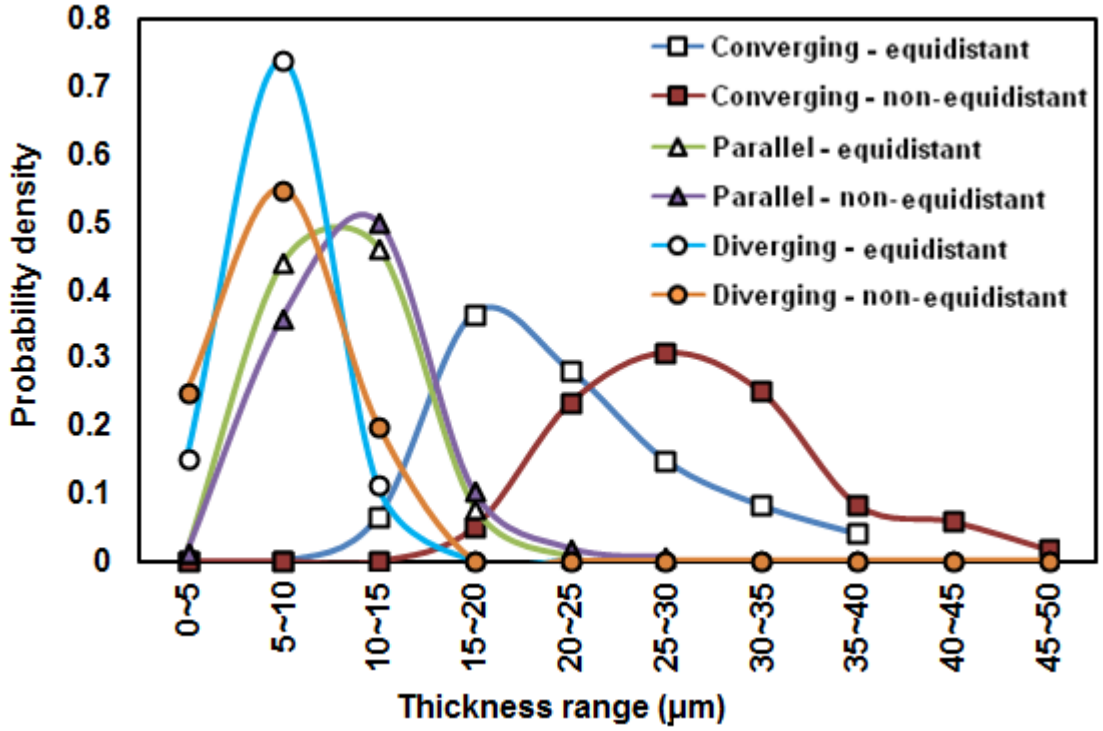

Fig. 4.7. Characteristics of coating morphology: Thickness distribution

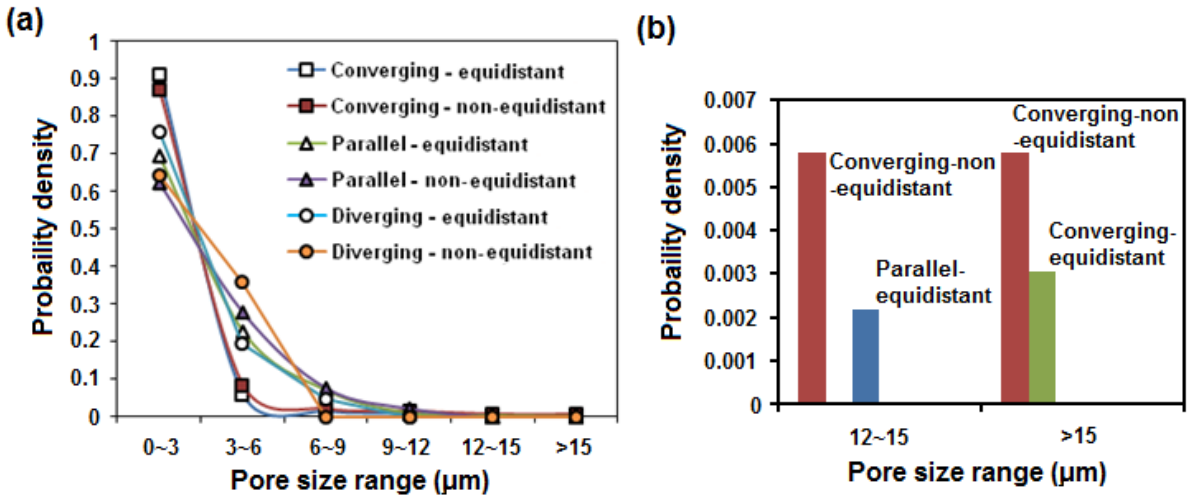

Fig. 4.8.Characteristics of coating morphology: (a) overall pore size distribution, (b) large pore size region.

Surface roughness is yet another factor that may affect the characteristics both of morphology and impedance. The roughness of both the coating surface and the coating/substrate interface is shown in Table 4.3. The data indicate that high roughness maybe not only present on the surface but also at the coating/substrate interface, and the coatings formed in non-equidistant electrode layouts tend to have slightly higher surface roughness.

Table 4.3. The surface and interface roughnesses of PEO coatings in different cell geometries

Process conditions		**Roughness (Rz) (μm)**	
Electric field	**Electrode layout**	**Surface**	**Interface**
Converging	equidistant	6.94	3.79
	non-equidistant	13.64	4.82
Parallel	equidistant	4.19	3.56
	non-equidistant	7.49	4.08
Diverging	equidistant	5.13	5.27
	non-equidistant	4.58	4.25

From the above results, PEO coating formation is strongly dependent on the electric field distribution. Therefore, the characteristics of coating morphology can be precepted as a direct reflection of the electric field effects. In comparison, the difference in thickness of PEO coatings produced under parallel and diverging electric field conditions with equidistant and non-equidistant electrode layouts is negligible as shown in Figure 4.7 and Table 4.2. This is however significant under converging electric field condition, this indicates that the effect of electrode layout under same electric field type is significant only under high enough current densities conditions. Under the converging electric field; the thick coating (~25μm) is produced, featuring numerous small and several big pores in the lower region, and relative dense coating in the upper region. The formation of PEO coating is due to the pulsed bipolar current mode of the power supply. During the positive half-cycle, the main mechanism of coating formation is according to the equation (2.1) and (2.2b). Al^{3+} are ejected from the region above the inner dense layer, react with the oxygen in the electrolyte and then are deposited, with high cooling rate (10^8K/s) to form the upper region. According to this mechanism, bigger size pores are formed above the inner dense layer because of Al^{3+} ejection. During the negative half-cycle, the OH^- from the electrolyte (equation 2.8), which diffused in the pores, react with Al to produce $Al_2(OH)_3$. These intermediate products are then rapidly transformed in Al_2O_3, with high temperature, environment to fill in the large

pores. In this case, the high density of small size pores occurred in the inner region of the outer porous layer.

Compared with converging electric field condition, the main pore size range for both parallel and diverging electric field conditions is smaller (3~9μm), but less probability density of pore size between 0~3μm in the inner porous region. These results can be explained by the weaker electric field effect and lower current density under these two electric field types. The activity of Al^{3+} ejection and the reaction during negative half-cycle is much weaker. On the other hand, from the cross-sections of PEO coatings produced under all electric field conditions and electrode layouts, it follows that the surface roughness of PEO coatings is strongly affected by the size and distribution of pores. Therefore, the surface roughness is significantly higher for the coatings produced under the converging electric field conditions.

Thus, the effects of electric field distribution on coating formation have been demonstrated by analysing the characteristics of the coating morphology. The difference of coating morphology under different electric field conditions and electrode layouts accords with the prediction from the COMSOL modeling.

4.6 Boundary conditions of in-situ impedance spectroscopy

The boundary conditions are the required input parameter for ISIS. In the traditional EIS method, the boundary conditions of impedance spectra are defined as the impedance value at f_∞ and f_0 (usually using the frequency range from 10^7 to10^{-2} Hz). When studying coatings, the impedance value at f_∞ can be seen as the resistance of electrolyte (Rs) and f_0 as the resistance of electrolyte plus the resistance of the coating (R_c). In the ISIS studies, the boundary conditions were evaluated from the results of COMSOL modeling and current density evolution for the impedance value at f_∞ and f_0, respectively.

For the upper boundary condition, the net resistance of the electrolyte near by the working electrode under all electric field types and electrode layouts was calculated from the COMSOL modeling results (figure 4.2 ~ 4.4). Data in Table 4.4, show that parallel type of electric field provides the highest net electrolyte resistance, which is 7 and 2.5 times higher than those for converging and diverging electric field types, respectively. It can also be found out that the equidistant electrode layouts provide slightly higher net electrolyte resistance than non-equidistant one, in all electric field conditions.

Table 4.4. Net electrolyte resistance (Ω) calculated using COMSOL package

Electric field type	**Cell layout**	
	Equidistant	Non-Equidistant
Parallel	43.6	34.4
Converging	6.4	5.9
Diverging	15.3	14.6

The lower boundary condition is the impedance value at $f_{0,}$ which can be simply calculated by using ohm's law ($R = V / I$). Here, both V and I were evaluated using the data recorded in the ISIS experiments. The positive voltage at the lowest frequency was chosen as the value of V. The I values were obtained using the current at the steady-state region of the current pulse. Such evaluation of the boundary conditions for the impedance spectra, allows higher accuracy of the ISIS results discussed in the next section.

4.7 ISIS results

Figure 4.9 shows the temporal evolution of in-situ impedance spectra of the studied PEO processes, presented in the form of Complex and Bode plots. In order to show the main features of the complex diagrams, the frequencies are restricted to the region from 20Hz to 20kHz. In all electric field conditions the shape of the arcs is quite unusual for impedance spectra, but similar shapes have been previously observed in certain situations [69,142-146]. Three distinct features were observed in this study. Firstly, the complex impedance plots attain a decrease behaviour of real impedance (Z') in the lower frequency range, and the point when Z' starts decreasing is always at Z"$>$0. In contrast, the Z' decrease in the medium frequency range (f=10^2 Hz~10^1Hz), which also the decrease of Z' start when Z"$<$0. Secondly, the decrease of Z' value occurs in the higher frequency range. Thirdly, a fragment of arc resembles the character "C" in the low frequency region.

The shape of impedance spectra is different under different electric field conditions

(figure 4.9(a)-(f)). It is however similar for the equidistant and non-equidistant electrode layout under the same electric field condition. However, the impedance arc at the equidistant condition is slightly bigger than the non-equidistant one. For example, the maximum value under parallel-equidistant condition is about Z" = -1600 (Ω/cm^2), and Z' = 1900 (Ω/cm^2) at 14 min, but only around Z" = -1500 (Ω/cm^2); max Z' = 1750 (Ω/cm^2) under parallel-non-equidistant layout. It is however characteristic of converging and diverging field (7(a), (b), (e) and (f)). This observation indicates that the electric field effect on the impedance of the PEO process carried out in the cells with different electrode layout is remarkable.

The other interesting phenomenon observed in the impedance spectra obtained under equidistant and non-equidistant electrode layouts of the converging electric field condition is significant difference in the last two minutes (t = 13min, 14min). In the low frequency domain, the decrease of the Z' becomes stronger at t = 14 min, as shown in figure 4.9(b), but it is totally opposite under the equidistant condition. This phenomenon is also observed under the parallel electric field condition. The reason for such behaviour occurred during the last 1~ 2 minutes of the process may be due to the coating layers grown to a thickness which is sufficient to retard the electric field effect and charge transfer under equidistant conditions, but at a shorter distance between the counter electrode and the sample in the non-equidistant condition, still provides a strong enough electric field to produce sufficient current flow. From figure 4.5, the current density evolution in both non-equidistant electrode layouts of the converging and parallel electric field conditions has not yet reached the steady state in the last 2 minutes. The recrystallization still occurs because the electric field is still high enough between the shorter distance of the counter and working electrode at 14 min.

Figure 4.9 (g) and (h) represent the comparison of different electric field conditions and electrode layouts at t = 1min and 14 min. Here, the highest impedance occurred under diverging electric field conditions with a non-equidistant electrode layout. This is consistent with the behaviour of current density evolution in figure 4.5 and the COMSOL modeling results in figure 4.2 ~ 4.4, hence, the effect of electric field type and location between samples and counter-electrodes is significant.

In EIS studies, different phenomena driven by different mechanisms can be indicated from various frequency regions of the impedance spectra. Therefore, the frequency is divided into four ranges as ultra-high (above 10^4Hz), high (10^3~10^4Hz), medium (10^2~10^3 Hz), and low (10^1~10^2 Hz) as shown in figure 4.10 (a) - (c).

In the ultra-high frequency region (around 10^5Hz), the behaviour of the impedance

spectra is characterised by the positive slope $\frac{dZ'}{df} > 0$. This phenomenon has been also observed by Hsieh et al. [147], who consider it as a massive distortion. However, due to this ultra high frequency range being beyond the range of 20Hz ~ 20 kHz used in this study (section 3.22), there are no data points in this frequency range. Shape of the same situation is also occurred in the part of the low frequency range, under 20 Hz. The behaviour of $\frac{dZ'}{df} > 0$ in the ultra-high frequency range is caused by the evaluated value of the boundary conditions at f_∞ and the impedance spectra is simulated by the spline program (section 3.26).

The high frequency range (10^3~10^4Hz) is common in several EIS references, however in this range, the arcs exhibit a skewed shape characteristic. This shape has been presented by Parfenov et al. [112], which indicated that it is common behaviour for a thick coatings. Due to the shape, it is believed that the impedance spectra in this frequency range can be fitted by a single RC loop.

In the medium range (10^2~10^3 Hz), the impedance spectra of $\frac{dZ'}{df} > 0$ occurred at around 400Hz. It is believed to be a complex region affected by plasma discharge. This part of impedance spectra may need to be fitted by loops with a negative resistance or an inductance. In references, the negative resistance and inductance loop are often used in equivalent circuits to describe relaxation reactions and adsorption of intermediate produces, respectively [69, 114].

In the low frequency range (10^1~10^2 Hz), the tendency of impedance spectra were followed from the medium frequency range. However, from the results of the system linearity evaluation for the PEO process (section 3.25), the maximum error of impedance modulus at about 10% is observed in this frequency range. Because it is such uncertainty, the data in this region are difficult to use for modelling.

Similar behaviour of impedance spectra ($\frac{dZ'}{df} > 0$) in the medium and low frequency ranges have been reported by Popkirov et al.[148]. From Popkirov's explanation, this behaviour is due to the current decay before the electro reduction process is completed and also the kinetics of the relaxation processes. In his case, he mentioned that the response amplitude spectra are not a superimposition of the original action of the perturbation signal, which indicates that the cell response signal is distorted. However, in this work, the impedance spectra have all been checked by the FR linearity check tool (section 3.25), which

the average system linearity estimated at ≥ 90% and the average error from both impedance and phase angle estimation are all ≤ 5% (Table 4.5), and the main error only occurred in the frequency range below 200Hz. Therefore, the studied PEO processes can be considered as a properly linearised system, and the behaviour of impedance spectra in the medium and low frequency range provide a true representation of the phenomena that occur during the PEO process. The designed equivalent circuits and the meaning of corresponding elements for all electric field distributions and electrode layouts are discussed in the next section.

Table 4.5. Linearity characteristics of the PEO processes operated under different electric fields and electrode layouts

Fields	Converging		Parallel		Diverging	
Layouts	equidistant	Non-equidistant	equidistant	Non-equidistant	equidistant	Non-equidistant
Linearity (%)	91.96	90.16	96.06	95.67	96.15	96.21
Average impedance error (%)	3.27	3.77	2.57	2.80	2.61	2.74
Average phase angle error (%)	4.12	3.95	3.36	3.55	3.43	3.37

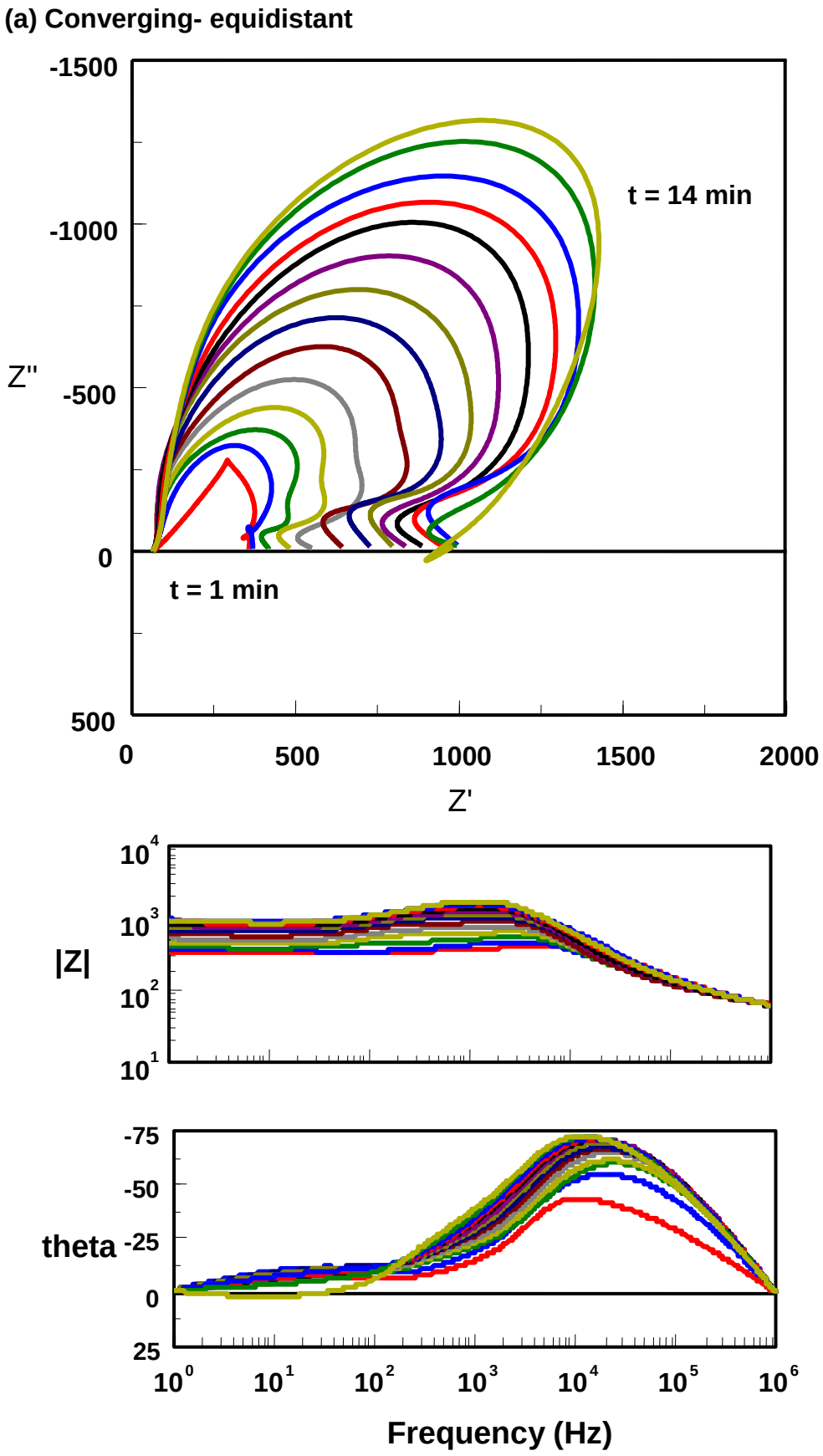

Fig. 4.9. (beginning) Complex and Bode plots of in-situ impedance spectra of PEO process carried out under different electric fields and electrode layouts: (a) converging (equidistant)

to be continued

continuing

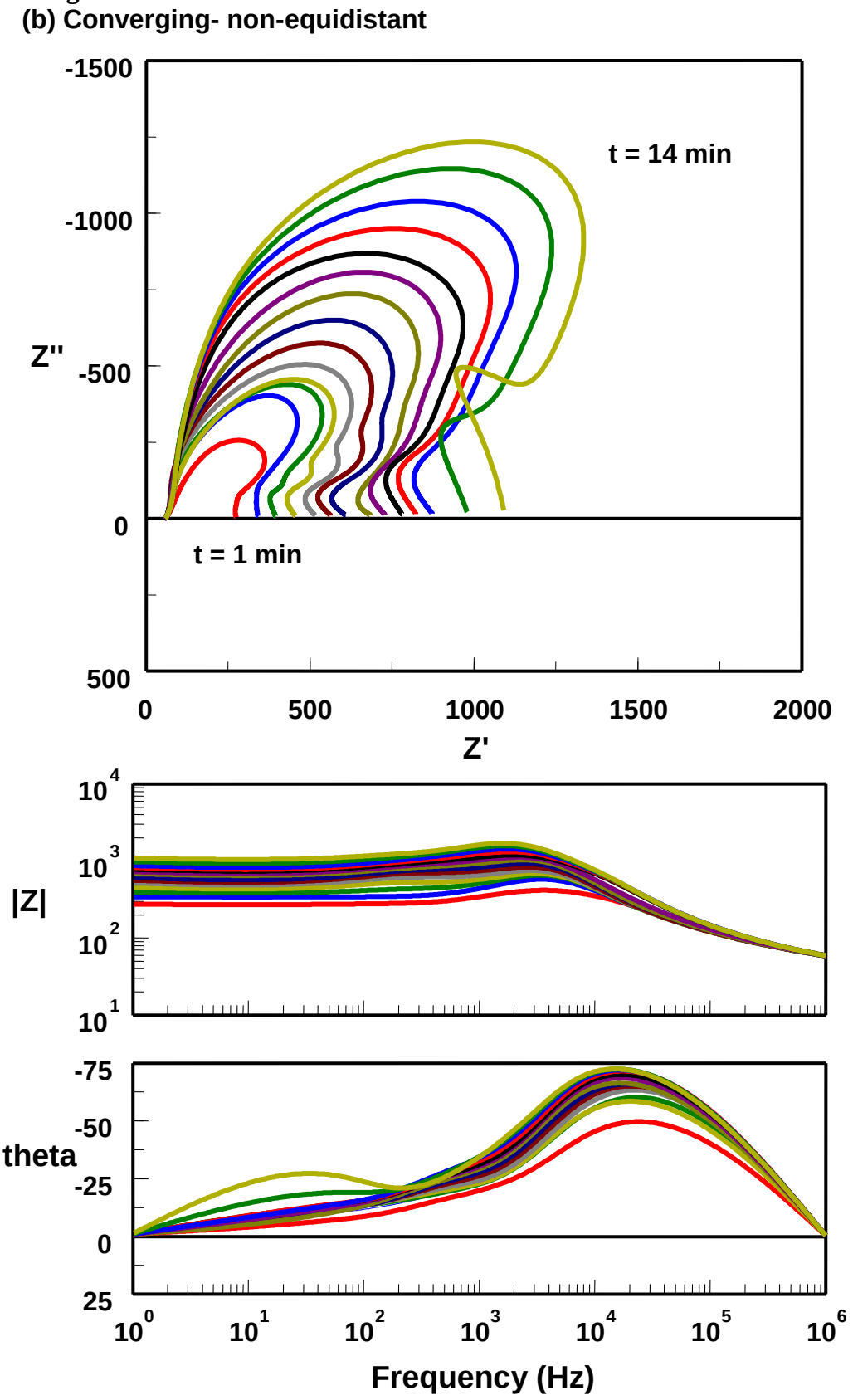

Fig. 4.9. Complex and Bode plots of in-situ impedance spectra of PEO process carried out under different electric fields and electrode layouts: (b) converging (non-equidistant)

continuing

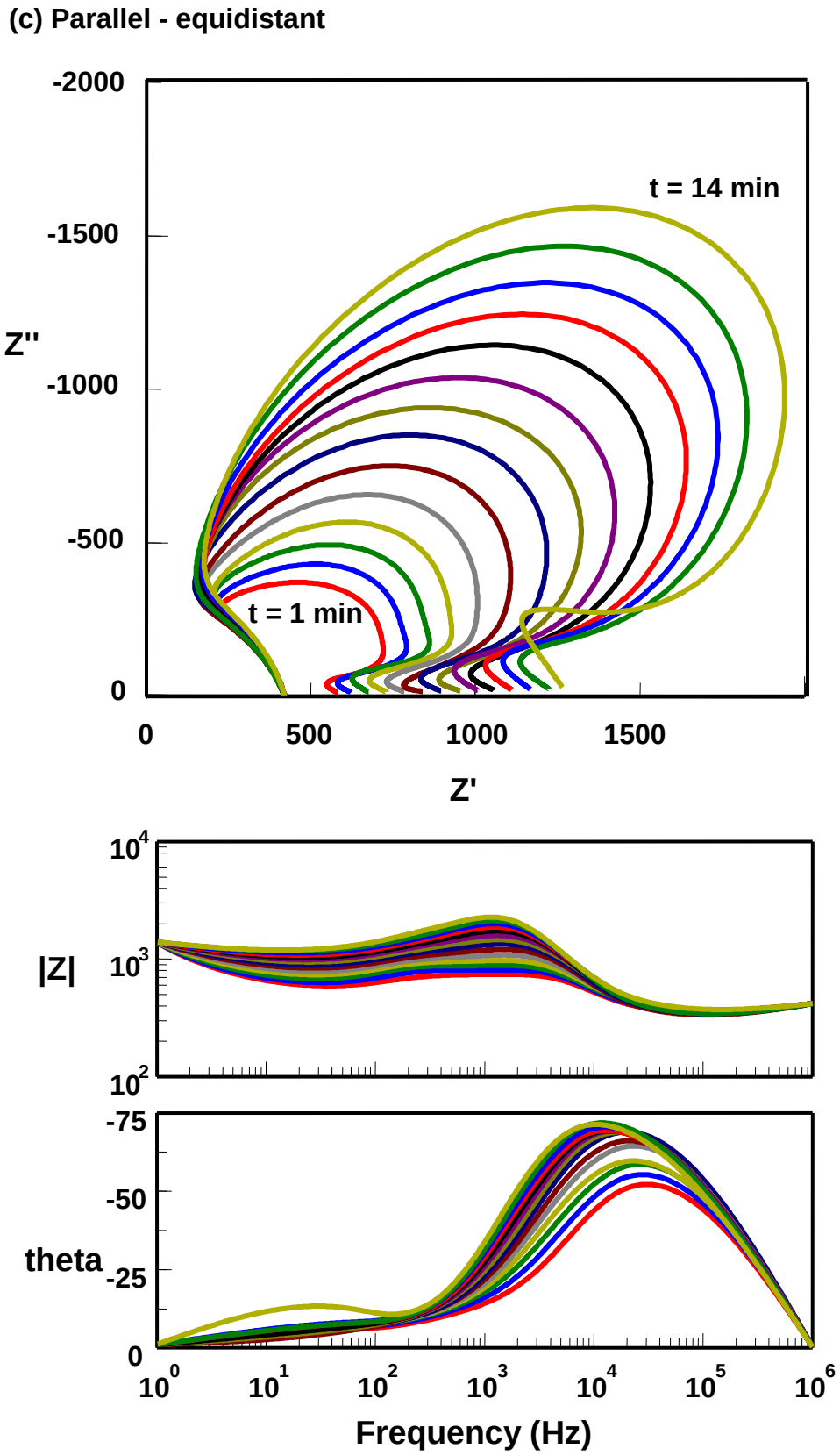

Fig. 4.9. Complex and Bode plots of in-situ impedance spectra of PEO process carried out under different electric fields and electrode layouts: (c) parallel (equidistant)

continuing

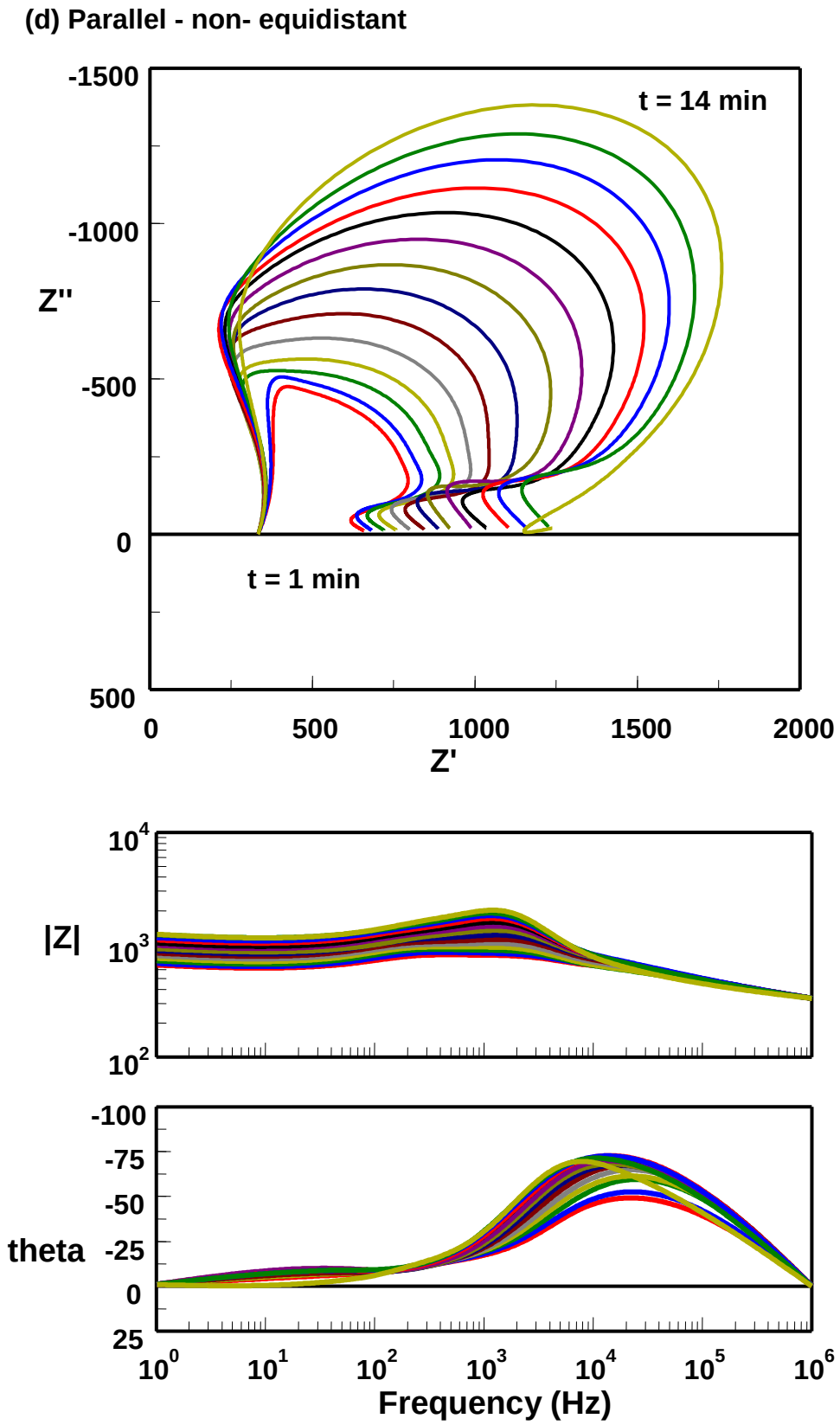

Fig. 4.9. Complex and Bode plots of in-situ impedance spectra of PEO process carried out under different electric fields and electrode layouts: (d) parallel (non-equidistant)

continuing

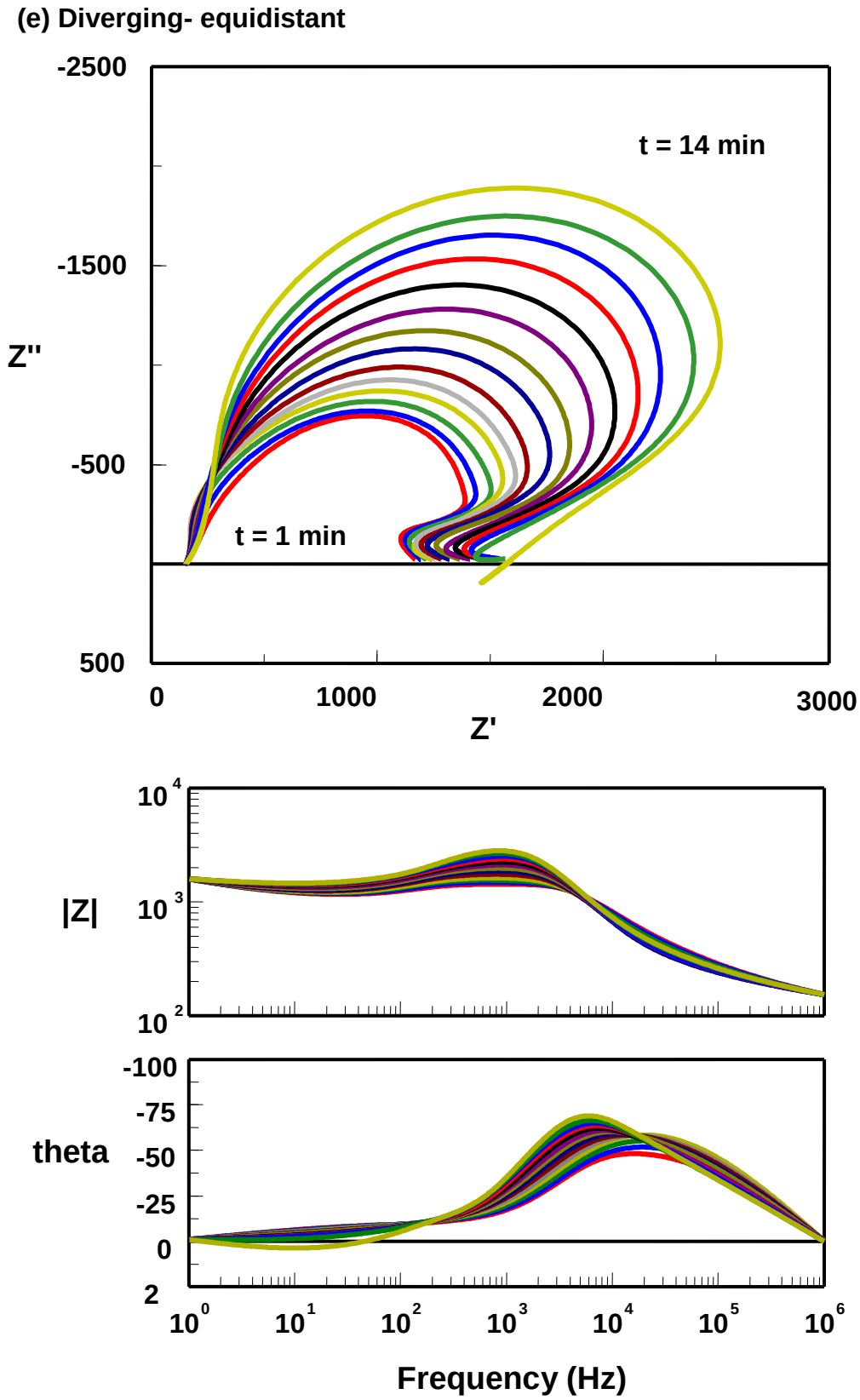

Fig. 4.9. Complex and Bode plots of in-situ impedance spectra of PEO process carried out under different electric fields and electrode layouts: (e) diverging (equidistant)

continuing

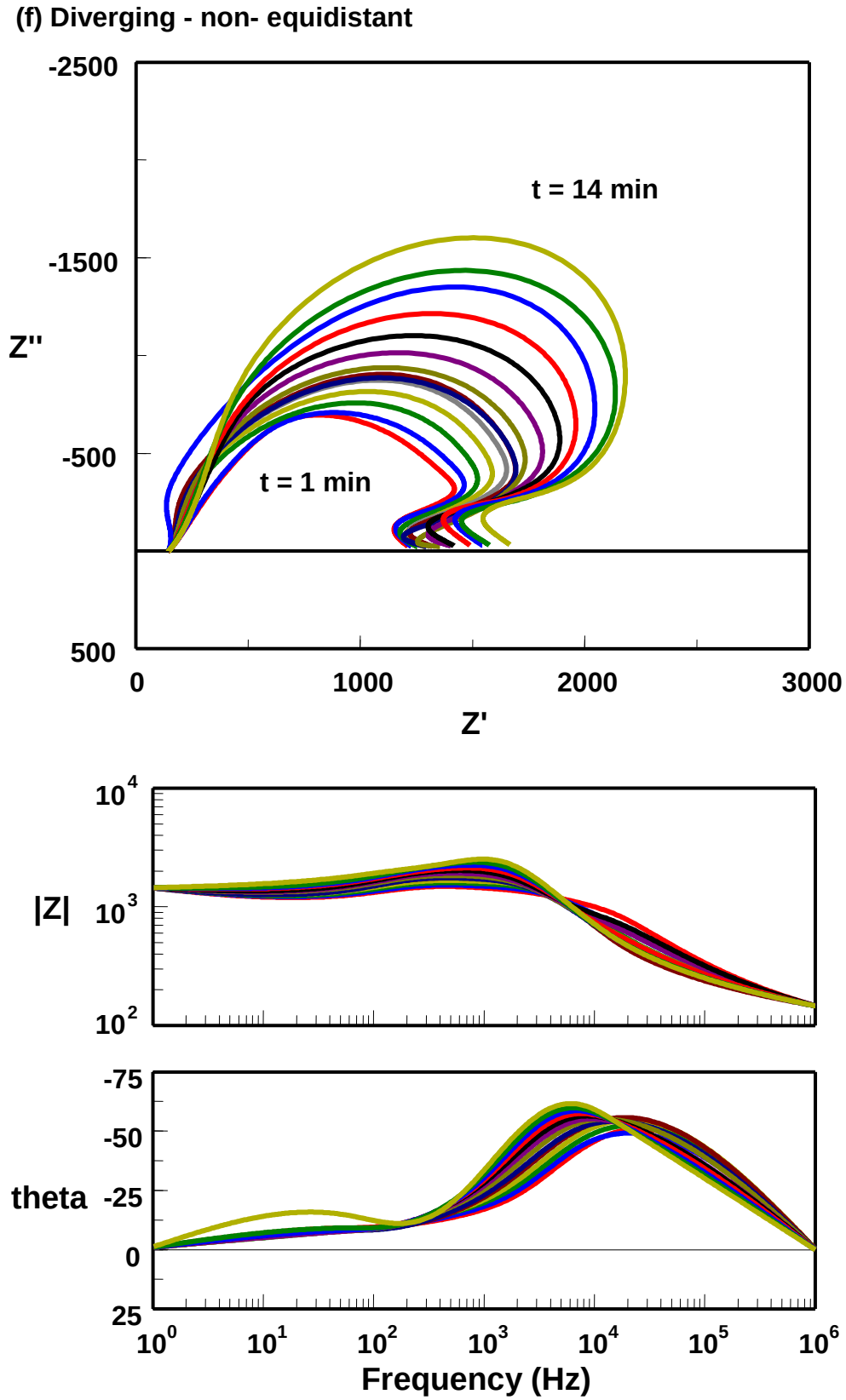

Fig. 4.9. Complex and Bode plots of in-situ impedance spectra of PEO process carried out under different electric fields and electrode layouts: (f) diverging (non-equidistant)

continuing

(g) Time at 1 min

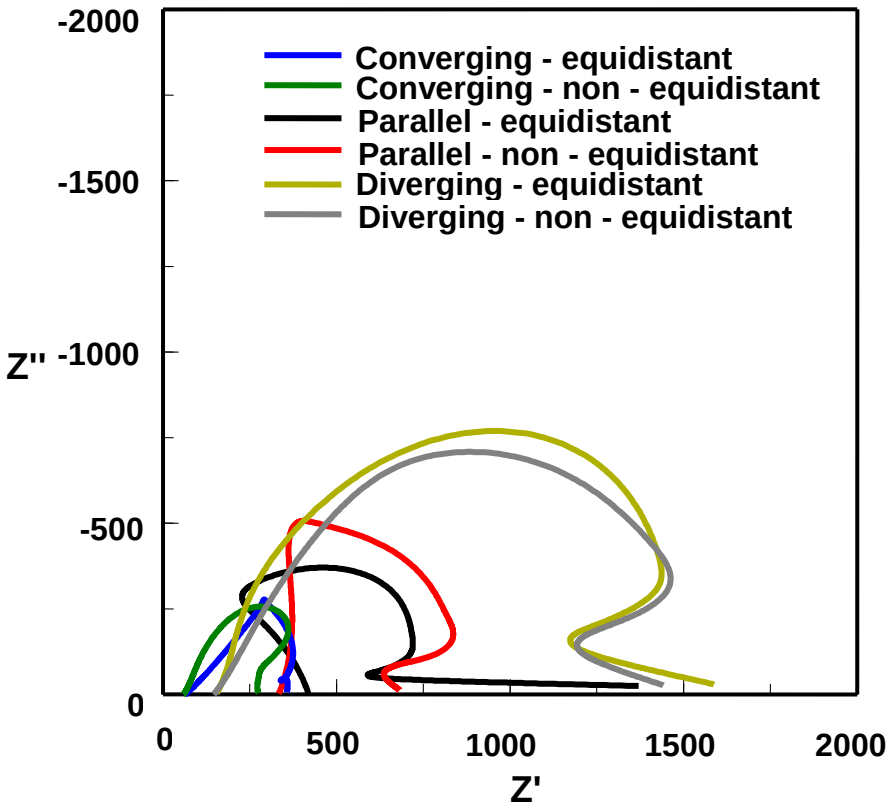

(h) Time at 14 min

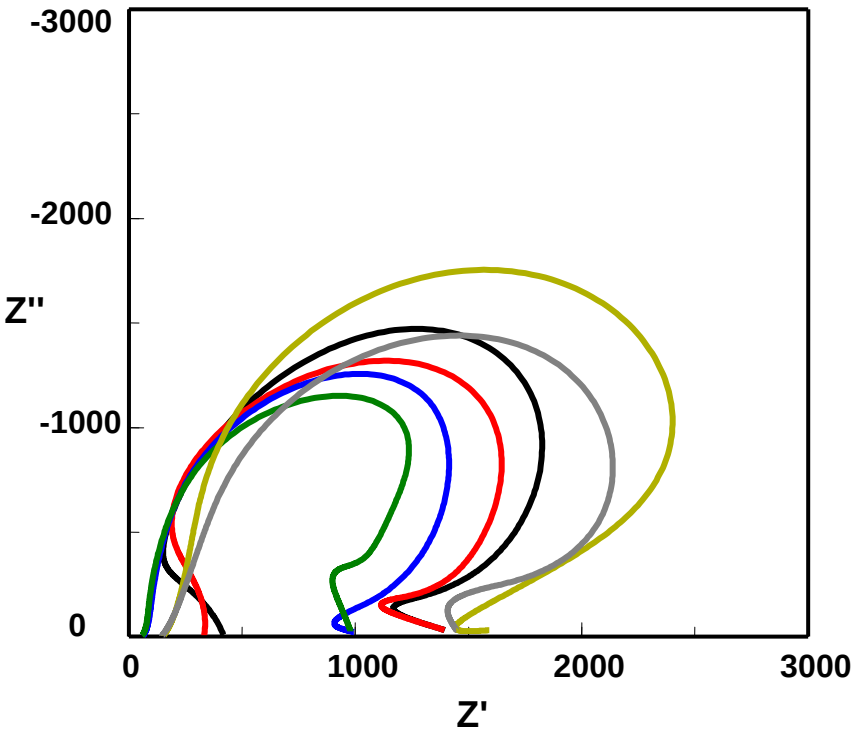

Fig. 4.9. Complex and Bode plots of in-situ impedance spectra of PEO process carried out under different electric fields and electrode layouts: (g) time = 1 min, (h) time = 14min

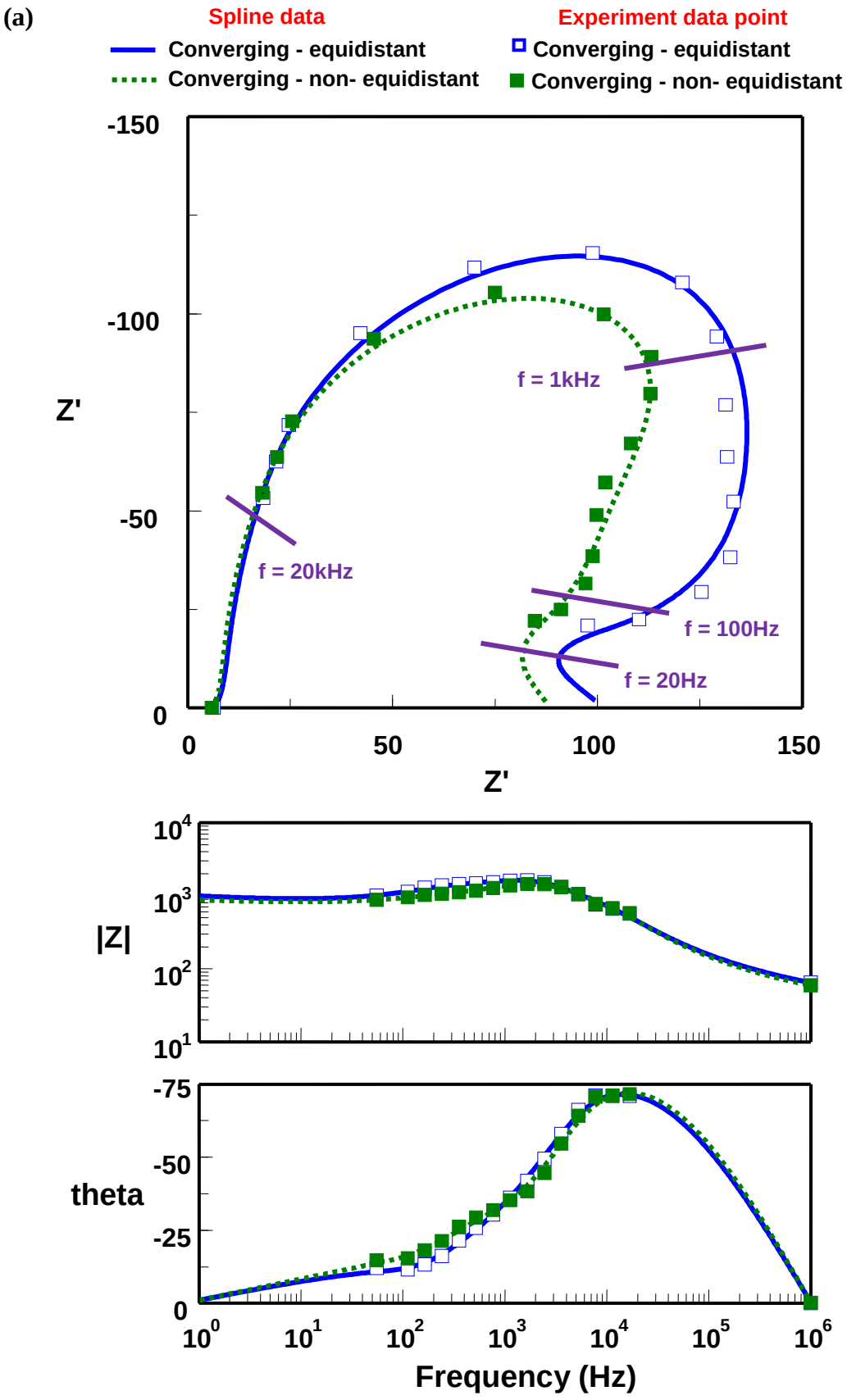

Fig. 4.10. (beginning) Complex and Bode plots of PEO process of Al samples in conditions of electric field types and cell geometries at time = 12 min. (a) converging type

to be continued

continuing

(b)

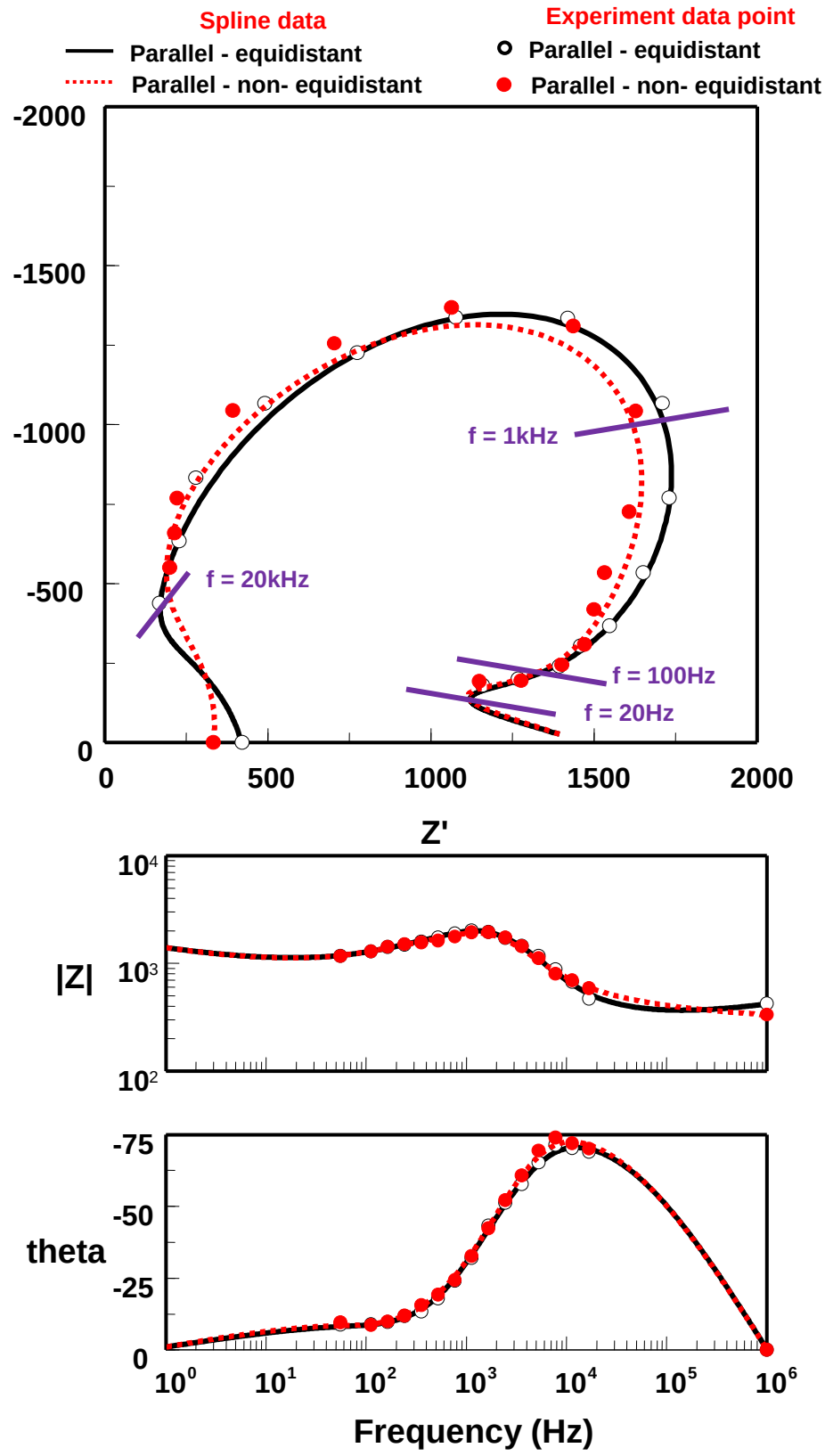

Fig. 4.10. Complex and Bode plots of PEO process of Al samples in conditions of electric field types and cell geometries at time = 12 min. (b) parallel type

to be continued

continuing

(c)

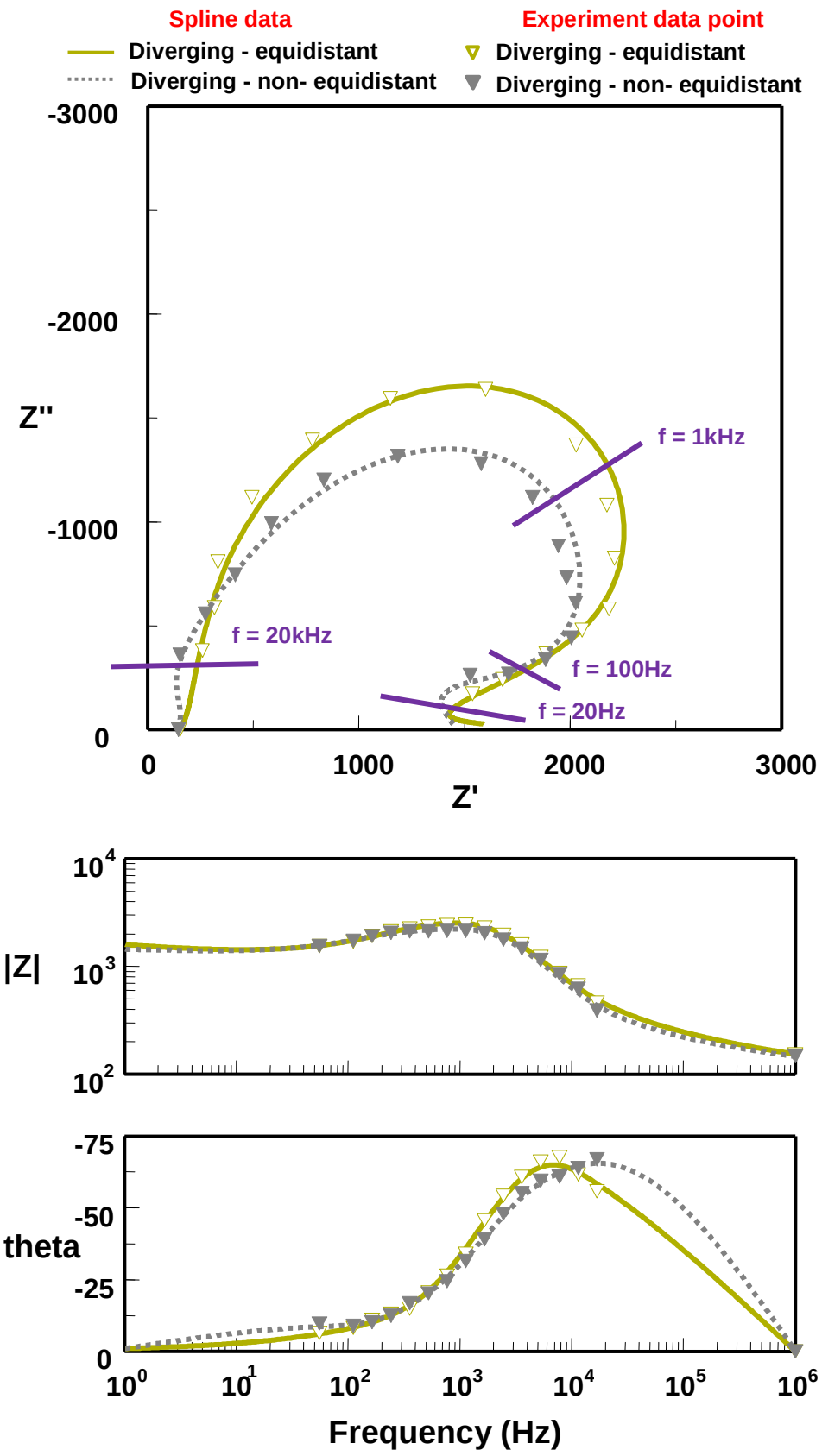

Fig. 4.10. Complex and Bode plots of PEO process of Al samples in conditions of electric field types and cell geometries at time = 12 min. (c) diverging type.

4.8 Developments of equivalent circuits and meaning of corresponding elements

As mentioned in the previous section, the shape of impedance spectra in the high frequency region of 10^3~10^4 Hz has indicated a common behaviour for thick coatings [4]. It can be fitted by a single RC loop equivalent circuit as shown in figure 4.11~4.13. The impedance spectra in both electrode layouts of converging electric field, were fitted in this frequency range by the loop with capacitance (C), although it was better represented by a constant phase element (CPE) in parallel-equidistant and the diverging-nonequidistant conditions.

From references [149,150,69] the high frequency behaviour usually presents the charge transfer through the interface. Therefore, the capacitance/CPE in this loop can reflect a non-uniform coating morphology. The investigation of correlations of the capacitance/CPE in this loop with corresponding coating morphologies by using fractal analysis is discussed in Chapter 6. In section 6.2, the results of the comparison of capacitance between theoretical and ISIS fitting value of CPE-T indicate that this loop does not represent the status of the whole PEO coating but only relate to the barrier layer at the bottom of discharge channel. Therefore, the thickness of the barrier layer (d_{BL}) can be evaluated from the capacitance/CPE-T values.

In the common corrosion study on coatings, CPE can be associated with several phenomena or processes (section 3.1.3). In the high frequency region, a CPE is commonly used instead of capacitance in the outer porous layer of an oxide coating, because of the porosity, roughness [151], reflected in elliptic shape of the arcs. Moreover, porosity in the outer porous layer of PEO coatings has been indicated by Curran et al. [48], to be affected by oxygen evolution during the PEO process. As pointed out in the previous paragraph, the RC loop here is only indicative of the barrier layer and the explanation associated with porosity does not appear to be applicable to our case, wherein the CPE element may be caused by non-uniform distribution of current on the barrier layer due to the coating morphologies. Another reason of using CPE here is due to the effects of other phenomena occurring during the PEO process. Studied from the Complex and Bode plots, the behaviour of the impedance spectra in the frequency range of 10^3~10^4 Hz seems to be a combination of several phenomena, especially in the medium frequency region. This behaviour indicates that the

time constants corresponding to the relevant process are very close, which will be discussed in the following section.

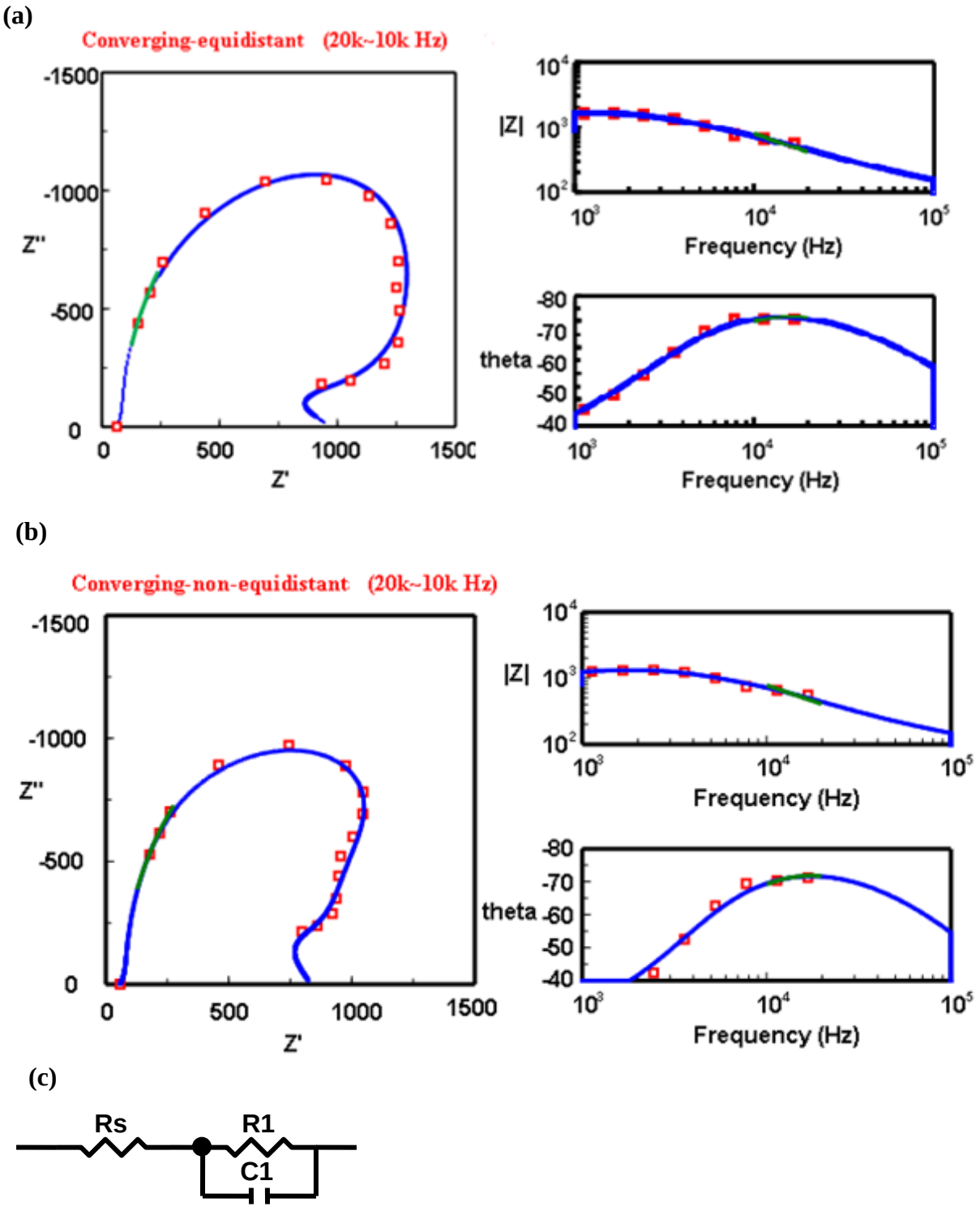

Fig. 4.11. Fitting results (green line) of the high frequency end of impedance spectrum range (20k to 10k Hz) for the PEO process operated under different electric field and electrode layout conditions (a) converging-equidistant, (b) converging-non-equidistant, and (c) single loop of equivalent circuit.

(a)

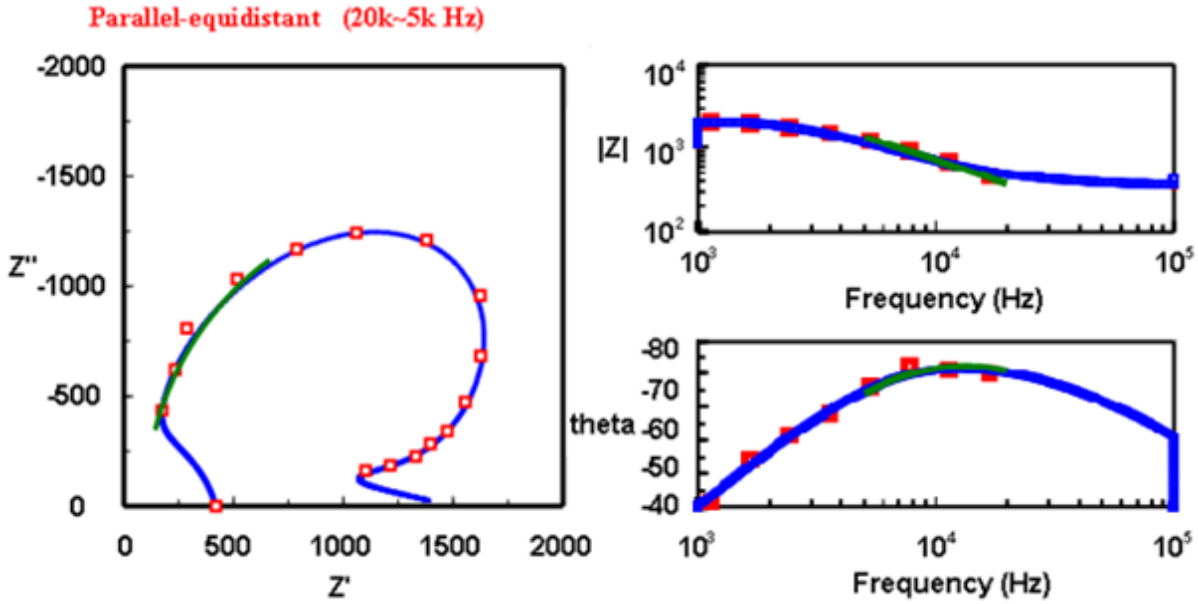

(b)

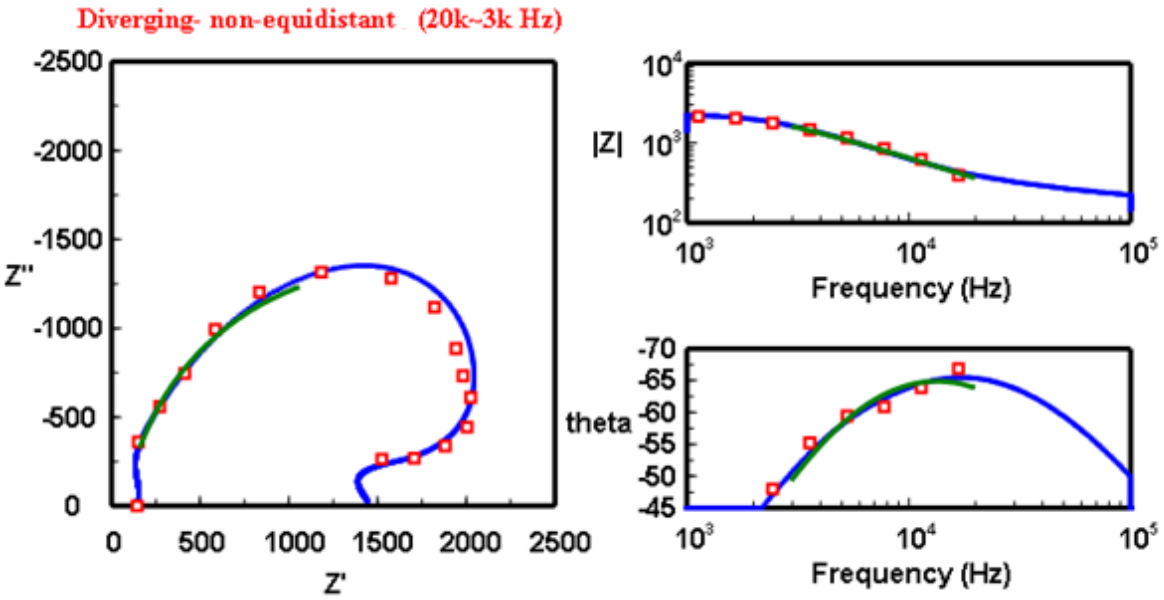

(c)

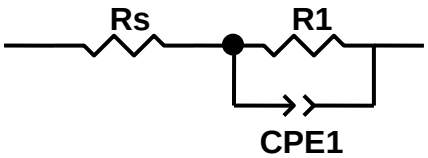

Fig. 4.12. Fitting results (green line) of the high frequency end of impedance spectrum range (20k to 3~5k Hz) for the PEO process operated under different electric field and electrode layout conditions (a) parallel-equidistant, (b) diverging-non-equidistant, and (c) single loop of equivalent circuit.

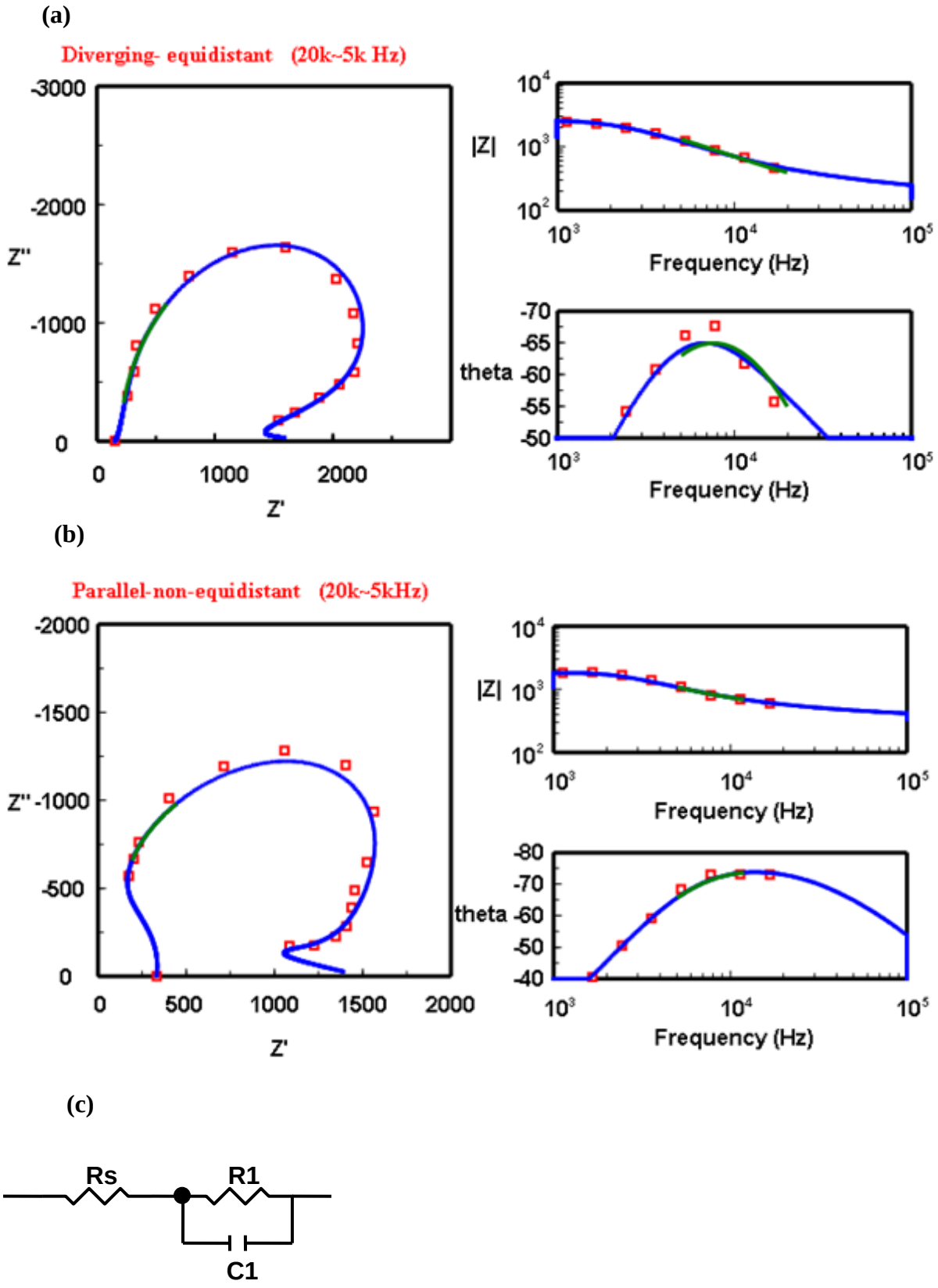

Fig. 4.13. Fitting results (green line) of the high frequency end of impedance spectrum range (20k to 3~5k Hz) for the PEO process operated under different electric field and electrode layout conditions (a) diverging-equidistant, (b) parallel-non-equidistant, and (c) single loop of equivalent circuit.

Continuing from the high frequency region, the impedance spectra are now fitted until 1kHz. Here, three different equivalent circuits were used for the three electric field types. In both the converging electric field conditions, the fitting results in this frequency range (20k ~ 1k Hz) is shown in figure 4.14, and three loops equivalent circuits were used as shown in figure 4.14 (c). The second loop of R4 and C4 is connected in parallel with the first one. Due to the fact that both the values of R4 and C4 are positive, the second loop is deduced to reflect a layer of the PEO coatings. However, from the figure 4.6 (a) and (b), the PEO coatings produced under converging electric field with both types of electrode layout have three obvious layers such as upper dense layer, inner fine porous layer and the barrier layer at the bottom of the discharge channel. Except for the barrier layer, which has been verified to be represented by the first loop, there is still not enough information to confirm which coating layer is indicated by the second loop. The physical meaning of this loop will be discussed later. The third loop of this equivalent circuit is constituted by a negative resistance (R2) and a positive capacitance (C2). From references [152-154], R2 and C2 probably indicate the resistance of charge transfer through the plasma sheath in the bubbles and the corresponding capacitance, respectively. The source of the charge in here is from the ionisation of H_2O to H_2O^+, yielding a primary electron e^-.

In the conditions of parallel electric field, the fitting results in a three loops equivalent circuit (figure 4.15 (c)). The behaviour of R1-C1/CPE1 and R2-C2 loops is similar to that in the converging electric field conditions. However, the loop of R4 and C4 is not applicable in the parallel electric field conditions and has been replaced by a loop constituted by another negative resistance (R3) with positive capacitance (C3). From reference [152], this loop is probably indicative of the thermal effect occurring in the discharge channel of the PEO coating. When the gas in the channel is heated during the discharge, it causes the temperature and the pressure to rise. Increase in pressure would cause the voltage across the discharge to increase, lagging behind current change. The corresponding capacitive effect may be caused by the above phenomenon, and the capacitance element in this loop would cause a relative slower time constant [152] for the loop used to fit the impedance spectra in the lower frequency region.

Results of the impedance spectra fitting for the diverging electric field conditions are shown in figure 4.16 (c). The two loops constituted by R1-C1/CPE1 and R2-C2, are the same as the loops in the model developed for the converging and parallel electric field conditions. From the above fitting results, due to the R4-C4 loop which occurred only in the converging electric field conditions, the effect of the fine porous layer of the PEO coating is verified, because only this layer is observed in the coating produced under converging electric field conditions (figure 4.6). The time constants corresponding to this loop are discussed later.

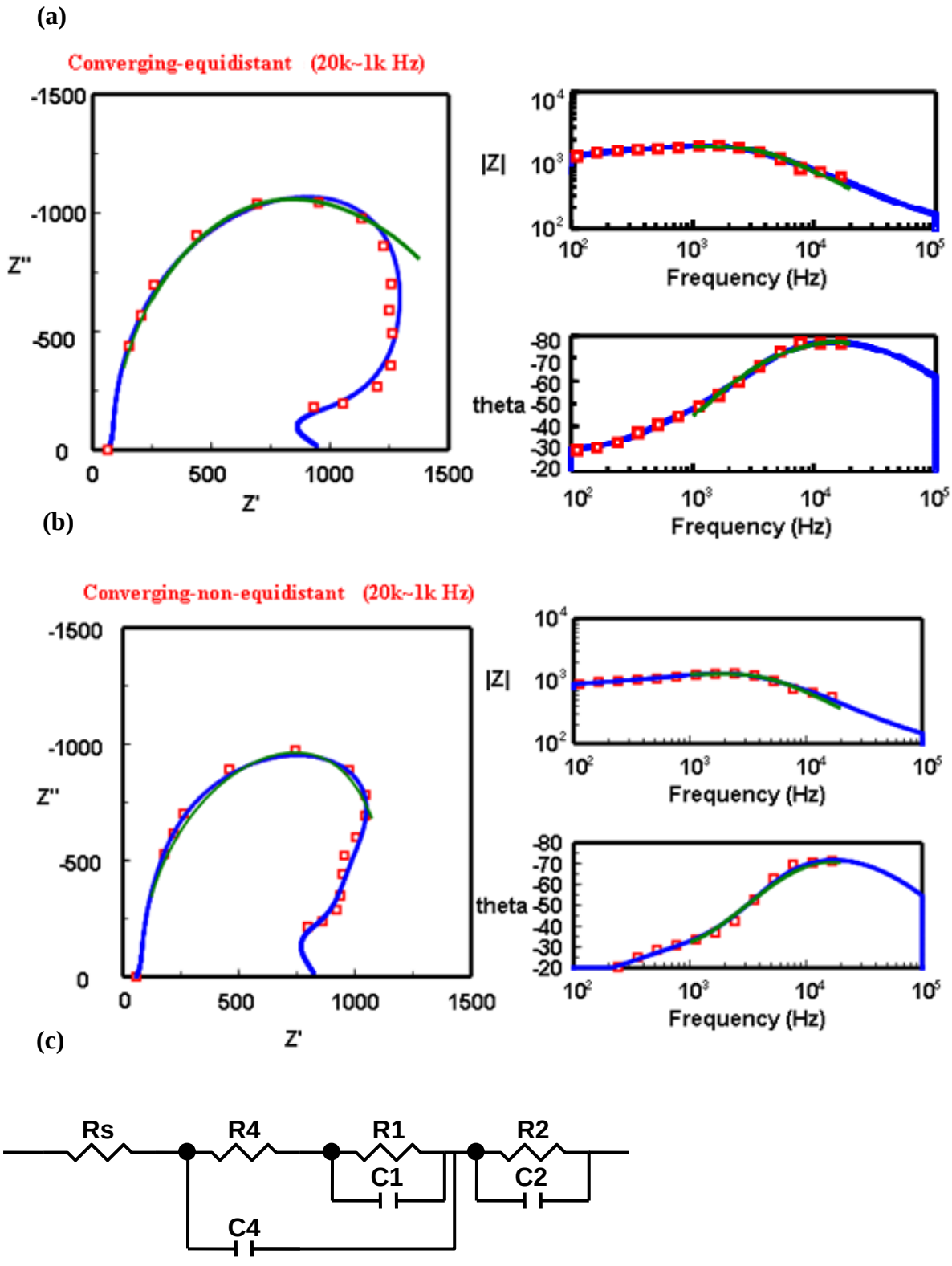

Fig. 4.14. Fitting results (green line) in the medium frequency range (20k to 1k Hz) for the impedance spectra of the PEO process operated under (a) converging-equidistant, (b) converging-non-equidistant electric field conditions, and (c) three loop equivalent circuit containing with one negative resistance loop R2.

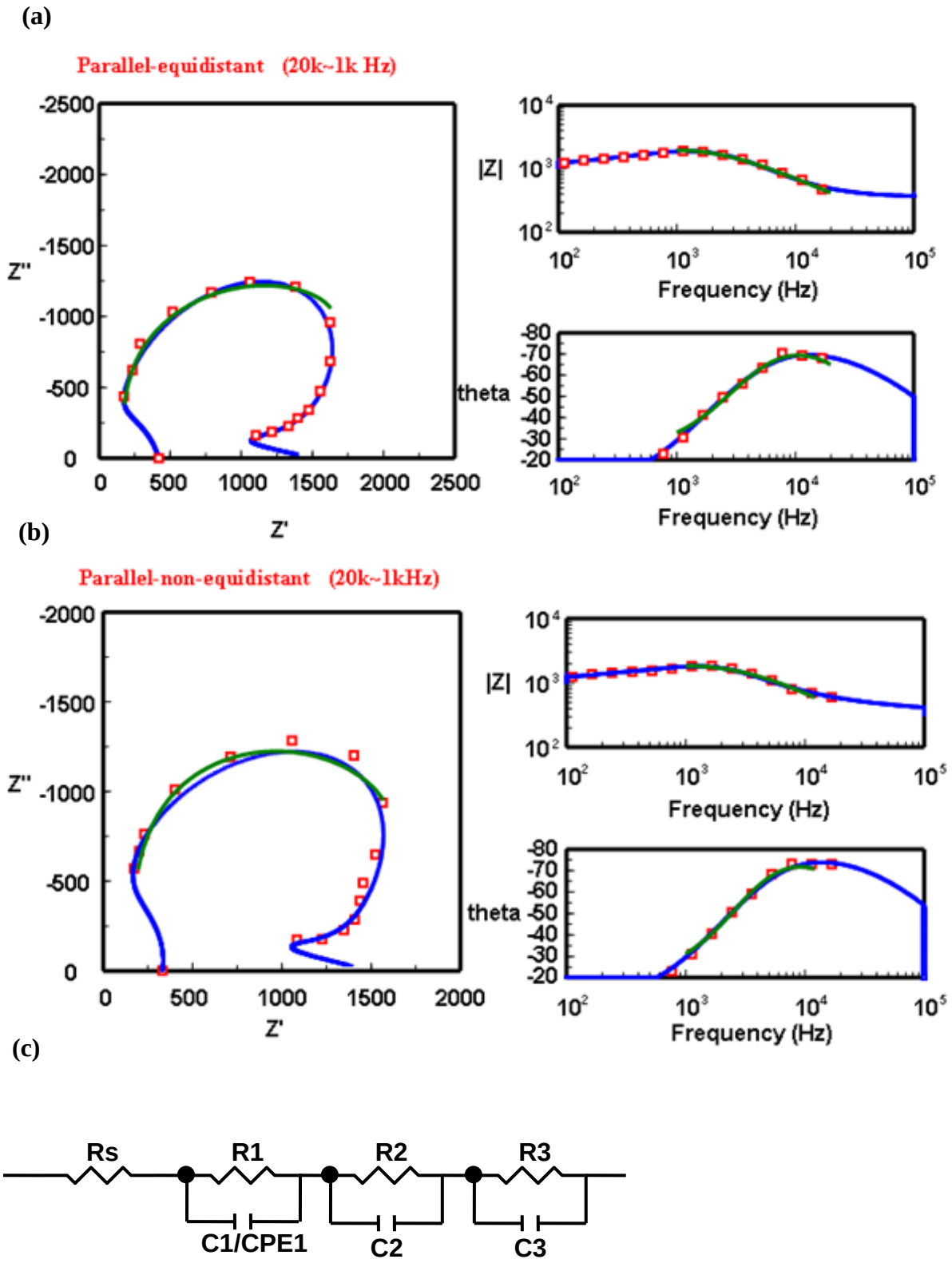

Fig. 4.15. Fitting results (green line) in the medium frequency range (20k to 1k Hz) for the impedance spectra of the PEO process operated under (a) parallel-equidistant, (b) parallel-non-equidistant electric field conditions, and (c) three loop equivalent circuit containing with two negative resistance loops R2, R3.

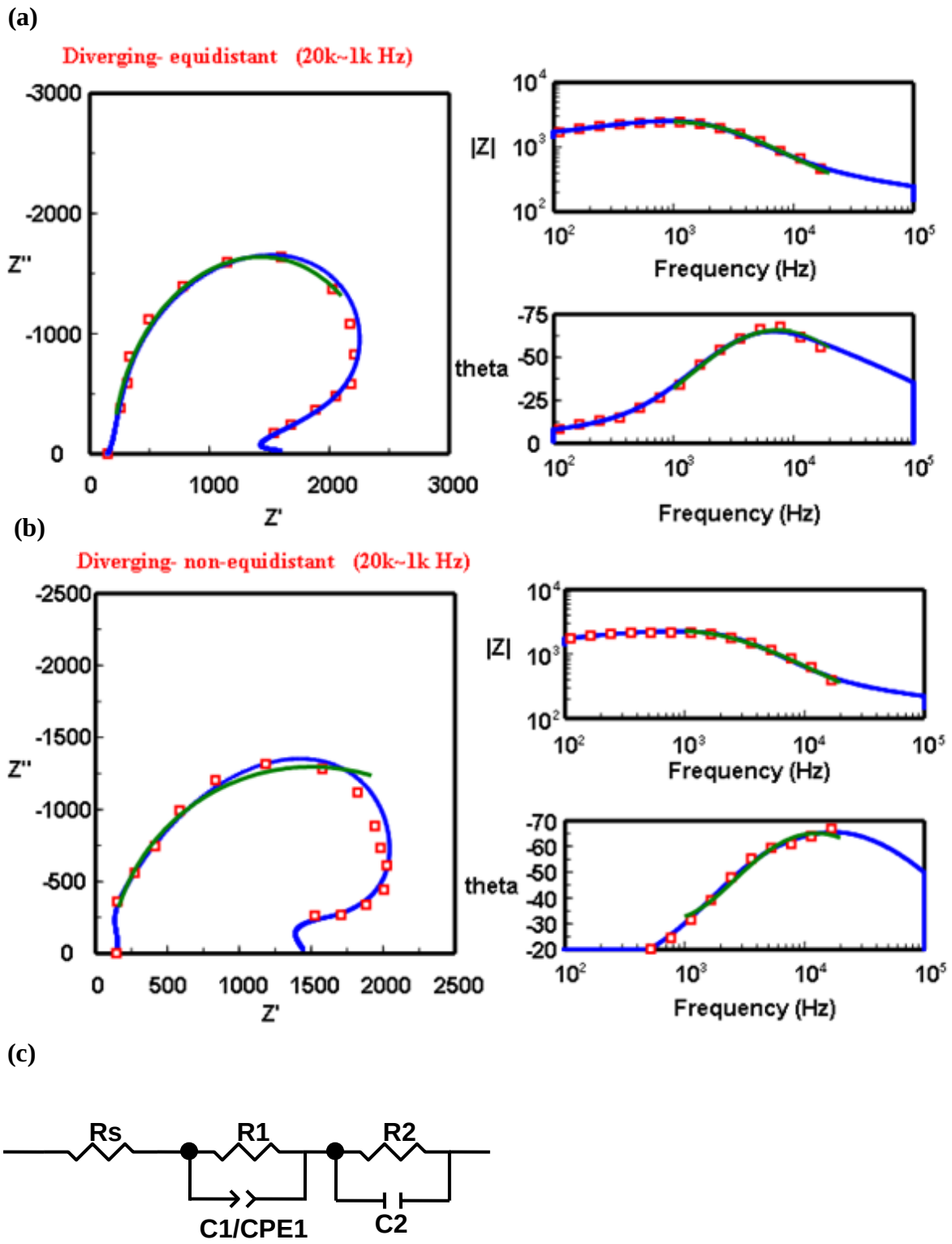

Fig. 4.16. Fitting results (green line) in the medium frequency range (20k to 1k Hz) for the impedance spectra of the PEO process operated under (a) diverging-equidistant, (b) diverging-non-equidistant electric field conditions, and (c) two loop equivalent circuit containing with one negative resistance loops R2.

The fitting results in the low frequency region (1k to 200 Hz) of the impedance spectra for the converging, parallel and diverging electric field conditions are shown in figure 4.17~ 4.19, respectively. In the all electric field conditions, R2-C2 loop is also used following the fitting exercise in the medium frequency range. Moreover, in this frequency range, the R3-C3 loop is used in both the converging and diverging electric field conditions. This indicates that the time constant of this loop (probably thermal effects) is relatively shorter under the parallel electric field than other conditions. According to the inference of the physical meaning of R2-C2 (charger transfer through the plasma sheath in the gaseous phase of the discharge) and R3-C3 (thermal effects) loops, the relevance between these two loops should be in parallel connection because of the duration and the shifting of the discharge events (section 7.4).

A new loop is used in the parallel and diverging electric field conditions of the low frequency range, which is constituted by a RL loop with R4' and L1 as shown in figure 4.18 (c) and 4.19 (c). This loop is likely to indicate phenomena taking place in the positive column of the plasma channel [152-156] with the large pores of the PEO coatings. Noteworthy, this loop is not applicable in the both converging electric field conditions. From current transients analysis in figure 4.5, indicate that the current density still decreases at the end of the PEO treatment under the both converging electric field conditions; a reasonable explanation for the absence of the RL loop is that the dense inner coating region is still growing at the last stage of the PEO treatment providing conductive paths for the current flow. Therefore, it appears that the formation of the positive column is hindered, and the corresponding behaviour in the impedance spectra is feebly, which means that the plasma for the converging electric field conditions can be seen as a hollow cathode discharge. Compared with the converging electric field conditions, the current transient for the parallel and diverging conditions become stable at around 1.5 minutes after the beginning of the PEO treatment, which means that the thickness of the PEO coatings observed in corresponding cross-sectional SEM images is already fully formed at this time point.

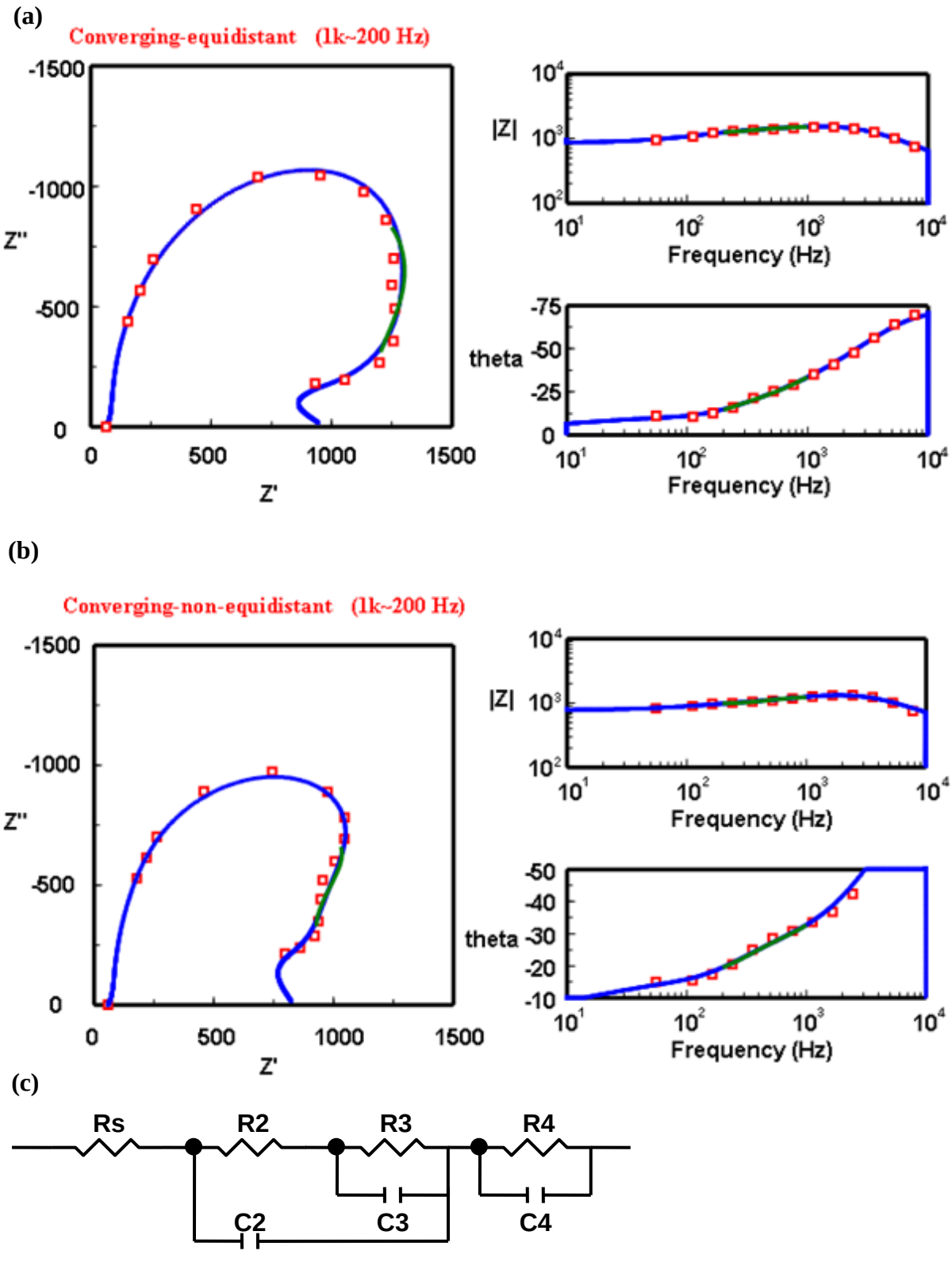

Fig. 4.17. Fitting results (green line) in the low frequency range (1k to 200 Hz) for the impedance spectra of the PEO process operated under (a) converging-equidistant, (b) converging-non-equidistant electric field conditions, and (c) three loop equivalent circuit containing with two negative resistances R_3 and R_4.

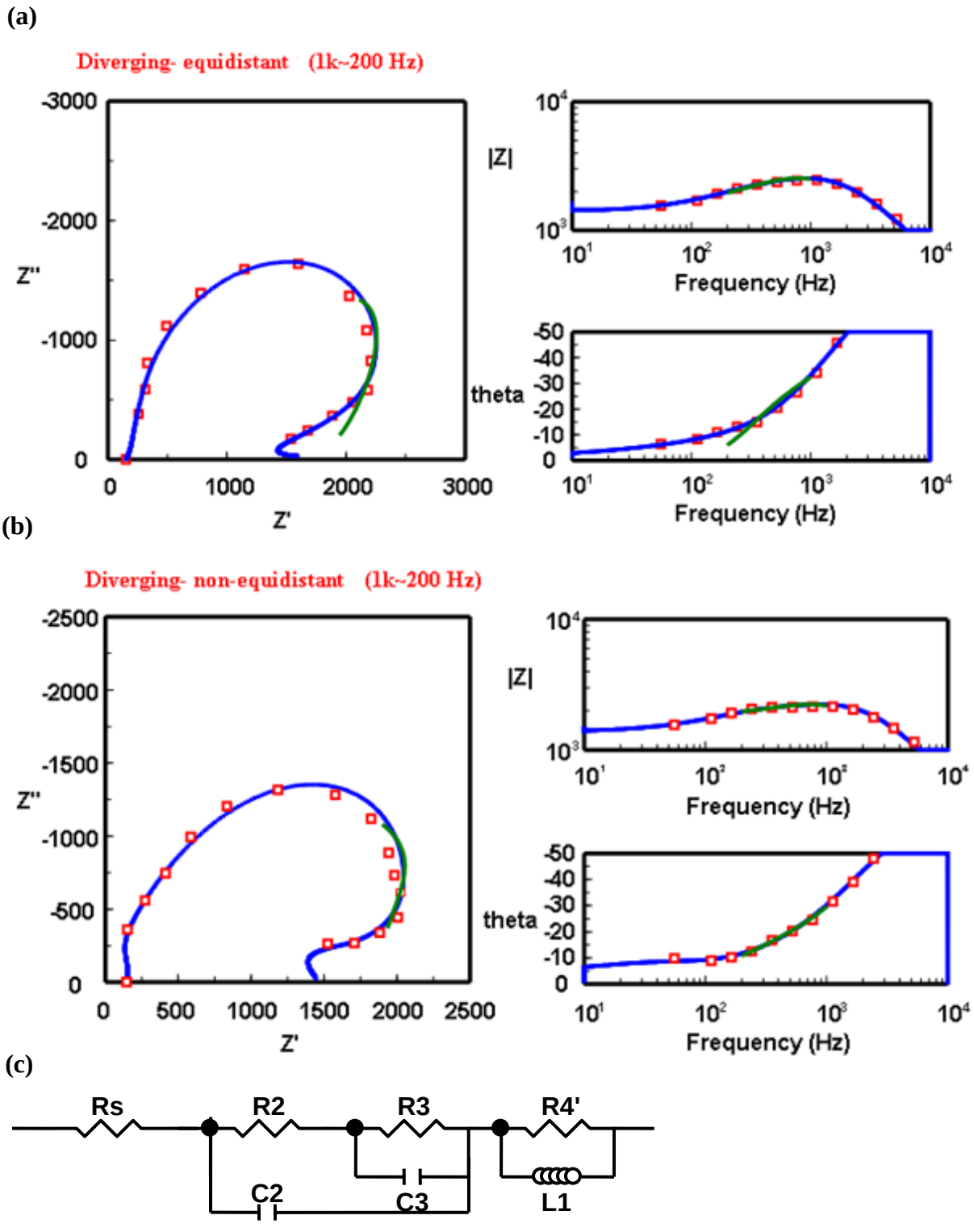

Fig. 4.18. Fitting results (green line) in the low frequency range (1k to 200 Hz) for the impedance spectra of the PEO process operated under (a) diverging-equidistant, (b) diverging-non-equidistant electric field conditions, and (c) three loop equivalent circuit involve two negative resistance loops and a LC loop.

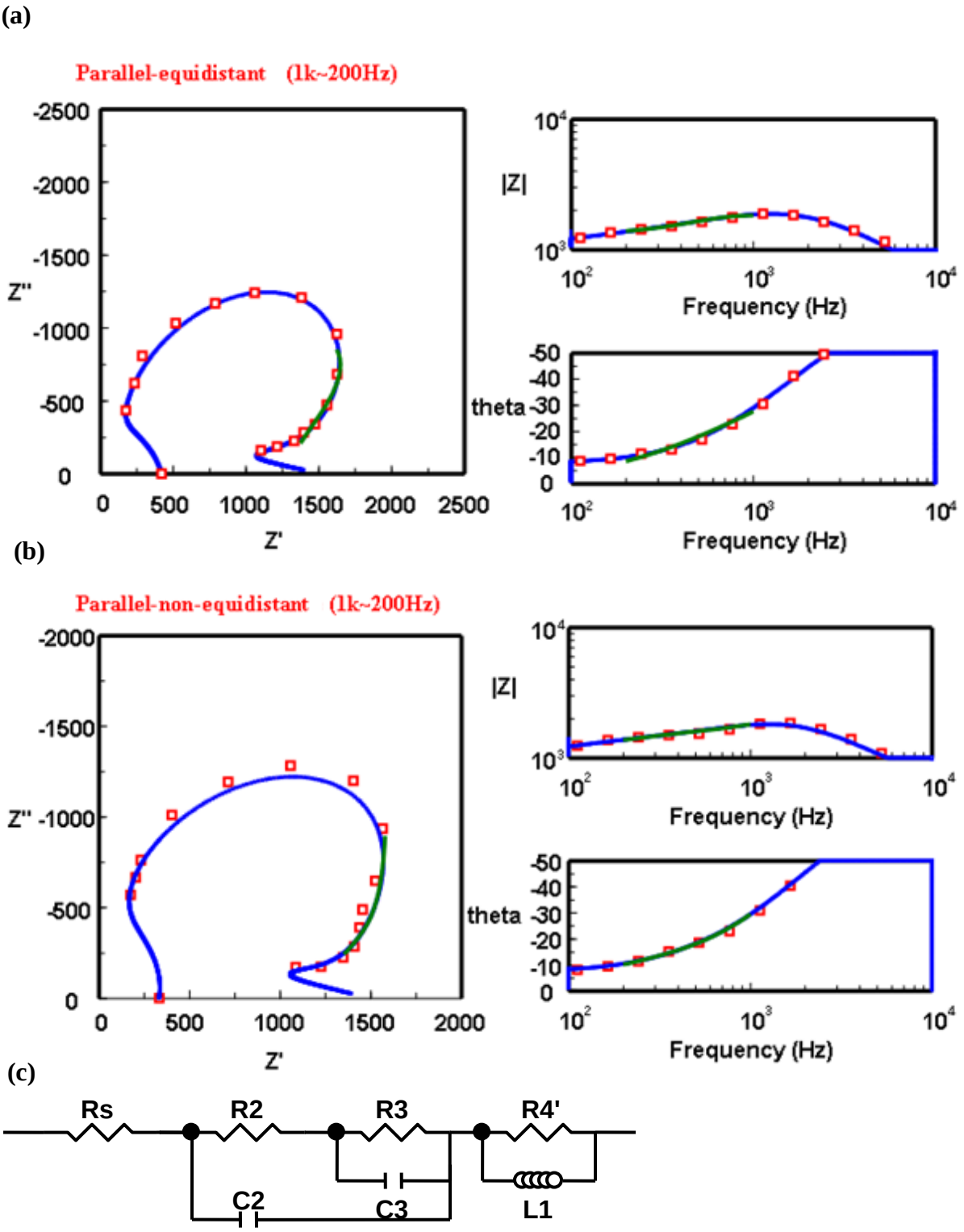

Fig. 4.19. Fitting results (green line) in the low frequency range (1k to 200 Hz) for the impedance spectra of the PEO process operated under (a) parallel-equidistant, (b) parallel-non-equidistant electric field conditions, and (c) three loop equivalent circuit involve two negative resistance loops and a LC loop.

Combining the above frequency ranges, three complete equivalent circuits were developed to fit the three groups of impedance spectra of PEO processes carried out under different electric field conditions and electrode layouts in the whole frequency range of 20 to 20k Hz, as shown in figure 4.17 ~ 4.19. The value of each element and the corresponding time constants of each loop at 12 min of the PEO treatment started are shown in Table 4.6. Here the time constants (τ) of RC and RL loops were calculated by the following equations:

$$\tau = R \times C \text{ or } (R \times CPE\text{-}T)^{(1/CPE\text{-}P)} \quad (4.1)$$

$$\tau = L / R \quad (4.2)$$

In Table 4.6, each time constant was calculated from the four loops equivalent circuits under the all electric field conditions and the electrode layouts. Beside the loops of R4-C4 and R4'-L1, the time constants from the same loop are in the similar time scale for the all treatment conditions. In the R1-C1 loops, the time constants (τ1) are all about 10μs. However, it is around 2~3 times longer under parallel and diverging conditions rather compared to the converging one. The difference in τ1 between the same condition of electric field but different electrode layouts are rare. The values of capacitance in this loop, are all of order 10^{-8} F/cm^2 for different PEO treatment conditions. According to Irvine, et al [157], a possible object developing capacitance in the range of 10^{-9} to 10^{-7} is a surface layer, which is consistent with the interpretation of the barrier layer in PEO coatings.

The time constants of R2-C2 loop (τ2) are about 10μs for the both converging electric field conditions, but they are only around 1μs under parallel and diverging conditions. Compared with τ2, the τ3 from the R3-C3 loop is 10 times longer in converging conditions and about 30~100 times longer in parallel and diverging conditions. In contrast with the R1-C1 loop, in the R2-C2/R3-C3 loops, both R2 and R3 are negative. Moreover, due to the equation 4.1, the values of τ2 and τ3 are both negative. The negative value of the time constant reflects a local unstable behaviour of the system/phenomenon. Therefore, in the previous section, these two loops were associated with the phenomena in the plasma sheath and the thermal effects in the gaseous phase, that could generate local instabilities in discharge events, causing their intermittent nature. Since τ3 being about 10~100 times longer than that of τ2, the thermal effect should be related to the R3-C3 loop, because of the duration of a discharge events is much shorter (section 7.4).

The R4-C4 loops for the converging electric field conditions, have similar element values and time constants (τ4) with R1-C1 loop, and due to the R4 being a positive and C4 being of the order of 10^{-8} F/cm^2, its interpretation may be similar to that R4-C4 loop for the coating layer. Because of the R4 values are larger than R1 and the C4 is smaller than C1, the coating layer here should be thicker than the barrier layer represented by R1-C1 loop.

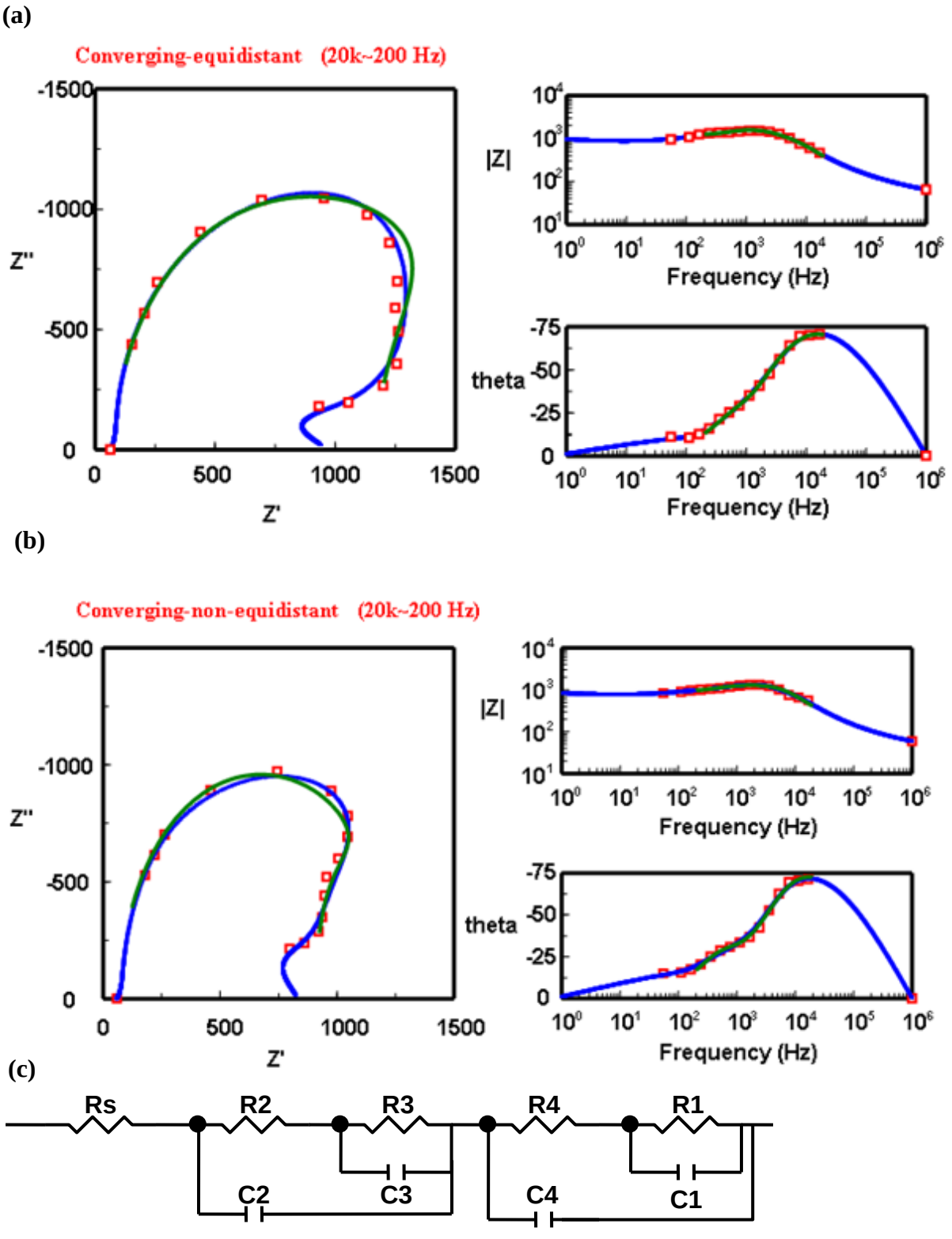

Fig. 4.20 Fitting results of in-situ IS record data in (a) converging-equidistant, (b) converging-non-equidistant, and (c) the setup equivalent circuit.

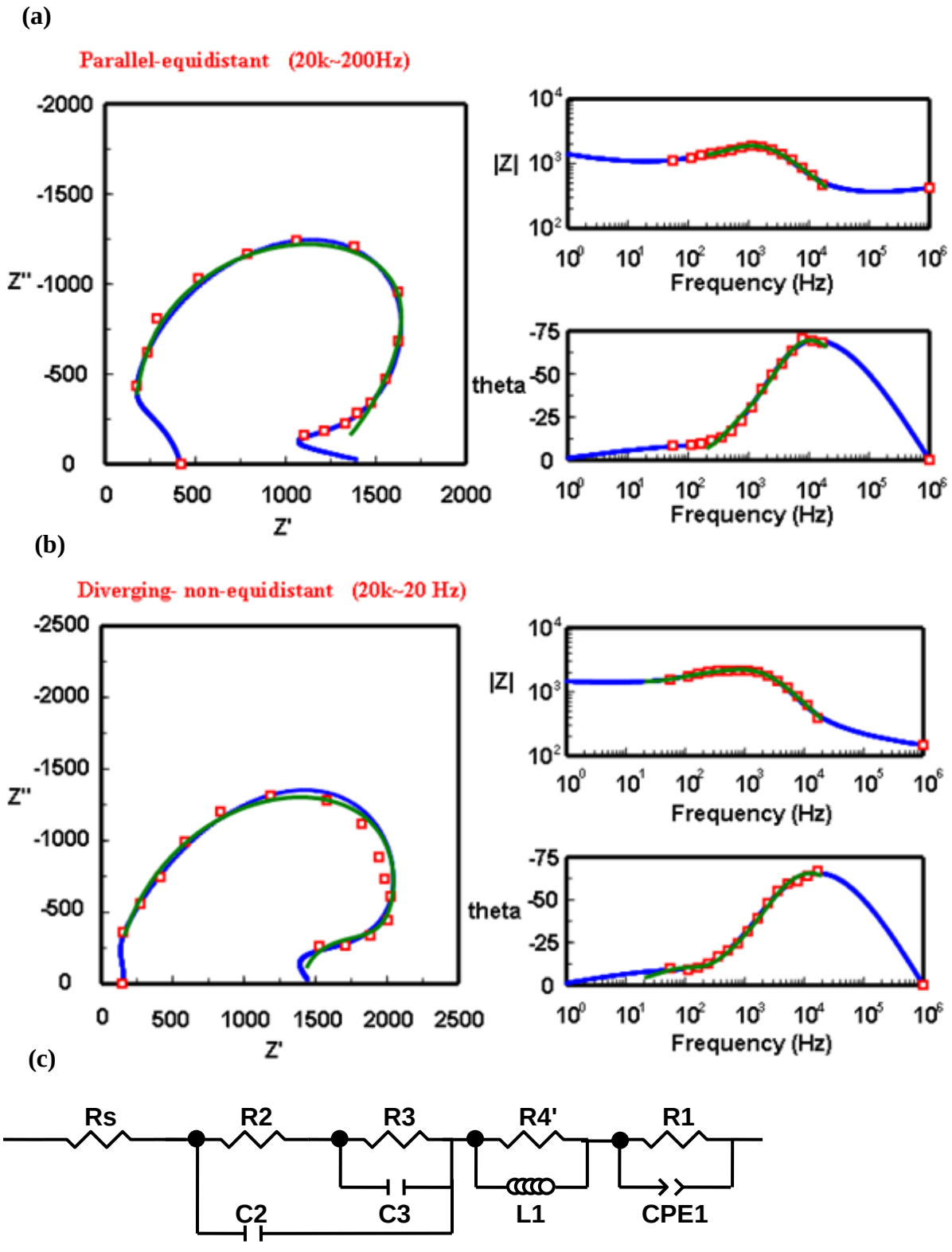

Fig. 4.21 Fitting results of in-situ IS record data in (a) parallel-equidistant, (b) diverging-non-equidistant, and (c) the setup equivalent circuit.

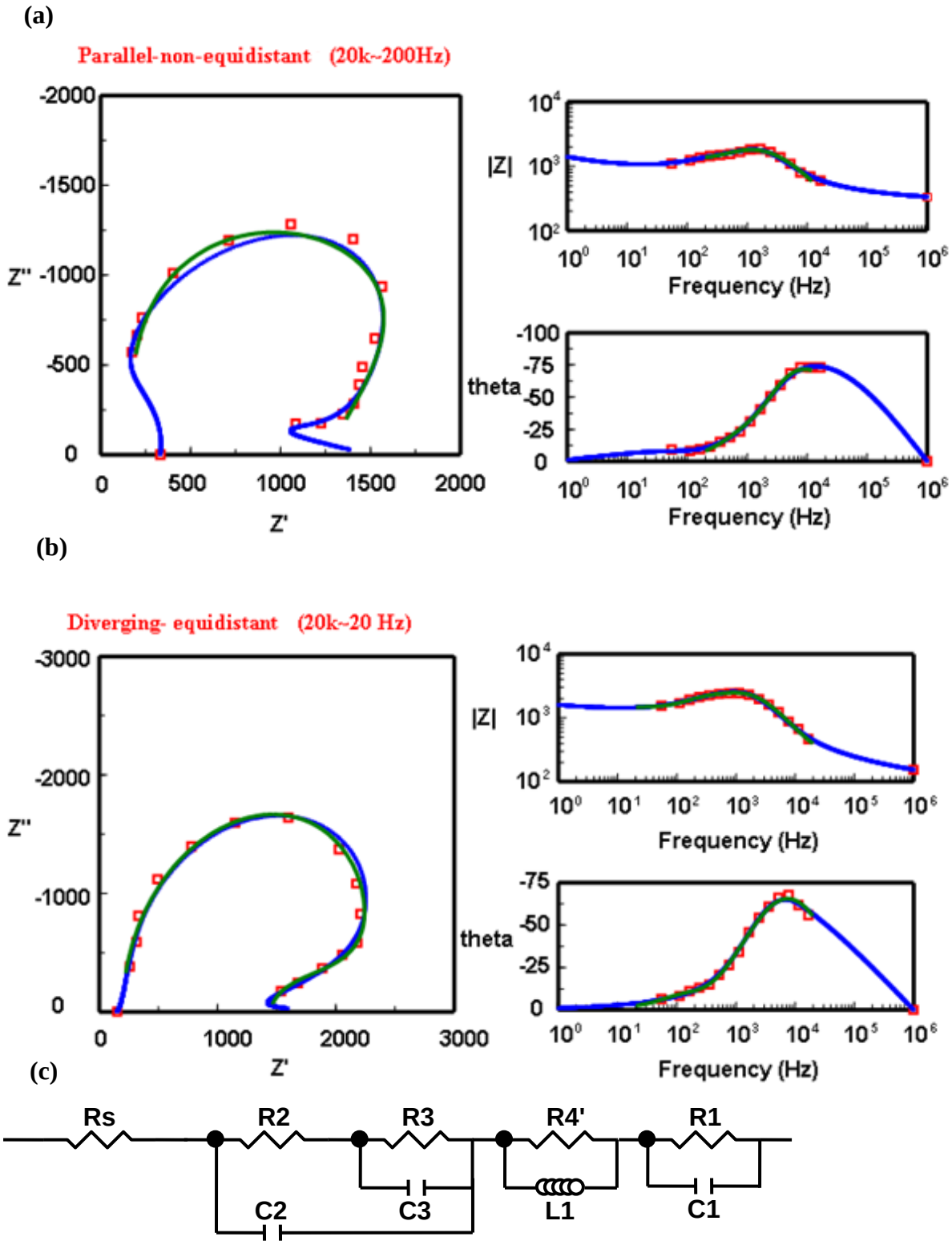

Fig. 4.22. Fitting results of in-situ IS record data in (a) parallel-non-equidistant, (b) diverging-equidistant, and (c) the setup equivalent circuit.

Table 4.6. Results of ISIS spectra fitting and the time constants evaluation of individual loop at 12min of PEO treatments.

Electric field-electrode layout	R_1 ($k\Omega \cdot cm^2$)	C_1 ($\mu F \cdot cm^{-2}$) /CPE_1-T ($S \cdot s^n$)	CPE_1-P	R_2 ($k\Omega \cdot cm^2$)	C_2 ($\mu F \cdot cm^{-2}$)	R_3 ($k\Omega \cdot cm^2$)	C_3 ($\mu F \cdot cm^{-2}$)	R_4/R_4' ($k\Omega \cdot cm^2$)	C_4 ($\mu F \cdot cm^{-2}$)	L_1 (H)	Chi-squared $\times 10^{-3}$	Weighted Sum of Squares
	τ_1 (μs)			τ_2 (μs)		τ_3 (μs)		$\tau_4/\tau_{4'}$ (μs)				
Converging-equidistant	0.88	0.038	-	-0.27	0.091	-0.57	0.44	1.09	0.022	-	0.5	0.205
	34			24		250		23				
Converging-Non-equidistant	0.51	0.069	-	-0.38	0.052	-0.64	0.34	1.29	0.019	-	0.8	0.24
	35					221		24				
Parallel-equidistant	2.89	0.034	0.976	-0.93	0.002	-0.64	0.26	0.88	-	0.163	0.2	0.090
	109			1.5		164		185				
Parallel-Non-equidistant	2.48	0.030	-	-0.64	0.007	-0.58	0.31	0.52	-	0.097	0.4	0.154
	72			4.5		174		186				
Diverging-equidistant	4.20	0.023	-	-0.19	0.038	-0.81	0.31	1.56	-	0.289	0.3	0.101
	88			7.2		252		186				
Diverging-Non-equidistant	2.66	0.034	0.986	-0.17	0.038	-0.60	0.35	0.24	-	0.043	0.8	0.477
	96			6.5		206		179				

The time constants (τ4') of R4'-L1 loop for both parallel and diverging electric field conditions are very similar (~180μs). As mentioned in the previous section, this loop can be attributed to the positive column. Combined with the analysis of current transients in figure 4.5, the PEO coatings are completely formed during the first 1.5 minutes, which means that the Al ejection does not occur after that. Therefore, it indicates that the positive column is formed in the pores of PEO coatings, and is actually a phenomenon, related to the glow discharge.

Evaluations of the element of the equivalent circuit and corresponding time constants are shown in figure 4.23~4.27. In the R1-C1 loop, R1 presents a linear trend with time, but the C1 decreases with time, which indicates the growth of the barrier layer. Two groups of data can be observed in both figure 4.23 (a) and (b), such as converging and other two electric field conditions. In the first group, the τ1 is relatively unstable during the first four minutes, which is consistent with sharp decrease in corresponding current transients. The values of C1 and τ1 in all electric field conditions and electrode layouts become similar at 12 min.

In the figure 4.24 and 4.25, both the R2/R3 and C2/C3 decrease slightly with time, but the value of τ2 and τ3 are seem in dependent of time. Comparison between figure 4.24 and 4.25 indicate that the effects of electric field conditions and electrode layouts are relatively weaker on R3-C3 loops. There is still no enough solid evidence to confirm the inferences of physical meaning of R2-C2 and R3-C3 loops. However, these appear to be the most reasonable explanations of the behaviour of these two loops.

The evolution of R4,C4 in figure 4.26 is consistent with the evaluation of the denser inner layer in the PEO coatings produced under the both converging electric field conditions, for which R4 increases and C4 and decreases with time. The time constants (τ4) here are relatively independent of treatment time.

Figure 4.27 shows that beside the diverging-equidistant conditions, the R4' and L1 increase slightly with time and the main trend observed for τ4' is to slightly decrease with time. These results can be explained by the polarization of the electrolyte near the barrier layer during the PEO process, but the growth of the PEO coatings stops. Therefore, the intensity of the positive column slightly increases with time.

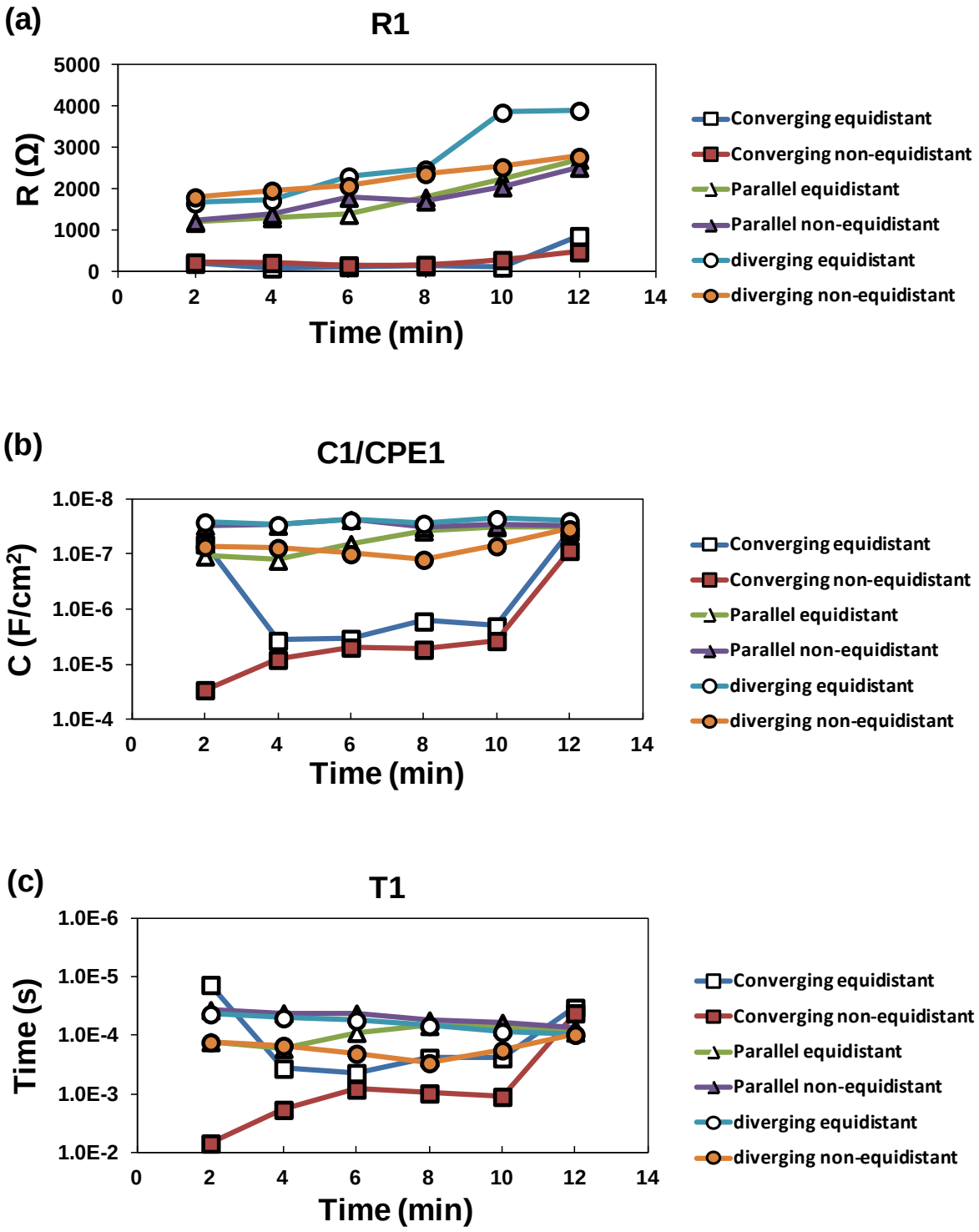

Fig. 4.23. Elements value and time constants evolution of the equivalent circuit used to fit all electric field conditions and electrode layouts: (a) R_1, (b) CPE_1-T/C_1, and (c) τ1.

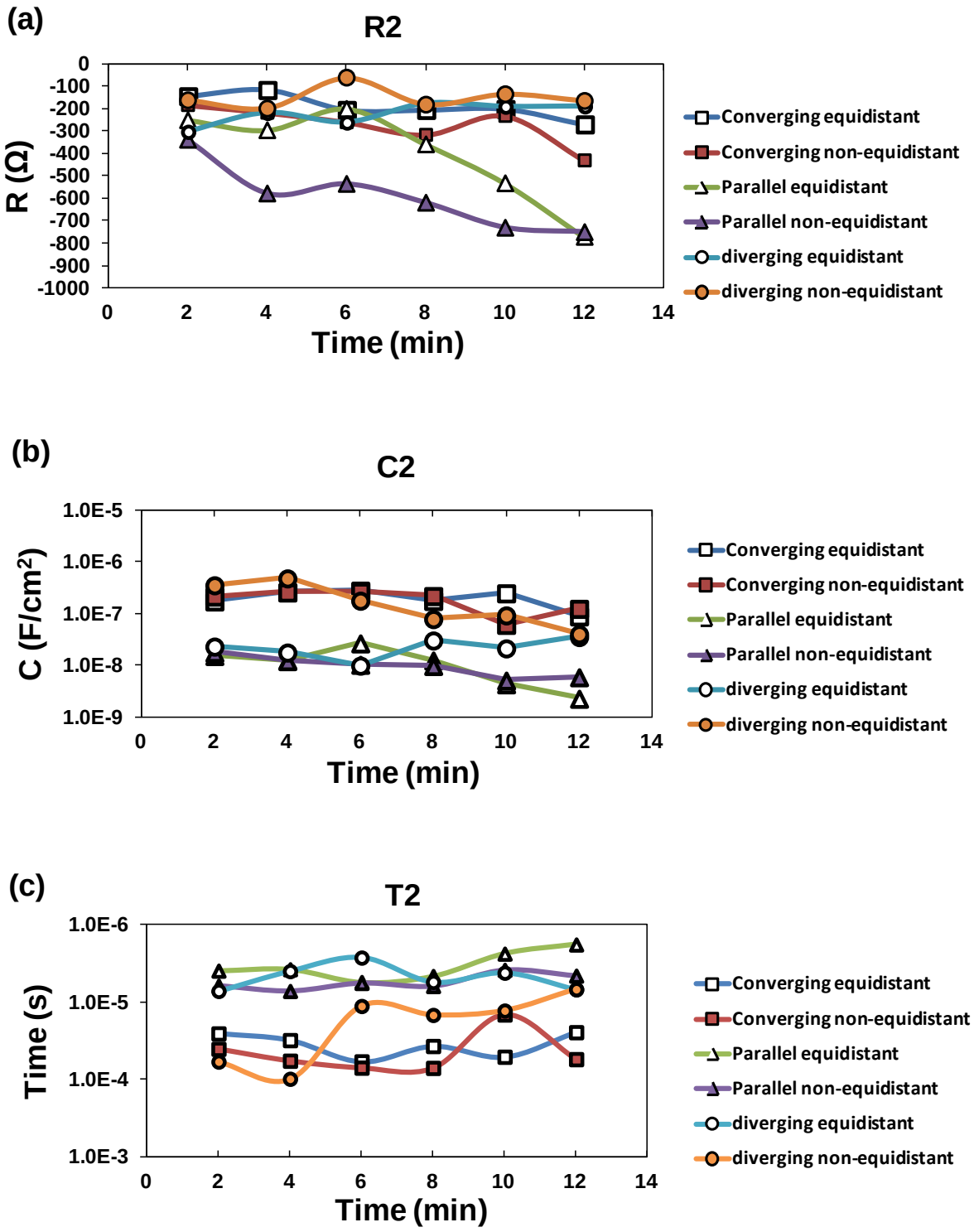

Fig. 4.24. Elements value and time constants evolution of the equivalent circuit used to fit all electric field conditions and electrode layouts: (a) R_2, (b) C_2, and (c) $\tau 2$.

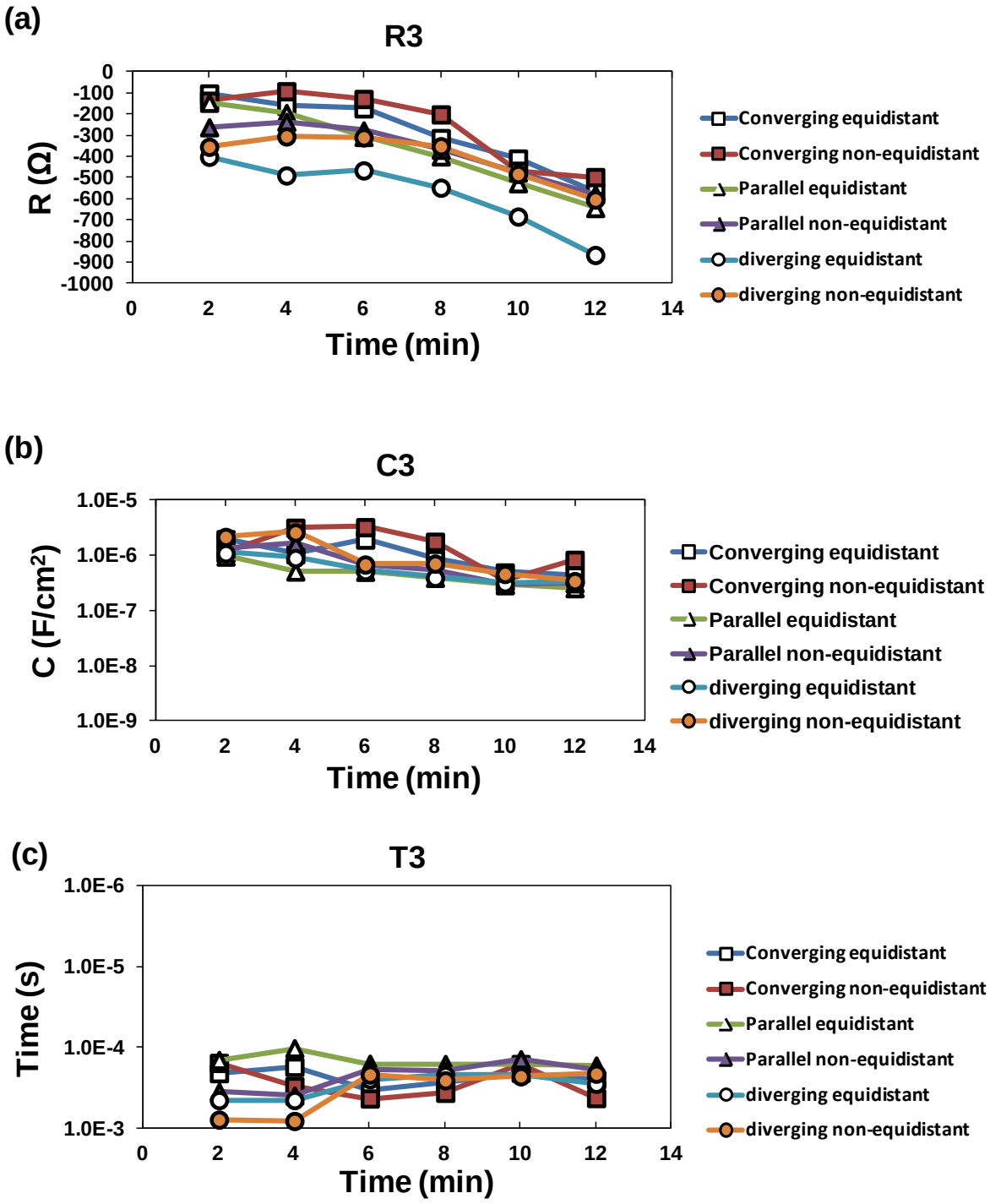

Fig. 4.25. Elements value and time constants evolution of the equivalent circuit used to fit all electric field conditions and electrode layouts: (a) R_3, (b) C_3, and (c) $\tau 3$.

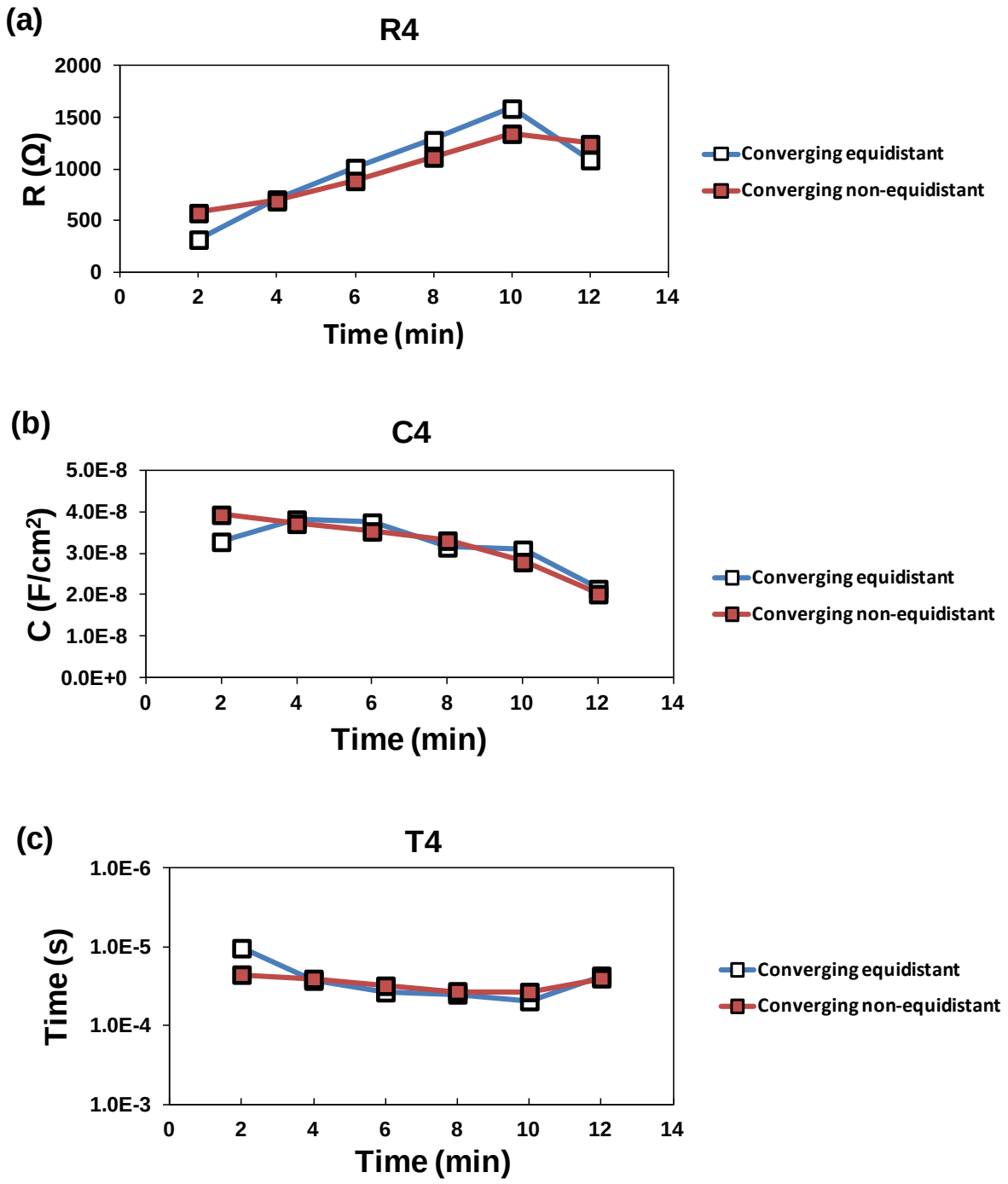

Fig. 4.26. Elements value and time constants evolution of the equivalent circuit used to fit both converging electric field conditions: (a) R_4, (b) C_4, and (c) $\tau 4$.

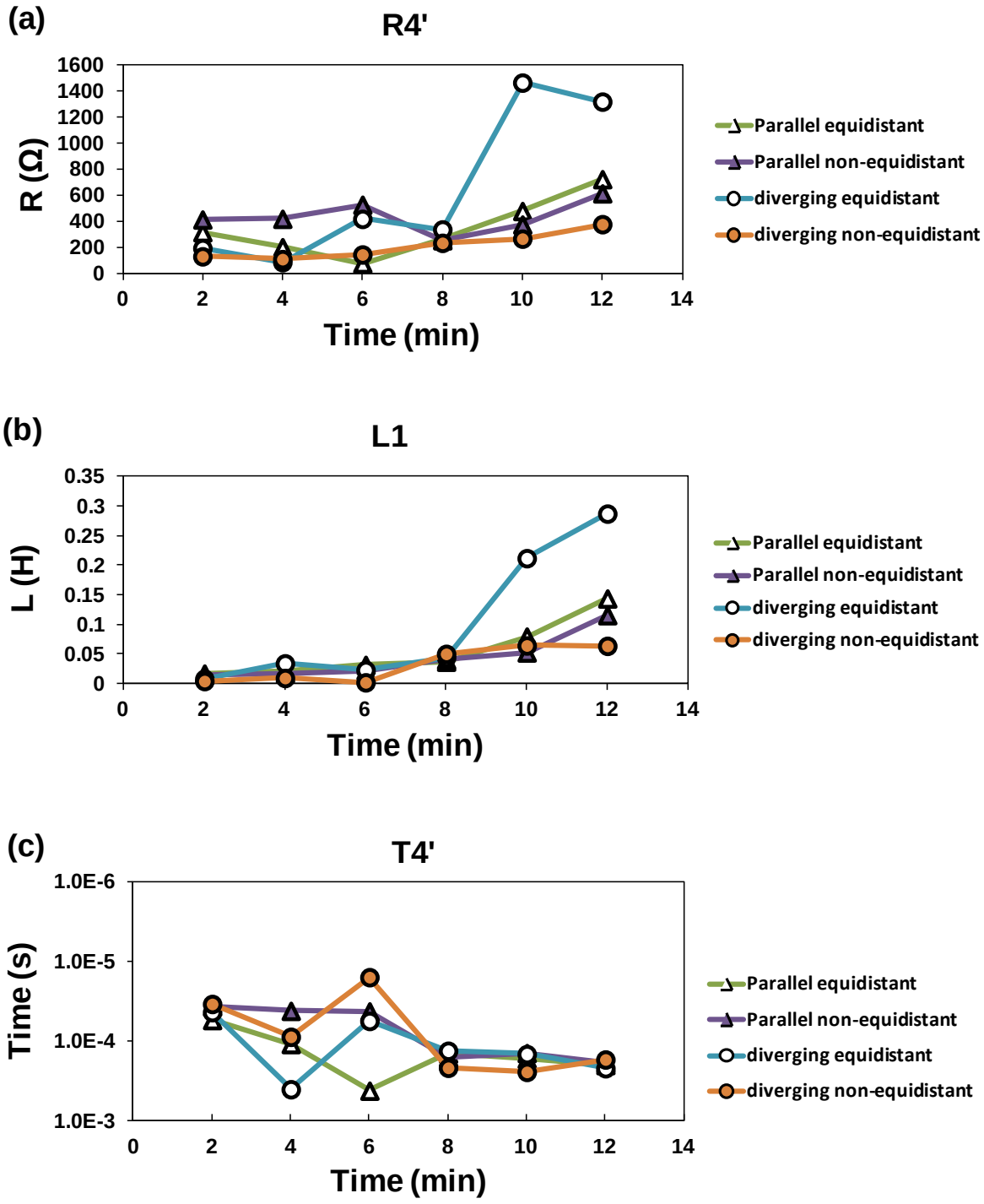

Fig. 4.27. Elements value and time constants evolution of the equivalent circuit used to fit the both electrode layouts of parallel and diverging electric field conditions: (a) R4, (b) L1, and (c) τ4'.

From the above fitting results of impedance spectra for all electric field conditions and electrode layouts and the explanation of the each loops, a possible simplified structure sketch of the PEO coating on Al together with the equivalent circuit can be developed, as shown in figure 4.28. At the moment, there is insufficient evidence to prove the interpretation of some parts of the loop. In the future, new experiments for the confirmation of those interpretations will be designed and carried out.

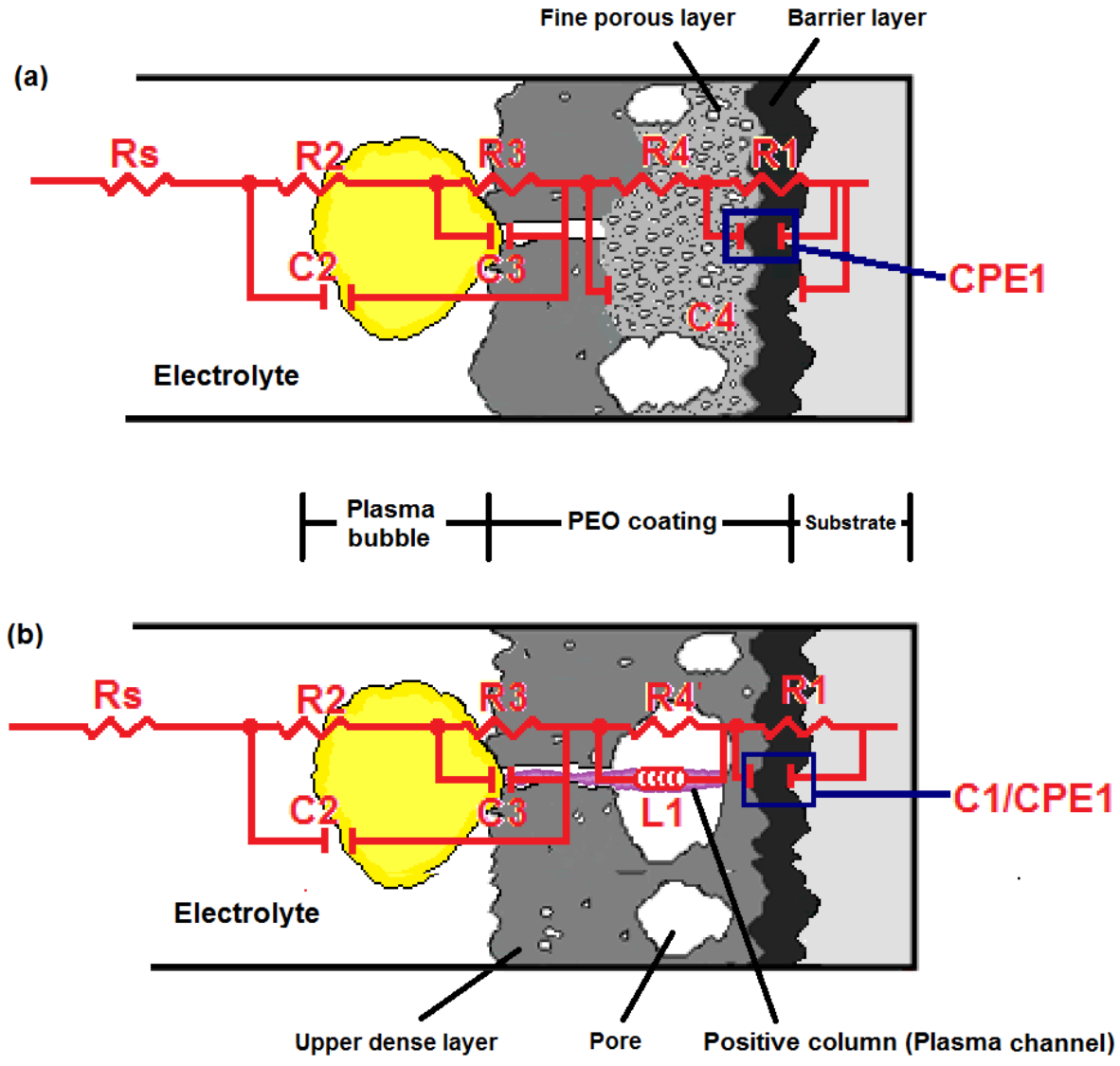

Fig. 4.28. Simplified structure sketch of PEO coating on Al with equivalent circuit used for impedance data fitting under: (a) converging (b) parallel and diverging electric field conditions.

4.9 Summary

In this part of the work, the effects of electric field distribution on the PEO process were studied using the experimental design involving converging parallel and diverging electric field conditions and equidistant/non-equidistant electrode layouts. COMSOL modelling was used to evaluate the distribution of electrolyte resistance, electric potential and total current density in the electrolyser. The difference between these three electric field distribution conditions was found significant.

During the PEO treatment, the current density evolution was recorded, and found to be relatively higher in both converging electric field conditions compared to the parallel and diverging electric field. It was also established that non-equidistant electrode layouts provide relatively high current densities compared to the equidistant geometries.

The difference in thickness of PEO coatings produced under diverging and parallel electric field conditions were found to be negligible. Similar results were also obtained for the coatings produced under equidistant and non-equidistant electrode layouts in these two electric field conditions. The difference was however significant for the coatings produced under converging electric field conditions. A substantial amount of small (0~3μm) and large (>15μm) pores is present in the coatings formed under both converging electric field conditions; coatings formed in non-equidistant geometries have slightly more pores in the range of 3~6μm. For parallel and diverging conditions the main pore size range is 0~9μm.

The boundary conditions of impedance spectra at f_0 and f_∞ in all electric field conditions and electrode layouts have been evaluated from Ohm's law and net electrolyte resistance modeled by COMSOL, respectively. The impedance values at f_∞ representing the net electrolyte resistance were found to be about 7 times and 2~3 times larger in the parallel electric field conditions than the converging and diverging conditions, respectively. In all electric field conditions, a relatively high net electrolyte resistance is developed in the equidistant electrode layout compared to the non-equidistant one.

In the ISIS results, firstly, the linearity of the PEO process operated under all electric field conditions and electrode layouts has been verified. The largest impedance spectrum was observed under the diverging electric field conditions, and the smallest one under the converging conditions. A relatively high impedance spectrum was observed in the equidistant electrode layouts in all electric field conditions. Two types of equivalent circuits were used to

fit the ISIS data under different treatment conditions, with four loops resolved in each equivalent circuit. Interpretations of each loop have been discussed, however, there is not enough solid evidence to prove the interpretations for some parts of the loops. The most reasonable explanation at the moment is the behaviour of the plasma sheath and a thermal effect. These investigations should be carried on in the future, with a different experimental design.

Chapter 5

Effects of Electrolyte Characteristics on the PEO Process of Al

5.1 Introduction and research aim

To study the mechanisms underlying the of PEO coating formation, several main factors have been considered, including current mode, composition of substrate, and electrolyte. As follows from the previous Chapter, electric field in the electrolyte exerts a strong influence on the impedance of the PEO process, kinetics of the coating formation and oxide layer morphology. The electric field affects the net electrolyte resistance, as demonstrated by COMSOL modelling. On the other hand, the electrolyte resistance depends upon solution conductivity and temperature that should also affect the impedance of the PEO process.

On account of electrochemical treatment, the characteristics of electrolyte solution are recognised as the main parameters influencing kinetics of the coating growth, its structure and properties. Characteristics of electrolyte solutions for PEO treatment such as composition, concentration, pH value and temperature are common parameters varied during experiments. For example, Xue et al. [158] investigated the PEO coating fabricated on Zr alloy in silicate electrolyte. In the report, thick ceramic coatings were fabricated by using a silicate electrolyte mainly composed of monoclinic ZrO_2 and tetragonal ZrO_2 phases. Lv et al. [159] reported the comparison of morphology, phase composition and corrosion resistance of coatings produced in electrolytes with F^- and AlO_2^- additives. Shin et al. [82] studied the effect of electrolyte on surface properties by PEO treatment on titanium substrate. In the results, the subtle difference in solution compositions, e.g. the use of potassium pyrophosphate or potassium triphosphate contributes to the surface roughness and volume fraction of metastable anatase phase in the coating. However, those studies were mainly focused on

different electrochemical reactions. In this study, physical characteristics of the electrolyte, such as conductivity and temperature, are considered to provide different bath resistances for investigation of the effects of electrolyte characteristics on coating formation and discharge phenomena during the PEO process.

5.2 Experimental set-up

To investigate the effects of electrolyte characteristics on the PEO process, the electrolyte conductivity, temperature and the thickness of the pre-formed coatings were chosen as the main variables. Therefore, 18 experiments (3 pre-formed coating thicknesses, 3 electrolyte temperatures and 2 electrolyte conductivities) were carried out to reveal effects of electrolyte characteristics on impedance of PEO process. The flowchart of experimental procedures is presented in figure 5.1. Two types of electrochemical impedance spectroscopy experiments, in-situ and ex-situ EIS were used. COMSOL was also utilised to model the distribution of the current density, electric potential, and evaluate the net resistance of the electrolyte.

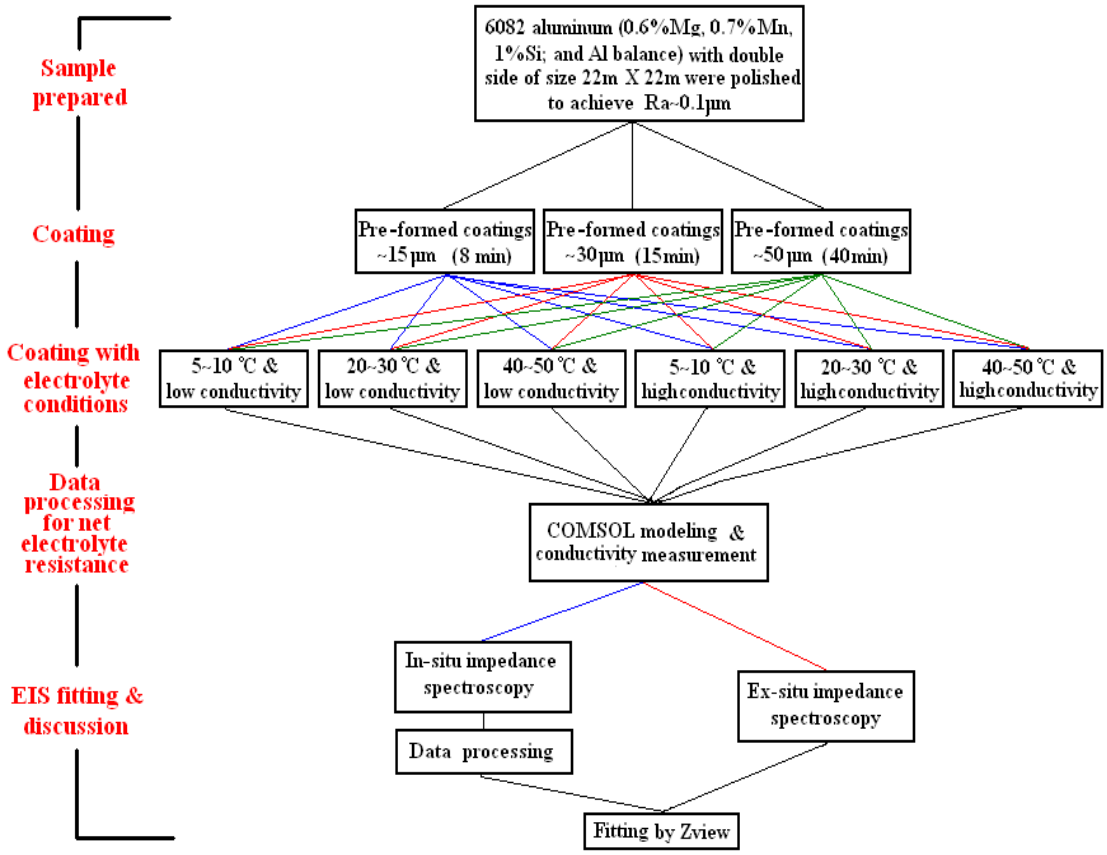

Fig. 5.1. Experimental design and procedures.

5.2.1 Sample preparation and experimental device setup

Figure 5.2. shows a schematic diagram of the experimental setup. Flat samples 22mm × 22mm × 1mm in size were preliminary polished to achieve Ra ~ 0.1μm. Two stainless steel flat sheets with an electrical insulator to select the same surface area were chosen for counter electrodes located on each side of the working electrode. Preformed coatings with thickness of 15, 30 and 50μm were produced by PEO treatment for 8, 15 and 40minutes, respectively in the medium conductivity electrolyte. The distance between the electrodes was fixed at 34mm. The surface area of the counter electrodes was selected to be twice of that of the working electrode. The PEO treatments were carried out with electrolyte cooling/heating and stirring to maintain constant processing temperature through out the experiment.

During the ISIS studies, the power supply has been setup for frequency variation with bipolar voltage control. The detailed information of the power supply and the current mode used is provided in section 3.2.2.

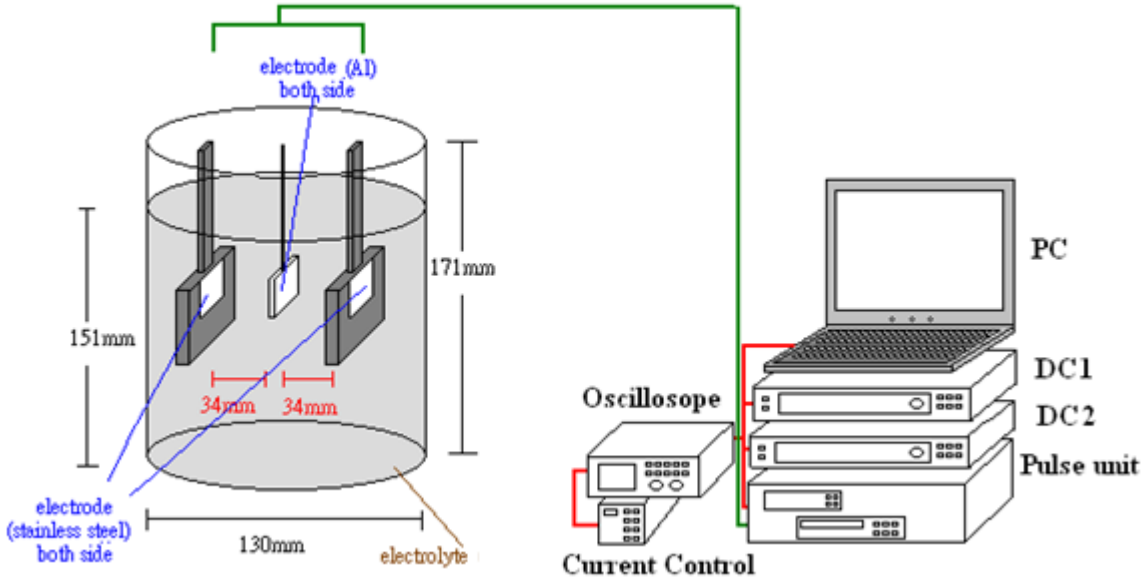

Fig. 5.2. Scheme of experimental device for PEO treatment.

5.2.2 Electrolyte characteristics and parameters control

PEO treatments are usually carried out in low-conductivity weak alkaline electrolytes

that are non-aggressive to the oxide coatings at the PEO potentials. The low conductivity is chosen because it provide high ohmic drop across the electrolyte; hence sufficient voltages can be easily achieved to initate the discharge phenomena [1].

In this work, three different electrolytes have been selected to achieve various conductivities within a pH at room temperature, by using three different phosphate salts with various concentrations of potassium hydroxide, as shown in Table 5.1. The other two solutions, of the higher and the lower conductivity (HC and LC electrolyte), were also used, operated at various temperatures 5~10, 20~30, and 40~50℃. Temperature dependencies of electrolyte conductivity and pH value were also studied. Additionally, the total electrolyte resistance under all experimental conditions was calculated by COMSOL modeling.

Table 5.1. Composition and characteristics of electrolytes at room temperature

KOH (g/l)	$Na_4P_2O_7 \cdot H_2O$ (g/l)	$Na_3PO_4 \cdot 12H_2O$ (g/l)	$NaH_2PO_4 \cdot H_2O$ (g/l)	Na_2SiO_3 (g/l)	Electrolyte Conductivity ($mS \cdot cm^{-1}$)	Electrolyte pH
1	2	-	-	2	5.39	12.09
1.2	-	1.9	-	2	7.29	12.22
0.5	-	-	0.78	2	3.02	11.41

5.2.3 In-situ and Ex-situ impedance spectroscopy response study

The impedance of the PEO process was studied using the ISIS method on the samples with the predetermined coating thickness [123,160]. Here the PEO treatment was performed by using bipolar pulse current mode. Details of the ISIS system setup is presented in section 3.2.2. The treatment time in all experimental conditions was fixed as 1.5 minutes.

The ex-situ impedance spectroscopy was performed at ambient conditions using SI 1286 Electrochemical Interface and an SI 1260 Impedance/Gain-phase Analyzer in the three-electrode cell (Figure 5.3.), and the system was computer-controlled using Z-plot software (Scribner Associates). Figure 5.4 represents the scheme of the electrochemical cell unit. Here, three electrodes are used in the cell unit: working, counter and reference electrode,

which are connected to the WE + RE2, CE and RE1 terminals, of the SI 1286 Electrochemical Interface, respectively. The surface area of the working electrode was 0.738cm^2. The same electrolytes as those used for the PEO treatments were employed, for comparative purposes.

Before the ex-situ EIS study, the evaluation of the open circuit potential (OCP) is needed. The OCP (or equilibrium potential) is defined as the potential at which no current occurred. In the OCP study, when the potential moves towards more negative values, it indicates active corrosion development; whereas the move towards more positive potentials, indicates passive film formation, or the passivation behaviour. Usually the OCP study takes a considerable amount of time after the initial immersion of the sample, which is about an hour in this work. After the steady state is established, ex-situ EIS can be carried out at this potential.

The fundamental theory of the EIS technique has been introduced in section 3.1. In this work, a sinusoidal AC perturbation of 5 mV amplitude was applied to the electrode at the OCP in a frequency range of 1 to 10^{6}Hz. After the data acquisition, Zview software was used to fit the both Complex and Bode plots with designed equivalent circuits.

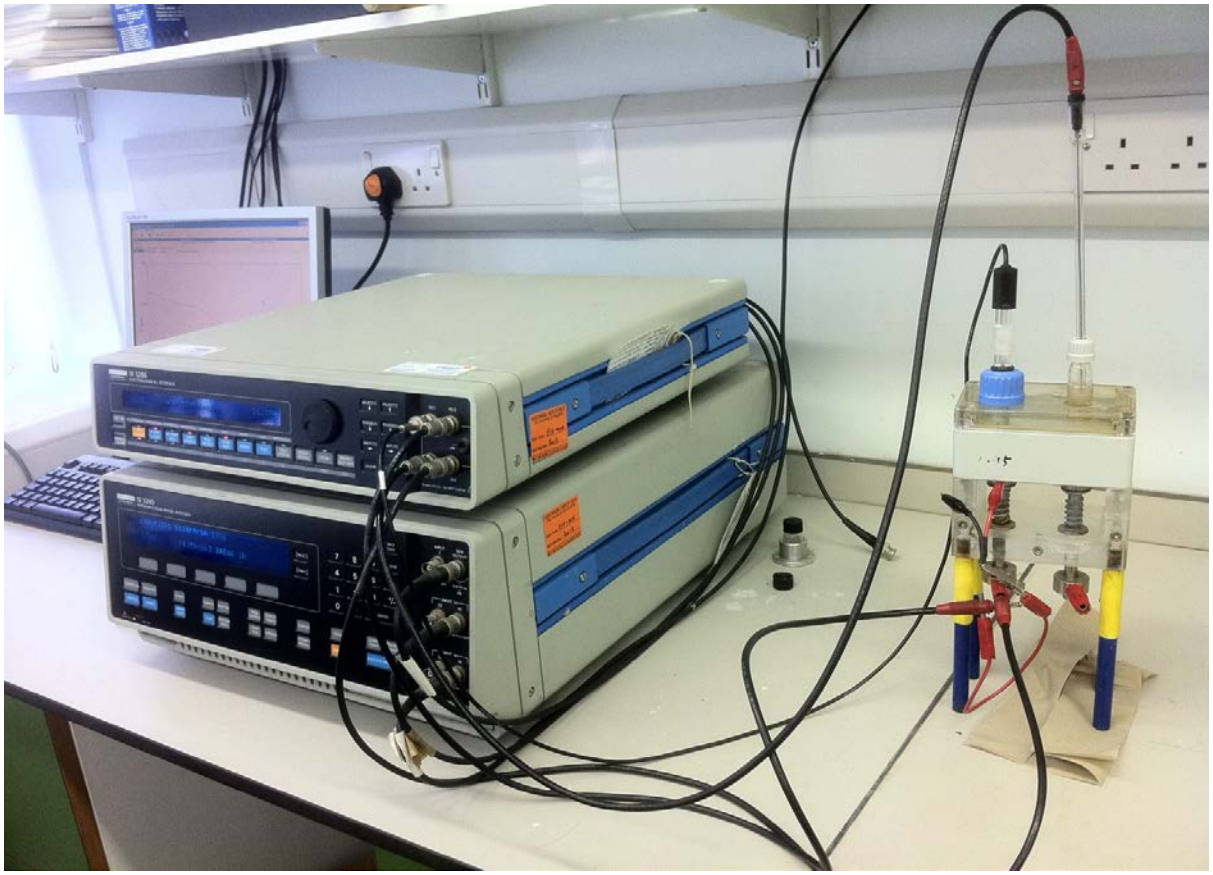

Fig. 5.3. SI 1286 Electrochemical Interface, SI 1260 Impedance/Gain-phase Analyzer and the cell device.

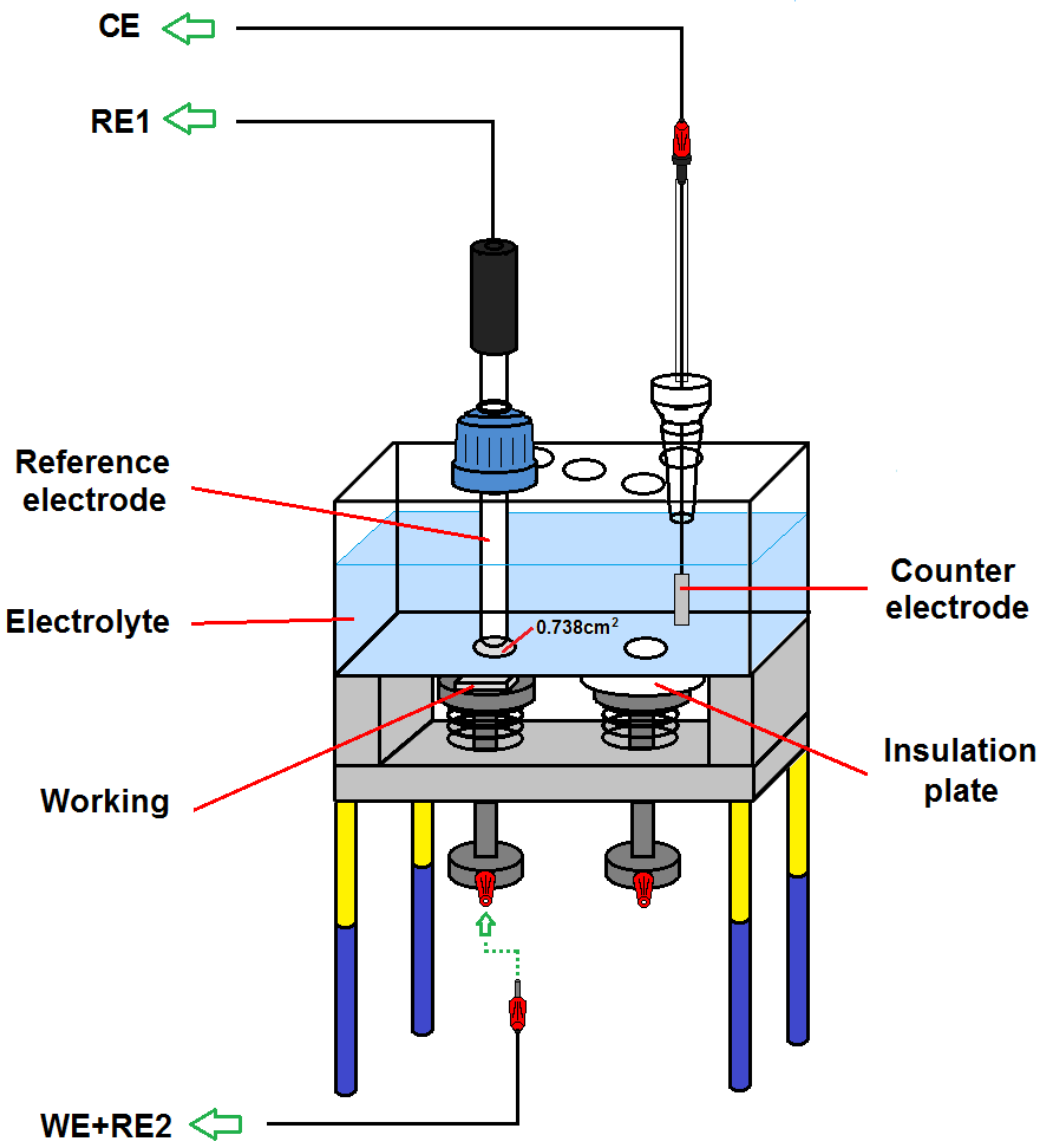

Fig. 5.4. Schematic diagram of the electrochemical cell unit for ex-situ EIS study.

5.3 Characteristics of electrolyte

During the PEO treatment, it is difficult to control the electrolyte temperature precisely, because of large heat input from the process. Therefore, measurements of electrolyte conductivity and pH value have been performed in the temperature range from 0 to 50℃ for both HC and LC electrolytes, as shown in figure 5.5. These characteristics exhibited linear but opposite dependencies on temperature. The conductivity of the solution is directly proportional to the temperature because both solutions belong to weak electrolytes that are

not completely dissociated, and the dissociation is enhanced with temperature, which contributes to the increase in the total number of ions. On the other hand, pH value decreases with temperature due to the hydrolysis intensification which causes the increase of H^+ ions. Subsequent, correlation studies between electrolyte conductivity/pH value and temperature, allow the average conductivity/pH value during the PEO process to be evaluated for the known average temperature in the electrolyser.

COMSOL modeling results of the distributions of current density, electric potential, and electrolyte resistance for all experimental conditions under the same electric field distribution and electrode layout (parallel equidistant) are shown in figure. 5.6. and Table 5.2.

Table 5.2. Results of electrolyte characteristics during PEO treatment

Treatment temperature (℃)	Pre-coating thickness (um)	Electrolyte type	Average temperature (℃)	Electrolyte Conductivity ($mS \cdot cm^{-1}$)	Electrolyte pH	Resistance of Electrolyte (Ω)
5~10	~15	HC	8.83	6.75	12.44	40.35
5~10	~30	HC	7.53	6.74	12.48	40.48
5~10	~50	HC	7.41	6.74	12.48	40.48
5~10	~15	LC	10.31	2.69	10.99	101.28
5~10	~30	LC	8.47	2.67	11.03	102.08
5~10	~50	LC	7.84	2.67	11.03	102.08
20~30	~15	LC	26.31	2.87	10.74	94.95
20~30	~30	LC	21.71	2.82	10.82	96.66
20~30	~50	LC	20	2.80	10.77	97.35
20~30	~15	HC	25.86	6.95	12.02	39.43
20~30	~30	HC	21.1	6.89	12.14	39.58
20~30	~50	HC	22.23	6.91	12.11	39.46
40~50	~15	HC	43.67	7.15	11.58	38.12
40~50	~30	HC	41.33	7.12	11.64	38.28
40~50	~50	HC	39.79	7.11	11.68	38.34
40~50	~15	LC	42.76	3.04	10.49	89.64
40~50	~30	LC	36.63	2.98	10.58	91.47
40~50	~50	LC	42.91	3.05	10.48	89.36

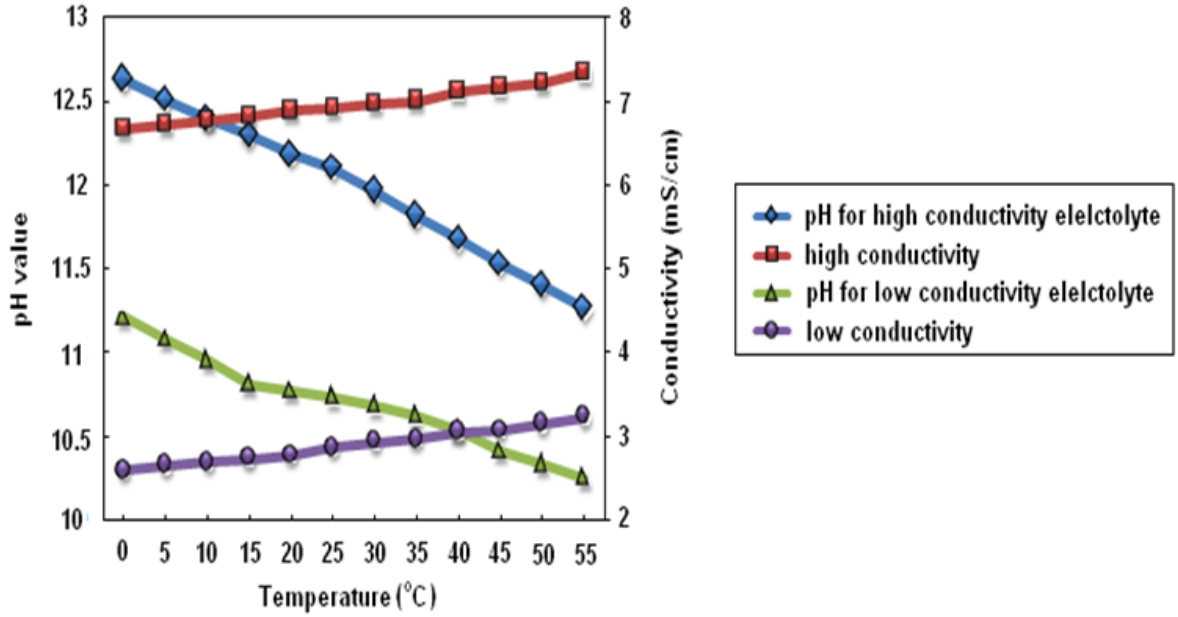

Fig. 5.5. Correlation between electrolyte temperature and conductivity/ pH value

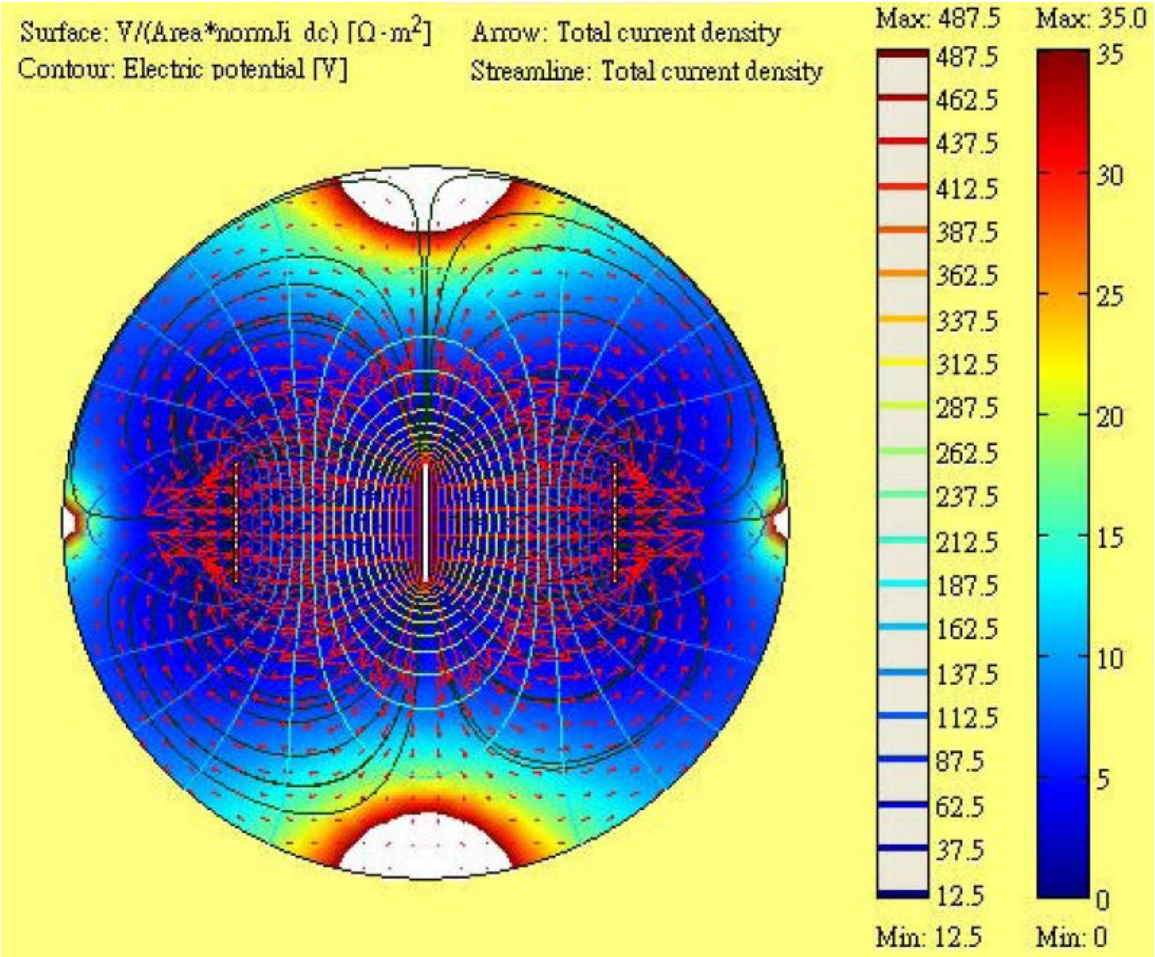

Fig. 5.6. The distribution of electric field in the electrolyte modeled by COMSOL

The electrolyte resistance shows similar behavior as the conductivity. Therefore, Table 5.2 can be compressed to Table 5.3, which directly presents the effects of conductivity and temperature on total electrolyte resistance.

As seen from Table 5.3, for the same electrolyte conductivity, the total resistance of electrolyte decreases with increasing electrolyte temperature; for the same electrolyte temperature, higher electrolyte conductivity causes lower total resistance of electrolyte. The influence of conductivity on resistance is much stronger than that of the temperature.

Table 5.3. Total resistance (Ω) of the electrolyte at different conditions

Electrolyte Conductivity ($mS \cdot cm^{-1}$)	Temperature conditions (℃)		
	5~10	20~30	40~50
6.91	40.48	39.58	38.28
2.82	102.08	96.66	89.64

5.4 Coating characteristics

Figure 5.7, presents three groups of SEM images of both surface and cross-section morphologies for the preformed coatings with thickness of 15, 30 and 50μm. During 1.5min of subsequent PEO treatments in the ISIS mode, only a negligible amount of oxide was formed; hence, the effects of different electrolyte application is difficult to visualise from the cross-sectional SEM images of the coatings. The coating thickness can therefore be considered unaffected by the ISIS experiments.

Two distinct layers with different morphology are observed in cross-sectional images for all coatings. These are normally termed the outer porous and the inner dense layers. From the SEM images, even though the overall coating thickness is different, the thickness of the inner dense layers does not obviously change.

The 15μm preformed coating has relatively high porosity, and the porosity decreases with an increase in thickness. However, the inverse relationship between pore size and coating thickness can also be observed. The characteristics of the pore size and porosity are

related to the microdischarge phenomena and the corresponding dielectric breakdown (section 2.6). During the PEO treatment, relatively large number of small size microdischarges appear at the beginning of the process. With the treatment time, the microdischarge population reduces, but the size of the discharges becomes larger [95,124], which is consistent with the porosity and pore size distribution evaluated in this study. It may be that when the coating thickness increases, the accumulation of charge traps becomes difficult and the discharge is localised. Therefore, because more energy concentrates at the same location, a more powerful oxide breakdown takes place and pores of larger size are produced. This can also explain the increase in surface roughness with increasing coating thickness observed in figure 5.7. It can also be observed that cracks appear in the preformed coatings with 30μm and 50μm thickness. This phenomenon can be explained as follows: the stresses (comprised of intrinsic, thermal and micro natures [46]) are generated when the coating thickness increases. When the coating grows to a certain thickness, the stress relaxation leads to cracking, so that the thicker the coating, the larger the cracks.

5.5 Results of ISIS studies

Before we discuss the results of ISIS experiments, it is necessary to point out the effects of electrolyte characteristics on the discharge intensity and population. During the PEO process, both the population and intensity of discharges are inversely proportional to the preformed coating thickness and directly proportional to the electrolyte temperature and conductivity. In other words, when a combination of low electrolyte temperature and conductivity with thicker coatings is employed, almost no sparking can be observed during the PEO process.

Figure 5.8. represents the results of the ISIS study on the Al samples with three different preformed coating thicknesses under different electrolyte conditions such as (a) high conductivity with low temperature, (b) low conductivity with low temperature, (c) high conductivity with high temperature, and (d) low conductivity with high temperature. A simplified Randles circuit was used to fit the above impedance spectra.

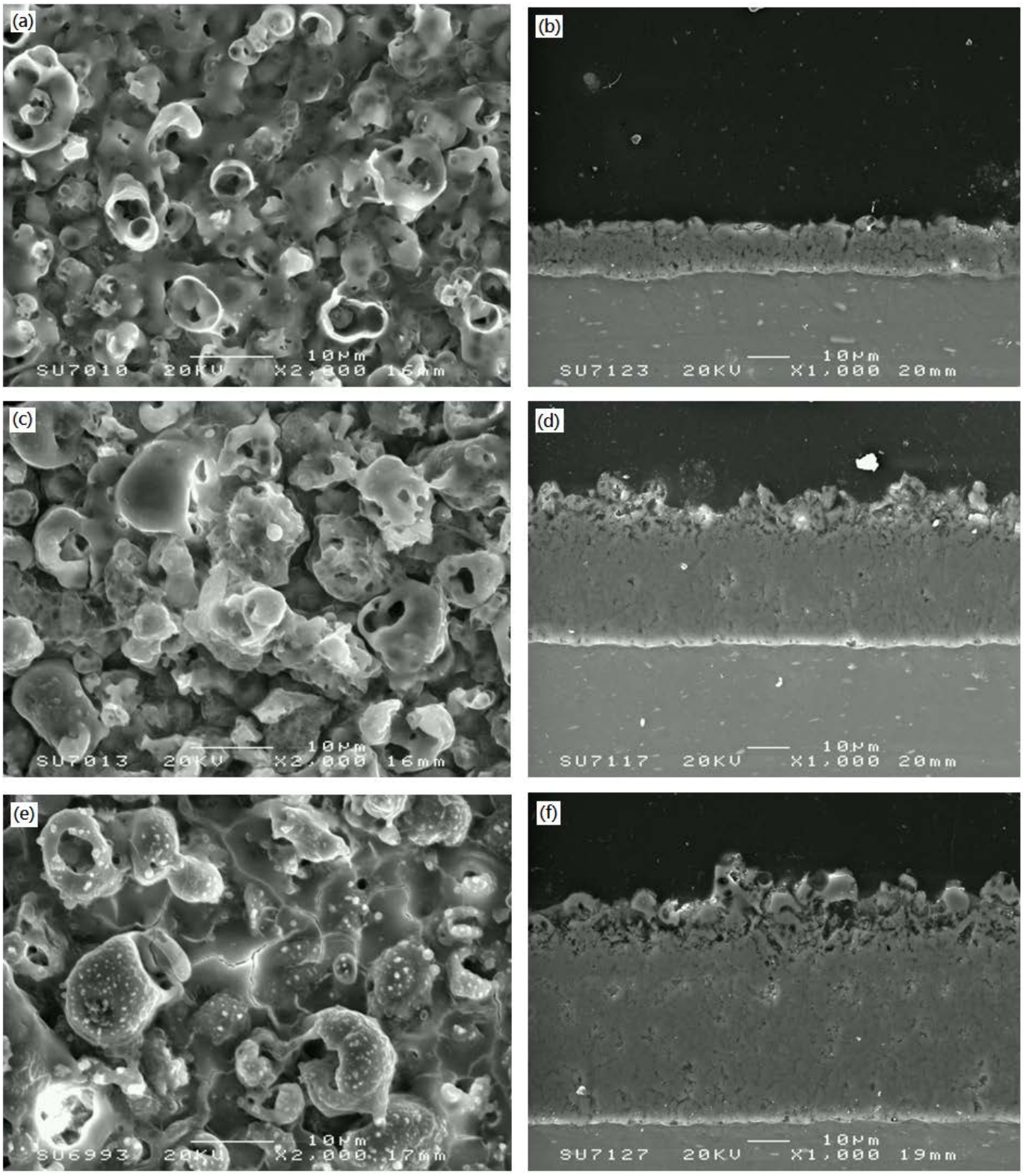

Fig. 5.7. SEM images of surface and cross-section coating morphology for 15μm (a) (b), 30μm (c) (d), and 50μm (e) (f).

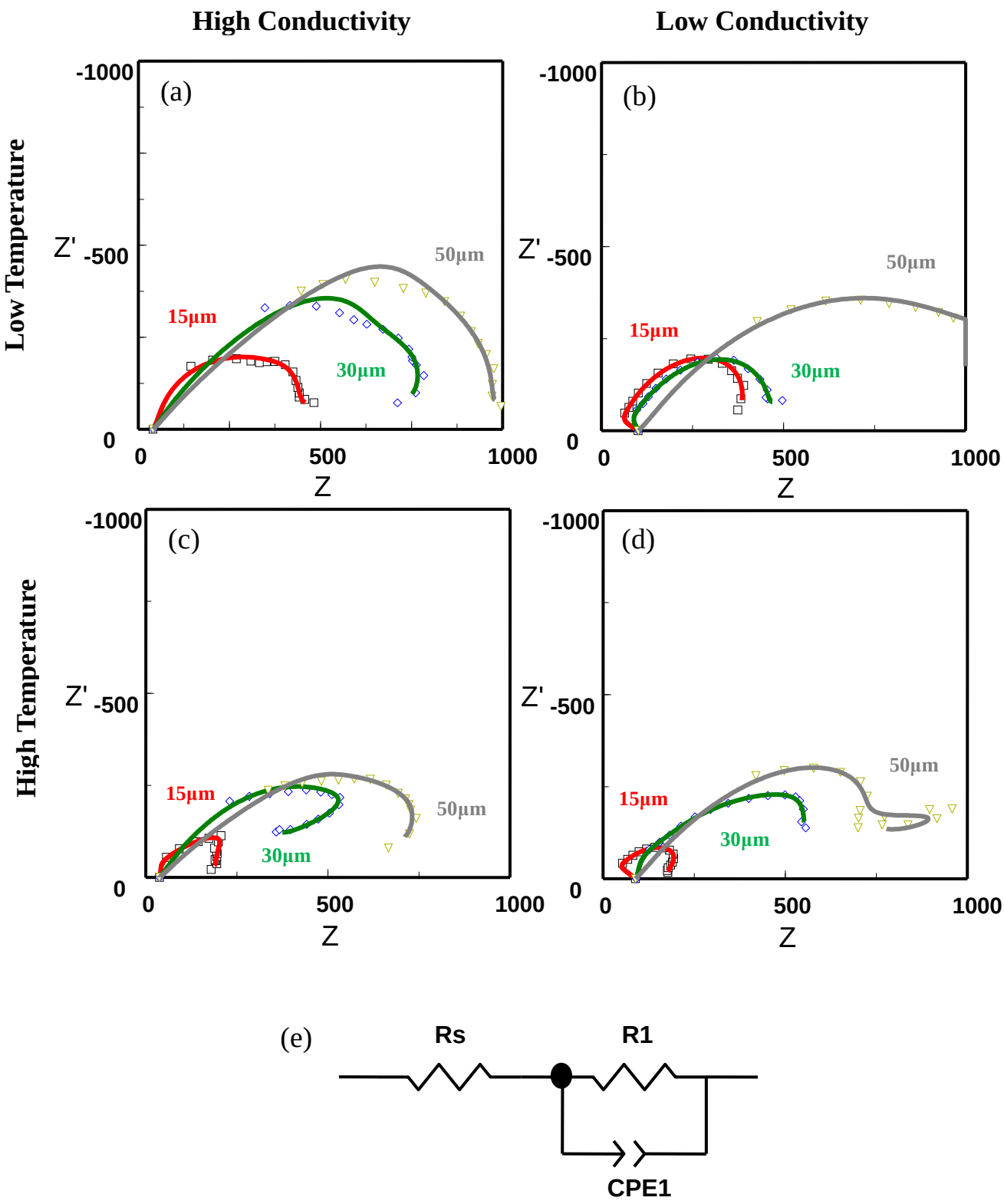

Fig. 5.8. Complex plots from ISIS method under (a) high conductivity (6.91mS·cm-1) with low temperature (5~10℃), (b) low conductivity (2.82mS·cm^{-1}) with low temperature (5~10 ℃), (c) high conductivity (6.91mS·cm^{-1}) with high temperature (40~50), (d) low conductivity (2.82mS·cm^{-1}) with high temperature (40~50℃), and (e) a simplified Randles circuit.

From the results, negative resistance occurs in the low frequency range under all electrolyte conditions, especially at high temperature. Following discussion in section 4.8, it can be speculated that this phenomenon is related to the discharge events during the PEO process. To compare the impedance spectra of the process carried out using coatings with different preformed thicknesses, in solutions with different properties, thicker preformed coatings present larger impedance arcs. At the same conductivity conditions, the effect of electrolyte conductivity is stronger in the low temperature electrolyte than the high temperature one. It can be also speculated that when the temperature increases, the ionization is more active, and this then decreases the impedance of the PEO process. However, even though the impedance spectra are similar, the region of negative resistance behavior is more obvious in the HC electrolyte. These results are supported by observations of discharge population and intensity during the PEO process. On the other side, when the treatment is carried out in the electrolytes with the same conductivity, smaller impedance spectra occur at higher temperatures.

As regards to the equivalent circuit, beside the low frequency regions exhibiting the negative resistance behavior, the spectra can be easily fitted with a single loop circuit, known as a simplified Randles circuit (figure 5.8e). The interpretation of the equivalent circuit elements were the same as discussed as in Chapter 4. As for the negative resistance parts, a more accurate equivalent circuit fitting and physical meaning of corresponding elements is discussed in Chapter 4.

5.6 Results of Ex-situ EIS studies

The PEO samples produced at above conditions were studied using conventional electrochemical impedance spectroscopy, at ambient temperature. This condition was applied because the correlation between solution temperature and impedance is already known as the smaller impedance spectra occur under higher temperature. Figure 5.9 represent the results of ex-situ EIS study under the controlled variable, such as three coating thicknesses: (a) 15, (b) 30, (c) 50μm, and three electrolyte conductivities: (d) high (C_H), (e) medium (C_M), and (f) low (C_L) conductivity. Here, three equivalent circuits are used to fit these impedance spectra (figure 5.10). The ex-situ EIS results indicate that, in all the different coating thickness, relatively high electrolyte conductivity provides smaller impedance spectra. Comparison with the ISIS spectra reveals tremendous differences for all electrolyte conductivities and coating thicknesses. When investigating the effects of different preformed coating thickness under the

same controlled solution conductivity, it can be seen that the largest EIS spectra corresponds to 15μm preformed coating. Referring back to the SEM images, this is associated with a relatively defect-free morphology of the surface layer compared to other two coatings.

Several equivalent circuits (figure 5.10) were developed to fit the impedance spectra obtained in the electrolytes with different conductivity. In these circuits, Rs is the electrolyte resistance, R_1 is the charge transfer resistance across the PEO coating and CPE_1 represents the geometrical capacitance affected by the coating morphology. For all electrolytes, the impedance spectra in the low frequency region present the behavior which can be described as diffusion or double layer. Therefore, the loop of R_2 and CPE_2 is used to present the double layer behaviour, and the Ws is used to present the diffusion behaviour in the low frequency region [114,117]. Due to the PEO coating morphologies, it is believed that both diffusion and double layer occurs during the EIS study. However, because of the difference of coating and electrolyte characteristics such as porosity, pore size, cracks, coating thickness and the electrolyte conductivity, the impedance spectra under above controlled variables were fitted by three equivalent circuits which were designed for three different conditions in the low frequency region such as (a) when the double layer behaviour is stronger, (b) the diffusion behaviour is stronger, and (c) both double layer and diffusion behaviour are not negligible. The fitting results are shown in Table 5.4.

From figure 5.9 and Table 5.4 it follows that the behavior of impedance spectra in the low frequency region is affected by the electrolyte conductivity. A stronger diffusion effect occurs at a lower electrolyte conductivity and a thicker coating thickness, while the effects of double layer is stronger at a higher electrolyte conductivity and at thinner coating thickness. Strong effects of both the double layer and the diffusion behaviour occur at the condition with the lowest electrolyte conductivity and the thickest coating.

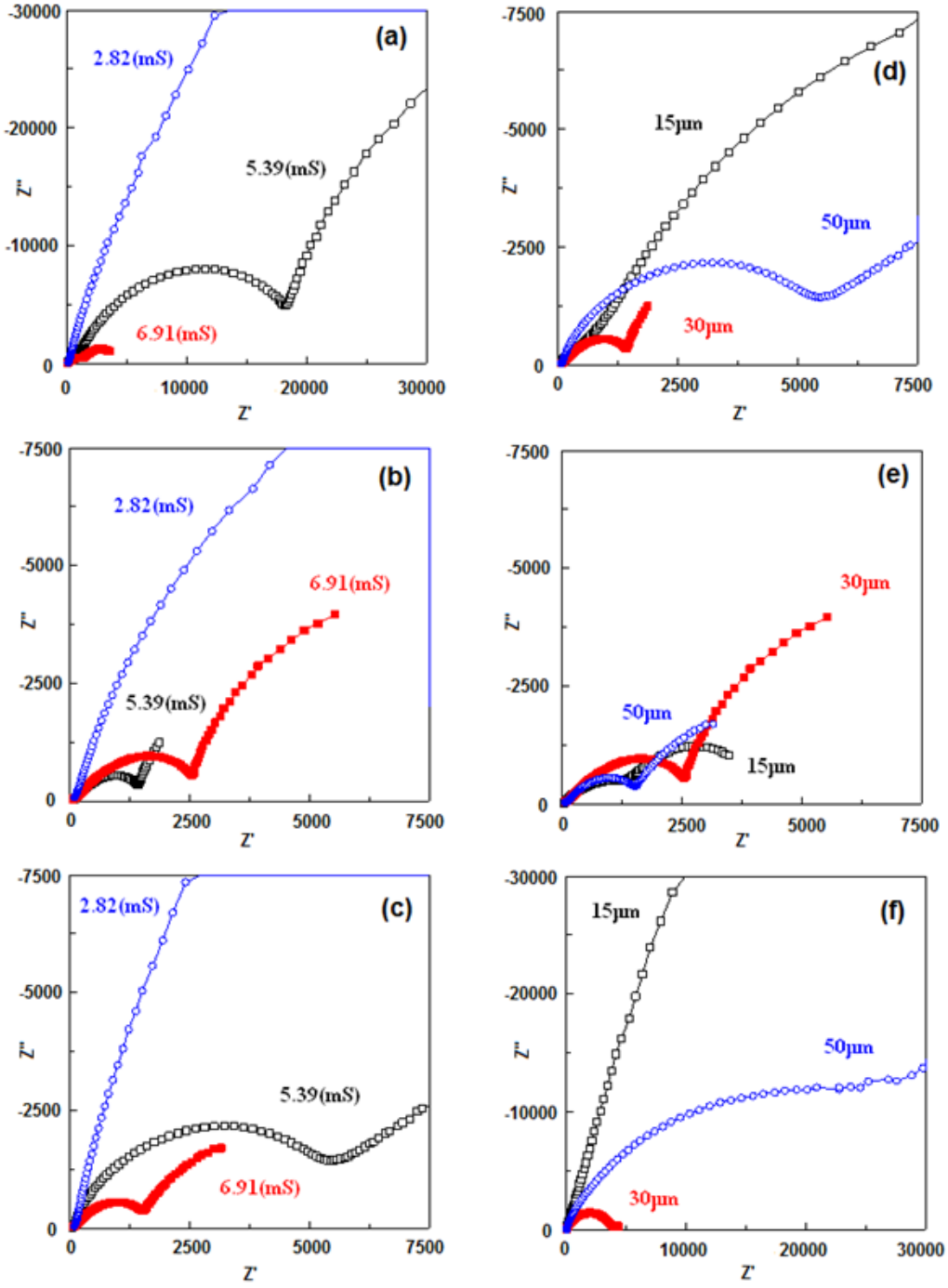

Fig. 5.9 Results from ex-situ impedance method under controlled variable, such as thickness (a) 15μm,(b) 30μm, (c) 50μm, and conductivity (d) 5.39 $mS \cdot cm^{-1}$, (e) 6.91 $mS \cdot cm^{-1}$, (f) 2.82 $mS \cdot cm^{-1}$.

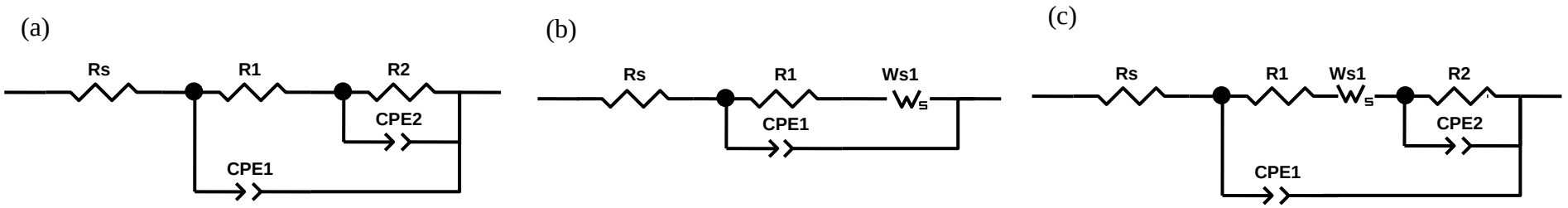

Fig. 5.10 Equivalent circuits for the results from ex-situ impedance spectroscopy.

Table 5.4. Fitting results of ex-situ EIS study under controlled variable:

Electrolyte conductivity ($mS \cdot cm^{-1}$)	Coating thickness (μm)	R ($\Omega \cdot cm^2$)	R1 ($\Omega \cdot cm^2$)	CPE1-T ($F \cdot cm^{-2}$)	CPE1-P	R2 ($\Omega \cdot cm^2$)	CPE2-T ($F \cdot cm^{-2}$)	CPE2-P	Ws-R ($k\Omega \cdot cm^2$)	Ws-T (s)	Ws-P
Medium conductivity	15	734.2	20282	1.3×10^{-6}	0.80	6.9×10^{4}	3.4×10^{-5}	0.98	—	—	—
	30	98.0	1480	4.6×10^{-5}	0.72	—	—	—	1.7×10^{3}	3.5	0.71
	50	57.8	5642	4.7×10^{-6}	0.79	—	—	—	1.1×10^{4}	6.8	0.58
High conductivity	15	5.7	1913	4.3×10^{-5}	0.55	2.7×10^{3}	2.5×10^{-4}	0.86	—	—	—
	30	137.9	2811	1.0×10^{-5}	0.70	8.9×10^{3}	2.3×10^{-4}	0.9	—	—	—
	50	111.2	1625	1.7×10^{-5}	0.71	4.6×10^{3}	4.5×10^{-4}	0.86	—	—	—
Low conductivity	15	87.6	99851	3.5×10^{-7}	0.86	9.0×10^{5}	4.1×10^{-7}	0.68	—	—	—
	30	55.0	37398	3.1×10^{-7}	0.81	—	—	—	6.2×10^{3}	2.1	0.42
	50	92.2	74134	4.0×10^{-7}	0.86	1.3×10^{5}	9.0×10^{-7}	0.78	1.8×10^{6}	348.1	0.42

5.7 Comparison between in-situ and ex-situ impedance behaviour

Figure 5.11 (a) and (b) visualise differences between the ISIS data and ex-situ EIS data, in high and low conductivity electrolytes, respectively. By comparing the impedance spectra from in-situ and ex-situ impedance spectroscopy, the following effects can be observed. Firstly, for the same electrolyte characteristics, it can be deduced that the difference of impedance spectra reveals the effects of discharge. Secondly, from the Bode plots, the impedance modulus decreases and the phase angle increases in the low frequency region in the ISIS spectra, which indicates a more active behavior of the system due to the discharge phenomena occurring during the PEO process. Thirdly, the phase angle approaches zero in the low frequency region of the ISIS spectra also representing active behavior.

From the results, it also follows that discharge effects are stronger in the low conductivity electrolyte. The low electrolyte conductivity provides a larger difference between the spectra from the ISIS method and ex-situ impedance spectroscopy in the complex plot. In the Bode plots, the discharge effect is observed among a longer frequency range, for the electrolyte with low conductivity.

Figure 5.12 compares discharge effects for different coating thicknesses. The results indicate that the effect of discharge is strongly influenced by the coating thickness, with the difference in impedance behaviour of in-situ and ex-situ reducing for thicker coatings. On the other hand, when PEO treatments are applied to a thicker performed coating, the frequency range of discharge effects becomes narrower. In the situation when no visible discharge was observed for the 50μm preformed coating, the effect of the discharge in the Bode plots is also diminished.

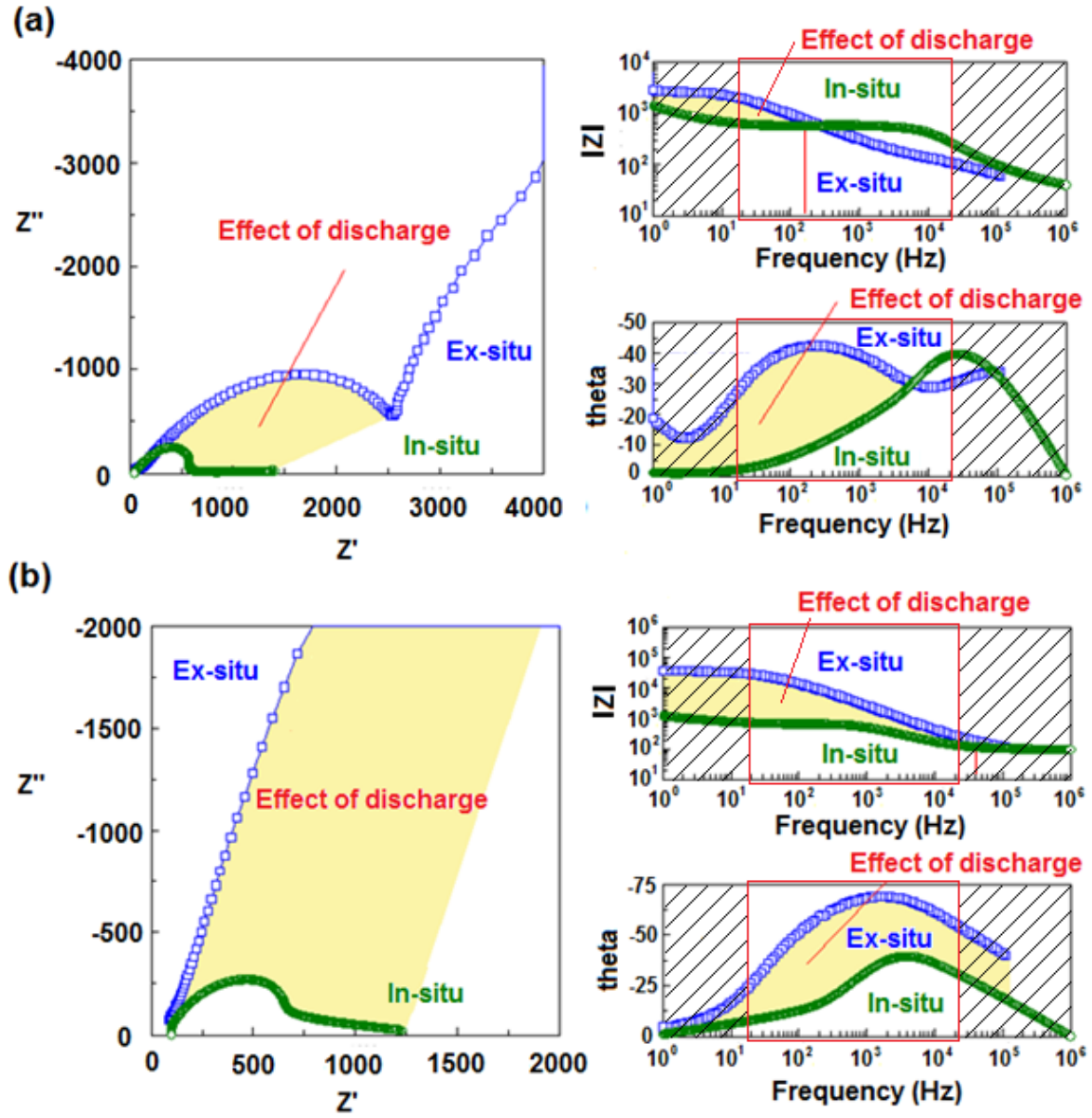

Fig. 5.11 Comparison between the impedance spectra from ISIS method and ex-situ EIS under (a) HC electrolyte, (b) LC electrolyte

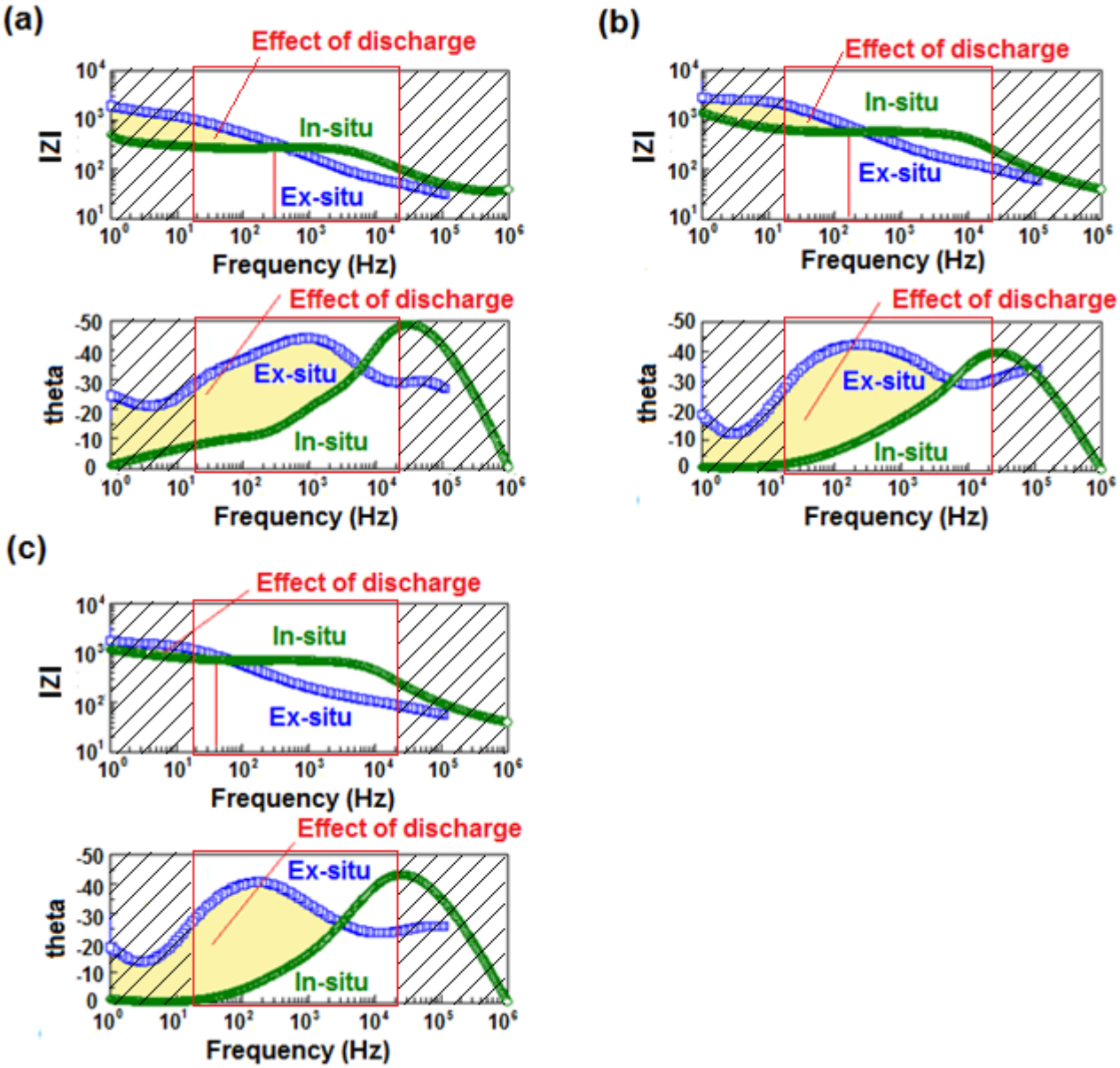

Fig. 5.12 Comparison between the results from ISIS method and ex-situ EIS under different preformed coating thickness: (a) 15μm,(b) 30μm, (c) 50μm

5.8 Summary

During the PEO process, the observed discharge density was reduced in the electrolytes with (a) low temperature, (b) low conductivity, and (c) thick pre-formed coating. No sparking is observed when all these conditions are combined.

The observed coating porosity decreases and the surface roughness increases with increasing thickness of pre-formed coating, with obvious cracks appearing on the surface of

the thicker coatings.

The differences in the in-situ impedance spectra clearly reflect the effects of pre-formed coating thickness, whereas the effects of electrolyte temperature and conductivity are less obvious and negligible, respectively. In the ex-situ impedance spectra, the smaller impedance is observed at the higher electrolyte conductivity; ~15μm preformed coatings provide the largest impedance spectra, which is probably associated with a relatively defect-free morphology of the coating. A more complex equivalent circuit is required to fit the impedance spectra from ex-situ impedance spectroscopy than those from the ISIS experiments. In the low frequency region of the EIS spectra, a much stronger diffusion effect is observed at a lower electrolyte conductivity and a thicker coating thickness, while the effects of the double layer are much stronger at a higher electrolyte conductivity and for a thinner coating. Strong effects of both the double layer and the diffusion behaviour are observed at the condition with the lowest electrolyte conductivity and the thickest coating.

Comparison between the ISIS and ex-situ EIS spectra provides clear evidence of the effect of the discharge; the total impedance is much higher for the ex-situ impedance spectra than for the ISIS ones. The difference is caused by the discharge events during the PEO process. In the Bode plots, the effects of the discharge appear to be stronger for the thinner coatings; the low electrolyte conductivity provides a larger difference between the in-situ and ex-situ impedance spectra in the complex plot.

Chapter 6

Effects of Coating Morphology on Impedance Spectra of the PEO Process

Previous chapters have demonstrated the utility of the ISIS method in investigation of the PEO process. It was also noticed that the in-situ impedance spectra of the process often feature evidence of distributed and unconventional lump elements present in the system; however the nature of such behavior is not clear.

In most cases, the distributed properties are modeled by including a constant phase element (CPE) which can be associated with different factors, including variable coating thickness, topology or composition. When the CPE element is used to represent the coating layers, the meaningful range of CPE-P value should be between 0.5 to 1. This follows from the properties of CPE discussed in section 3.1.3. When the CPE-P = 1, the CPE element is treated as a pure capacitance which is usually used to fit a dense and smooth coating layer; when CPE-P = 0.5, the CPE element represents the same behavior as Warburg element, which is often used to describe the diffusion process, e.g. in a porous medium.

In this chapter, the effects of coating morphology on in-situ impedance spectra of the PEO process on Al are studied using a fractal approach. As discussed in section 3.5, fractal analysis is a useful method to investigate the properties of heterogeneous (e.g. rough, porous or multiphase) materials, which can provide a direct link to the CPE characteristics. The fractal analysis is applied to surface plane and cross-sectional SEM images of the PEO coatings with a range of nominal thicknesses produced during different treatment times. Fractal dimensions of morphological characteristics of the PEO coatings are derived and related to CPE elements that appear in the models used for the fitting of impedance spectra.

Further comparisons is made with the results of conventional EIS analysis performed on the PEO coatings in working silicate-alkaline electrolytes.

6.1 Introduction

A fractal dimension is very often a non-integer number used to describe the fractals, which provides a measure of irregularity, or boundary fragmentation degree different from Euclidean objects (point, line, plane, etc.) [131]. Fractal analysis is a method to evaluate fractal behavior and fractal dimension from images, that is, complex graphics or multi phase images can be transformed to a simple value (fractal dimension) for investigation and comparison. In 1984, this method was proposed to be applied to materials surfaces in the micro scale [132]. The relation of the fractal dimension to the CPE-P value in equivalent circuits used to simulate EIS data was also proposed in 1985 [137]. This study demonstrated that the correlation between the CPE-P value and the fractal dimension of the object is possible to trace, although with a limited degree of accuracy. Therefore, fractal analysis is considered to be a method which can contribute to a better understanding of the PEO process.

The purpose of this part of the study is to investigate the effects of coating characteristics on the ISIS spectra of the PEO process of Al by comparing two characteristics: the α value which is used to describe the effects of coating morphology and the CPE-P value from the equivalent circuit of the ISIS spectrum, which is used as a measure of the effects of both the coating morphology and the electric field distribution in the electrolyser during the PEO process. The comparison between α and CPE-P is used to reveal the electric field effect on the PEO process.

6.2 Coating morphology

The experimental setup employed for this part of the work is discussed in Chapter 4 (fig. 4.1); this was used together with fractal analysis to study the coating morphology effects on impedance spectra of the PEO process under different types of electric field and electrode outs. Therefore, the influence of various electric field conditions is also investigated.

Capacitance is the element used to present the coating properties and morphology in the analysis of ISIS data. The coating capacitance (C) can be calculated by the following

equation:

$$C = \varepsilon_r \varepsilon_0 \frac{A}{d} \tag{6.1}$$

where the ε_0 is the vacuum permittivity with the value ≒ 8.854×10^{-12} (F/m), ε_r is relative permittivity (or dielectric constant) of the material, A is the surface area and d is the coating thickness. From the equation, for the same coating on the same substrate, A and d are the two main parameters that affect the capacitance. This provides correlations with several coating characteristics, such as average coating thickness, porosity, surface and interfacical roughness.

To calculate the theoretical value of the coating capacitance, the characteristics of PEO coatings were analysed by SEM (Jeol JSM 6400), which was used to produce a large number of cross-sectional images to study the coating morphology. Next, a specialised morphology analysis software ZEISS-KsRun was used to evaluate the distribution of PEO coating features (thickness, porosity, surface and interface roughness) on SEM images. The results of these analyses are summarised in Table 6.1.

Table 6.1 Coating characteristics under different types of electric field and electrode layout.

Electric field	Layout	Average thickness (μm)	Porosity (%)	Surface roughness (Rz) (μm)	Interfacial roughness (Rz) (μm)	Specific surface area (per 100 μm^2)	Specific interface area (per 100 μm^2)
Converging	equidistant	22.02	3.83	6.94	3.79	190.72	118.81
	non-equidistant	29.12	3.58	13.64	4.82	147.38	135.96
Parallel	equidistant	10.63	4.19	4.19	3.56	132.71	114.70
	non-equidistant	11.35	3.37	7.49	4.08	113.21	114.17
Diverging	equidistant	7.38	3.58	5.13	5.27	159.01	126.16
	non-equidistant	7.25	4.4	4.58	4.25	113.00	116.21

Coating thickness and porosity are the two characteristics that affect the d parameter in equation 6.1. From table 6.1, converging electric field conditions produced the thickest coatings around 2 ~ 2.5 and 3 ~ 3.5 times thicker than those produced under parallel and diverging conditions, respectively. Porosity is similar for different coatings, in the range of 3.5 ~ 4.5 %. However, the pore size varied in two extreme ranges for the coatings produced under converging electric field. Figure 6.1 reveals that the pore size is mainly distributed in the range of 0 ~ 6μm in all coatings. Under all electric field conditions, the equidistant electrode layout provides in relatively higher probability density in the range of pore size under 3μm, and a higher in the range of 3 to 6μm for all non-equidistant layouts.

To evaluate the actual surface area A, both surface and interface roughnesses were measured. Among all conditions, the coatings produced under the converging electric field have the highest surface roughness; however, the interface roughness is similar. The non-equidistant layouts provide relatively higher interface and surface roughnesses than the equidistant ones, except for the diverging field. Using the values of surface and interface roughness, specific surface/interface areas were analysed. Here, the average roughness of both surface and interface under all electric field conditions and electrode layouts were analysed by using the ten-point mean roughness method (Rz). Additionally, both the specific surface and interfacial areas were calculated by using the square of the average physical length of PEO coating per 100μm.

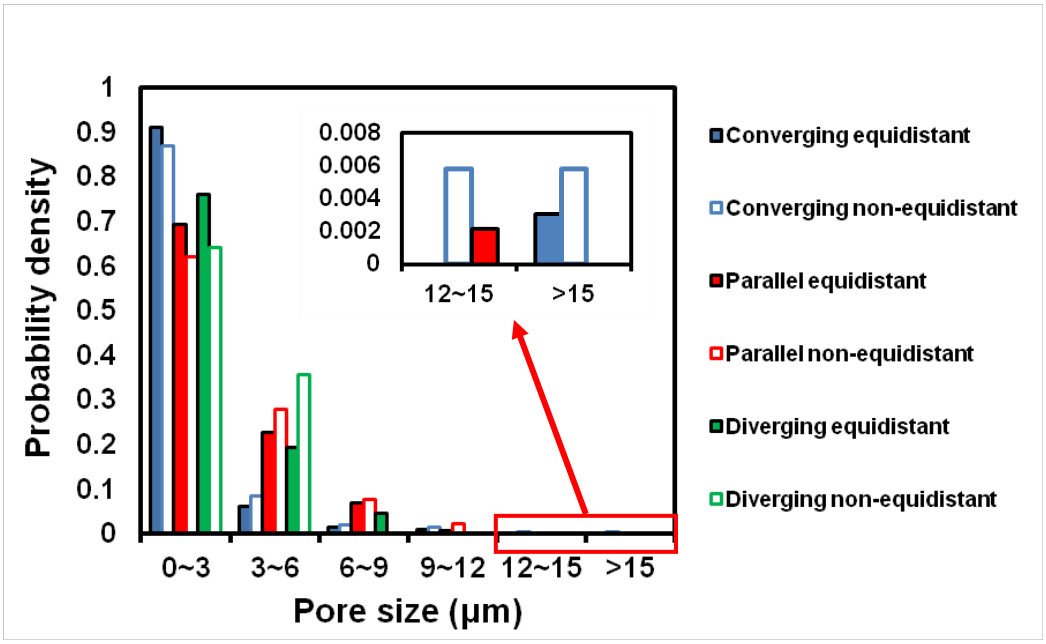

Fig. 6.1. Pore size distribution under different conditions of electric field and electrode layouts.

To calculate the theoretical capacitance, the values of average coating thickness from Table 6.1 were used as the parameter d in equation 6.1. For the surface area A, the values of the specific surface area were calculated using equation 6.2:

$$A = S\textit{pecific surface area (per } 1\mu m^2\textit{)} \times \textit{total surface area of the working electrode} \quad (6.2)$$

where the specific surface area (per $1\mu m^2$), have been calculated and shown in Table 6.2. The value of $\varepsilon_r = 10.8$ was accepted, corresponding to pure alumina ceramic with 1% porosity [161]. The results of theoretical capacitance evaluation are presented in Table 6.2. The capacitance from ISIS fitting was also evaluated using a model with single RC loop in the high frequency range (2 to 20kHz); this is associated with charge transfer across the PEO coating. When comparign the theoretical and ISIS derived capacitance values, it should be noticed that the value of CPE-T is around 10 times higher than the theoretical value for the parallel and diverging field conditions, but around a hundred times and two hundred times higher for the converging-equidistant and non-equidistant conditions, respectively. The difference may caused by the CPE-T values from the ISIS fitting not indicating the status of the whole PEO coating but only relating to the barrier layer at the bottom of the discharge channel. Therefore, the thickness of the barrier layer (d_{BL}) can be calculated from the CPE-T values, specific interface area and by using equation 6.1. The evaluated d_{BL} values in Table 6.2 are around 0.1 to 1μm, which are consistent with the cross-sectional SEM images of PEO coatings in section 4.5.2 (figure 4.6). The results in Table 6.2 are also consistent with the results of comparison of the ISIS spectra with ex-situ EIS spectra discussed in section 5.7, which indicates that the effects of discharge reduce both the real (pure resistance) and imaginary (impedance from capacitance and inductance) impedance components during the PEO process. Moreover, the largest difference between CPE-T and theoretical capacitance occurred under the converging electric field condition, which also matches with the results of evaluation of the effects of electric field distribution discussed in section 4.7 (figure 4.9.), wherein the smallest impedance spectra occurred under converging types of electric field.

Table 6.2 Comparison of capacitance between theoretical and ISIS fitting value of CPE-T.

Field	Layout	Specific surface area (per $1\mu m^2$)	Capacitance (theoretical) (F)	CPE-T (In-situ IS) ($S \cdot s^n$)	d_{BL} (μm)
Converging	equidistant	1.55	8.42×10^{-9}	7.63×10^{-7}	0.17
	non-equidistant	1.42	5.83×10^{-9}	9.17×10^{-7}	0.18
Parallel	equidistant	1.24	1.08×10^{-8}	9.19×10^{-8}	1.16
	non-equidistant	1.14	9.27×10^{-9}	$5.97E\times10^{-8}$	1.77
Diverging	equidistant	1.43	1.80×10^{-8}	1.63×10^{-7}	0.72
	non-equidistant	1.15	1.47×10^{-8}	1.60×10^{-7}	0.68

6.3 Fractal analysis of the coating morphology

The fractal analysis was carried out using a frac347e software [136] to evaluate fractal dimensions (D) of background (substrate and epoxy resin from cold mounting) removed coating layers in the cross-sectional gray-scale SEM images. As discussed in the introduction, the value of D can be transferred to a value of α (morphology effect) for comparison with in-situ CPE-P value by using Nyikos and Paikossy's equation [137]:

$$\alpha = \frac{1}{\text{D-1}} \tag{6.3}$$

Fractal dimensions were measured from around 50 background-removed gray-scale cross-sectional SEM images, typical examples of which are provided in figure 6.2. The values of fractal dimension were averaged to provide more accurate estimates of D in all electric field conditions and corresponding electrode layouts as shown in Table 6.3. The above values have also been transformed to α values for comparison with in-situ impedance spectroscopy data. As follows from Table 6.3, for all electric field conditions the equidistant geometries provide slightly higher fractal dimension than the non-equidistant ones. The difference in fractal dimensions between the electric field conditions is negligible, even through the morphology difference is obvious in the above images.

Table 6.3 Fractal dimension from all electric field conditions, and transformed α value

Field	Layout	Fractal dimension (D)	α
Converging	equidistant	2.23 ± 0.03	0.82 ± 0.02
	non-equidistant	2.17 ± 0.02	0.86 ± 0.01
Parallel	equidistant	2.19 ± 0.03	0.84 ± 0.02
	non-equidistant	2.18 ± 0.02	0.85 ± 0.02
Diverging	equidistant	2.23 ± 0.03	0.82 ± 0.02
	non-equidistant	2.21 ± 0.03	0.83 ± 0.02

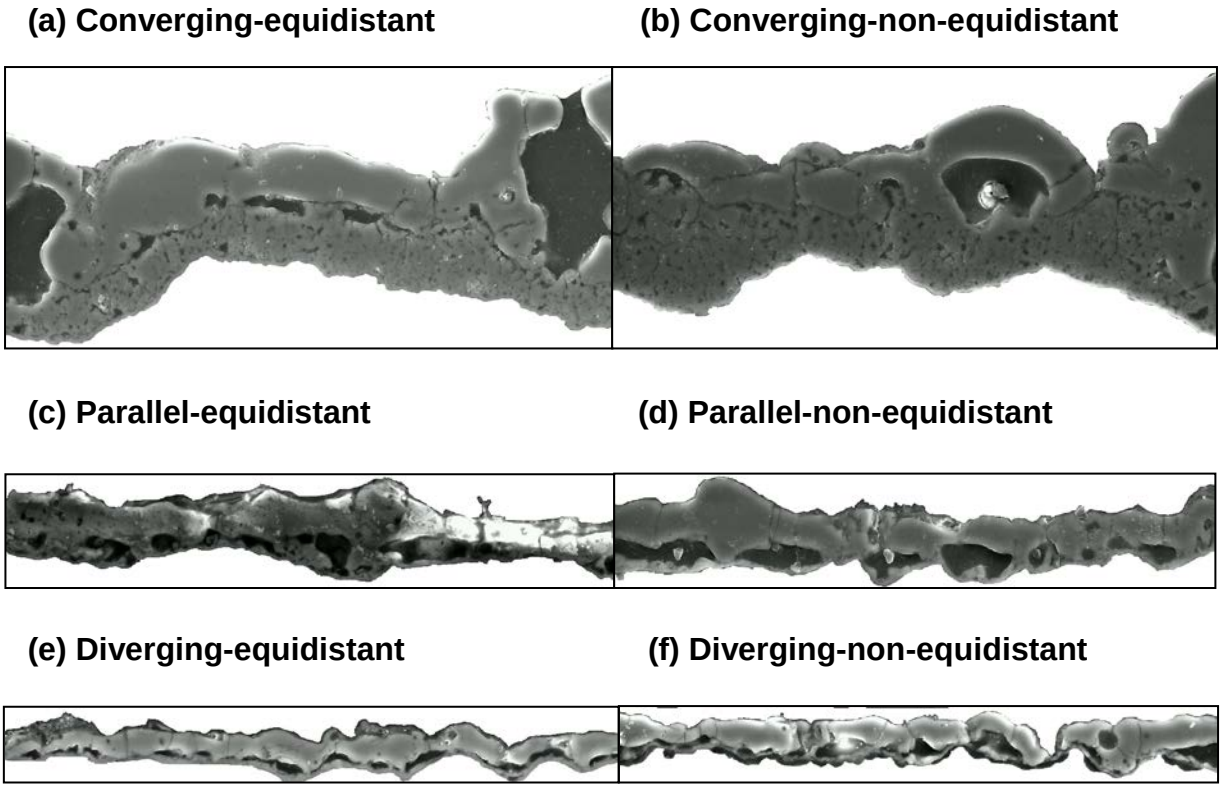

Fig. 6.2. Typical examples of gray-scale images of PEO coatings produced in different electric field conditions, with background removed.

The CPE-P values from the circuits developed to fit ISIS data are affected by both electric field and coating morphology, evolving during the PEO process. Comparison of the coating morphology effect (α value) with the combined effect of the coating morphology and electric field (CPE-P value) is shown in Table 6.4. As mentioned in the Introduction, smaller values present stronger effects of coating morphology or electric field. From Table 6.4, the mean average α values with the corresponding standard deviations indicate that the effects of coating morphology under all conditions of electric field and electrode layouts are similar. However, combined effects of coating morphology and electric field are relatively stronger under the converging conditions than under others. The values of difference in CPE-P values between the converging and other conditions are around 0.2~0.25 whereas corresponding standard deviations of all condition is about 0.02~0.03, which is similar and even higher than those for the parallel and diverging electric field conditions, respectively. Another point is that under the same electric field conditions, the difference in CPE-P values between equidistant and non-equidistant electrode layouts is negligible.

To separate the effects of electric field, a difference between CPE-P and α is considered (Table 6.4). The negative values observed for both converging conditions can be interpreted as an amplifying effect of the non-homogeneous electric field distribution, and the positive values obtained for the parallel condition indicate a rectifying effect of the uniform electric field on the impedance affected by the heterogeneous coating morphology. In fig. 6.3, the comparison between α and CPE-P values is shown, indicating that converging type of electric field provide the strongest effect compared to the parallel and diverging fields.

Table 6.4 Comparison of coating morphology and electric field effects

Field	Layout	α (Effect of coating morphology)	CPE-P (Sum coating and electric field effect)	CPE-P — α (Effect of Electric field)	Meaning
Converging	equidistant	0.82 ± 0.02	0.67 ± 0.03	-0.15	Both heterogeneous coating morphology and non-uniform electric field contribute significantly to the impedance spectra of the PEO process.
	non-equidistant	0.86 ± 0.01	0.65 ± 0.03	-0.21	
Parallel	equidistant	0.84 ± 0.02	0.87 ± 0.03	+0.03	The impedance is mainly affected by the heterogeneous coating morphology
	non-equidistant	0.85 ± 0.02	0.90 ± 0.03	+0.05	
Diverging	equidistant	0.82 ± 0.02	0.82 ± 0.02	0	The impedance is affected only by the coating morphology
	non-equidistant	0.83 ± 0.02	0.82 ± 0.01	-0.01	

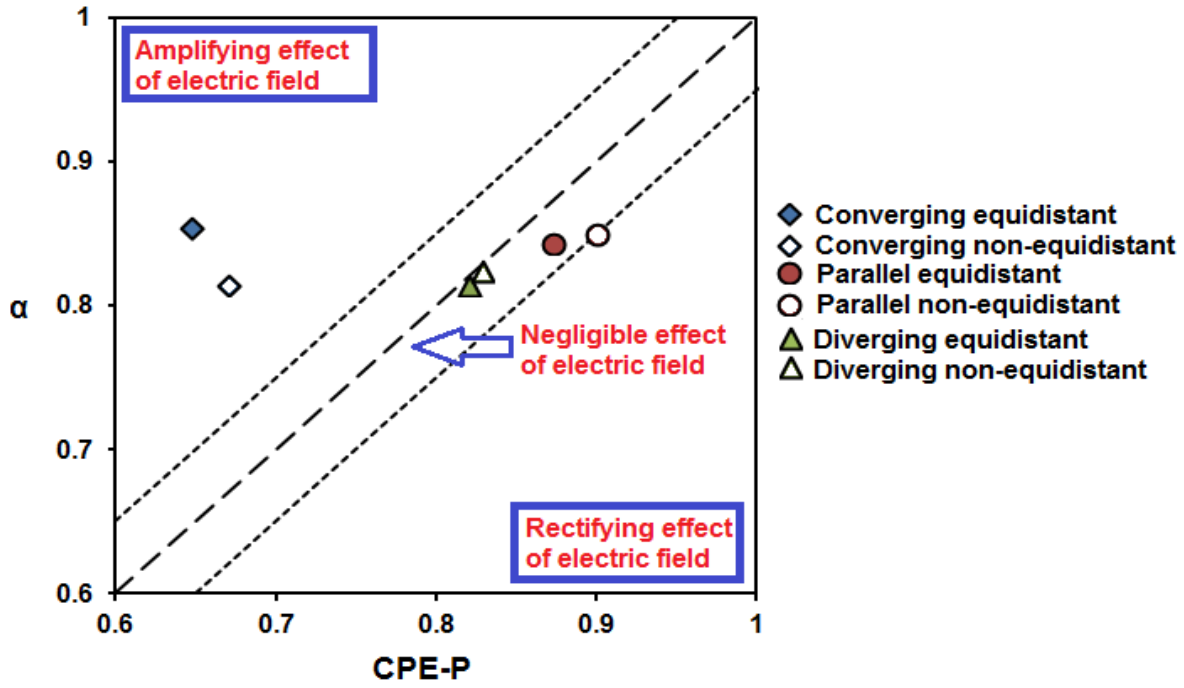

Fig. 6.3 The effects of electric field and coating morphology under different electric field types during the PEO process.

In terms of fractal analysis of cross-sectional SEM images, the above-mentioned parameters such as thickness, porosity, surface and interfacial roughness are the main morphological characteristics affecting the fractal dimension of the PEO coatings. Correlations between these morphological characteristics and fractal dimension/CPE-P value from the ISIS data are analysed as shown in fig 6.4~6.7. From the trend line equations and corresponding standard deviations, CPE-P presents much higher correlation than the α values with the coating thickness (R^2= 0.77). Both the values of CPE-P and α present weak correlations with surface roughness (R^2= 0.42 and 0.44). As regards to the porosity and interface roughness, both values present very low correlations (R^2 <0.1).

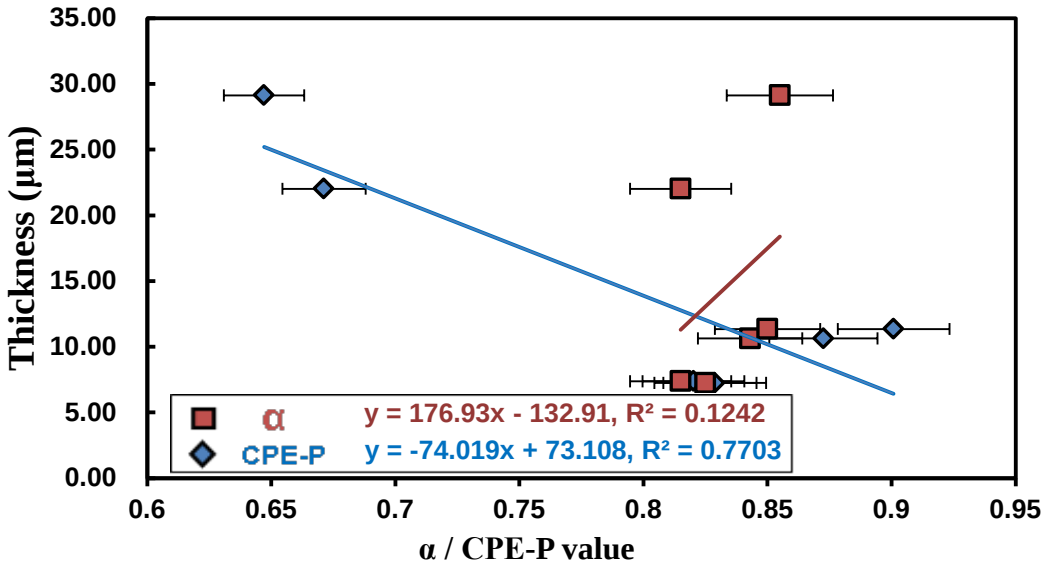

Fig. 6.4 Correlation between thickness and fractal dimension/ CPE-P values

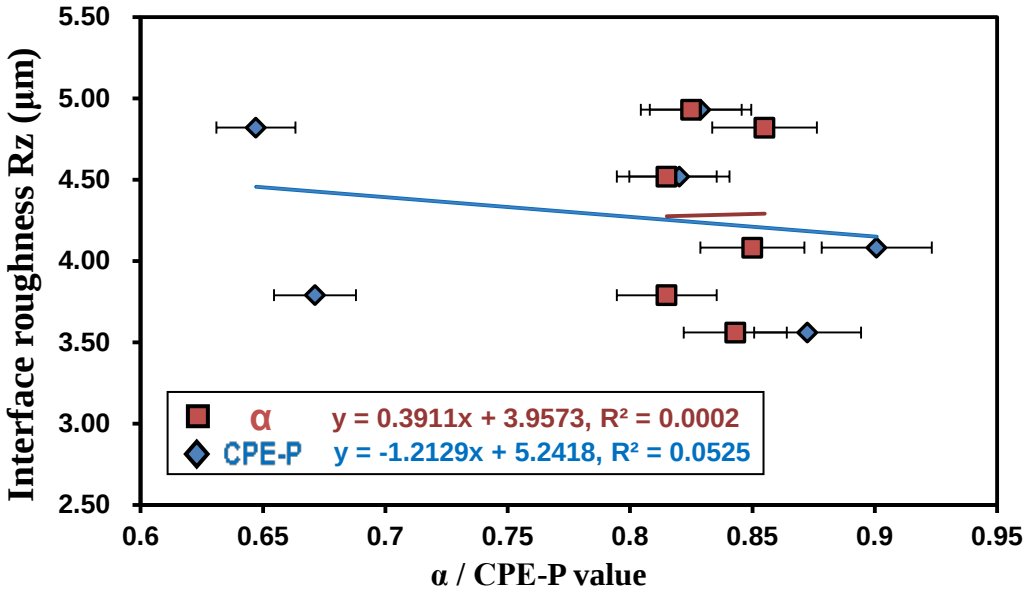

Fig. 6.5 Correlation between interface roughness and fractal dimension/ CPE-P values

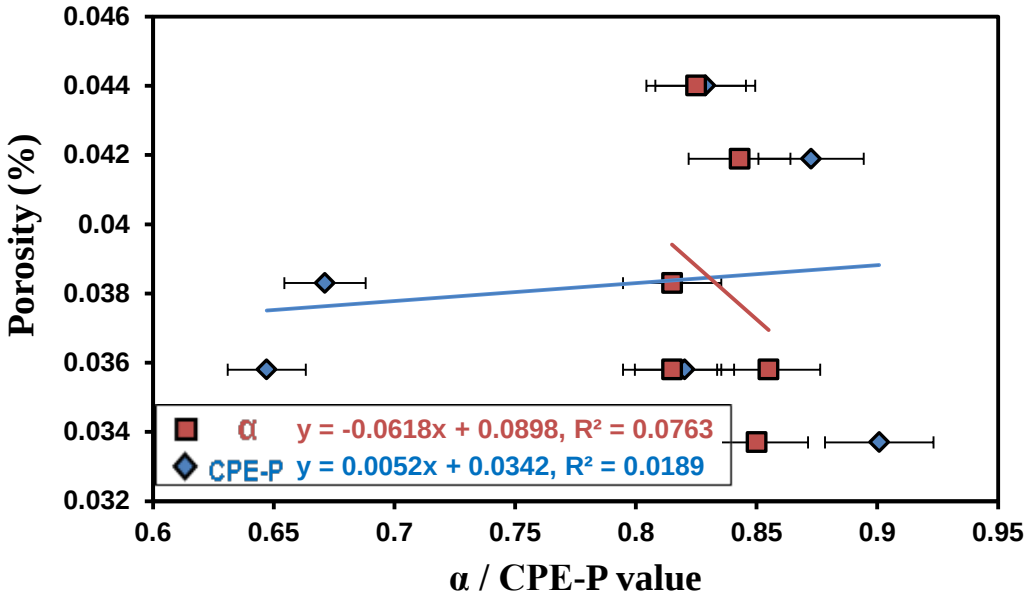

Fig. 6.6 Correlation between porosity and fractal dimension/ CPE-P values

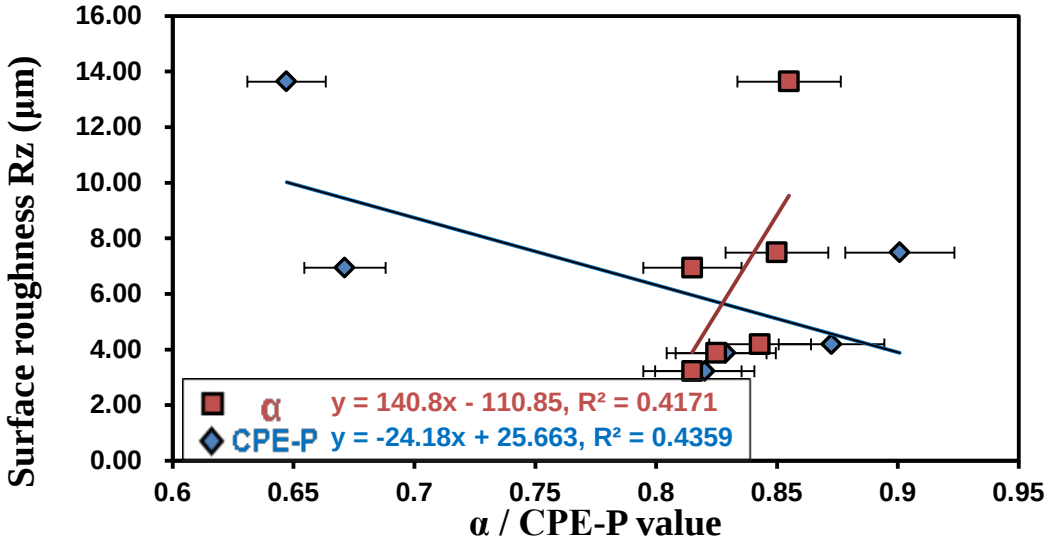

Fig. 6.7 Correlation between surface roughness and fractal dimension/ CPE-P values

To confirm that the differences between CPE-P and α values are caused by the electric field distribution, 2D images of electric field distribution obtained by COMSOL modelling of corresponding electrode geometries and layouts in the cell were transferred to the gray-scale images as shown in figure 6.8 and subjected to fractal analysis. In the figure, white regions indicate the electrodes, while the gray-scale gradient indicates the distribution of the electric field between these. In the converging electric field conditions, the non-equidistant electrode layout provides a larger field distribution region and a relatively stronger intensity near the working electrode (centre) than the equidistant one. Similar to the converging condition, the non-equidistant electrode layout under the parallel electric field condition provides a stronger intensity of electric field between the working electrode and the near side of the counter electrode (figure 6.8 d). The difference in the electric field intensity is inconspicuous between the equidistant and non-equidistant electrode layouts under the diverging electric field condition; the distribution of electric field is even between the electrodes in the equidistant electrode layout under all electric field conditions.

Table 6.5 shows the fractal dimension of electric field distribution modeled by COMSOL and transferred to α_e values using equation 6.1. In the table, the strongest effect of electric field distribution occurs under the converging condition, with α_e = 0.85 and 0.88 obtained for the equidistant and non-equidistant electrode layouts, respectively. The effects of electric field distribution are slightly stronger for the diverging electric field conditions (~0.90) than for the parallel ones (~0.93). The only obvious effect of the inter-electrode distance is observed for the converging type of electric field, for which the α_e values are different in 0.03. The correlation between electric field distribution (α_e) and CPE-P/α value is shown in figure 6.9, from which it follows that the electric field distribution provides a strong correlation with the CPE-P value, and a weak correlation with the α value. These results are consistent with data of Table 6.4, indicating that relatively strong effects of electric field occurred in the both converging electric field conditions, whereas the effects of electrode layouts are negligible under the parallel and diverging electric field conditions.

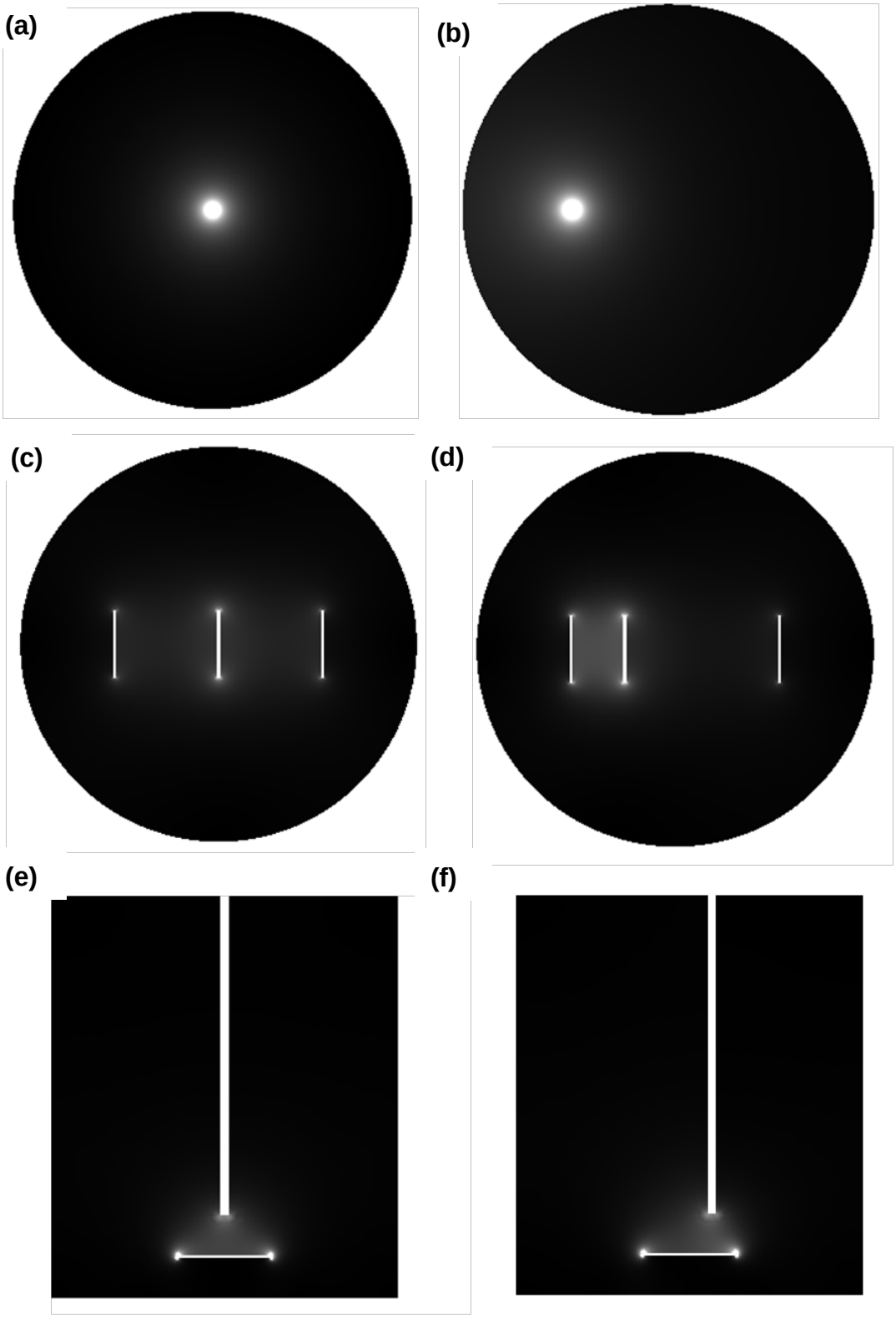

Fig. 6.8 Gray-scale images of electric field distributions obtained from the COMSOL modeling of the PEO process in the cells providing different types of electric field and electrode layout: (a) converging - equidistant, (b) converging - non-equidistant, (c) parallel - equidistant, (d) parallel - non-equidistant, (e) diverging - equidistant, (f) diverging - non-equidistant.

Table 6.5 Fractal dimensions of COMSOL modeled electric field distribution

Field	Layout	Fractal dimension of Electric field	α_e
Converging	equidistant	2.18	0.85
	non-equidistant	2.13	0.88
Parallel	equidistant	2.08	0.93
	non-equidistant	2.09	0.92
Diverging	equidistant	2.11	0.90
	non-equidistant	2.11	0.90

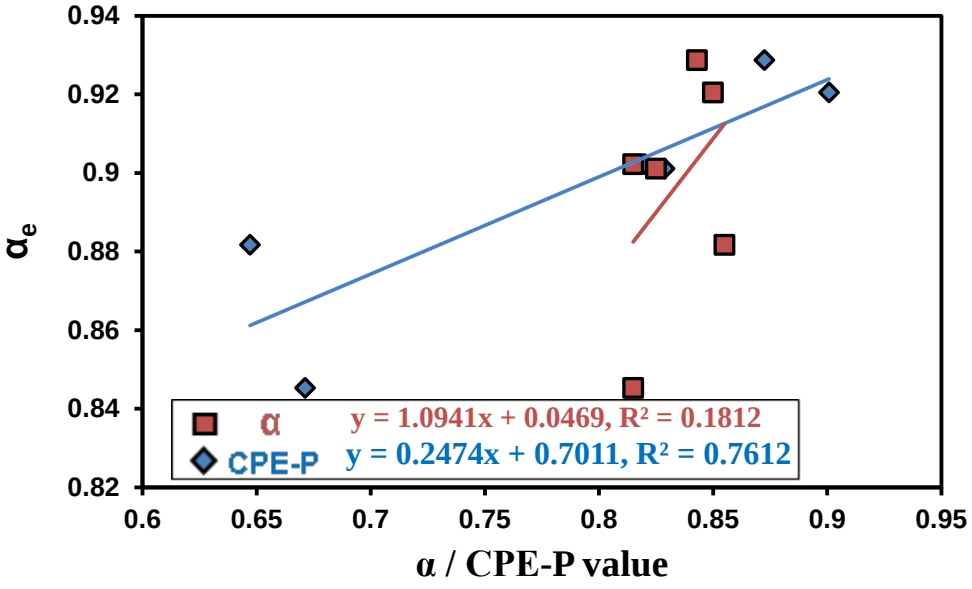

Fig. 6.9 Correlation between electric field distribution and fractal dimension/ CPE-P values

6.4 Summary

In this part of the work, fractal analysis was used to investigate the coating morphology presented in a simple form of α. The α value was compared with the CPE-P values obtained using the ISIS method to understand the effects of coating morphology and electric field on the working electrode during the PEO process. The coating characteristics under different electric field conditions and electrode layouts were studied. The difference in the thickness of PEO coatings produced in parallel and diverging electric fields with equidistant and non-equidistant electrode layouts is negligible. This is however significant for the converging field. The coating porosity is similar for all conditions, ranging from 3.5 ~ 4.5 %. Surface roughness was found to be higher for the coatings produced in the converging electric field, whereas the interfacial roughness, is similar for all coatings.

Comparison between the theoretical capacitance, which accounts for the specific surface and interface area of the coating, and corresponding CPE-T values derived by ISIS fitting in the high frequency domain shows that the CPE-T values are around 10 times larger than the theoretical capacitance in parallel and diverging conditions, and around 100 times larger in the converging one. These results can reveal that the CPE-T values from the ISIS fitting do not indicate the status of the whole PEO coating but only relate to the barrier layer at the bottom of the discharge channel. Therefore, the thickness of the barrier layer (d_{BL}) can be evaluated from the CPE-T value and specific interface area. The results of d_{BL} are consistent with the cross-sectional SEM images of PEO coatings.

Comparison of the α values from fractal analysis with corresponding CPE-P values obtained by the ISIS method indicates that: (1) for the converging field conditions, both heterogeneous coating morphology and non-uniform electric field contribute significantly to the impedance spectra of the PEO process, (2) for the parallel field conditions, the impedance is mainly affected by the heterogeneous coating morphology, and (3) for the diverging field conditions, the impedance is affected only by the coating morphology.

The studies into correlations between morphology characteristics and the α value/CPE-P have demonstrated relatively strong correlations between the CPE-P value (including the effect of coating morphology and electric field distribution) and the coating thickness. Both CPE-P and α values presented weak correlations with surface roughness and no correlations with interfacial roughness and porosity. The electric field distribution obtained by COMSOL modelling and presented in the form of α_e value has a strong correlation with the CPE-P value from ISIS, and weak correlation with the α value from the coating morphology

analysis.

Chapter 7

Characterisation of discharge events during plasma electrolytic oxidation of Al

7.1 Introduction

Results of ISIS studies discussed in previous chapters have revealed uncertainties in interpretation of the PEO system behaviour outside the range of available frequencies (20 Hz to 20kHz). The data processing procedures and analytical methods for evaluation of the boundary conditions do not allow elimination of these uncertainties. This outlines the need for application of frequency response characteristics of the PEO system at high and low frequency ends. This also limits the studied current modes to the DC PEO regime as there is no technical possibility at the moment to carry out PBC PEO treatments outside the above frequency range.

Yet another challenge remains in identification of discharge specific optical emission with fluctuations in the electrical signal from the PEO system. The overview of the state-of-the-art in this field (Chapter 2) has revealed the need in careful time-resolved imaging, study of individual discharge events in a wide range of exposure times. To address these problems, high-resolution imaging and current probe methods are applied in this Chapter to the DC PEO process of Al carried out at different voltages.

7.2 Methodology of discharge events investigation

7.2.1 Experimental details

Rectangular samples with size 20mm x 25mm x 5mm made from 6082 Al alloy with the main surfaces preliminary polished to achieve Ra ~ 0.1μm were used in experiments. The electrolyte was composed of 1.5 g/L KOH, 1.5 g/L $Na_4P_2O_7 \cdot 10H_2O$, 2 g/LNa_2SiO_3. The PEO treatments were carried out in a 10-litre glass tank equipped with cooling and agitation systems to control the temperature of electrolyte around 30℃. The duration of PEO treatment was setup at 20min in each experiment. A DC power supply was chosen to provide a simple steady power source and avoid discharge interruption due to the changing polarity or pause introduced in the bipolar and unipolar pulsed modes respectively.

A Specialised Imaging Multi-Channel (SIM) Framing Camera was used to obtain ultra-high speed images (UHSIs) of the sample surface during the PEO process. Further details of this equipment are provided in sections 3.6. The SIM camera was controlled by specialised software via a standard ethernet link. The pixel images were recorded in the form of digital *.TIF file containing information on relative intensity (0~4095 arbitrary unit) and coordinate position.

Tektronix A6303 current probe with TM502A amplifier (100A, 200MHz) used for data acquisition. NI PXI-5922 dual-channel digitalizer on PXie-1071 chassis were used to record the current signal and analyse fast current transients in different time scales 10^{-3} to 10^{-6}s (Figure 7.1). The signal can be plotted in time domain and transferred by Fast Fourier Transform (FFT) to Power Spectral Density (PSD) in frequency domain. The vertical resolution at this device is 16 bits and 24 bits at samples rate of 15MS/s and 500k/s, respectively. The PXie-1071 interface was also used to control the power supply for the PEO treatment.

By using the above equipment, two types of experiments were designed to investigate the discharge events occurring during the PEO process. The first type of the experiment was carried out using a fixed exposure time to study lifetimes and trajectories of discharge events. Variable exposure time experiments were also carried out to investigate correlations between the exposure time and discharge size and intensity. Further details of these experiments are discussed in the following sections.

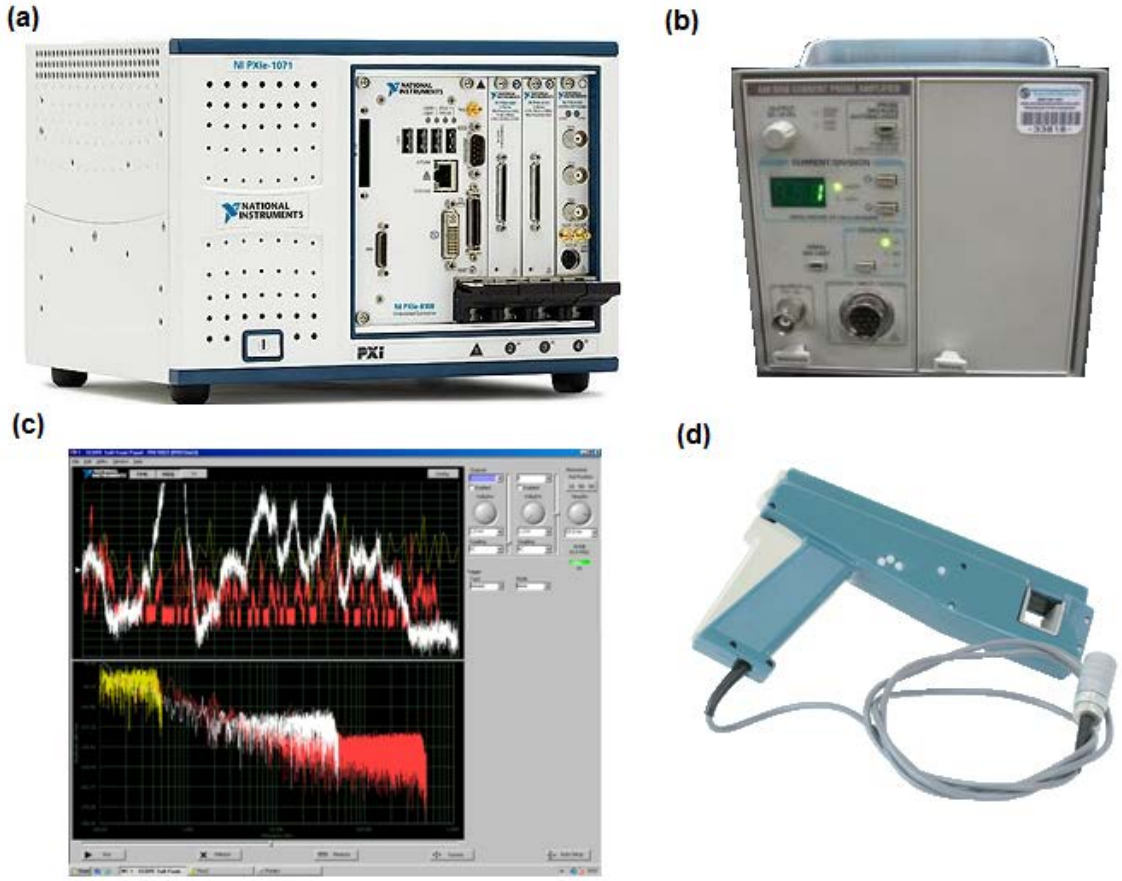

Fig. 7.1 Data acquisition accessories on NI PXie-1071 platform (a), including TM502A amplifier (b), NI PXI-5922dual-channel digitalizer (interface) (c), and Tektronix A6303 current probe (d).

7.2.2 Fixed exposure time experiments

The UHSIs were captured under applied voltages of 500V, 550V and 600V. A fixed exposure time was setup in the range from10ns to 1ms and kept constant for all frames. The captured UHSIs were used to reveal characteristics as lifetime, relative intensity, size and trajectories of individual discharge events. These characteristics were also correlated with coating morphology from SEM images.

7.2.3 Variable exposure time experiments

It is believed that the exposure time in fast video imaging affects the evaluation of characteristics of discharge events, such as intensity, size and lifetime. Therefore, it was

necessary to investigate various exposure times. The exposure times of 16 channels were set in 8 groups at 10ns, 30ns, 100ns, 300ns, 600ns, 1μs, 6μs and 10ms and the inter frame time was set as 100ns. These experiments were implemented under two applied voltages of 450V and 500V. To investigate the effects of exposure time at different stages of the PEO process, the UHSIs were captured every 5 minutes of processing.

7.2.4 Image analysis

A *.TIF file of UHSI was initially accessed by a Golden software Surfer 10 to transfer the digital image data to numerical of relative intensity with coordinate position. This step is required, as the information in the *.TIF file cannot be used directly. Here, the relative intensity with coordinate position were used to identify the location of discharge event. The small regions with around 50x50 pixel area with a discharge in the centre were then marked. After that, a SigmaPlot software was used to select that small region for individual discharge event analysis. The data were then presented in the form of a 3D plot with relative intensity versus coordinate position as shown in figure 7.2. From these 3D plots, the information of each individual discharge event was gathered directly in the form of peak intensity, full width at half maximum (FWHM) and the peak coordinates of the discharge. Moreover, the integrated optical emission intensity of the individual discharge is calculated as follows:

$$I = 0.785 \cdot (FWHM)^2 \cdot I_{peak} \tag{7.1}$$

which is the volume of each individual discharge in the 3D plot. However, this method was admitted to be laborious and time consuming, resulting in very slow data processing.

To speed up the process, a special program was then developed based on MATLAB software in collaboration with Dr. E. Parfenov and Ms. V. Mukaeva. This special program can directly present the information with values from each location of digital UHSI and distinguish the discharge events, with information provided on their location, relative intensity, centre of discharge, FWHM. In the case of over range intensity, the peak intensity can be estimated by Gauss fitting (figure 7.3). The range of coordinate position can also be selected easily for the individual discharge event analysis.

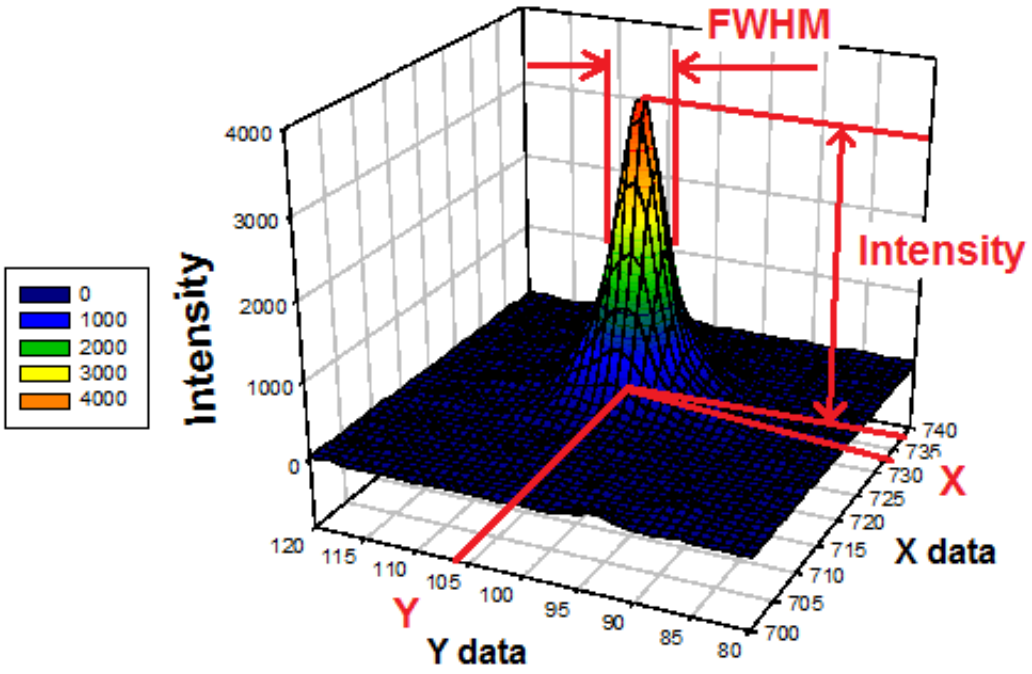

Fig. 7.2 A typical example of 3D plot representing an individual discharge event (500V DC power supply with 1μs exposure time) with the main characteristics transferred from digital *.TIF image.

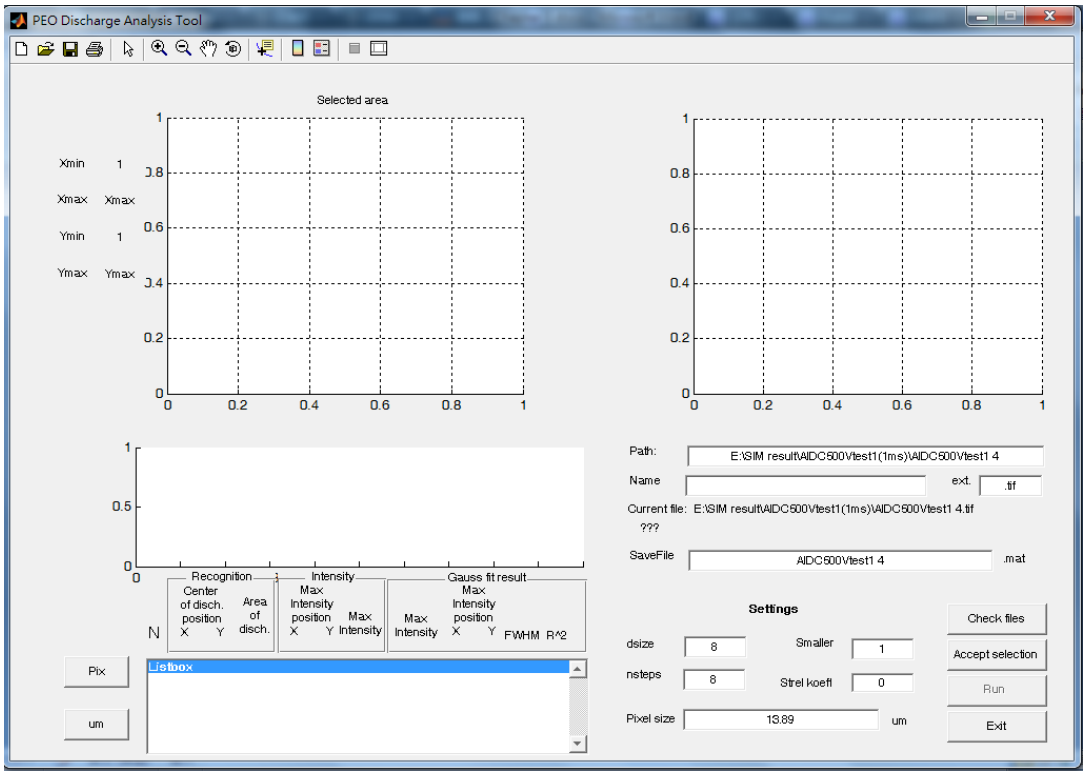

Fig. 7.3 The window of a MATLAB program for discharge event analysis.

7.3 Spectral analysis of current signal

PEO is a multiscale process, during which main process characteristics, including electrical signals, evolve both gradually (i.e. during the treatment period of several minutes) and instantly (i.e. current fluctuations and flashes of light are observed in a sub-second scale). The analysis of the current signal was therefore performed on two scales: as a slowly evolving current transient and as a fast (sub-second) transient, bearing information on individual discharge events.

7.3.1 Slow current transient

During PEO processing, the current signal was recorded by a data acquisition device with the sampling rate of 0.5 Hz. Under the voltage control mode, the current transient can be used to represent the coating growth during the PEO process. The current density increased sharply in the first 15s to reach the maximum of 6.2 A/dm^2 and 15.8 A/dm^2 at the applied voltages of 450V and 500V, respectively (figure 7.4). The current densities then decreased until nearly constant values were achieved at around 6 and 13 minutes for 450 and 500V, respectively. The corresponding values of the steady state current density were around 0.15 $A/dm^2$and 1.25 A/dm^2. A correlation with variation of the density and size of discharge events during the PEO process was observed similar to work by Yerokhin, et al [100]. In the early stage of the PEO processing, in the sharply dropping down region of current density, the discharge events were relatively active, characterised by high spatial density and small size. In the middle stage, while the current density reduction rate slowed down compared with the previous stage, the density of discharge events decreased and the average size obviously increased. The current density was at the steady state with a constant value in the last stage. In this period, the average size of discharge events slightly increased while the spatial density decreased significantly.

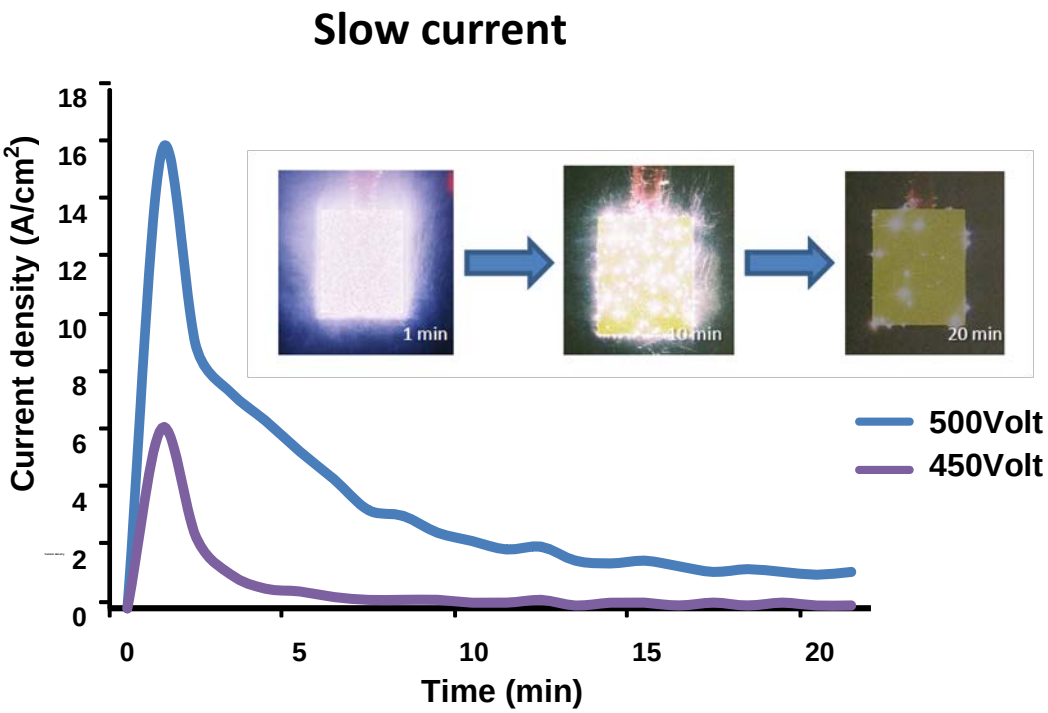

Fig. 7.4 Temporal evolution of current density and discharge appearance during PEO of Al under potentiostatic conditions.

7.3.2 Fast current transient

In addition to the slow current evolution, current transients were also investigated in the sub-second time scale (Fig.7.4) with current signal oscillograms with NI PXI-5922dual-channel digitalizer (figure 7.5). Both the current signal from the PEO process and the so called 'blank' signal (representing noise in the system at the open circuit) were recorded for 2ms at a sampling rate of 15×10^{7}S/s, and 100mA/div. and at 16 Bit vertical resolution. The amplitude range of current signal is from ~100 to ~300mA, with the background noise being only ±25mA. This value is higher than the previously reported as the largest current pulses to be ~ 70 mA at 8 Bit vertical resolution [97]. The current spectra were presented in different time scales as shown in figure 7.6. In the figure, the amplitude and waveform of current signal in different time scales can be observed correlated to the frequency domain as 1k~10kHz, 10k~100kHz, and 100k~1000kHz, respectively. Figure 7.6 (a) represents the oscillogram of current signal recorded during 1ms, in which around 20 obvious peaks can be observed. This corresponds to a resulting rate of a peak about $3\times10^{4}s^{-1}$, which can be observed directly in figure 7.6 (b). Figure 7.6 (c) represents the duration of a single current peak (~7μs), which matches well with the data of work [97]. According to these results, discharge events should be observed under the time scale range from 10^{-6} to 10^{-5}s by UHSIs. The UHSIs analysis is presented in section 7.4.

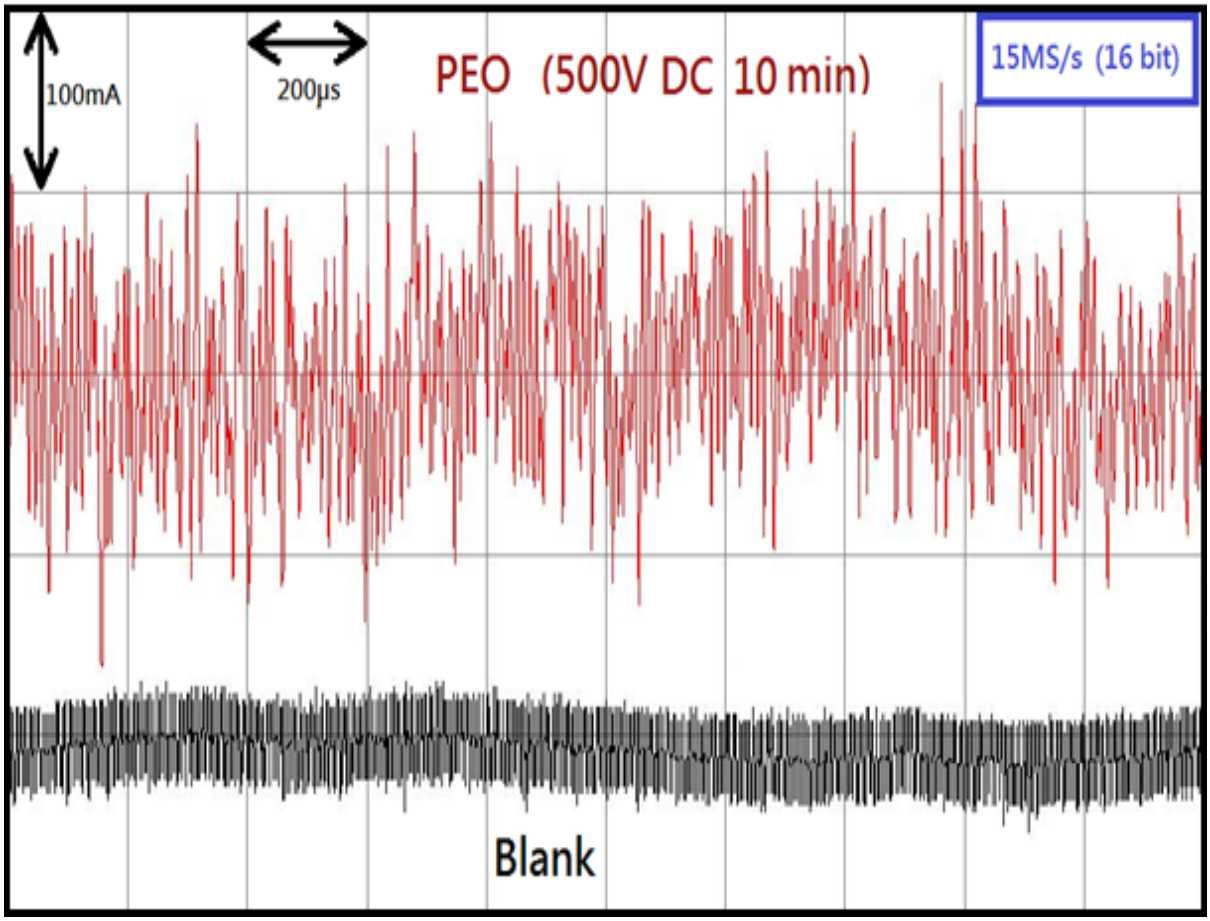

Fig. 7.5 Oscillogram of current transient during DC PEO process at 500V.

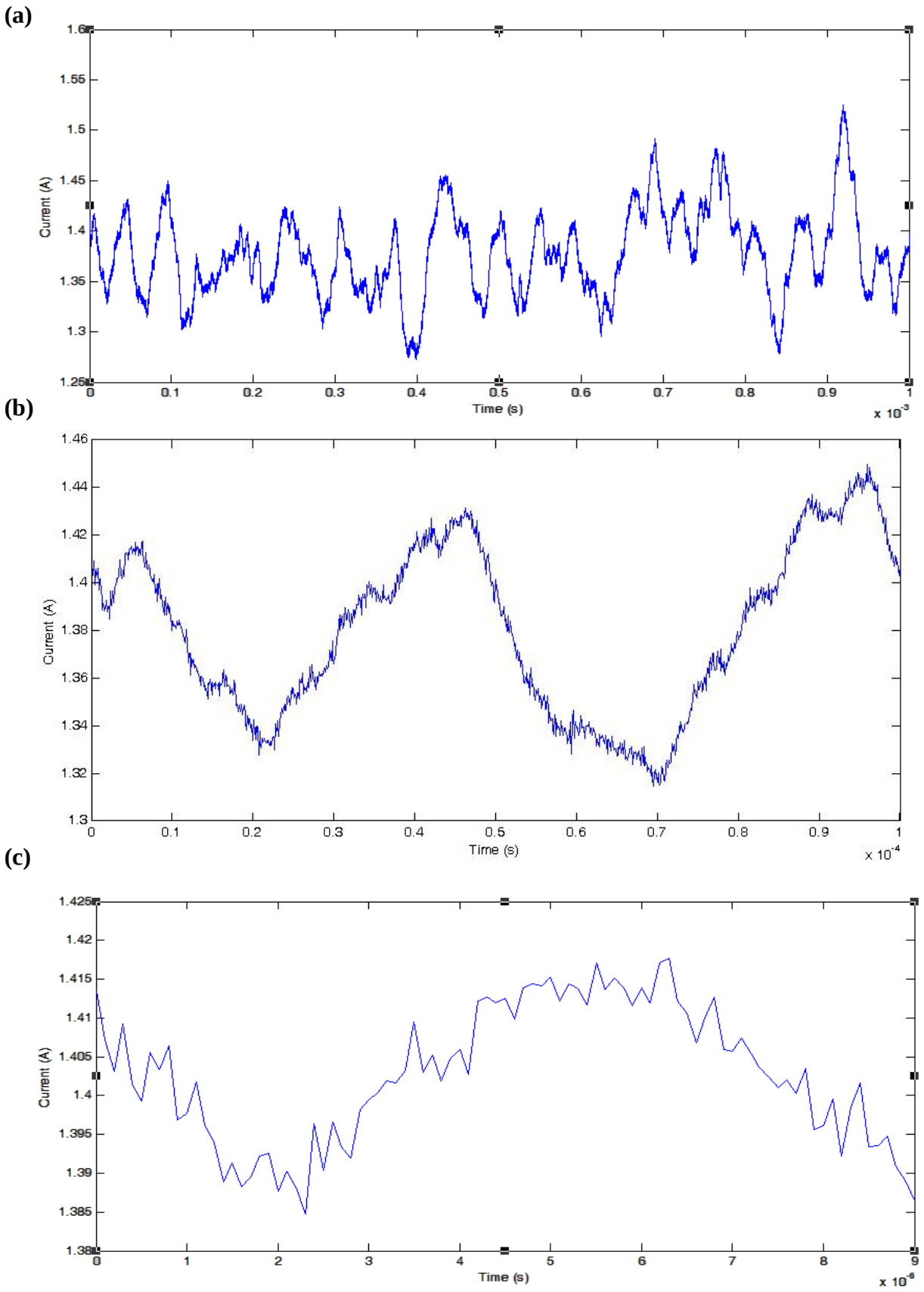

Fig. 7.6 Oscillograms of current signal in different time scales (a) 10^{-3}s, (b) 10^{-5} s (c) 10^{-7} s.

7.3.3 Spectral analysis in frequency domain

A typical power spectrum of the currents signal obtained by the FFT into the frequency domain is shown in figure 7.7. Compared with the blank current signal (background signal), the current pulses of the DC PEO process appear in the frequency range of 1...300 kHz, which is wider than the range reported by Dunleavy et. al (4...170 kHz) [97]. The current transients were also studied at different stages of the PEO process (figure 7.8). It can be seen that the current spectra vary significantly with processing time, and the spectral amplitude is gradually reduced. Four different main slopes can resolved in the spectral in frequency ranges of 300...~600Hz, ~700...~9kHz, ~9k...300kHz, and 300k...1mHz. Several peaks could also be observed in the relatively low and middle frequency regions around 2...7 kHz (I) and 20...30 kHz (II), which corresponds to about 150...500μs and 33...50μs, respectively, in the time domain. The peak in the frequency range 20...30kHz is consistent with the previous study [97]. These results exactly match the time constants of the two negative resistance loops in the equivalent circuits obtained by fitting ISIS data in Chapter 4. These peaks become more obvious in the later stages of the PEO process. The peaks in the frequency range 2...7 kHz may be due to discharge clustering, which is consistent with the observed increase in the size of discharge at longer treatment times. The peak in the range 20...30kHz is conjectured to be due to dielectric breakdown, for which the coating thickness increases with treatment time. More energy is therefore required to trigger the dielectric breakdown. A correlation between the above two phenomena is considered plausible. Current signal oscillograms in these two frequency ranges are presented in figure 7.6 (a) and (b).

Figure 7.9 features the power spectra of the currents signal in the frequency range from 0 to 30kHz, which overlaps to the frequency range chosen in the ISIS experiments. Four different slopes can be observed in different frequency regions. In the lowest frequency region (0...2kHz), the first (negative) slope occurred and the spectra decreased sharply to around -90...-95 dBV. The value of power spectrum further decreased at the later stage of the PEO process, beside the first two minutes. The second slope occurs in the range of 2k...10kHz, which are positive at spectrum of 2min and 5min, and nearly horizontal at others. A peak occurs at the end of the second slope throughout the PEO process. On the spectrum recorded at 2min, the peak is located at 10kHz, but it shifts toward lower frequencies at later PEO stages and resides at ~5kHz after 15 minutes of treatment. The third slope occurs directly after the peak. 10, 15 and 20min of the PEO treatment, the third and the fourth slope occur in the frequency ranges 6...10kHz and 10...30kHz, respectively. For the first two spectra, it is difficult to separate the third and the fourth slopes. Consistent with figure 7.8, a

peak occurs at ~25kHz on the spectra recorded at 10, 15 and 20min of the PEO process.

Different slopes and peaks in the power spectrum are indicative of different processes taking place during PEO treatment. However, the physical meaning of these processes is not clear and further investigation is required. Four slopes present in the power spectrum, coincide with the number of loops used in the equivalent circuit to fit the ISIS. Both the ISIS and power spectrum density method are based on the frequency domain approach and should therefore be complimentary.

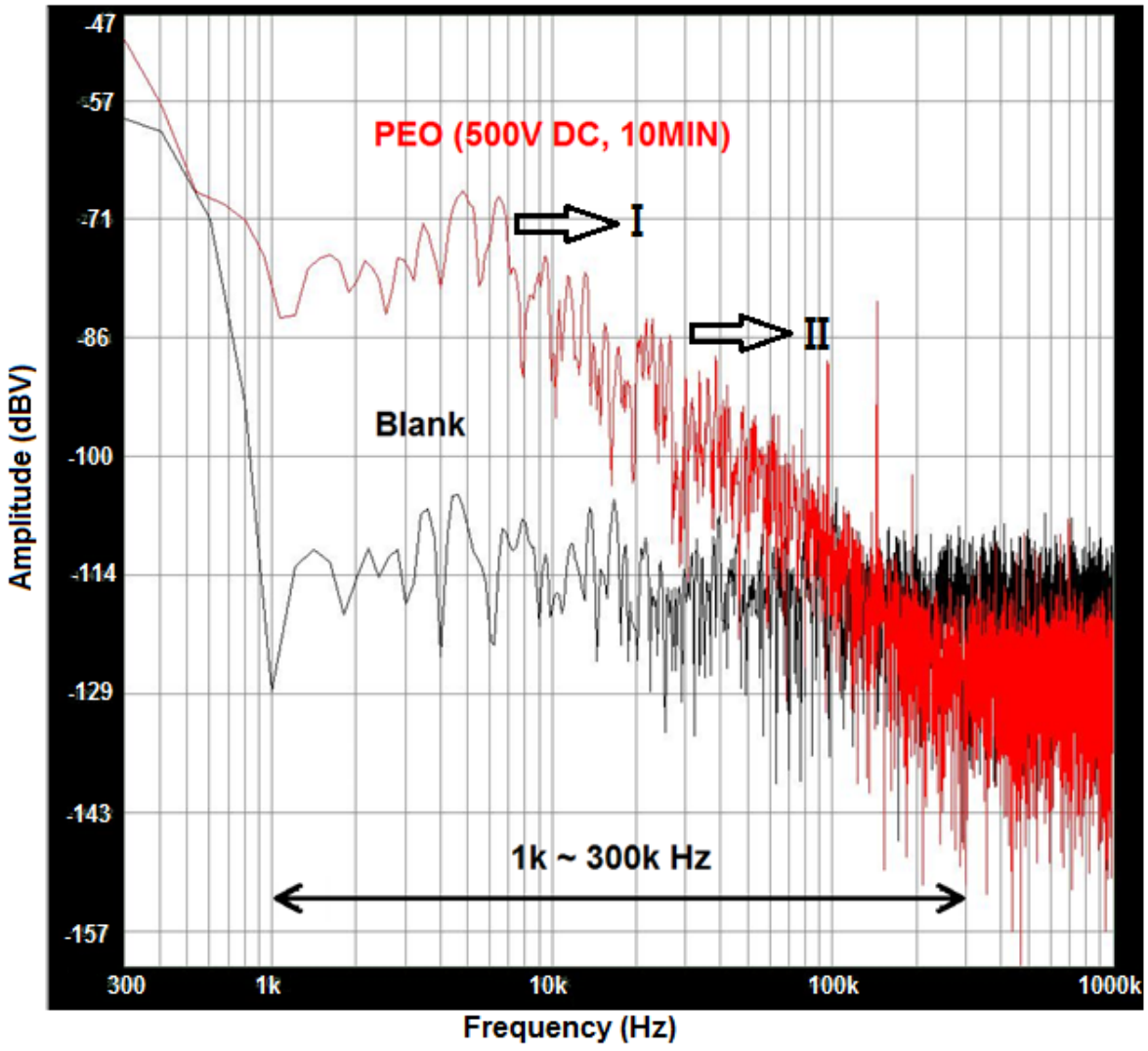

Fig. 7.7 Spectra of fast current transients of current signals recorded for the unloaded (blank) and DC PEO process of Al operated at 500V.

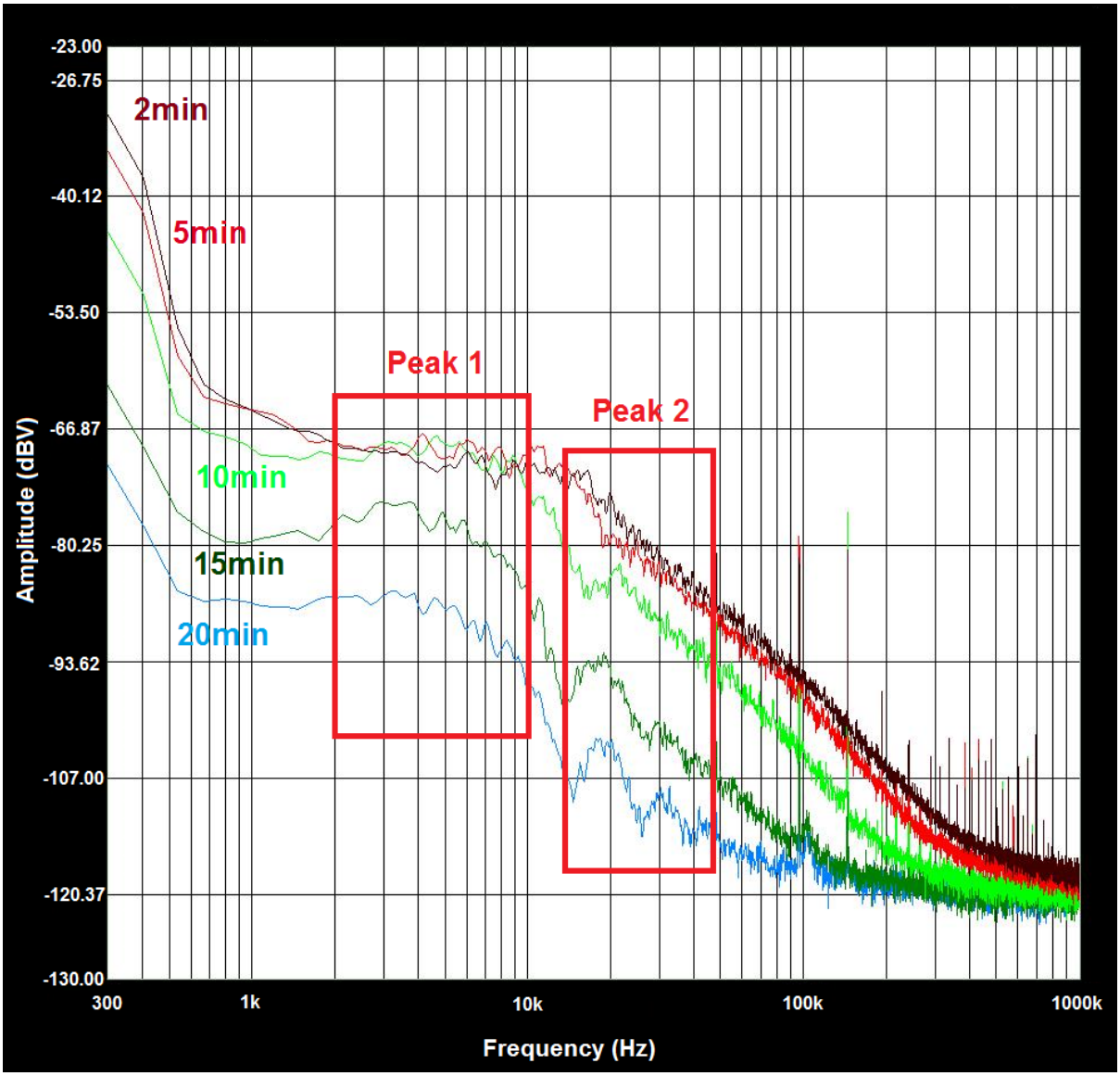

Fig. 7.8 Comparison of FFT spectra of current for different time stages of the DC PEO process operated at 500V.

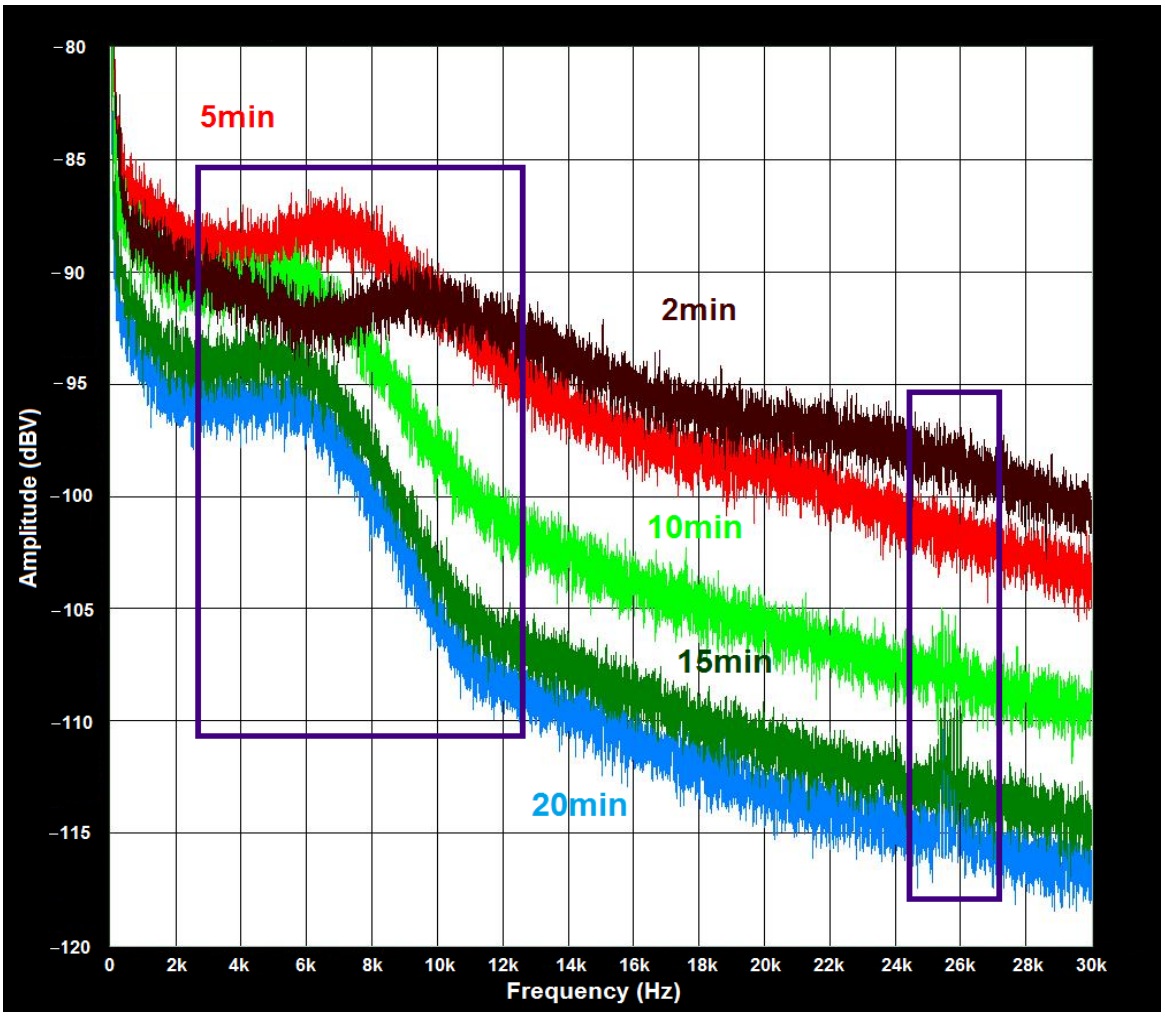

Fig. 7.9 Comparison of FFT spectra of current under low frequency region (0...30k Hz) for different time stages of the DC PEO process operated at 500V.

7.4 Analysis of discharge behaviour

7.4.1 Duration of discharge events

Duration of individual discharge events can be determined directly from the variation of optical emission in the images taken in 16 frames as shown in figure 7.10. To present it in a more apparent way, each individual discharge event was plotted in 3D with x and y axes corresponding to the position coordinates and the z axis to the relative intensity (figure 7.11). Rising and falling of intensity of each discharge during its lifetime can be seen in the 3D plots. Therefore, the duration of individual discharge events was studied under two different exposure times of 1 and 0.5μs. The results presented in figures 7.12 and 7.13, indicate that the

duration of individual discharge event varies between 1 to 12μs, and the longer exposure times provide longer discharge durations. These ranges of discharge duration are consisted with the current signal recorded in figure 7.4. However, the duration of a discharge event of around 10μs is shorter than the previous studies [97,109,162,163,165]. To compare with the ISIS results in Chapter 4, the nearest time constant were from the first and second RC loops of equivalent circuit which the time range of 10~100μs. It can be therefore speculated that the first and second loop are associated with the breakdown and discharge phenomena, respectively, during the PEO process.

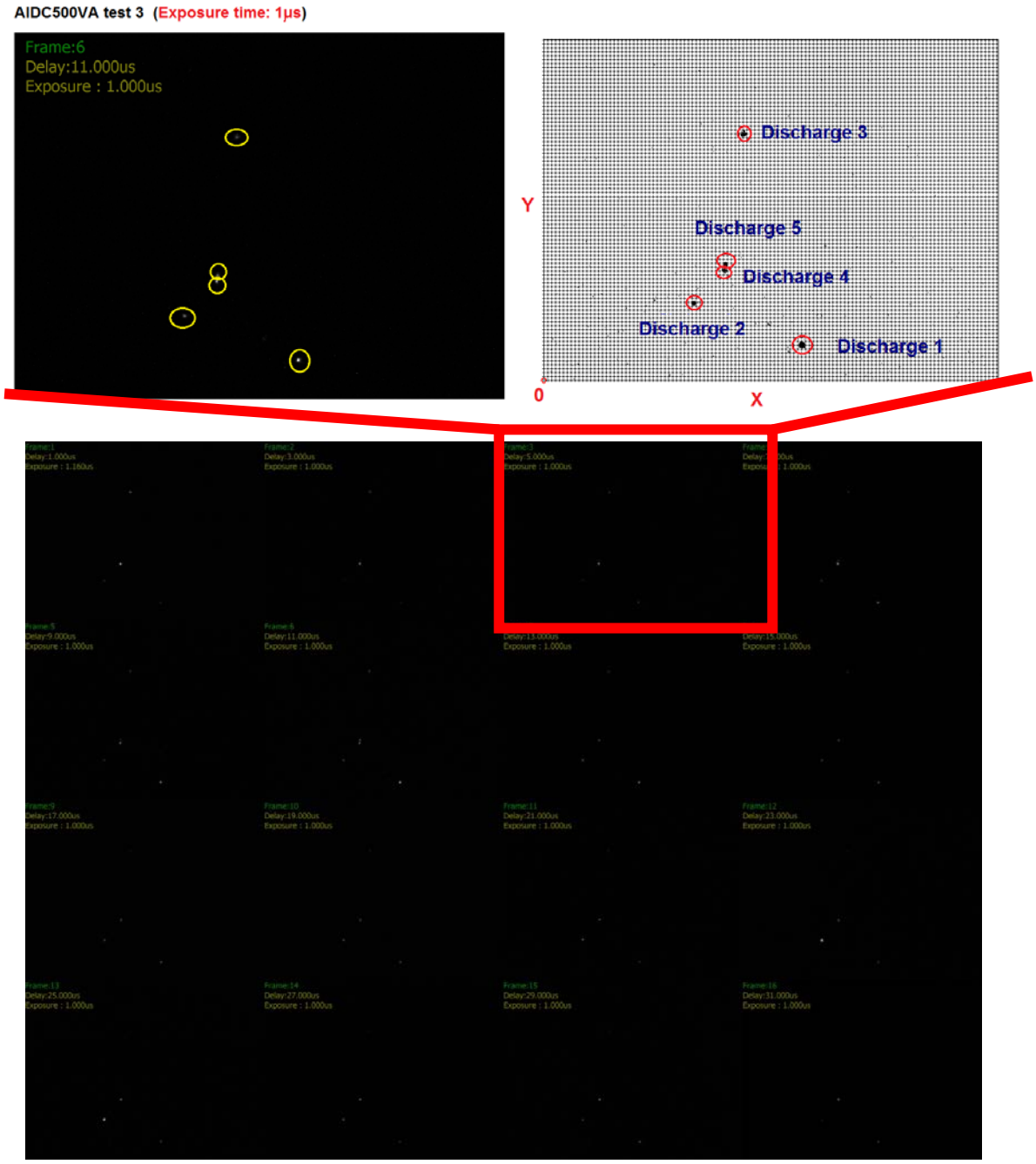

Fig. 7.10 16 UHSIs of discharge events obtained using SIM-16 camera with interframe and exposure times set of 2μs and1μs, respectively.

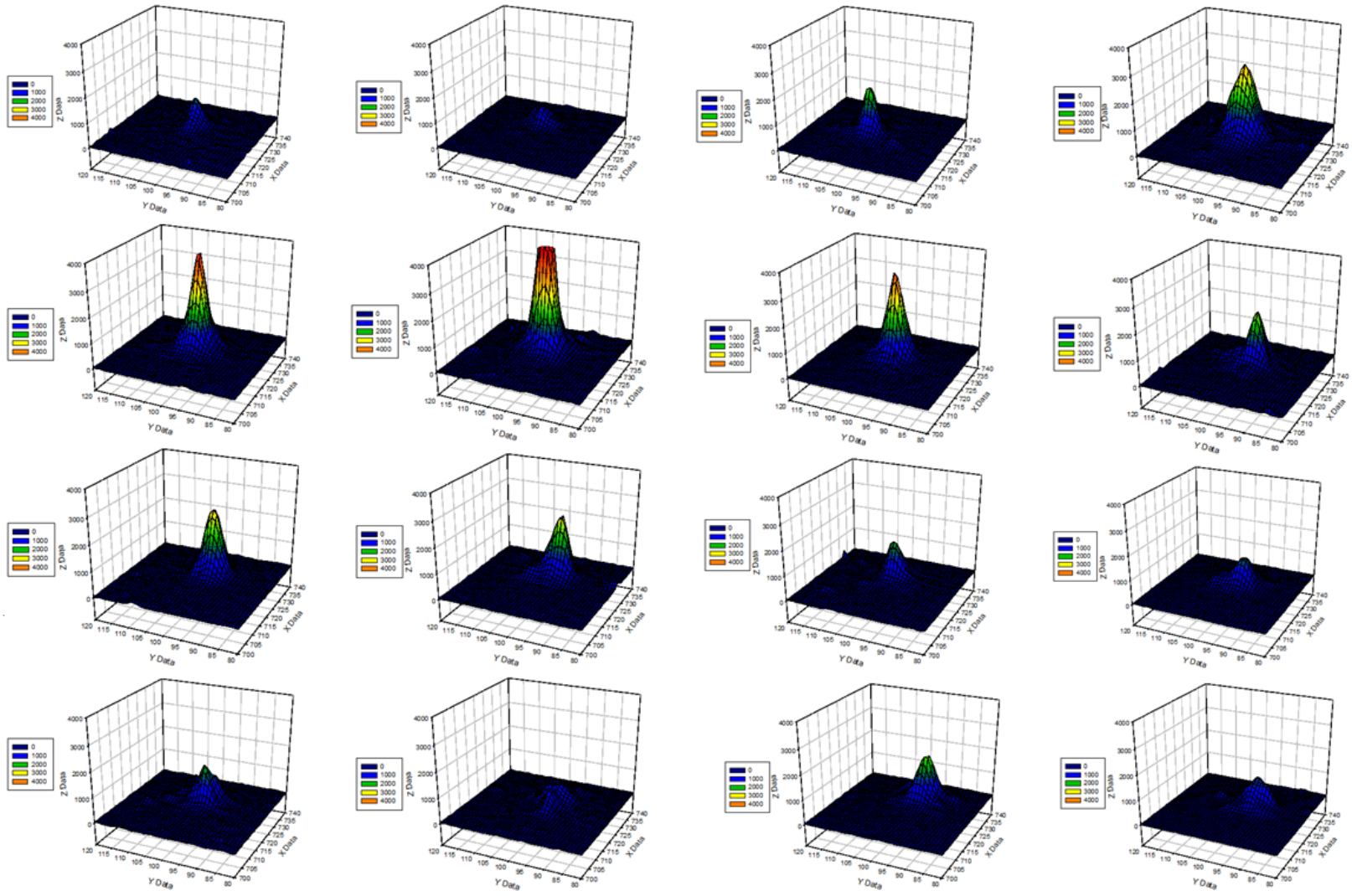

Fig. 7.11 3D plots of an individual discharge event showing variation of its location and intensity with time.

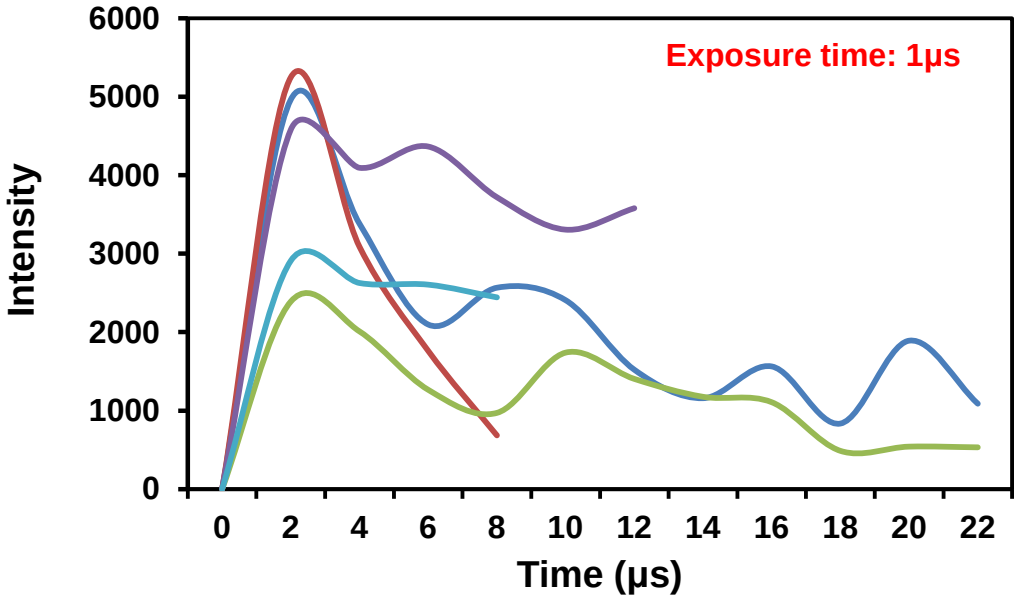

Fig. 7.12 Duration of individual discharges during 500V DC PEO process observed at 1µs exposure time.

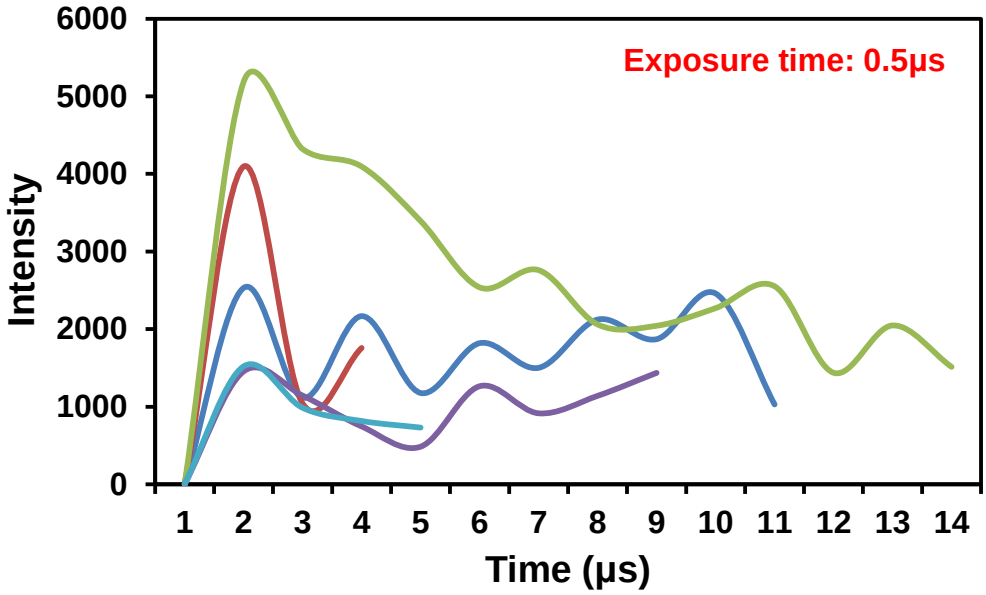

Fig. 7.13 Duration of individual discharges during 500V DC PEO process observed at 0.5µs exposure time.

7.4.2 Characteristics of individual discharge events

Beside the duration of discharge events, other characteristics can also be derived from the 3D plots, such as FWHM, peak intensity, and coordinates (figure 7.2). For the analysis of these characteristics, the spatial resolution was estimated by conversion of pixel to real micrometer scale (1 pixel = 30.5μm). The peak intensity indicates the discharge optical emission activity. Usually, the peak with the location region of light emission spot not exactly in the centre. From the 3D plots of discharge events, it is clear that the intensity decreases from the centre to the periphery, so the Gaussian distribution of optical emission intensity can be considered as a good approximation. FWHM were calculated to present the average diameter of the individual discharge. When integrated over the sample surface, this characteristic indicates the fraction of the coating affected by the discharge. The magnitude of peak intensity and FWHM varied with time as shown in figure 7.14. The integrated optical emission intensity of the individual discharge was calculated from the 3D plots and by equation 7.1. Variations of integrated optical emission intensity of selected discharges with time are shown in figure 7.15. Comparing figures 7.14 and 7.15 with the current oscillations in figure 7.6 (c), the duration of an integrated optical intensity peak is consistent with the current oscillation, which is around ~10μs. It can be said that the current evolution in the time scale of 10^{-6}s indicates the duration of discharge events.

The peak centre was considered as the discharge location which allows to trace the trajectory of the discharge displacement from frame to frame. To verify the displacement of individual discharge is genuine, a possible interference caused by the system vibration was evaluated and found insignificant. Displacements of discharges from frame to frame were random, well exceeding the pixel resolution, and indicated a typical movement within ~200μm from the initial location during the period of imaging (figure 7.16). The average velocity of the discharge displacement was of the order of 33.5m/s.

The characteristics of an individual discharges were presented above. However, it is believed that different camera exposure time may affect the UHSI analysis of the discharge characteristics, such as intensity and FWHM. Therefore, it is necessary to investigate the correlation between discharge characteristics and different exposure times. The results are presented and discussed in the next section.

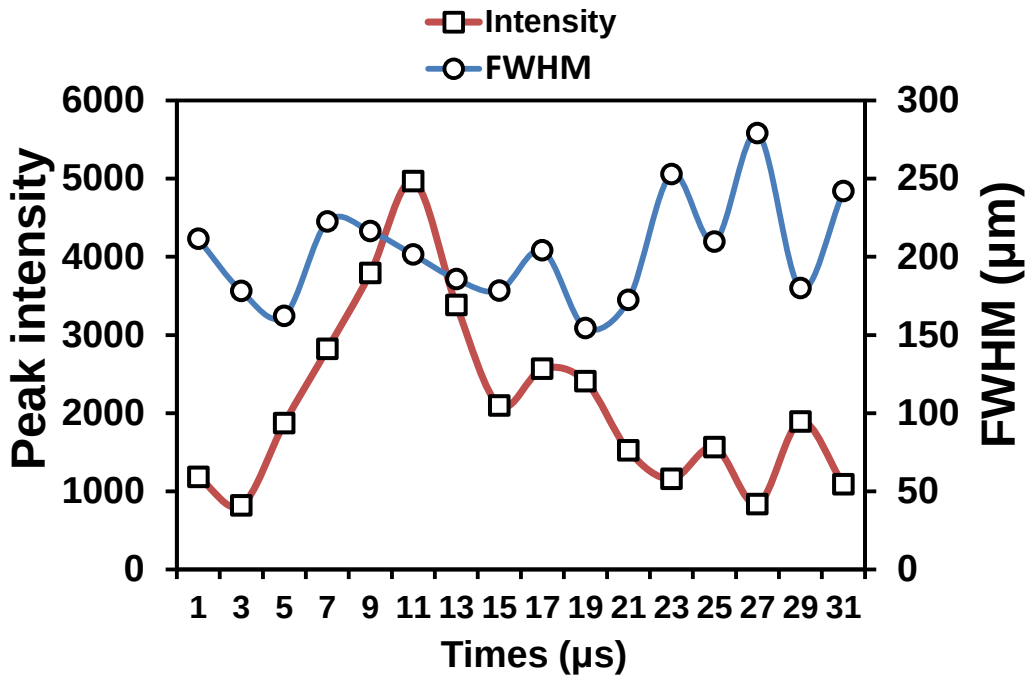

Fig. 7.14 Temporal evolution of peak intensity and FWHM of an individual discharge varying with time (500V DC PEO with 1μs exposure time).

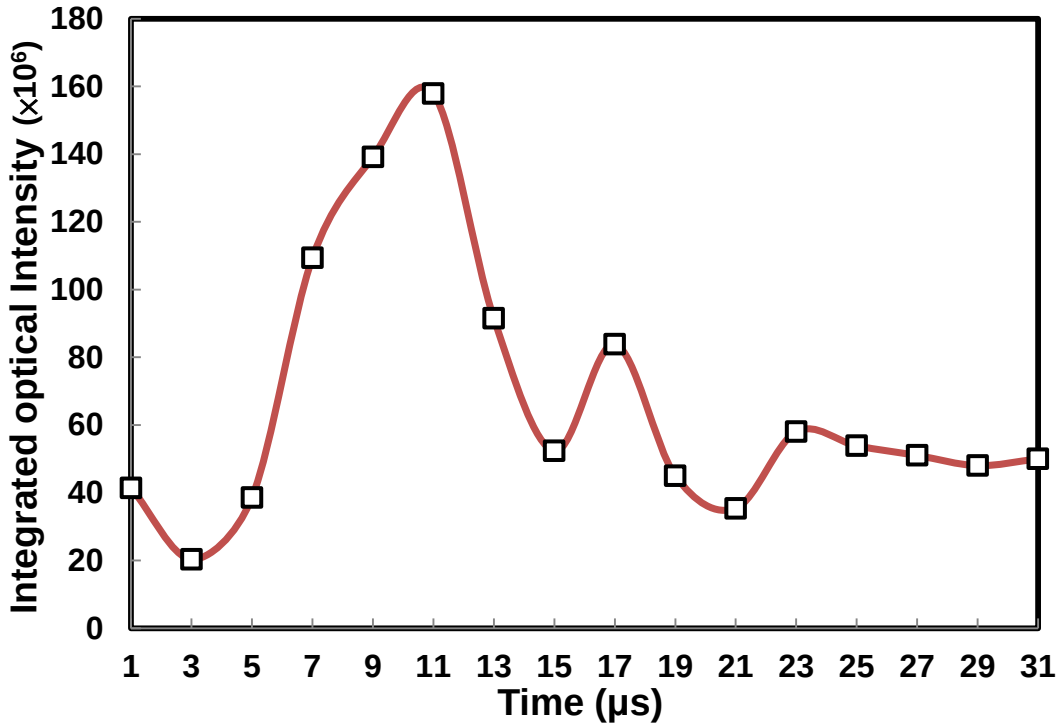

Fig. 7.15 Temporal evolution of integrated optical emission intensity of an individual discharge varying with time (500V DC PEO with 1μs exposure time).

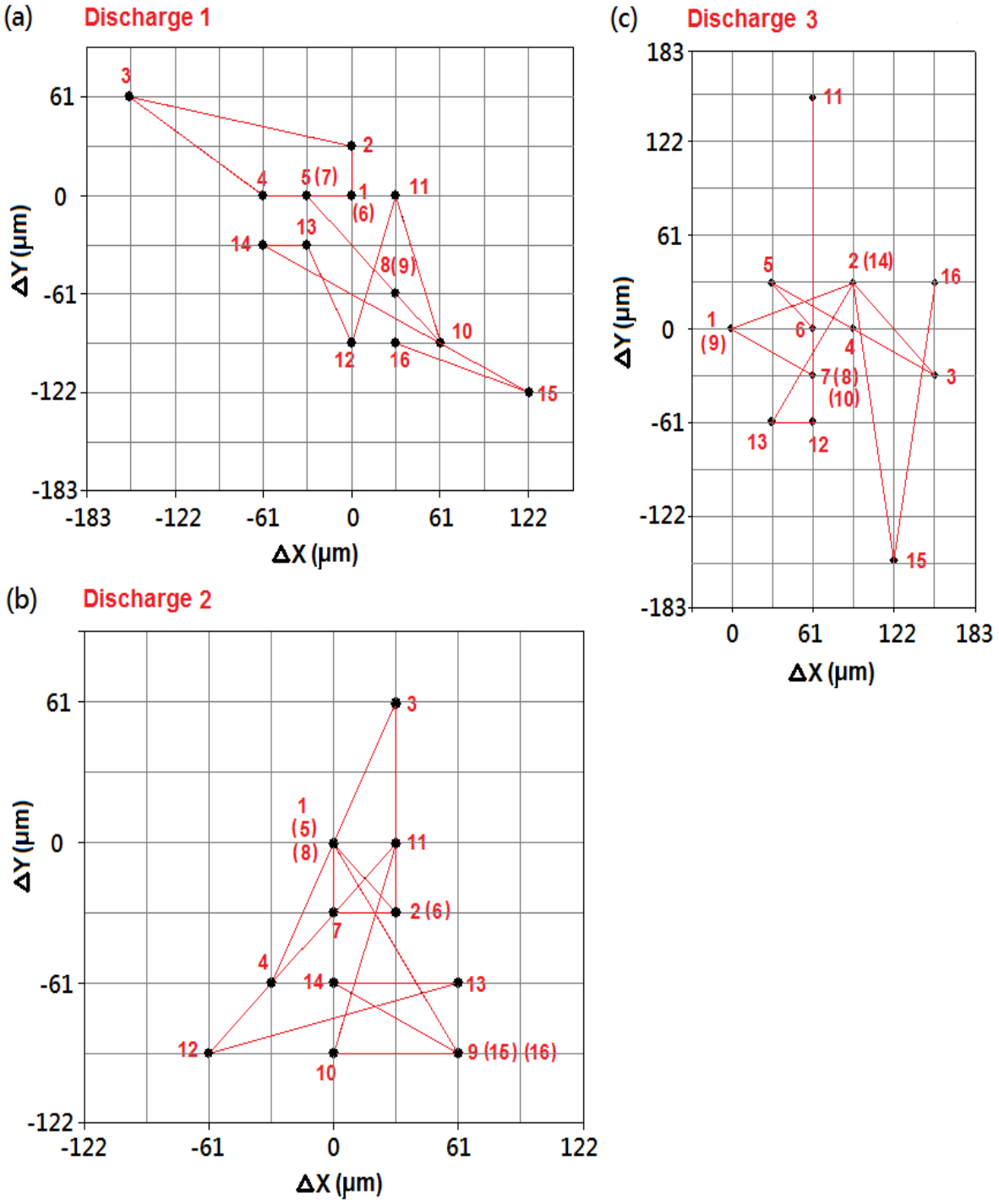

Fig. 7.16 Trajectories of three individual discharges in the same UHIS collection during 31μs.

7.5.Effects of variable exposure time

To investigate the effects of exposure time on discharge characteristics, the UHSIs from 14 fragments of same frame collection were separated into 7 groups with the exposure time varied from 10ns to 3μs and with 100ns separation between each frame (figure 7.17). The last two frames were taken with longer exposures to verify the sample position. In this study, the spatial resolution was estimated at 14μm, which allows direct investigations of the effects of exposure time on discharge size. During the images analysis, the discharges were difficult to observe frames taken with shorter exposure times, for which the peak intensities were usually lower than the 500 a.u. To identify the discharge in these frames, the location of discharge in the frames obtained with exposure of 3μs was initially identified and then traced back to shorter exposure times.

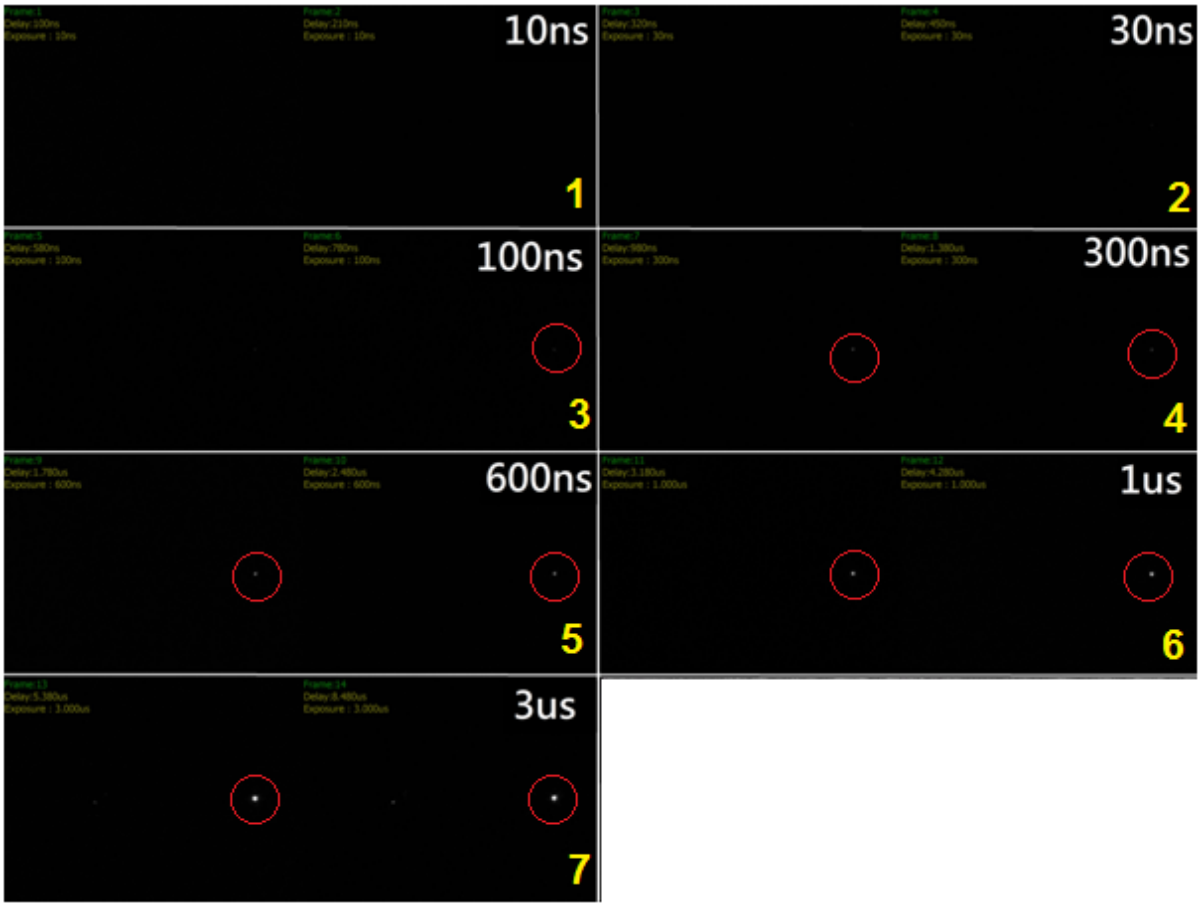

Fig. 7.17 Seven images taken at the same instance of PEO processing with different exposure time varied from 10ns to 3μs and separated by a 100ns pause between the frames.

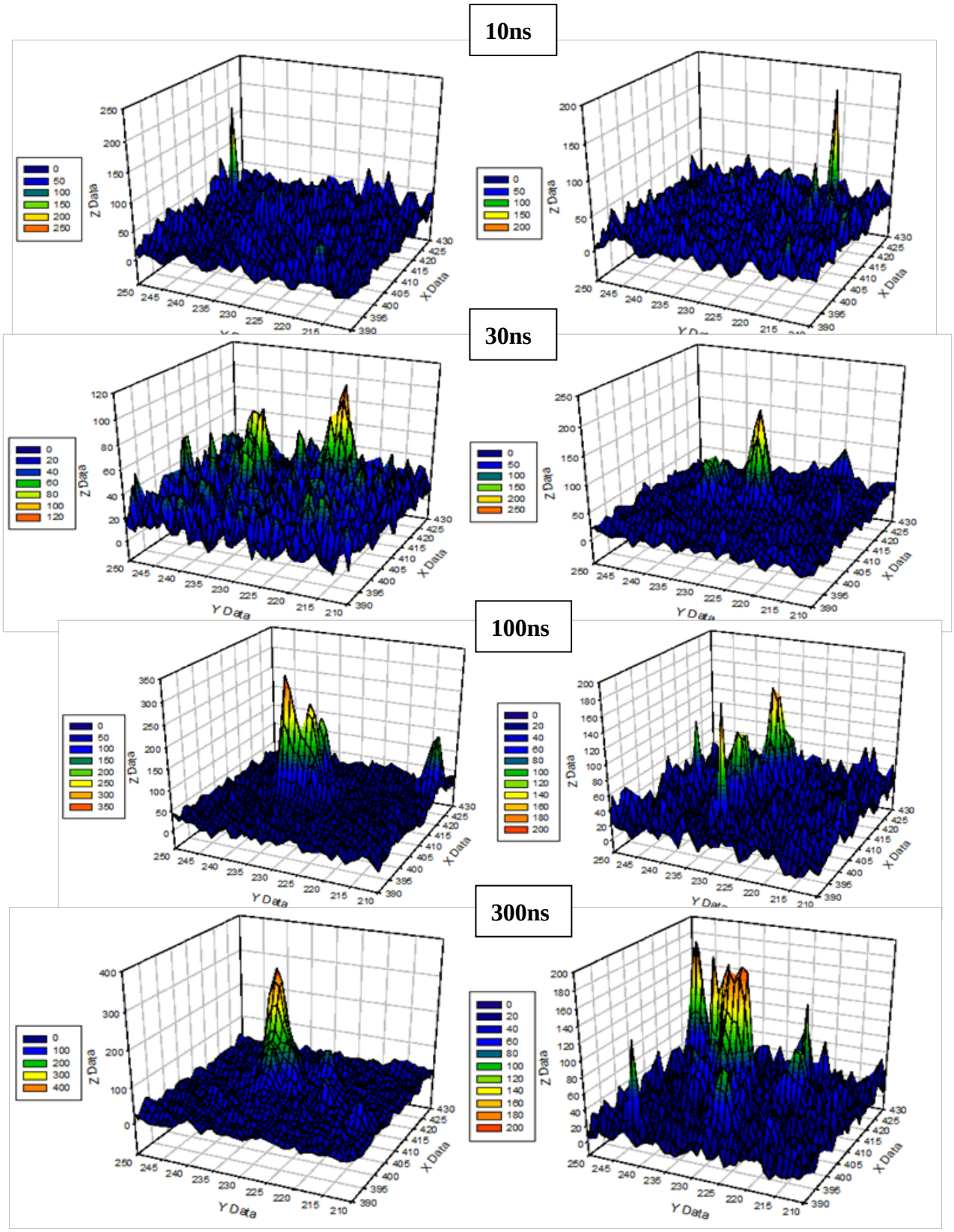
10ns
30ns
100ns
300ns
Z Data
X Data
Y Data

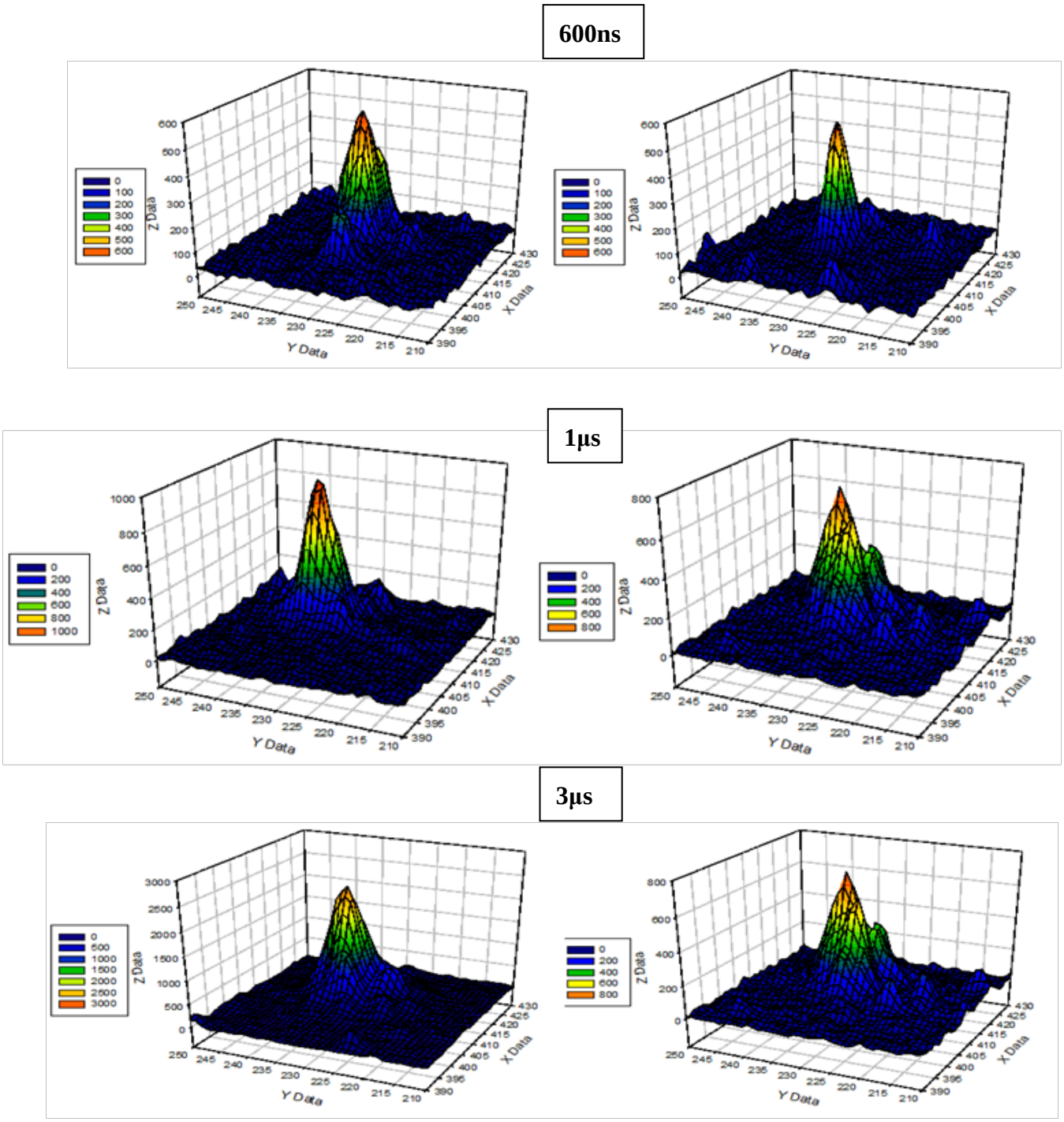

Fig. 7.18 3D plots (under pixel) of individual discharge in seven groups of different exposure time varied from 10ns to 3µs.

Dependencies of discharge intensity/FWHM on exposure time at 5th, 10th, 15th and 20th minute of treatment are presented in figures 7.19 and 7.20, respectively, covering different stages of the PEO process. In the figures, both the peak intensity and the FWHM mainly increase with increasing exposure time. Figure 7.21 shows the correlation between the integrated optical intensity and the exposure time, which follows a power law. It is worth mentioning that the UHSIs captured at 5 minute provide relatively higher peak intensities and FWHM. This may be caused by relatively high current densities during the early stage of the PEO process. After 10 minutes of treatment at 500V, the current densities become nearly constant (figure 7.4), and therefore the peak intensities and FWHMs at 10th, 15th and 20th minute were similar at all exposure times. It should also be mentioned that the peak FWHMs under the exposure time ranging from 0.1 to 1μs are consistent with previous observations [100,162,163,165]. As mentioned above, the discharge is difficult to observe when the exposure time is shorter a 0.1μs at all treatment stages. Therefore, it is difficult to discuss the discharge behaviour under these conditions.

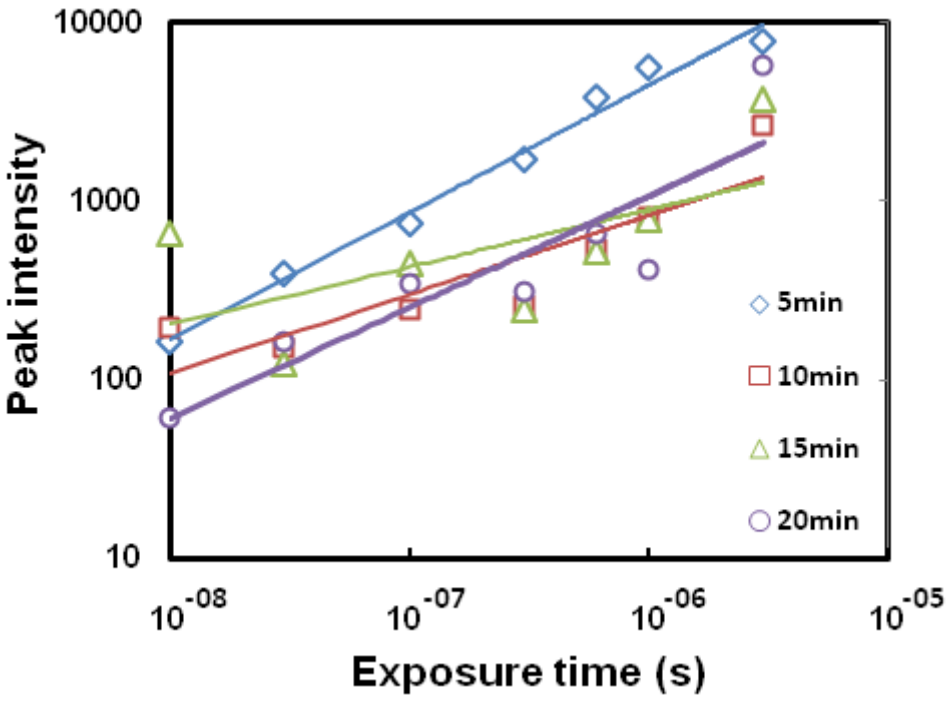

Fig. 7.19 Correlation between discharge intensity and exposure time at the 5th, 10th, 15th and 20th minute of the PEO process (500V).

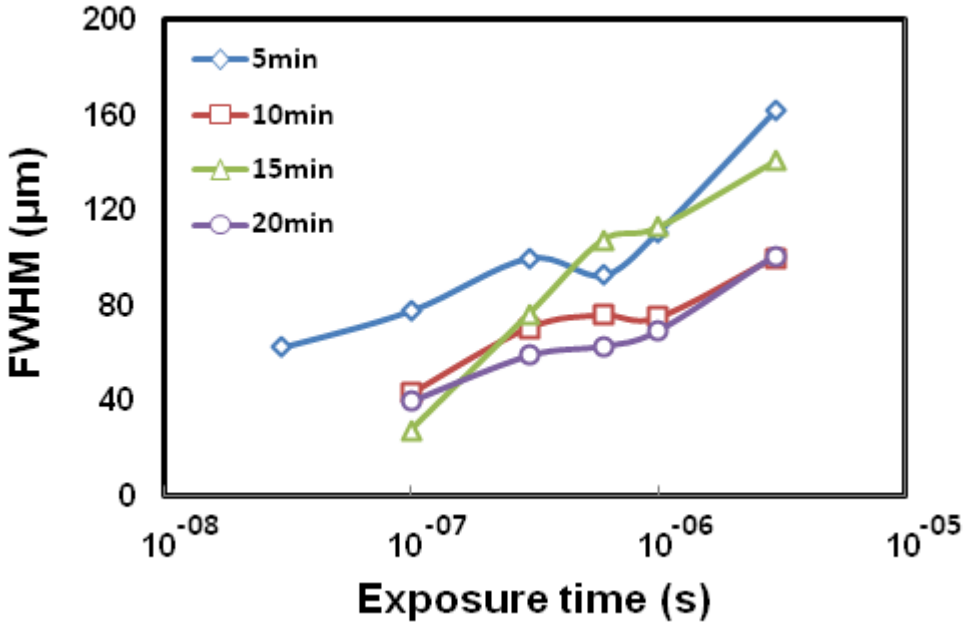

Fig. 7.20 Correlation between FWHM of discharge and exposure time at the 5th, 10th, 15th and 20th minute of the PEO process (500V).

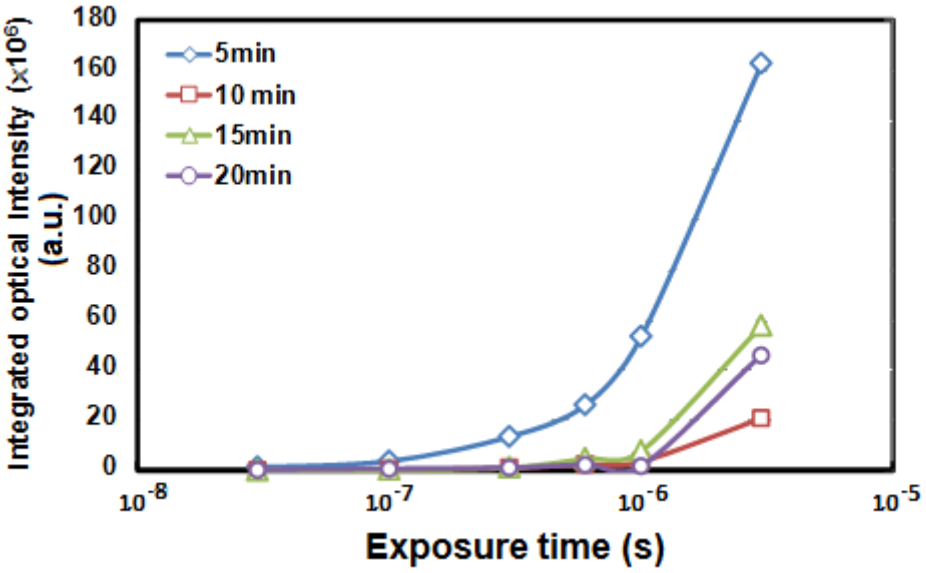

Fig. 7.21 Correlation between integrated optical intensity of discharge and exposure time at the 5th, 10th, 15th and 20th minute of the PEO process (500V).

In the paper by Dunleavy, et al [98], the radius of plasma bubble generated by the discharge is expressed as a function of discharge peak current (figure 7.22). Therefore, the FWHM of discharge events can be used to calculate the peak current (figure 7.24). The sum of FWHMs for all discharges identified on the sample surface in each individual frame can therefore be correlated with the current signal recorded as discussed in section 7.3.2. The sum of FWHMs was also calculated for different exposure time conditions to obtain the discharge peak current transient under different time scales as in figure 7.24 (a), (b) and (c).

At 0.5μs exposure time (figure 7.24 (c)), the time scale and the magnitude of discharge peak current is correlated with the fast current transients as discussed previously (figure 7.6 (c)). However, the oscillation behavior (in both amplitude and frequency) of the observed fast current transient during 9μs is different from the calculated peak event current in figure 7.24 (c). The difference may be due to the following two reasons. Firstly, the integrated optical intensity of an individual discharge event was estimated as (I) $\times$ FWHM as shown in figure 7.14. However, the discharge events actually occur as plasma bubbles (figure 7.23 a) during the PEO process, but the plasma emission actually came through the channels on the coating (figure 7.23 b). Therefore, the discharge diameter should be chosen the same as the pore diameter, and this may have caused a deviation. Secondly, the optical energy may be emitted when the hydrogen atoms return from the excited state to the ground state during the plasma bubble evolution. This phenomenon affects the integrated optical intensity, rather than the fast current transient.

With regard to the effects of the exposure time on discharge displacement, the trajectories of individual discharges were investigated for three different exposure times of 1μs, 0.5μs and 0.1μs, as shown in figures 7.25 (a), (b) and (c), respectively. The results show that the discharge displacement is independent of the exposure time. The velocity and the spatial range of discharge displacement are similar, except for the point (#5) fig 7.25 (0.1μs exposure), which may be affected by the background noise or another discharge event. The connection between the discharge characteristics and coating morphologies were investigated in next section.

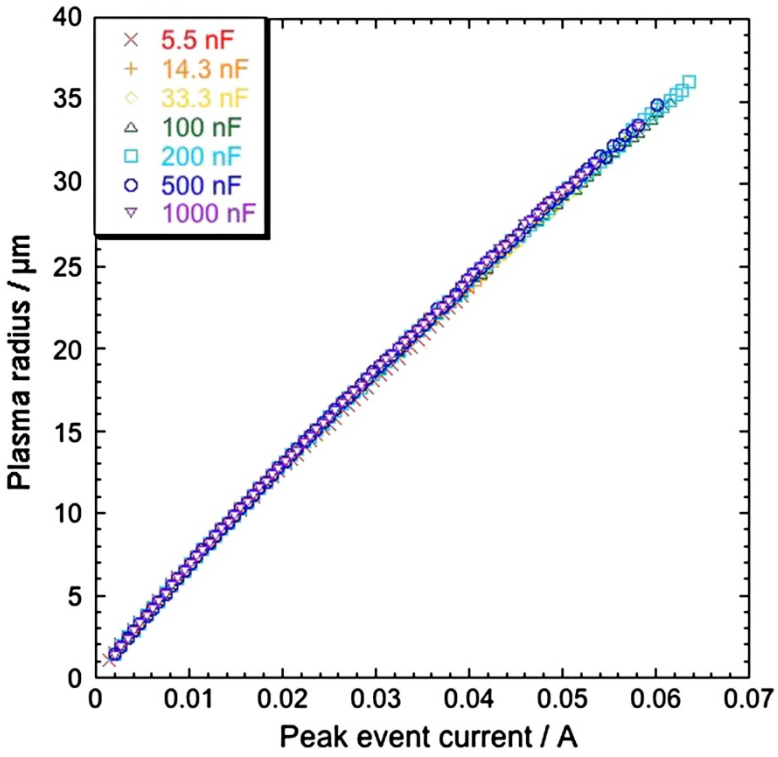

Fig. 7.22 Predicted radius of the plasma bubble as the function of discharge peak current [98]

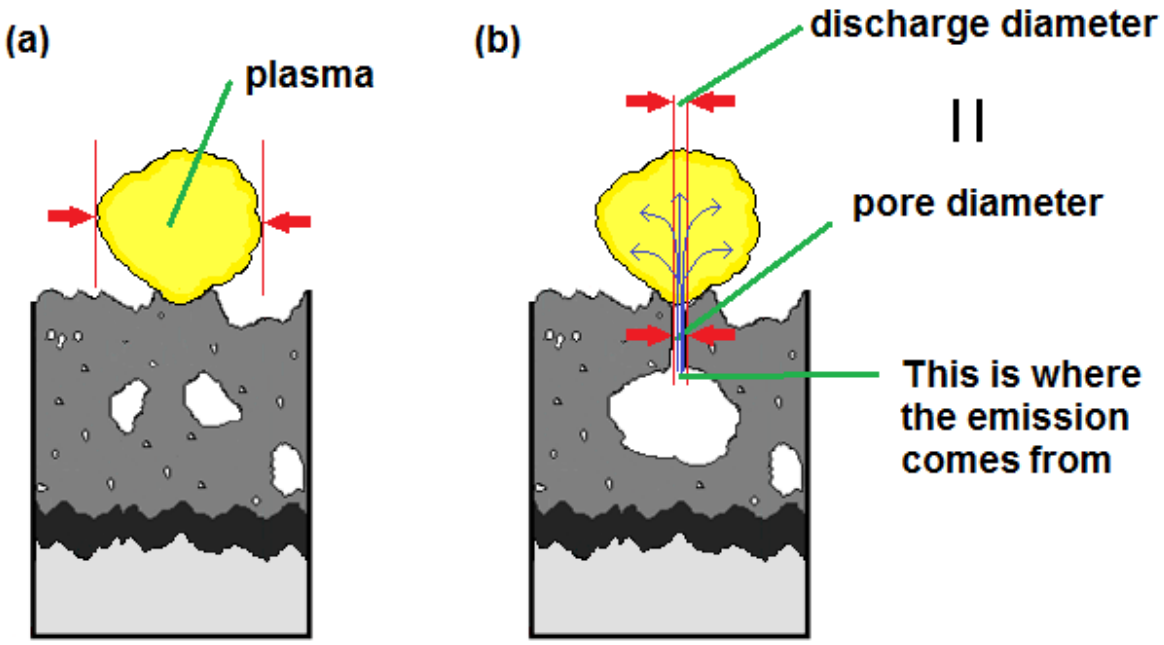

Fig. 7.23 Methods to evaluate the discharge diameter, (a) Dunleavy's model [98], (b) a more likely model occurring in reality.

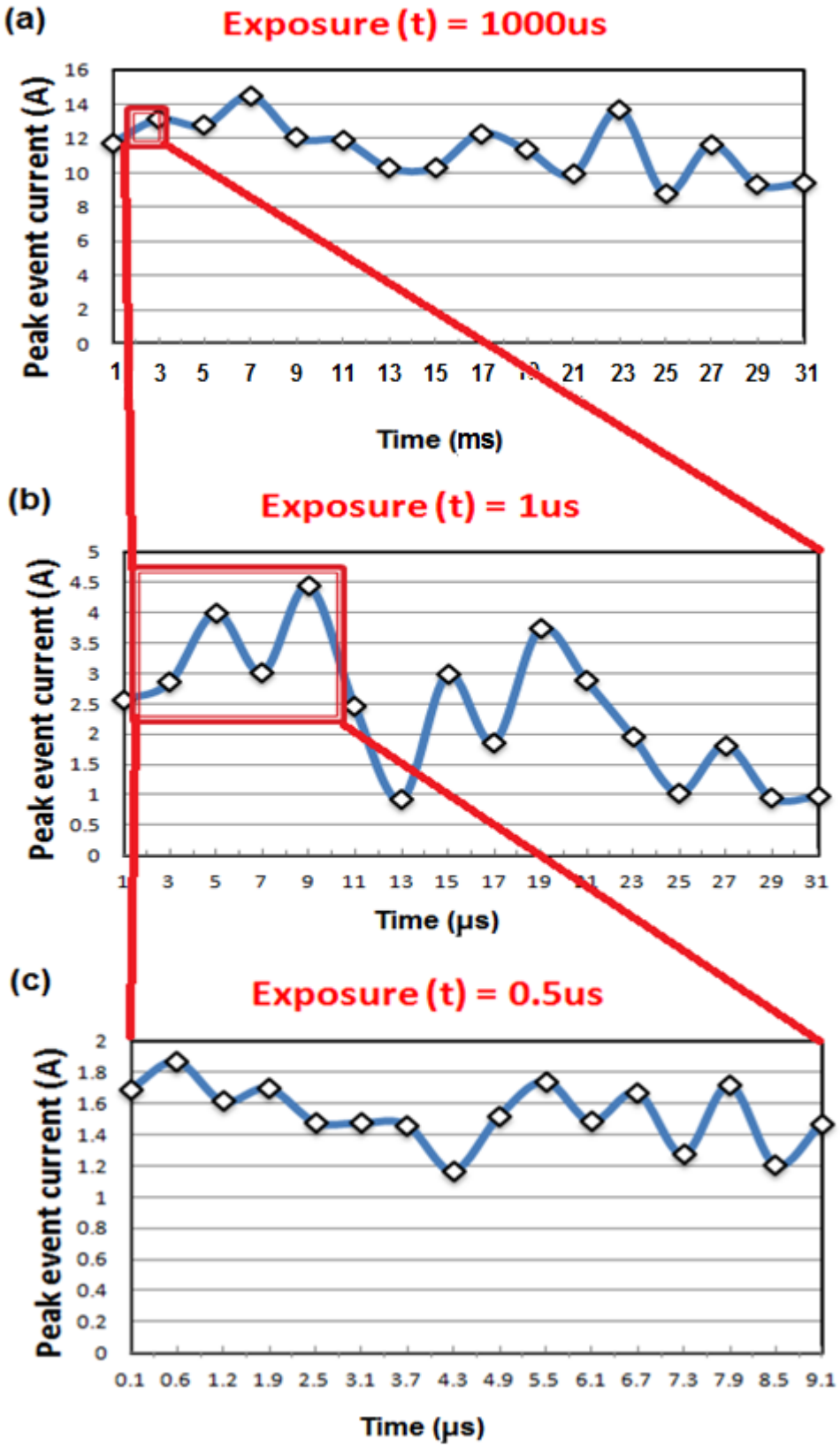

Fig. 7.24 The peak event current calculated by FWHM in different time scales as the exposure times were: (a)1000µs,(b)1µs, and (c)0.5µs.

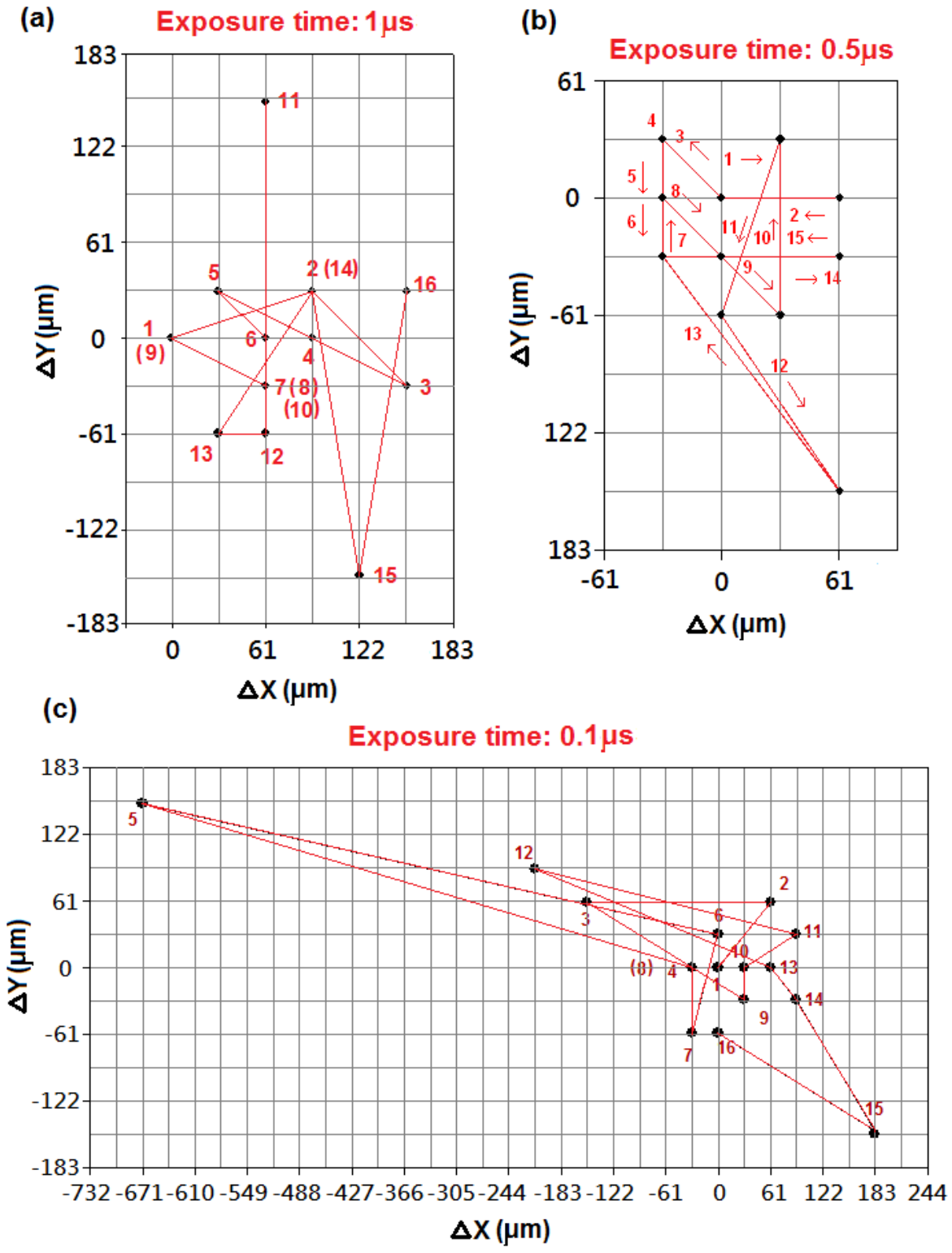

Fig. 7.25 The trajectories of individual discharges captured with different exposure times as (a) 1μs,(b) 0.5μs, and (c) 0.1μs.

7.6 Correlation of discharge characteristics with surface morphology

It is reasonable to assume that discharge size and trajectory should therefore be reflected in the surface morphology. Figure 7.26 shows the trajectory of individual discharge superimposed with the microscopic image of coating morphology; here the exposure time was selected at 0.5μs because both discharge size peak current were consistent with the current response signal during the PEO process. As mentioned in the previous section, the average speed of the discharge displacement is estimated at about 33.5m/s.

To compare with discharge size, the FWHM can be represented as a diameter of individual discharge. At 0.5μs exposure time, the discharge size varies from 57 to 95μm depending on the time stage of the PEO process (figure 7.27). Therefore, tens to hundreds of pores can be related to one discharge which lasts half of a microsecond. To combine the results with discharge trajectory, the displacement of discharge from frame to frame appears to be smaller than the discharge size in most of the situations. Which means that once the dielectric breakdown and the discharge occurred, the source emission from the same pores can sustain the discharge for around 10μs long. By knowing the average diameter of discharge and the speed of the discharge displacement, it can be calculated that the duration for an individual discharge event walk through the whole sample surface (t_w) is about 0.58 and 0.97s at early and later stage of the PEO process, and the average is 0.775s. The growth rate (Δh) of the PEO coating affected by one time of the discharge event occurred can be calculated with the following equation:

$$\Delta h = h_T / ((n_d \times (t_T / t_w)) \quad (7.2)$$

were h_T is the total coating thickness, n_d is the number of discharge events occurred at the same time, and t_T is the total PEO treatment time. In this work, the duration of the treatment time is 20 minutes; the measured coating thickness is 8.1±0.3μm; and the n_d is about 50 on the whole sample. The Δh is evaluated to be about 0.1nm for the single discharge occurence.

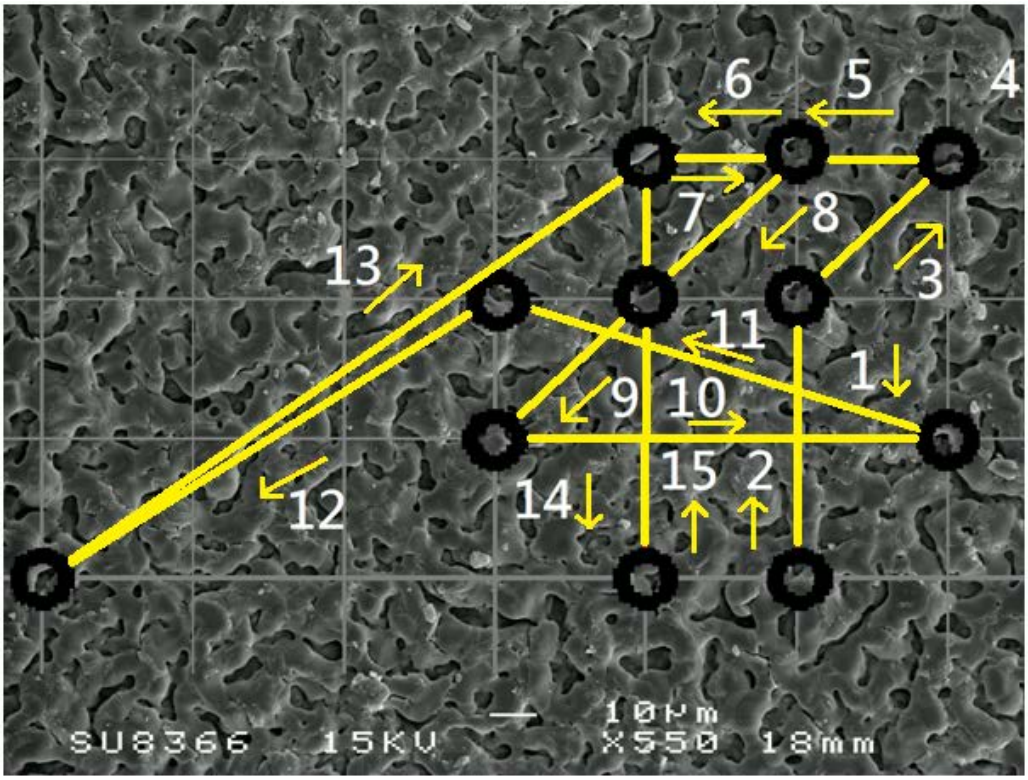

Fig. 7.26 Trajectory of individual discharge (capture with 0.5μs exposure time) superposed with the coating morphology

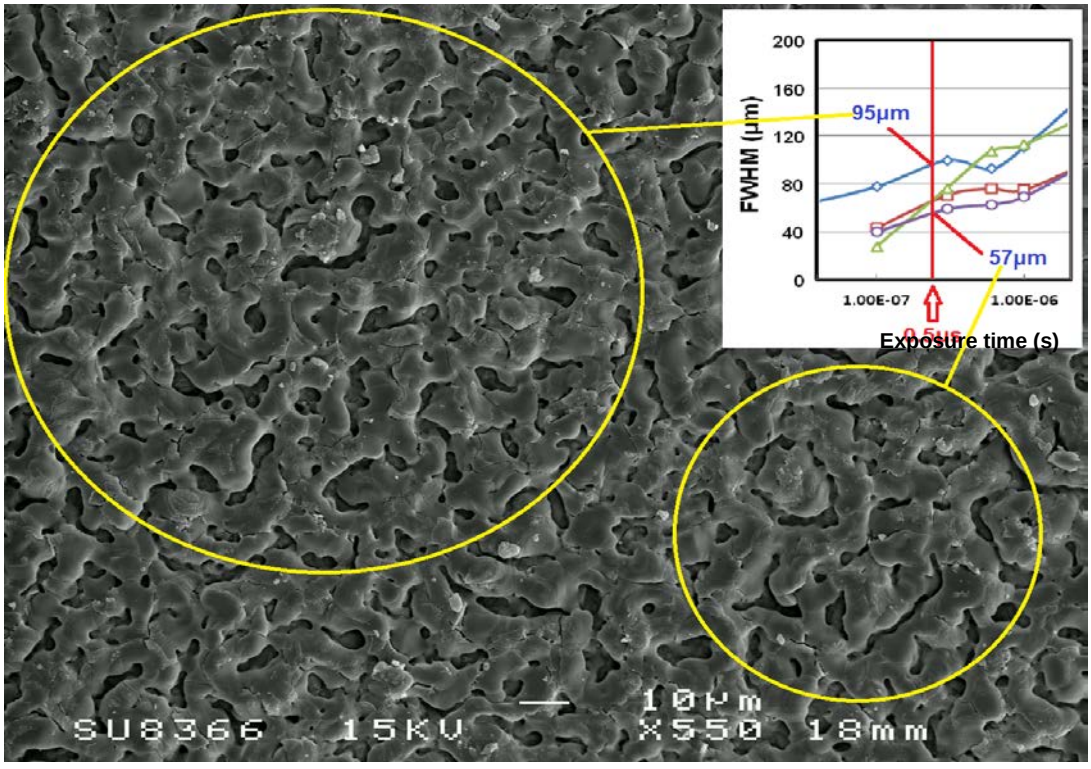

Fig. 7.27 Correlation of average discharge size with surface morphology

7.7 Summary

The characteristics of discharge events have been investigated using SIM camera, high-resolution 16 Bit oscilloscopic measurements and a specially developed discharge analysis program. The intensity, FWHM, displacement and duration of individual discharge events were studied at different time scales and for different stages of the PEO process under both fixed and variable camera exposure time conditions.

The FFT spectrum of current response signal during the PEO process on Al lies in the frequency range from 1 to 300 kHz, which is wider than previously considered [97]. Two obvious peaks were observed at 2~7 and 20~30 kHz, which may be due to the discharge clustering and the dielectric breakdown, respectively. These conjectures can also explain why the peaks are more obvious in the later stage of the PEO process.

The discharge lifetime evaluated by both high speed imaging and oscilloscopic measurements is around 10μs which is shorter than previously reported. Integrated optical intensity was calculated as a product of the peak intensity and the FWHM of discharge events. Moreover, the sum of FWHM for all discharges identified on the sample surface in each individual frame was used to evaluate the peak event current and compared with the fast current transients. The difference between these two results may be due to the way the integrated optical intensity was calculated and the nature of light emission process

The trajectory of discharge displacement was found to be random, with average speed around 33.5m/s. The average displacement range is about 200μm around the original location for all studied exposure times. A correlation of average discharge size with coating morphology was also considered, which means that once the dielectric breakdown and the discharge occurred, the emission source from the same pores can sustain the discharge for around 10μs long. The growth rate of coating thickness increment due to the single discharge event is estimated to be about 0.1nm in this work.

Chapter 8

Conclusions and future work

8.1 Conclusions

The PEO process was investigated and modeled using the ISIS method in conjunction with other techniques. The COMSOL Mutiphysics package was used to understand the electric field distribution and electrolyte resistance in the electrolyser. Ex-situ EIS analysis was employed for impedance spectra comparison with ISIS results; fractal analysis was used to reveal the effects of coating morphology on the impedance spectrum. Also, a Specialized Imaging Multi-channel (SIM) framing camera was used for real-time observation of individual discharge events; and FFT analysis of high-resolution current signals - for studying their collective behaviour. These studies have resulted in the following overall conclusions:

8.1.1 Impedance characteristics of PEO process

ISIS experiments revealed several phenomena occurring during the PEO process, which can be attributed to: (1) the charge transfer through the gas/solution interface (plasma sheath) of plasma bubbles; (2) the thermal effects with the coatings; (3) the charge transfer through the fine porous layer of the PEO coating; (4) the process in the positive column (plasma); and (5) the charge transfer through the barrier layer at the bottom of the discharge channel.

Comparison with ex-situ EIS spectra has demonstrated that the total impedance is much higher for the ex-situ impedance spectra than for the in-situ ones, which provides evidence of the effects of the discharge on the formation of PEO coatings. This difference is even more obvious under the low electrolyte conductivity conditions. The results also indicate that the effect of the discharge is strongly influenced by the coating thickness, and appears to be

stronger for the thinner coatings. These observations confirm that ISIS method is a useful tool to study and understand the PEO process.

8.1.2 Effects of electric field distribution on the PEO process

Results of the studies into effects of electric field distribution in the PEO electrolyser have demonstrated that the largest net electrolyte resistance occurred in the parallel electric field conditions, and is about 7 and 2.5 times larger than those for converging and diverging electric field types, respectively. There is a relatively high net electrolyte resistance in the equidistant electrode layout than the non-equidistant one. These results are consistent with the current density evolution during the PEO treatment.

The largest impedance was observed under the diverging electric field conditions while the smallest one is occurred in the converging one. Moreover, relatively large impedance was present in the cells with equidistant electrode layouts for all electric field conditions. Two types of equivalent circuits were developed to fit the ISIS spectra for converging and parallel/diverging conditions. In the latter, the loop used to interpret the behaviour of the positive column was missing in both converging electric field conditions, and were displaced by a loop used to interpret the behaviour of charge transfer through the fine porous layer of PEO coatings. These results are consistent with the cross-sectional morphology of the PEO coatings.

Studies of the electric field effects on coating characteristics indicate that (1) the difference in the thickness of PEO coatings produced under all parallel and diverging electric fields conditions is negligible; this is however significant for the converging field. (2) The coating porosity is similar for all conditions, ranging from 3.5 ~ 4.5 %. (3) Surface roughness was found to be about 1.5 to 2 times higher for the coatings produced in the converging electric field, whereas the interfacial roughness is similar for all coatings (~4μm). From this work, it follows that the electric field distribution and the electrode layout are important parameters affecting thickness and morphology of PEO coatings.

8.1.3 Effects of electrolyte characteristics on the PEO process

Studies into effects of electrolyte characteristics on the PEO process have shown that the

discharge density is reduced in the electrolytes with (1) low temperature, (2) low conductivity, and (3) thick pre-formed coating. No sparking could be observed when all these conditions are combined.

The differences in the ISIS spectra clearly reflect the effects of pre-formed coating thickness, whereas the effects of electrolyte temperature and conductivity are less obvious and negligible, respectively. Strong diffusion effect was observed in the impedance spectra obtained in lower conductivity electrolyte and on thicker coatings, while the effects of the double layer were much stronger at a higher electrolyte conductivity and at a thinner coating. Thus, the behaviour of double layer and diffusion during the PEO process can be controlled via the temperature of the electrolyte.

8.1.4 Effects of electrolyte characteristics on impedance spectra of the PEO process

It was established that for converging field conditions, both heterogeneous coating morphology and non-uniform electric field contribute significantly to the impedance spectra of the PEO process, for the parallel field conditions, the impedance is mainly affected by the heterogeneous coating morphology, and for the diverging field conditions the impedance is affected only by the coating morphology.

A relatively strong correlation was found between the CPE-P value in the equivalent circuit used to fit the ISIS data and the coating thickness, whereas both the CPE-P value and the coating morphology as defined by the fractal dimension presented weak correlations with surface roughness and no correlations with interfacial roughness and porosity. The electric field distribution has also a strong correlation with the CPE-P value, and weak correlation with the coating morphology. Importantly, this clarifies the effects of coating morphology and electric field distribution on the impedance of PEO process.

8.1.5 Characterisation of discharge events during the PEO process.

The discharge lifetime has been evaluated to be around 10μs which is shorter than previously reported. This is consistent with the FFT spectrum of the current response signal during the PEO process on Al, which lies in the frequency range from 1 to 300 kHz, also wider than previously reported. The trajectory of discharge displacement was found to be

random, with average speed around 33.5m/s. The average displacement range is about 200μm around the original location under all various exposure time. The mean coating thickness increment due to the single discharge event has been estimated to be about 0.1nm.

8.2 Future work

Discharge phenomena occurring during the PEO process are governed by complex mechanisms and are difficult to study unless different research methods are applied conjointly. From the results of this work, effects of electric field distribution, electrolyte characteristics, coating morphology and behavior of discharge events have become clearer. However, to completely understand the characteristics of the PEO process, the investigation needs to continue with different experimental designs involving other research methods and instruments. Existing research methods can also be improved and extended. Moreover, some of the results obtained this work would benefit from additional verification.

8.2.1 In the short-term future, the following studies could be carried out:

- New experiments are required to support physical interpretation of some loops in the equivalent circuits. For example, different viscosity or volatility of the electrolyte may change the characteristics of the plasma bubble on the working electrode during the PEO process.

- Investigate the effects of electrolyte characteristics under different types of electric field, and also using electrolytes with different cationic composition e.g. including Ca^{2+} and Al^{3+} on other metals.

- A more careful investigation of the contribution of coating morphology into CPE values is required to enhance the statistical significance of data.

- Investigate the effects of shapes of working electrodes, composition of electrolyte and different treatment duration on discharge characteristics and coating morphology, combining UHSI, in-situ and ex-situ EIS methods.

- It is worth investigating the effects of discharge characteristics on coating

morphology under different PEO treatment conditions, such as various electrolyte composition and different substrate materials.

8.2.2 For the long-term research plan:

- The COMSOL-Multiphysics modelling package is a powerful modelling software which should be used for more complex modelling, including oxide coating formation during PEO process with chemical reaction under plasma electrolysis, breakdown phenomena, growth rate, and effects of working electrode shapes.

- Investigate the possibility of achieving specific coating characteristics, e.g. uniform coating thickness on complex-shape substrates by incorporating the ISIS technique into the PEO process control module.

References

[1] A.L. Yerokhin, X. Nie, A. Leyland,A. Matthews, S.J. Dowey, '*Plasma electrolysis for surface engineering*', Surface & Coatings Technol., 122 (1999) 73-93.

[2] F. C. Walsh, C. T. J. Low, R. J. K. Wood, K. T. Stevens, J. Archer, A. R. Poeton, A. Ryder, '*Plasma electrolytic oxidation (PEO) for production of anodised coatings on lightweight metal (Al, Mg, Ti) alloys*', Transactions of the Institute of Metal Finishing, 87 (2009) 122-135.

[3] A. Günterschultze, H. Betz, ElectrolytkondensatorenKrayn, Berlin (1937)

[4] W. McNiell, G.F. Nordbloom, US Patent 2 854 390, September 30, 1958

[5] W. McNiell, L.L. Gruss, US Patent 3 293 158, 1966

[6] G.A. Markov, G.V. Markova, USSR Patent 526 961, 1976.

[7] K.H. Dittrich, W. Krysmann, P. Kurze, H.G. Schneider, '*Structure and properties of ANOF Layers'*, Crystal Research and Technology, 19 (1984) 93-99

[8] W. Krysmann, P. Kurze, K.H. Dittrich, H.G. Schneider, ' *Process characteristics and parameters of Anodic Oxidation by spark discharge (ANOF)'*, Crystal Research and Technology, 19 (1984) 973-979

[9] R.J. Gradkovsky, S.N. Bayles, US Patent 3 956 080, 1974

[10] S.D. Brown, K.J. Kuna and Tran Bao Van, '*Anodic Spark Deposition from Aqueous Solutions of NaAlO2 and Na2SiO3*', Journal of the American Ceramic Society, 54 (1971) 384-390

[11] W.Xue, Z. Deng, Y. Lai, R. Chen, '*Analysis of phase distribution for ceramic coatings formed by microarc oxidation on aluminum alloy*', Journal of the American Ceramic Society, 81 (1998) 1365-1368

[12] G.P. Wirtz, S.D. Brown, W.M. Kriven, '*Ceramic Coatings by Anodic Spark Deposition*', Materials and Manufacturing Processes,6 (1991) 87-115

[13] M. Tarakci, K. Korkmaz, Y. Gencer, M. Ustat, '*Plasma electrolytic surface carburizing and hardening of pure iron*', Surface & Coatings Technol., 199 (2005) 205– 212

[14] X. Nie, L. Wang, Z.C. Yao, L. Zhang, F. Cheng, '*Sliding wear behaviour of electrolytic plasma nitrided cast iron and steel*', Surface & Coatings Technol., 200 (2005) 1745 – 1750

[15] C. Kaptay, S.A. Kuznetsovb, '*Electrochemical synthesis of refractory borides from molten salts*', Plasmas and Ions (1999) 2,45-56.

[16] T.H. Teh, A. Berkani, S. Mato, P. Skeldon, G.E. Thompson, H. Habazaki, K. Shimizu, '*Initial stages of plasma electrolytic oxidation of titanium*', Corrosion Science 45 (2003) 2757–2768

[17] L.O. Snizhko, A.L. Yerokhin, A. Pilkington, N.L. Gurevina, D.O. Misnyankin, A. Leyland, A. Matthews, '*Anodic processes in plasma electrolytic oxidation of aluminium in alkaline solutions*', Electrochim. Acta 49 (2004) 2085–2095.

[18] P. Wang, '*Research Description of MAO treatment on Al/Mg alloys*', Special Casting and Nonferrous alloys, (2003) 23-26

[19] G. Sundararajan and L. Rama Krishna, '*Mechanisms underlying the formation of thick alumina coatings through the MAO coating technology*'. Surface & Coatings Technol., 167 (2003) 269-277

[20] C.B. Wei, X.B. Tian, S.Q. Yang, X.B. Wang, R.K.Y. Fu and P.K. Chu, '*Anode current effects in plasma electrolytic oxidation*', Surface & Coatings Technol., 201 (2007) 5021-5024.

[21] Jane McEntegart, '*VIDEO: Every HTC One S Case Gets Blasted with 10,000 Volts*'. Available at http://www.tomsguide.com/us/HTC-One-S-Strong-Case-Ceramic-Metal-Process,news-14451.html, last accessed on 14th July 2012.

[22] Witte, F., '*The history of biodegradable magnesium implants: A review'*. Acta Biomaterialia, 6 (2010) 1680-1692.

[23] Wang, Y.M., et al., '*Microstructure and corrosion behavior of coated AZ91 alloy by microarc oxidation for biomedical application'*. Applied Surface Science, 255 (2009) 9124-9131.

[24] G.Y. Liu, J. Hu, Z.K. Ding, C. Wang, '*Bioactive calcium phosphate coating formed on micro-arc oxidized magnesium by chemical deposition*', Applied Surface Science, 257 (2011) 2051-2057

[25] L.H Li, Y.M. Kong, H.W. Kim, Y.W. Kim, H.E. Kim , S.J. Heo, J.Y. Koak, '*Improved biological performance of Ti implants due to surface modification by micro-arc oxidation*', Biomaterials, 25 (2004) 2867

[26] Brian O'Regan, Michael Grätzel, '*A low-cost, high-efficiency solar cell based on dye-sensitized colloidal TiO_2 films*', Nature, 353 (1991) 737-740

[27] P.J. Chu, S.Y. Wu, K.C. Chen, J.L. He, A. Yerokhin, A. Matthews, '*Nano-structured TiO_2 films by plasma electrolytic oxidation combined with chemical and thermal post-treatments of titanium,*

for dye-sensitised solar cell applications ', Thin Solid Film, 519 (2010) 1723-1728.

[28] Elwin L. Rooy, *'Introduction to Aluminum and Aluminum Alloys in ASM Metals Handbook Volume 02: Properties and selection: nonferrous alloys and special-purpose materials'*, 1990, ASM International: USA.

[29] EAA/OEA Recycling Division, *'Aluminium recycling in Europe'*, Organusation of European Aluminium Refiners and Remelters. Available at: http://www.world-aluminium.org/cache/fl0000217.pdf

[30] B. Z. Shakhashiri, *'Chemical of the week - Aluminum'*. Available at: http://scifun.chem.wisc.edu/chemweek/Aluminum/ALUMINUM.html

[31] European Aluminium Association,*' Aluminium recycling'*. Available at: http://www.azom.com/article.aspx?ArticleID=1388

[32] J. R. Davis, *'ASM Materials Engineering Dictionary'*, 1992, ASM International, p15.

[33] Yujun Zhang, *'Structure ceramic materials and application', 2005,* Chemical science and engineering, Beijing, p1-4.

[34] R.W. Cahn, P. Hassen, E.J, Kramer, *'Materials Science and Technology Volume 11: Structure and properties of ceramics'*, 1994, VCH, New York, p85-88.

[35] J.F. Shackelford • Robert H. Doremus, '*Ceramic and Glass Materials - Structure, Properties and Processing* ', 2008, Springer Science+Business Media, LLC, New York, p1-26.

[36] P. Fang, M. He, Y.L. Xie, M.F. Luo, ' *XRD and Raman Spectroscopic Comparative Study on Phase Transformation of γ-Al2O3 at High Temperature*', Spectroscopy and Spectral Analysis, 26 (2006) p2039-2042.

[37] M. Plummer, '*The formation of metastable aluminas at high temperatures*', Journal of Applied Chemistry, 8 (1958) p35-44.

[38] R. McPherson, '*Formation of metastable phases in flame- and plasma- prepared alumina*' Journal of Materials Science, 8 (1973) p851-858.

[39] W. Xue, Z. Deng, R. Chen, T. Zhang, H. Ma, '*Microstructure and properties of ceramic coatings produced on 2024 aluminum alloy by microacr oxidation*', Journal of Materials Science, 36 (2001) p2615-2619.

[40] J.A. Curran, '*Thermal and mechanical properties of plasma electrolytic oxidation coatings*', PhD (2005), University of Cambridge, UK.

[41] G.M. Pharr, '*Measurement of mechanical properties by ultra-low load indentation*', Materials

Science and Engineering: A, 253 (1998) p151-159.

[42] G. Brady, H. Clauser, Materials Handbook (11 ed.), 1977,McGraw Hill, New York.

[43] G. Alcala, P. Skeldon, G.E. Thompson, A.B. Mann, H. Habazaki, K. Shimizu, 'M*echanical properties of amorphous anodic alumina and tantala films using nanoindentation*', Nanotechnology, 13 (2002), p 451-455.

[44] C.W. Kim, J.H. Choi, H.J. Kim, D.W. Lee, C.Y. Hyun, S.M. Nam, '*Effects of interlayer roughness on deposition rate and morphology of aerosol-deposited Al_2O_3 thick films*', Ceramics International, 38 (2012) p5621-5627.

[45] X.Shen, X. Nie, H. Hu, J.Tjong, '*Effects of coating thickness on thermal conductivities of alumina coatings and alumina/aluminum hybrid materials prepared using plasma electrolytic oxidation*', Surface & Coatings Technol., 207 (2012) p96-101.

[46] R.H.U. Khan, A. Yerokhin, T. Pilkington, A. Leyland, A. Matthews, '*Residual stresses in plasma electrolytic oxidation coatings on Al alloy produced by pulsed unipolar current*', Surface & Coatings Technol., 200 (2005) p1580-1586.

[47] J.A. Curran, T.W. Clyne, '*Thermo-physical properties of plasma electrolytic oxide coatings on aluminum*', Surface & Coatings Technol., 199 (2005) p168-176.

[48] J.A. Curran, T.W. Clyne, '*Porosity in plasma electrolytic oxide coatings*', Acta Materialia, 54 (2006) p1985-1993.

[49] R.O. Hussein, D.O. Northwood, X. Nie, '*Coating growth behaviour during the plasma electrolytic oxidation process*', Journal of Vacuum Science and Technology A, 28 (2010) p766-773.

[50] L.O. Snizhko, A.L. Yerokhin, A. Pilkington, N.L. Gurevina, D.O. Misnyankin, A. Leyland, A. Matthews, '*A model for galvanostatic anodizing of Al in alkaline solutions*', Electrochim. Acta 50 (2005) p5458–5464.

[51] S.M. Moon, Su-II Pyun, '*The formation and dissolution of anodic oxide films on pure aluminium in alkaline solution*', Electrochim. Acta 44 (1999) p2445-2454.

[52] R. Krishna, L.G. Poshal, and G. Sundararajan, '*Influence of Electrolyte Chemistry on Morphology and Corrosion Resistance of Micro Arc Oxidation Coatings Deposited on Magnesium*'. Metallurgical and Materials Transactions A, 41 (2010) p3499-3508.

[53] A.L. Yerokhin, A. Shatrov, V. Samsonov, P. Shashkov, A. Pilkington, A. Leyland, A. Matthews, '*Oxide ceramic coatings on aluminium alloys produced by a pulsed bipolar plasma electrolytic oxidation process*'. Surface & Coatings Technol., 199 (2005) p150-157.

[54] Y. G. Ko, S. Namgung, D.H. Shin, '*Correlation between KOH concentration and surface propertier os AZ91 magnesium alloy coated by plasma electrolytic oxidation*' Surface & Coatings Technol., 205 (2010) p2525-2531.

[55] Y. Guangliang, L. Xianyi, B.Yizhen, C. Haifeng, J. Zengsun, '*The effects of current density on the phase composition and microstructure properties of micro-arc oxidation coating*', Journal of Alloys and Compounds, 345 (2002) p196-200.

[56] R.H.U. Khan, A. Yerokhin, X. Li, H. Dong, A. Matthews, '*Surface characterisation of DC plasma electrolytic oxidation treated 6082 aluminium alloy: Effect of current density and electrolyte concentration*', Surface & Coatings Technol., 200 (2010) p1679-1688.

[57] J. Liang, B. Guo, J. Tian, H. Liu, J. Zhou, T. Xu, '*Effect of potassium fluoride in electrolytic solution on the structure and properties of microarc oxidation coatings on magnesium alloy*', Applied Surface Science, 252 (2005) p345-351.

[58] L. Wang, X. Nie, '*Silicon effects on formation of EPO oxide coatings on aluminum alloys*', Thin Solid Films, 494 (2006) p211-218.

[59] F. Jin, P. K. Chu, H.i Tong, J. Zhao, '*Improvement of surface porosity and properties of alumina films by incorporation of Fe micrograins in micro-arc oxidation*', Thin Solid Films, 253 (2006) p863-868.

[60] K. Wang, B.H. KOO, C.G. Lee, Y.J. Kim, S.H. Lee, E. Byon, '*Effects of electrolytes variation on formation of oxide layers of 6061 Al alloys by plasma electrolytic oxidation*', Transactions of Nonferrous Metals Society of China, 19 (2009) p886-870.

[61] S. Stojadinovic, R. Vasilic, I. Belca, M. Petkovic, B. Kasalica, Z. Nedic, L. Zekovic, *'Characterization of plasma electrolytic oxidation of aluminium in sodium tungstate*', Corrosion Science, 52 (2010) p3258-3265.

[62] A. L. Yerokhin, L. O. Snizhko, N. L. Gurevina, A. Leyland, A. Pilkington1 and A.Matthews, '*Discharge characterization in plasma electrolytic oxidation of aluminium*', J.Phys. D: Appl. Phys, 36 (2003) p2110-p2120.

[63] V. S. Rudnev, I.V. Lukiyanchuk, V.G. Kuryavyi, '*Electrolytic-Plasma Oxidation in Borate Electrolytes*', Protection of Metals, 42 (2006) p55-59.

[64] X Nie, E.I Meletis, J.C Jiang, A Leyland, A.L Yerokhin, A Matthews, '*Abrasive wear/corrosion properties and TEM analysis of Al2O3 coatings fabricated using plasma electrolysis*', Surface & Coatings Technol., 149 (2002) p245-251

[65] W. C. Gu, G. H. Lv, H. Chen, G.L. Chen, W. R. Feng, G. L. Zhang, S. Z. Yang, '*Investigation of morphology and composition of plasma electrolytic oxidation coatings in systems of*

Na2SiO3–NaOH and (NaPO3)6–NaOH', Journal of Materials Processing Technology, 182 (2007) 28-33.

[66] W. C. Gu, G. H. Lv, H. Chen, G.L. Chen, W. R. Feng, G. L. Zhang, S. Z. Yang, '*Characterisation of ceramic coatings produced by plasma electrolytic oxidation of aluminum alloy*', Materials Science and Engineering: A, 447 (2007) p158-162.

[67] Ye. V. Khokhryakov, P. I. Butyagin and A. I. Mamaev, '*Formation of dispersed particles during plasma oxidation*', Journal of Materials Science, 40 (2005) p3007-3008.

[68] J.Liang, P.B. Srinivasan, C. Blawert, W. Dietzel, '*Influence of chloride ion concentration on the electrochemical corrosion behaviour of plasma electrolytic oxidation coated AM50 magnesium alloy*', Electrochimica Acta, 55 (2010) p6802-6811.

[69] A. Ghasemi, V.S. Raja, C. Blawert, W. Dietzel, K.U. Kainer, '*The role of anions in the formation and corrosion resistance of the plasma electrolytic oxidation coatings'*, Surface & Coatings Technol., 204 (2010) p1469-1478.

[70] F. Lin, D. Shan, Y. Song, E.H. Han, '*Effect of additives on the properties of plasma electrolytic oxidation coatings formed on AM50 magnesium alloy in electrolytes containing* K_2ZrF_6', Surface & Coatings Technol., 206 (2011) P455-463.

[71] J.Liang, P.B. Srinivasan, C. Blawert, W. Dietzel, '*Electrochemical corrosion behaviour of plasma electrolytic oxidation coatings on AM50 magnesium alloy formed in silicate and phosphate based electrolytes*', Electrochimica Acta, 54 (2009) p3842-3850.

[72] S. Yagi, A. Sengoku, K. Kubota, E. Matsubara, '*Surface modification of ACM522 magnesium alloy by plasma electrolytic oxidation in phosphate electrolyte*', Corrosion Science, 57 (2012) p74-80.

[73] L. Wang, L. Chen, Z. Yan, H. Wang, J.Peng, '*Effect of potassium fluoride on structure and corrosion resistance of plasma electrolytic oxidation films on AZ31 magnesium alloy*', Journal of Alloys and Compounds, 480 (2009) p469-474.

[74] S. Lu, W. Qin, X. Wu, X. Wang, G. Zhao, '*Effect of* Fe^{3+} *ions on the thermal and optical properties of the ceramic coating grown in-situ on AZ31 Mg Alloy*', Materials Chemistry and Physics, 135 (2012) p58-62.

[75] P. B. Srinivasan, J. LIANG, C. Blawert, M. Stormer, W. Dietzel, '*Characterization of calium containing plasma electrolytic oxidation coatings on AM50 magnesium alloy*', Applied Surface Science, 256 (2010) p4017-4022.

[76] D. Sreekanth, N.Rameshbabu, K. Venkateswarlu, '*Effect of carious additives on morphology and corrosion behaviour of ceramic coatings developed on AZ31 magnesium alloy by plasma*

electrolytic oxidation', Ceramics International, 38 (2012) p4607-4615.

[77] L.R. Krishna, G.Poshal, G. Sundararajan, '*Influence of electrolyte chemistry on morphology and corrosion resistance of micro arc oxidation coatings deposited on magnerium*', Metallurgical and Materials Transactions A, 4 (201) p3499-3508.

[78] J. Liang, P.B. Srinivasan, C. Blawert, W. Dietzel, '*Comparison of electrochemical corrosion behaviour of MgO and ZrO2 coatings on AM50 magnesium alloy formed by plasma electrolytic oxidation*', Corrosion Science,51 (2009) p2483-2492.

[79] J. Liang, P.B. Srinivasan, C. Blawert, W. Dietzel, '*Influence of pH on the deterioration of plasma electrolytic oxidation coated AM50 magnesium alloy in NaCl solutions*', Corrosion Science,52 2010) p540-547.

[80] H. Duan, C. Yan, F. Wang, '*Effect of electrolyte addivtives on performance of plasma electrolytic oxidation films formed on magnesium alloy AZ91D*', Electrochimica Acta, 52 (2007) p3785-3793.

[81] T.S. Lim, H.S. Ryu, S.H. Hong, '*Electrochemical corrosion properties of CeO_2-containing coatings on AZ31 magnesium alloys prepared by plasma electrolytic oxidation*', Corrosion Science, 62 (2012) p104-111.

[82] K.R. Shin, Y.G. Ko, D.H. Shin, '*Effect of electrolyte on surface properties of pure titanium coated by plasma electrolytic oxidation*', Journal of Alloys and Compounds, 509S (2011) pS478-S481.

[83] V.S. Rudnev, S. Wybornov, I.V. Lukiyanchuk, T. Strasdler, X. Jiang, A.Y. Ustinov, M.S. Vasilyeva, '*Thermal behaviour of Ni- and Cu-containing plasma electrolytic oxide coatings on titanium*', Applied Surface Science, 258 (2012) p8667-8672.

[84] S. Stojadinovic, R. Vasilic, M. Petkovic, L. Zekovic, '*Plasma electrolytic oxidation of titanium in heteropolytungstate acids'*, Surface & Coatings Technol., 206(2011) p575-581.

[85] A.L. Yerokhin, A. Leyland, A. Matthews, '*Kinetic aspects of aluminium titanate layer formation on titanium alloys by plasma electrolytic oxidation*', Applied Surface Science, 200 (2002) p172–184.

[86] F. Jin, P. K. Chu, G. Xu, J. Zhao, D. Tang, H. Tong, '*Structure and mechanical properties of magnesium alloy treated by micro-arc discharge oxidation using direct current and high-frequency bipolar pulsing modes*', Materials Science and Engineering: A, 435-436 (2006) p123-126.

[87] A.L. Yerokhin, X. Nie, A. Leyland, A. Matthews, '*Characterisation of oxide films produced by plasma electrolytic oxidation of a Ti–6Al–4V alloy*', Surface & Coatings Technol., 130 (2000) p195–206.

[88] S. Xin, L. Song, R. Zhao, X. Hu, '*Influence of cathodic current on composition, structure and*

properties of Al2O3 coatings on aluminum alloy prepared by micro-arc oxidation process'. Thin Solid Films, 2006. 515(1): p. 326-332.

[89] C.T. Wu, F.H. Lu, '*Corrosion resistance of $BaTiO_3$ films prepared by plasma electrolytic oxidation*', Surface & Coatings Technol., 166 (2002) p31–36.

[90] X. Nie, A. Leyland, H.W. Song, A.L. Yerokhin, S.J. Dowey, A. Matthews, '*Thickness effects on the mechanical properties of micro-arc discharge oxide coatings on aluminium alloys*', Surface & Coatings Technol., 116–119 (1999) p1055.

[91] A.L. Yerokhin, A.A. Voevodin, V.V. Lyubimov, J. Zabinski, M. Donley, '*Plasma electrolytic fabrication of oxide ceramic surface layers for tribotechnical purposes on aluminium alloys*', Surface & Coatings Technol., 110 (1998) 140

[92] C.S Dunleavy, JA Curran, TW Clyne, '*Plasma Electrolytic Oxidation- Can Plasma Physics help us to make better Coating?*' Available from: http://www.admin.cam.ac.uk/offices/research/documents/local/events/downloads/mh/1.3 Clyne.pdf

[93] A.L. Yerokhin, A. Shatrov, V. Samsonov, P. Shashkov, A. Leyland, A. Matthews, '*Fatigue properties of Keronite coatings on a magnesium alloy*', Surface & Coatings Technol., 182 (2004) p78–84.

[94] S. Matsuzawa, N. Baba, S. Tajima, '*Effect of crystal orientation on anodic oxide film growth of Al*', Electrochim. Acta, 26 (1981) p161–165.

[95] A.L. Yerokhin, L.O. Snizhko, N.L. Gurevina, A. Leyland, A. Pilkington, A. Matthews, '*Spatial characteristics of discharge phenomena in plasma electrolytic oxidation of aluminium alloy*', Surface & Coatings Technol.,177 –178 (2004) p779–783.

[96] E. Matykina, A. Berkani, P. Skeldon, G.E. Thompson, '*Real-time imaging of coating growth during plasma electrolytic oxidation of titanium*', Electrochim. Acta 53 (2007) p1987–1994.

[97] C.S. Dunleavy, I.O. Golosnoy, J.A. Curran, T.W. Clyne, '*Characterisation of discharge events during plasma electrolytic oxidation*', Surface & Coatings Technol., 203 (2009) p3410-3419.

[98] C.S. Dunleavya, J.A. Currana, b, T.W. Clynea, '*Self-similar scaling of discharge events through PEO coatings on aluminium*', Surface & Coatings Technol., 206 (2011) p1051-1061.

[99] R. Arrabal, E. Matykina, T. Hashimoto, P. Skeldon, G.E. Thompson, '*Characterization of AC PEO coatings on magnesium alloys*', Surface & Coatings Technol., 203 (2009) p2207-2220.

[100] A.L. Yerokhin, L.O. Snizhko, N.L. Gurevina, A. Leyland, A. Pilkington, A. Matthews, '*Spatial characteristics of discharge phenomena in plasma electrolytic oxidation of aluminium ally*', Surface & Coatings Technol., 177-178 (2004) p779-783.

[101] B. Kasalica, M. Petkovic, I. Belca, S. Stojadinovic, Lj Zekovic, '*Electronic transitions during plasma electrolytic oxidation of aluminum*', Surface & Coatings Technol., 203 (2009) p3000-3004.

[102] J. Jovovic, S. Stojadinovic, N.M. Sisovic, N. Konjevic, '*Spectroscopic study of plasma during electrolytic oxidation of magnesium- and aluminium- alloy*', Journal of Quantitative Spectroscopy and Radiative Transfer, 113(2012) p1925-1937.

[103] J. Jovovic, S. Stojadinovic, N.M. Sisovic, N. Konjevic, '*Spectroscopic characterization of plasma during electrolytic oxidation (PEO) of aluminium*', Surface & Coatings Technol., 206 (2011) p24-28.

[104] R.O. Hussein, X. Nie, D.O. Northwood, A. Yerokhin, A. Matthews, '*Spectroscopic study of electrolytic plasma and discharging behaviour during the plasma electrolytic oxidation (PEO) process*', Journal of physics D: Applied Physics, 43 (2010) 105203 (13pp).

[105] L. Wang, L. Chen, Z. Yan, W. Fu, '*Optical emission spectroscopy studies of discharge mechanism and plasma characteristics during plasma electrolytic oxidation of magnesium in different electrolytes*', Surface & Coatings Technol., 205 (2010) p1651-1658.

[106] G. C. Wood, C. Pearson, '*Dielectric breakdown of anodic oxide films on valve metals*', Corrosion Science, 7 (1967) p119-125.

[107] S. Ikonopisov, '*Theory of electrical breakdown during formation of barrier anodic films*', Electrochimica Acta, 22 (1977) p1077-1082.

[108] N. Azizi, P. Yiannacouras, '*Gate oxide breakdown*', December 2, 2003, Available from: http://www.azizi.ca/school/ece1768/breakdown.pdf.

[109] B. H. Long, H. H. Wu, B. Y. Long, J. B. Wang, N. D Wang, X. Y. Lu, Z. S. Jin, and Y. Z. Bai, '*Characteristics of electric parameters in aluminium alloy MAO coating process*', Journal of Physics D: Applied Physics, 38 (2005) P3491-3496.

[110] V. Dehnavi, B. L. Luan, D.W. Shoesmith, X.Y. Li, S. Rohani, '*Effect of duty cycle and applied current frequency on plasma electrolytic oxidation (PEO) coating growth behavior*', Surface & Coatings Technol., 226 (2013) 100–107

[111] P.B. Srinivasan, J. Liang, R.G. Balajeee, C. Blawert, M. Störmer, W. Dietzel, '*Effect of pulse frequency on the microstructure, phase composition and corrosion performance of a phosphate-based plasma electrolytic oxidation coated AM50 magnesium alloy*', Applied Surface Science, 256 (2010) p3928-3935.

[112] E.V. Parfenov, A.L. Yerokhin, A. Matthews, '*Impedance spectroscopy characterisation of PEO process and coatings on aluminium*', Thin Solid Films, 516 (2007) p428-432.

[113] D.D. Macdonald, '*Reflections on the history of electrochemical impedance spectroscopy*', Electrochimica Acta, 51 (2006) p1376-1388.

[114] M.E. Orazem, B. Tribollet, (2008) '*Electrochemical Impedance Spectroscopy'*, John Wiley & Sons, Inc., Hoboken, New Jersey.

[115] C. Cao, J. Zhang, (2002),' *An Introduction to Electrochemical Impedance Spectroscopy"*, Science press, Beijing.

[116] R.A. Cottis, R. Newman, (1999), ' *Corrosion Testing Made Easy: Electrochemical Impedance and Noise*', NACE International.

[117] E. Barsoukov, J. R. Macdonald, (2005), *'Impedance Spectroscopy Theory, Experiment, and Applications 2nd* ', John Wiley & Sons, Inc., Hoboken, New Jersey.

[118] A.M. Kauffman, (1997), ' *Understanding electrochemical cells- Technical report 17* ', Solartron Instruments- a division of Solartron Group Ltd, Farnborough, UK

[119] W.H. Mulder, J.H. Sluyters, T. Pajkossy, I. Nyikos, '*Tafel current at fractal electrodes. Connection with admittance spectra*', J. Electroanal. Chem., 285 (1990) p103-115.

[120] C.H. Kim, S.I. Pyun, J.H. Kim, '*An investigation of the capacitance dispersion on the fractal carbon electrode with edge and basal orientations*', Electrochimica Acta, 48 (2003) p3455-3463.

[121] C.A. Schiller, W. Strunz, '*The evaluation of experimental dielectric data of barrier coatings by means of different models*', Electrochimica Acta, 46 (2001) 3619.

[122] J.B. Jorcin, M.E. Orazem, N. Pebere, B. Tribollet, ' *CPE analysis by local electrochemical impedance spectroscopy*', Electrochimica Acta, 51 (2006) p1473-1479.

[123] E.V. Parfenov, A.L. Yerokhin, A. Matthews, '*Frequency response studies for the plasma electrolytic oxidation process*', Surface & Coatings Technol., 201 (2007) p8661-8670.

[124] E.V. Parfenov, A.L. Yerokhin, A. Matthews, '*Small signal frequency response studies for plasma electrolytic oxidation*' Surface & Coatings Technol., 203 (2009) p2896-2904.

[125] E.V. Parfenov, A.L. Yerokhin, (2012), '*Process Control: Problems, Techniques and Applications- Chapter 3: Methodology of Data Acquisition and Signal Processing for Frequency Response Evaluation D uring Plasma Electrolytic Surface Treatments*', Nova Science Publisher,Inc. New York.

[126] W.B..J. Zimmerman, (2006), '*Multiphysics Modelling with Finite Element Methods*', World Scientific Publishing Co. Pte. Ltd., London, UK.

[127] V. Thomée, '*From finite differences to finite elements: A short history of numerical analysis of*

partial differential equations', Journal of Computational and Applied Mathematics, 128 (2001), p1-54.

[128] K.D. Vernon-Parry, '*Scanning electron microscopy: An introduction*', III-Vs Review, 13 (2000) p40-44.

[129] S. Swapp, '*Scanning Electron Microscopy (SEM)*', University of Wyoming, available from: http://serc.carleton.edu/research_education/geochemsheets/techniques/SEM.html.

[130] T. J. Collins, '*ImageJ for microscopy*', BioTechniques, 43 (2007) p S25-S30.

[131] O. Zmeskal, M. Vesely, M. Nezadal, M. Buchnicek, '*Fractal Analysis of Image structures*' HarFA- Harmonic and Fractal Image Analysis, (2001), p3-5. available at: http://www.fch.vutbr.cz/lectures/imagesci/download_ejournal/09_C.Morency.pdf

[132] B.B. Mandelbrot, D.E. Passoja, A.J. Paullay, Nature, 308 (1984) 721–722.

[133] C. S. Lu, International Journal of Fracture, 69 (1995) R77.

[134] C. Morency and R. Chapleau, '*Fractal geometry for the characterisation of urban-related states: Greater Montreal Case*', (2003) available at: http://www.fch.vutbr.cz/lectures/imagesci/download_ejournal/09_C.Morency.pdf

[135] Q. Cheng, Computers & Geosciences, 25 (1999) 1037.

[136] National institute of Llivestock and Grassland Science Nishinasuno, Land Evaluation lab, Dr. Hiroyuki Sasaki, Tochigi, Japan. available from: http://cse.naro.affrc.go.jp/sasaki/fractal/fractal-e.html.

[137] L. Nyikos, T. Pajkossy, ' *Fractal dimension and fractional power frequency-dependent impedance of blocking electrodes* ', Electrochim. Acta 30 (1985) 1533.

[138] S. M. Poljacek, D. Risovic, K. Furic, M. Gojo, '*Comparison of fractal and profilometric methods for surface topography characterization*', Applied Surface Science, 254 (2008) p3449-3458.

[139] G. Guisbiers, O.V. Overschelde, M. Wautelet, P. Leclere, R. Lazzaroni, '*Fractal dimension, growth mode and residual stress of metal thin films*', J. Phy. D: Appl. Phys, 40 (2007) p1077-1079.

[140] D. Risovic, S. M. Poljacek, K. Furic, M. Gojo, '*Inferring fractal dimension of rough/porous surface-A comparison of SEM image analysis and electrochemical impedance spectroscopy methods*', Applied Surface Science, 255 (2008) p3063-3070.

[141] D. Risovic, S. M. Poljacek, M. Gojo, '*On correlation between fractal dimension and*

profilometric parameters in characterization of surface topographies', Applied Surface Science, 255 (2009) p4283-4288.

[142] J.B. Bessone, D.R. Salinas, C.E. Mayer, M. Ebert, W.J. Lorenz, '*An EIS study of aluminium barrier-type oxide films formed in different media*', Electrochim. Acta 37 (1992) 2283.

[143] J.B. Bessone, C. Mayer, K. Juttner, W.J. Lorenz, '*AC-impedance measurements on aluminium barrier type oxide films*', Electrochim. Acta 28 (1983) 171.

[144] H.J.W. Lenderink, M. V.D. Linden, J.H.W. DE Wit, '*Corrosion of aluminium in acidic and neutral solutions*', Electrochim. Acta 38 (1993) 1989.

[145] L. Garrigues, N. Pebere, F. Dabosi, '*An investigation of the corrosion inhibition of pure aluminum in neutral and acidic chloride solutions*', Electrochim. Acta 41 (1996) 1209.

[146] J. Maddala, K. Sambath, V. Kumar, S. Ramanathan, ' *Identification of reaction mechanism for anodic dissolution of metals using Electrochemical Impedance Spectroscopy*', J. Electronal. Chem. 638 (2010) 183.

[147] G. Hsieh, S.J. Ford, T.O. Mason, L.R. Pederson, ' *Experimental limitations in impedance spectroscopy: Part VI. Four-point measurements of solid materials systems* ', Solid State Ionics 100 (1997) 297.

[148] G.S. Popkirov, R.N. Schindler, '*Validation of experimental data in electrochemical impedance spectroscopy*', Electrochim. Acta 38 (1993) 861.

[149] H. Duan, K. Duc, C. Yan, F. Wang, '*Electrochemical corrosion behavior of composite coatings of sealed MAO film on magnesium alloy AZ91D*', Electrochim. Acta, 51 (2006) 2898–2908.

[150] P.L. Bonora, F. Deflorian, L. Fedrizzi, ' *Electrochemical impedance spectroscopy as a tool for investigating underpaint corrosion*', Electrochimica Acta, 41 (1996) 1073-1082.

[151] M.E.P. Souza, M. Ballester b, C.M.A. Freire, ' *EIS characterisation of Ti anodic oxide porous films formed using modulated potential* ', Surface & Coatings Technol., 201 (2007) 7775.

[152] D.J. Marcer, '*Impedance-frequency characteristics of glows, coronas and arcs*', PhD. Thesis, Department of Electronic and Electrical Engineering, University of Sheffield, 1971.

[153] K.Barker, '*Spectral noise and impedance characteristic of glow and corona discharges*', PhD. Thesis, Department of Electronic and Electrical Engineering, University of Sheffield, 1966.

[154] M.W. Bradshaw, '*Impedance-frequency characteristics of glow discharges*' PhD. Thesis, Department of Electronic and Electrical Engineering, University of Sheffield, 1964.

[155] M. Venugopalan, '*Basic process in glow discharge plasmas*', Nuclear Instruments and Methods

in Physics Research B23 (1987) p4025-417.

[156] H. Conrads and M. Schmidt, '*Plasma generation and plasma sources*', Plasma Sources Sci. Technol. 9 (2000) p441-454.

[157] J.T.S. Irvine, D.C. Sinclair and A.R.West, '*Electroceramics: Characterization by Impedance Spectroscopy*', Adv. Mater. 2 (1990) No.3.

[158] Wenbin Xue, Qingzhen Zhu, Qian Jin, Ming Hua, '*Characterization of ceramic coatings fabricated on zirconium alloy by plasma electrolytic oxidation in silicate electrolyte*', Materials Chemistry and Physics, 120 (2010) 656.

[159] Guo-Hua Lv, Huan Chen, Xing-Quan Wang, Hua Pang, Gu-Ling Zhang, Bin Zou, Heon-Ju Lee, Si-Ze Yang, '*Effect of additives on structure and corrosion resistance of plasma electrolytic oxidation coatings on AZ91D magnesium alloy in phosphate based electrolyte*', Surface & Coatings Technol., 205 (2010) S36.

[160] S. P. Werther, (2011) *Process Control: Problems, Techniques, and Applications (Mechanical Engineering Theory and Applications)*, Nova Science Pub Incorporated, New York.

[161] Anonymous, 'Table of physical and chemical constants, chapter 2.6.5 "Dielectric properties of materials", available at: http://www.kayelaby.npl.co.uk/general_physics/2_6/2_6_5.html

[162] A.L. Yerokhin, L.O. Snizhko, N.L. Gurevina, A. Leyland, A. Pilkington, A. Matthews, '*Discharge characterisation in plasma electrolytic oxidation of aluminium*', Journal of Physics D: Applied Physics, 36 (2003) p2110-2120.

[163] R. Arrabal, E. Matykina, T. Hashimoto, P. Skeldon, G.E. Thompson, '*Characterisation of AC PEO coatings on magnesium alloys*', Surface & Coatings Technol., 203 (2009) p2207-2220.

[164] A. L. Yerokhin, V. V. Lyubimov, R. V. Ashitkov, '*Phase formation in ceramic coatings during plasma electrolytic oxidation of aluminium alloys*', Ceramics International, 24 (1998) p l-6.

[165] E. Matykina, A. Berkani, P. Skeldon, G.E. Thompson, '*Rea-time imagimg of coating growth during plasma electrolytic oxidation of titanium*', Electrochimica Acta, 53 (2007) p1987-1994.

[166] Y. Cheng, F. Wu, E. Matykina, P. Skeldon, G.E. Thompson, '*The influences of microdischarge types and silicate on the morphologies and phase compositions of plasma electrolytic oxidation coatings on Zircaloy-2*', Corrosion Science, 59 (2012) p307-315.

[167] S. Moon, Y. Jeong, '*Generation mechanism of microdischarges during plasma electrolytic oxidation of Al in aqueous solutions*', Corrosion Science, 51 (2009) p1506-1512.

[168] S. Stojadinovic, J. Jovovic, M. Petkovic, R. Vasilic, N. Konjevic, '*Spectroscopic and real-time imaging investigation of tantalum plasma electrolytic oxidation (PEO)*', Surface & Coatings

Technol., 205 (2011) p5406-5413.